



THESIS  
3  
2009



This is to certify that the  
dissertation entitled

NUMERICAL ANALYSIS OF TURBULENT REACTING  
FLOWS IN COMPLEX COMBUSTION SYSTEMS

presented by

MURAT YALDIZLI

has been accepted towards fulfillment  
of the requirements for the

Ph.D. degree in MECHANICAL ENGINEERING

  
Major Professor's Signature

03/27/2009  
Date

**PLACE IN RETURN BOX** to remove this checkout from your record.  
**TO AVOID FINES** return on or before date due.  
**MAY BE RECALLED** with earlier due date if requested.

<b>DATE DUE</b>	<b>DATE DUE</b>	<b>DATE DUE</b>

NUMERICAL ANALYSIS OF TURBULENT REACTING FLOWS IN  
COMPLEX COMBUSTION SYSTEMS

by

MURAT YALDIZLI

A DISSERTATION

Submitted to  
Michigan State University  
in partial fulfillment of the requirements  
for the degree of

DOCTOR OF PHILOSOPHY  
MECHANICAL ENGINEERING

2009

ABSTRACT

NUMERICAL ANALYSIS OF TURBULENT REACTING FLOWS IN  
COMPLEX COMBUSTION SYSTEMS

BY

MURAT YALDIZLI

The main objective of this study is to investigate hydrocarbon flames when they are strongly affected by turbulence and/or fuel spray via numerical analysis of chemically reacting turbulent flows in simple and complex combustion systems.

First, direct numerical simulations (DNS) are conducted to study the structure of partially-premixed and non-premixed methane flames in high-intensity two-dimensional isotropic turbulent flows. The results obtained via “flame normal analysis” show local extinction and reignition for both non-premixed and partially-premixed flames. Dynamical analysis of the flame with a Lagrangian method indicates that the time integrated strain rate characterizes the finite-rate chemistry effects and the flame extinction better than the strain rate. It is observed that the flame behavior is affected by the “pressure-dilatation” and “viscous-dissipation” in addition to strain rate. Consistent with previous studies, high vorticity values are detected close to the reaction zone, where the vorticity generation by the “baroclinic torque” was found to be significant. The influences of (initial) Reynolds and Damköhler numbers, and various air-fuel premixing levels on flame and turbulence variables are also studied.

For more complex systems, the subgrid-scale (SGS) filtered mass density function (FMDF) model is employed for large eddy simulations (LES) of partially-premixed methane jet flames and two-phase turbulent reacting flows in a spray-driven axisymmetric dump combustor, respectively. The FMDF is the joint probability density function (PDF) of the scalars and is determined via the solution of a set of stochas-

tic differential equations (SDE).

In the analysis of partially-premixed methane jet flames, the single phase LES/-FMDF is implemented using a highly scalable, parallel hybrid Eulerian-Lagrangian numerical scheme and its applicability and the extent of validity for SGS closure of turbulent hydrocarbon combustion are further established by simulating different methane-air jet flames with the “flamelet” and “finite-rate” kinetics models such as the 1-step global and 12-step reduced chemistry mechanisms. The higher heat release by the flamelet or 1-step models are observed to suppress the strong straining/extinction effects of turbulence on the flame at high jet speeds, while the 12-step model successfully predicts the extend of flame extinction at higher jet speeds. Various formulations of the linear mean square estimation (LMSE) model are employed for the conditional mixing of the scalars in the FMDF equation.

For turbulent spray combustion in the axisymmetric dump combustor, a new two-phase LES model based on a Lagrangian-Eulerian-Lagrangian numerical scheme is introduced. The model is applied here to high Reynolds number compressible turbulent reacting flows in a spray-controlled lean premixed dump combustor. The velocity field is obtained by a high-order compact finite difference method in Eulerian framework, where as the spray is modeled with a Lagrangian mathematical/computational method that allows two-way mass, momentum and energy coupling between phases. The subgrid gas-liquid combustion is modeled with a PDF-based two-phase subgrid combustion model, termed the filtered mass density function (FMDF). Several cases are simulated by using different initial values of Sauter mean diameter, spray and injection angles, liquid fuel to gas mass loading ratio, droplets injection velocity, pulsative spray injection frequency, carrier gas equivalence ratio, inlet temperature and turbulence forcing amplitude.

To my beloved wife Sinem

## ACKNOWLEDGEMENTS

I wish to express my sincere thanks to the National Science Foundation (NSF) and the Office of Naval Research (ONR) for giving me the opportunity to complete this work. I owe my deepest gratitude to my supervisor Dr. Farhad A. Jaber, Professor and Director of Computational Fluid Dynamics Laboratory, first introduced me to the fascinating field of turbulent combustion research. His excellent guidance in the numerical analysis of turbulent reacting flows has been essential for the accomplishment of this work. I am also grateful to my committee members and professors: Dr. Charles Petty, Dr. Nikolai Priezjev, Dr. Indrek Wichman, and Dr. Mei Zhuang for their valuable comments and constructive criticism on this dissertation. Finally, my loving thanks go to my beloved wife Sinem, who has shown great understanding, patience and continuous support towards my PhD research as well as everything else I do.

# TABLE OF CONTENTS

ABSTRACT . . . . .	ii
LIST OF TABLES . . . . .	viii
LIST OF FIGURES . . . . .	ix
<b>1 THE STRUCTURE OF PARTIALLY-PREMIXED METHANE FLAMES IN HIGH-INTENSITY TURBULENT FLOWS . . . . .</b>	<b>1</b>
1.1 Introduction . . . . .	1
1.2 Governing Equations . . . . .	3
1.3 Numerical Solution . . . . .	5
1.4 Results and Discussion . . . . .	7
1.4.1 Physical Flame and Turbulence Structures . . . . .	8
1.4.2 Turbulence and Flame Statistics . . . . .	9
1.4.3 Compositional Flame Structure . . . . .	11
1.4.4 Flame Normal Analysis . . . . .	12
1.4.5 Lagrangian Flame Analysis . . . . .	17
1.4.6 Effects of Various Flow and Flame Parameters . . . . .	21
1.5 Summary and Conclusions . . . . .	24
1.6 Tables and Figures . . . . .	27
<b>2 LARGE-EDDY SIMULATIONS OF TURBULENT METHANE JET FLAMES WITH FILTERED MASS DENSITY FUNCTION . . . . .</b>	<b>50</b>
2.1 Introduction . . . . .	50
2.2 Formulation . . . . .	53
2.2.1 The Filtered Transport Equations . . . . .	53
2.2.2 The Filtered Mass Density Function (FMDF) . . . . .	55
2.3 Numerical Solution . . . . .	59
2.3.1 The Lagrangian Monte Carlo Method . . . . .	60
2.3.2 Consistency . . . . .	61
2.3.3 Parallelization . . . . .	62
2.3.4 Chemistry . . . . .	65
2.3.5 Jet Parameters and Boundary Conditions . . . . .	66
2.4 Results and Discussion . . . . .	67
2.4.1 Turbulence and Flame Statistics . . . . .	68
2.4.2 Compositional Flame Structure . . . . .	70
2.4.3 Subgrid-Scale Mixing . . . . .	74
2.5 Summary and Conclusions . . . . .	78
2.6 Tables and Figures . . . . .	80

3	LARGE-SCALE SIMULATIONS OF TURBULENT SPRAY COMBUSTION IN A DUMP COMBUSTOR VIA TWO-PHASE FMDF . . . . .	100
3.1	Introduction . . . . .	100
3.2	Two-Phase LES/FMDF Model Equations . . . . .	105
3.2.1	Eulerian Gas-Phase LES Equations . . . . .	105
3.2.2	Lagrangian Liquid/Droplet-Phase Equations . . . . .	107
3.2.3	Two-Phase FMDF Formulation . . . . .	110
3.3	Numerical Solution . . . . .	112
3.3.1	Consistency of FMDF . . . . .	114
3.3.2	Combustor Parameters And Boundary Conditions . . . . .	116
3.4	Results and Discussion . . . . .	117
3.4.1	Effect of Sauter Mean Diameter (SMD) . . . . .	117
3.4.2	Effect of Spray Angle ( $\alpha$ ) . . . . .	120
3.4.3	Effect of Injection Angle ( $\beta$ ) . . . . .	122
3.4.4	Effect of Mass Loading Ratio ( $\Gamma$ ) . . . . .	123
3.4.5	Effect of Droplet Injection Velocity ( $u_p$ ) . . . . .	125
3.4.6	Effect of Injection Frequency ( $\psi$ ) . . . . .	126
3.4.7	Effect of Equivalence Ratio ( $\phi$ ) . . . . .	128
3.4.8	Effect of Inlet Gas Temperature ( $T_{in}$ ) . . . . .	130
3.4.9	Effect of Inflow Turbulence . . . . .	132
3.5	Summary and Conclusions . . . . .	134
3.6	Tables and Figures . . . . .	137
3.7	Nomenclature . . . . .	178
	REFERENCES . . . . .	180

# LIST OF TABLES

1.1	Various non-dimensional statistics of the developed initial turbulence field. . . . .	27
1.2	Turbulence parameters in various simulations. . . . .	27
1.3	Flame parameters in various simulations. . . . .	27
2.1	Important parameters of Sandia's piloted turbulent methane jet flames D and F. . . . .	80
3.1	Spray parameters of various tested cases. . . . .	138

# LIST OF FIGURES

1.1	Computational domain, boundary conditions, and initial vorticity and flame fields. . . . .	28
1.2	A schematic view of the flame surface, illustrating various methods employed for the analysis of DNS data. . . . .	28
1.3	Instantaneous contours of temperature for case I-3 at different times; (a) $t/\tau_o = 0.0$ , (b) $t/\tau_o = 1.0$ , (c) $t/\tau_o = 1.5$ and (d) $t/\tau_o = 2.0$ . . . .	29
1.4	Instantaneous contours of $OH$ mass fraction for case I-3 at different times; (a) $t/\tau_o = 0.0$ , (b) $t/\tau_o = 1.0$ , (c) $t/\tau_o = 1.5$ and (d) $t/\tau_o = 2.0$ . . . .	30
1.5	Instantaneous contours of various scalars for case I-3 at $t/\tau_o = 2.0$ ; (a) mixture fraction, (b) $CO$ mass fraction, (c) $CO_2$ mass fraction and (d) $H$ mass fraction. . . . .	31
1.6	Instantaneous contours of various flow variables for case I-3 at $t/\tau_o = 2.0$ ; (a) vorticity and (b) baroclinic torque. . . . .	32
1.7	Two-dimensional energy spectral density function in reacting case I-3 at different times; $t/\tau_o = 0.0$ , (dashed-dot line), $t/\tau_o = 2.0$ (solid line). . . .	33
1.8	The conditional probability density function (PDF) of (a) temperature and (b) strain rate, conditioned on the mixture fraction being between $0.21 < Z < 0.578$ . The PDFs are calculated from the Eulerian data at $t/\tau_o = 0.5$ (solid line), $t/\tau_o = 1.0$ (dotted line) and $t/\tau_o = 2.0$ (dashed-dot line). . . . .	34
1.9	Scatter plots of the temperature in the mixture fraction space for case I-3 at (a) $t/\tau_o = 0.25$ , (b) $t/\tau_o = 1.0$ , (c) $t/\tau_o = 1.5$ and (d) $t/\tau_o = 2.0$ . Solid lines show the initial laminar profiles. . . . .	35
1.10	Scatter plots of different species mass fractions in the mixture fraction space for case I-3 at $t/\tau_o = 1.0$ ; (a) $CO$ mass fraction, (b) $OH$ mass fraction, (c) $CO_2$ mass fraction and (d) $H$ mass fraction. Solid lines show the initial laminar profiles. . . . .	36

1.11	Positions of the flame normal cross-sections on the (a) stoichiometric mixture fraction iso-surface and (b) temperature contours. Flame normal A is at node 425, B is at node 1109, B' is at node 1265, C is at node 1425 and D is at node 1715. . . . .	37
1.12	Comparison of various turbulent variables along the flame normal direction with the corresponding laminar values at different locations and at normalized time of $t/\tau_o = 2.0$ for case I-3; (a) temperature, (b) OH mass fraction, (c) production rate of OH, and (d) CO mass fraction. Laminar profiles; dashed line, turbulent profiles along flame normal A; squared line, B-B'; circled line, C; triangled line; D; plused line. . . . .	38
1.13	Variations of various turbulence and flame variables along the stoichiometric mixture fraction iso-surface at $t/\tau_o = 2.0$ for case I-3; (a) temperature, (b) scalar dissipation rate, (c) OH production rate, and (d) tangential strain rate. . . . .	39
1.14	Variations of (a) total kinetic energy, and (b) pressure-dilatation term in the kinetic energy equation along the stoichiometric mixture fraction iso-surface at $t/\tau_o = 2.0$ for case I-3. . . . .	40
1.15	Variations of (a) vorticity magnitude, and (b) baroclinic term in the vorticity equation along the stoichiometric mixture fraction iso-surface at $t/\tau_o = 2.0$ for case I-3. . . . .	41
1.16	The location of Lagrangian particles at different sections on the stoichiometric mixture fraction iso-surface or perpendicular to this surface for case X-3; (a) $t/\tau_o = 0.0$ , (b) $t/\tau_o = 0.5$ and (c) $t/\tau_o = 1.0$ . . . . .	42
1.17	Temporal variations of the Lagrangian particle properties; (a) temperature, (b) mixture fraction, and (c) strain rate. Each symbol represents a particle initially located at different positions in the domain. Particle A is represented with "●", particle B with "▼", particle C with "◇", particle D with "⊕" and particle E with "■". Initially the relative distance of the particles with respect to the stoichiometric mixture fraction surface is the same. . . . .	43
1.18	Temporal variations of the conditional mean temperature conditioned on the strain rate and mixture fraction; (a) low mixture fraction range, (b) stoichiometric mixture fraction range, (c) high mixture fraction range. (d) Percentage of the difference of the conditional average values of the particle temperature. . . . .	44

1.19	Temporal variations of the probability density function (PDF) of the temperature and the strain rate conditioned on $Z = Z_{stoich}$ at $t/\tau_o = 2.0$ . The crosses refer to Eulerian (grid) data, the circles refer to Lagrangian (particle) data; (a) PDF of temperature, (b) PDF of strain rate. . . . .	45
1.20	The scatter plots of temperature in the mixture fraction space for different cases at $t/\tau_o = 1.5$ ; (a) case I-3, (b) case I-2 and (c) case I-1. (d) The scatter plot of temperature for low strain rate case, case VIII-3. Solid lines show the initial laminar profiles. . . . .	46
1.21	The percentage of the difference between the laminar and average turbulent temperatures at $t/\tau_o = 1.5$ in the mixture fraction domain for various fuel-air premixing levels. The data are gathered from the Eulerian grid points. . . . .	47
1.22	Instantaneous contours of the $CO$ mass fraction for (a) case I-3 and (b) case IX-3 at $t/\tau_o = 1.5$ . . . . .	48
1.23	Temporal variations of the percentage of grid points in the vicinity of the flame surface ( $Z \approx Z_{stoich}$ ) with temperatures less than 1400 K; (a) various Reynolds numbers, and (b) various Damköhler numbers. The data are gathered from the Eulerian grid points. . . . .	49
2.1	Schematic view of the Sandia's piloted methane jet flame. Main jet and pilot jet diameters are $7.2mm$ and $18.2mm$ , respectively. . . . .	81
2.2	Comparison between Monte Carlo (MC) and finite difference (FD) values of the normalized instantaneous filtered temperature; (a) $\Delta_E = 2\Delta$ , and $C_\phi = 8, 16$ , (b) $\Delta_E = \Delta$ , and $C_\phi = 8, 16$ . MC with $C_\phi = 8$ ; thick solid line, FD with $C_\phi = 8$ ; thick dashed line, MC with $C_\phi = 16$ ; solid line, FD with $C_\phi = 16$ ; dashed line. . . . .	82
2.3	Speed-up of the parallelized LES/FMDF calculations relative to those conducted on a 2-processor node. . . . .	83
2.4	Isosurfaces and isocontours of vorticity magnitude, $\Omega$ , obtained by LES/FMDF with the 12-step chemistry model; (a) flame D and (b) flame F. . . . .	84
2.5	Isosurfaces and isocontours of filtered temperature, $\langle T \rangle_L$ , obtained by LES/FMDF with the 12-step chemistry model; (a) flame D and (b) flame F. . . . .	85

2.6	The time-averaged (mean) values and the RMS values of the filtered axial velocity field at $x/D = 15$ ; (a) mean velocity for flame D, (b) mean velocity for flame F, (c) velocity RMS for flame D and (d) velocity RMS for flame F. Symbols, experimental data; dashed-dot line, 1-step model; dashed line, flamelet model; solid line, 12-step model. .	86
2.7	The time-averaged (mean) temperature and RMS of temperature at $x/D = 15$ ; (a) mean temperature for flame D, (b) mean temperature for flame F, (c) RMS of temperature for flame D and (d) RMS of temperature for flame F. Symbols, experimental data; dashed-dot line, 1-step model; dashed line, flamelet model; solid line, 12-step model. .	87
2.8	Profiles of various species mass fractions as predicted by LES/FMDF with the 12-step model at $x/D = 15$ ; (a) $CO_2$ (b) $H_2$ , (c) $CO$ , (d) $OH$ . Circles, measured flame D; squares, measured flame F; dashed line, computed flame D; solid line, computed flame F. . . . .	88
2.9	Profiles of mean heat release for the flamelet and 12-step models in flame D (dashed line, flamelet; solid line, 12-step) and in flame F (long dashed line, flamelet; dashed-dot line, 12-step) at $x/D = 7.5$ . . . . .	89
2.10	Conditional mean temperature and $O_2$ , $CO$ , $H_2$ mass fractions for flame D as predicted by LES/FMDF with 12-step kinetics mechanism and with $C_\phi = 10$ ; (a) and (b) show the results, at $x/D = 7.5$ ; (c) and (d) show the results, at $x/D = 15$ (lines, calculations; symbols, measurements). . . . .	90
2.11	Conditional mean temperature and $O_2$ , $CO$ , $H_2$ mass fractions for flame F as predicted by LES/FMDF with 12-step kinetics mechanism and with $C_\phi = 10$ ; (a) and (b) show the results, at $x/D = 7.5$ ; (c) and (d) show the results, at $x/D = 15$ (lines, calculations; symbols, measurements). . . . .	91
2.12	Scatter plots of temperature vs. mixture fraction at $r/D = 0.83$ for flame D; (a) measurements at $x/D = 7.5$ (975 sample points); (b) measurements at $x/D = 15$ (780 sample points); (c) calculations with LES/FMDF and 12-step mechanism at $x/D = 7.5$ (973 sample points); (d) calculations with LES/FMDF and 12-step mechanism at $x/D = 15$ (762 sample points). . . . .	92

2.13	Scatter plots of temperature vs. mixture fraction at $r/D = 0.83$ for flame F; (a) measurements at $x/D = 7.5$ (1550 sample points); (b) measurements at $x/D = 15$ (976 sample points); (c) calculations with LES/FMDF and 12-step mechanism at $x/D = 7.5$ (1347 sample points); (d) calculations with LES/FMDF and 12-step mechanism at $x/D = 15$ (1097 sample points). . . . .	93
2.14	Comparison between LES/FMDF and experimental data in the mixture fraction space for the 12-step model with $C_\phi = 10$ at $x/D = 15$ ; (a) mean temperature and $O_2$ mass fraction for flame D; (b) mean temperature and $O_2$ mass fraction for flame F; (c) mean $CO$ and $H_2$ mass fractions for flame D; (d) mean $CO$ and $H_2$ mass fractions for flame F (lines, calculations; symbols, measurements). . . . .	94
2.15	The radial variations of the mean temperature as obtained by LES/FMDF with 12-step model and different $C_\phi$ values at $x/D = 15$ ; (a) flame D and (b) flame F (symbols, measurements; long-dashed line, $C_\phi = 6$ ; dashed-dot line, $C_\phi = 8$ ; solid line, $C_\phi = 10$ ; dashed-dot-dot line, $C_\phi = DM1$ ; dashed line, $C_\phi = DM2$ ). . . . .	95
2.16	Conditional mean and RMS of various flame variables as obtained by LES/FMDF with the 12-step model and different $C_\phi$ values for flame D; (a) mean and RMS of temperature at $x/D = 7.5$ ; (b) mean of $CO$ and $H_2$ mass fractions at $x/D = 7.5$ ; (c) mean and RMS of temperature at $x/D = 15$ ; (d) mean of $CO$ and $H_2$ mass fractions at $x/D = 15$ (symbols, measurements; long-dashed line, $C_\phi = 6$ ; dashed-dot line, $C_\phi = 8$ ; solid line, $C_\phi = 10$ ; dashed-dot-dot line, $C_\phi = DM1$ ; dashed line, $C_\phi = DM2$ ). . . . .	96
2.17	Conditional mean and RMS of various flame variables as obtained by LES/FMDF with the 12-step model and different $C_\phi$ values for flame F; (a) mean and RMS of temperature at $x/D = 7.5$ ; (b) mean of $CO$ and $H_2$ mass fractions at $x/D = 7.5$ ; (c) mean and RMS of temperature at $x/D = 15$ ; (d) mean of $CO$ and $H_2$ mass fractions at $x/D = 15$ (symbols, measurements; long-dashed line, $C_\phi = 6$ ; dashed-dot line, $C_\phi = 8$ ; solid line, $C_\phi = 10$ ; dashed-dot-dot line, $C_\phi = DM1$ ; dashed line, $C_\phi = DM2$ ). . . . .	97
2.18	Scatter plots of temperature vs. mixture fraction as obtained by LES/FMDF with the 12-step model and different $C_\phi$ values for flame D at $x/D = 7.5$ , and $r/D = 0.83$ ; (a) $C_\phi = 6$ (1102 sample points); (b) $C_\phi = 8$ (1022 sample points); (c) $C_\phi = DM1$ (1042 sample points); (d) $C_\phi = DM2$ (973 sample points). . . . .	98

2.19	Scatter plots of temperature vs. mixture fraction as obtained by LES/FMDF with the 12-step model and different $C_\phi$ values for flame F $x/D = 7.5$ , and $r/D = 0.83$ ; (a) $C_\phi = 6$ (1418 sample points); (b) $C_\phi = 8$ (1350 sample points); (c) $C_\phi = DM1$ (1376 sample points); (d) $C_\phi = DM2$ (1134 sample points). . . . .	99
3.1	The Eulerian and the Lagrangian fields of the two-phase LES/FMDF methodology. . . . .	139
3.2	Iso-contours of the instantaneous filtered temperature and fuel mass fraction in the non-reacting axisymmetric dump combustor without spray as obtained by LES/FDMF; (a) FD values of temperature, (b) MC values of temperature, (c) FD values of fuel mass fraction, and (d) MC values of fuel mass fraction. . . . .	139
3.3	Iso-contours of the instantaneous filtered temperature and fuel mass fraction in the reacting axisymmetric dump combustor without spray as obtained by LES/FDMF; (a) FD values of temperature, (b) MC values of temperature, (c) FD values of fuel mass fraction, and (d) MC values of fuel mass fraction. . . . .	140
3.4	Iso-contours of the instantaneous filtered temperature and fuel mass fraction in the reacting axisymmetric dump combustor with spray as obtained by LES/FDMF; (a) FD values of temperature, (b) MC values of temperature, (c) FD values of fuel mass fraction, and (d) MC values of fuel mass fraction. . . . .	140
3.5	Radial variations of the instantaneous filtered temperature and fuel mass fraction at axial locations of $x/D = 2$ and $x/D = 4$ ; (a) Non-isothermal non-reacting case without spray, (b) Non-isothermal reacting case without spray, (c) Non-isothermal reacting case with spray. The results are obtained by averaging the instantaneous data in the azimuthal direction and not in time. . . . .	141
3.6	Images of the axisymmetric dump combustor; (a) Picture of experimental setup [1] and (b) Illustration of computational domain and droplet injection. . . . .	142
3.7	Iso-contours of the instantaneous of filtered temperature and fuel mass fraction as obtained by LES/FDMF with various SMD values; (a) $SMD = 30\mu m$ , (b) $SMD = 45\mu m$ , (c) $SMD = 60\mu m$ , (d) $SMD = 90\mu m$ , (e) $SMD = 120\mu m$ . . . . .	143

3.8	Radial variations of various quantities at axial locations of $x/D = 3$ and $x/D = 6$ with various SMD values; (a) Instantaneous filtered temperature, (b) Instantaneous filtered fuel mass fraction, (c) Root mean square (RMS) of filtered pressure (solid line, $30\mu m$ ; dashed line, $45\mu m$ ; long-dashed line, $60\mu m$ ; dashed-dot line, $90\mu m$ ; dashed-dot-dot line, $120\mu m$ ). . . . .	144
3.9	Axial variations of integrated droplet number density with various SMD values (solid line, $30\mu m$ ; dashed line, $45\mu m$ ; long-dashed line, $60\mu m$ ; dashed-dot line, $90\mu m$ ; dashed-dot-dot line, $120\mu m$ ). . . . .	145
3.10	Radial variations of various droplet quantities at axial locations of $x/D = 3$ and $x/D = 6$ with various SMD values; (a) Mean droplet temperature, (b) Mean droplet axial velocity (solid line, $30\mu m$ ; dashed line, $45\mu m$ ; long-dashed line, $60\mu m$ ; dashed-dot line, $90\mu m$ ; dashed-dot-dot line, $120\mu m$ ). . . . .	146
3.11	Iso-contours of the instantaneous filtered density and fuel mass fraction as obtained by LES/FDMF with various spray angles; (a) $\alpha \approx 0$ , (b) $\alpha \approx 20$ , (c) $\alpha \approx 40$ , (d) $\alpha \approx 80$ . . . . .	147
3.12	Radial variations of various quantities at axial locations of $x/D = 3$ and $x/D = 6$ with various spray angles; (a) Instantaneous filtered temperature, (b) Instantaneous filtered fuel mass fraction, (c) Root mean square (RMS) of filtered pressure (solid line, $\alpha \approx 0$ ; dashed line, $\alpha \approx 20$ ; long-dashed line, $\alpha \approx 40$ ; dashed-dot line, $\alpha \approx 80$ ). . . . .	148
3.13	Axial variations of integrated droplet number density with various spray angles (solid line, $\alpha \approx 0$ ; dashed line, $\alpha \approx 20$ ; long-dashed line, $\alpha \approx 40$ ; dashed-dot line, $\alpha \approx 80$ ). . . . .	149
3.14	Radial variations of various droplet quantities at axial locations of $x/D = 3$ and $x/D = 6$ with various spray angles; (a) Mean droplet temperature, (b) Mean droplet axial velocity (solid line, $\alpha \approx 0$ ; dashed line, $\alpha \approx 20$ ; long-dashed line, $\alpha \approx 40$ ; dashed-dot line, $\alpha \approx 80$ ). . . . .	150
3.15	Iso-contours of the instantaneous filtered density and temperature as obtained by LES/FDMF with various injection angles; (a) $\beta \approx 0$ , (b) $\beta \approx 30$ , (c) $\beta \approx 45$ , (d) $\beta \approx 60$ . . . . .	151
3.16	Radial variations of various quantities at axial locations of $x/D = 3$ and $x/D = 6$ with various injection angles; (a) Instantaneous filtered temperature, (b) Instantaneous filtered fuel mass fraction, (c) Root mean square (RMS) of filtered pressure (solid line, $\beta \approx 0$ ; dashed line, $\beta \approx 30$ ; long-dashed line, $\beta \approx 45$ ; dashed-dot line, $\beta \approx 60$ ). . . . .	152

3.17	Axial variations of integrated droplet number density with various injection angles (solid line, $\beta \approx 0$ ; dashed line, $\beta \approx 30$ ; long-dashed line, $\beta \approx 45$ ; dashed-dot line, $\beta \approx 60$ ).	153
3.18	Radial variations of various droplet quantities at axial location of $x/D = 3$ with various injection angles; (a) Mean droplet temperature, (b) Mean droplet axial velocity (solid line, $\beta \approx 0$ ; dashed line, $\beta \approx 30$ ; long-dashed line, $\beta \approx 45$ ; dashed-dot line, $\beta \approx 60$ ).	154
3.19	Iso-contours of the instantaneous of filtered temperature and fuel mass fraction as obtained by LES/FDMF with various droplet mass loading ratios; (a) $\Gamma = 0.01$ , (b) $\Gamma = 0.055$ , (c) $\Gamma = 0.11$ , (d) $\Gamma = 0.22$ , (e) $\Gamma = 0.44$ .	155
3.20	Radial variations of various quantities at axial locations of $x/D = 3$ and $x/D = 6$ with various droplet mass loading ratios; (a) Instantaneous filtered temperature, (b) Instantaneous filtered fuel mass fraction, (c) Instantaneous filtered pressure (solid line, $\Gamma = 0.01$ ; dashed line, $\Gamma = 0.055$ ; long-dashed line, $\Gamma = 0.11$ ; dashed-dot line, $\Gamma = 0.22$ ; dashed-dot-dot line, $\Gamma = 0.44$ ).	156
3.21	Axial variations of integrated droplet number density with various droplet mass loading ratios (solid line, $\Gamma = 0.01$ ; dashed line, $\Gamma = 0.055$ ; long-dashed line, $\Gamma = 0.11$ ; dashed-dot line, $\Gamma = 0.22$ ; dashed-dot-dot line, $\Gamma = 0.44$ ).	157
3.22	Radial variations of various droplet quantities at axial location of $x/D = 3$ with various droplet mass loading ratios; (a) Mean droplet temperature, (b) Mean droplet axial velocity (solid line, $\Gamma = 0.01$ ; dashed line, $\Gamma = 0.055$ ; long-dashed line, $\Gamma = 0.11$ ; dashed-dot line, $\Gamma = 0.22$ ; dashed-dot-dot line, $\Gamma = 0.44$ ).	158
3.23	Iso-contours of the instantaneous of filtered temperature and fuel mass fraction as obtained by LES/FDMF with various droplet injection velocities; (a) $u_p = 15m/s$ , (b) $u_p = 30m/s$ , (c) $u_p = 60m/s$ .	159
3.24	Axial variations of integrated droplet number density with various droplet injection velocities (solid line, $u_p = 15m/s$ ; dashed line, $u_p = 30m/s$ ; long-dashed line, $u_p = 60m/s$ ).	159
3.25	Radial variations of various quantities at axial locations of $x/D = 3$ and $x/D = 6$ with various droplet injection velocities; (a) Instantaneous filtered temperature, (b) Instantaneous filtered fuel mass fraction, (c) Instantaneous filtered total kinetic energy (TKE) (solid line, $u_p = 15m/s$ ; dashed line, $u_p = 30m/s$ ; long-dashed line, $u_p = 60m/s$ ).	160

3.26	Iso-contours of the instantaneous filtered temperature and fuel mass fraction as obtained by LES/FDMF with various injection frequencies; (a) $\psi = 38Hz$ , (b) $\psi = 250Hz$ , (c) $\psi = 500Hz$ , (d) $\psi = 1kHz$ . . . . .	161
3.27	Iso-surfaces of the instantaneous filtered pressure as obtained by LES/FDMF with various injection frequencies; (a) $\psi = 38Hz$ , (b) $\psi = 250Hz$ , (c) $\psi = 500Hz$ , (d) $\psi = 1kHz$ . . . . .	162
3.28	Radial variations of various quantities at axial locations of $x/D = 3$ and $x/D = 6$ with various injection frequencies; (a) Instantaneous filtered fuel mass fraction, (b) Root mean square (RMS) of filtered pressure (solid line, $\psi = 38Hz$ ; dashed line, $\psi = 250Hz$ ; long-dashed line, $\psi = 500Hz$ ; dashed-dot line, $\psi = 1kHz$ ). . . . .	163
3.29	Iso-contours of the instantaneous of filtered temperature and fuel mass fraction as obtained by LES/FDMF with various initial equivalence ratios; (a) $\phi = 0.01$ , (b) $\phi = 0.1$ , (c) $\phi = 0.4$ , (d) $\phi = 0.7$ , (e) $\phi = 1.00$ , (f) $\phi = 2.00$ . . . . .	164
3.30	Iso-surfaces of the instantaneous vorticity field as obtained by LES/FDMF with various initial equivalence ratios; (a) $\phi = 0.01$ , (b) $\phi = 0.1$ , (c) $\phi = 0.4$ , (d) $\phi = 0.7$ , (e) $\phi = 1.00$ , (f) $\phi = 2.00$ . . . . .	165
3.31	Radial variations of various quantities at axial locations of $x/D = 3$ and $x/D = 6$ with various initial equivalence ratios; (a) Instantaneous filtered temperature, (b) Instantaneous filtered fuel mass fraction, (c) Root mean square (RMS) of filtered pressure (solid line, $\phi = 0.01$ ; dashed line, $\phi = 0.1$ ; long-dashed line, $\phi = 0.4$ ; dashed-dot line, $\phi = 0.7$ ; dashed-dot-dot line, $\phi = 0.1$ ; dotted-delta line $\phi = 0.2$ ). . . . .	166
3.32	Radial variations of various droplet quantities at axial location of $x/D = 3$ with various initial equivalence ratios; (a) Mean droplet temperature, (b) Total droplet number (solid line, $\phi = 0.01$ ; dashed line, $\phi = 0.1$ ; long-dashed line, $\phi = 0.4$ ; dashed-dot line, $\phi = 0.7$ ; dashed-dot-dot line, $\phi = 0.1$ ; dotted-delta line $\phi = 0.2$ ). . . . .	167
3.33	Iso-contours of the instantaneous of filtered temperature and fuel mass fraction as obtained by LES/FDMF with various inlet temperatures; (a) $T_{in} = 375^{\circ}K$ , (b) $T_{in} = 475^{\circ}K$ , (c) $T_{in} = 575^{\circ}K$ , (d) $T_{in} = 675^{\circ}K$ , (e) $T_{in} = 775^{\circ}K$ , (f) $T_{in} = 1100^{\circ}K$ . . . . .	168
3.34	Iso-surfaces of the instantaneous vorticity field as obtained by LES/FDMF with various inlet temperatures; (a) $T_{in} = 375^{\circ}K$ , (b) $T_{in} = 475^{\circ}K$ , (c) $T_{in} = 575^{\circ}K$ , (d) $T_{in} = 675^{\circ}K$ , (e) $T_{in} = 775^{\circ}K$ , (f) $T_{in} = 1100^{\circ}K$ . . . . .	169

3.35	Radial variations of various quantities at axial locations of $x/D = 3$ and $x/D = 6$ with various inlet temperatures; (a) Instantaneous filtered temperature, (b) Instantaneous filtered fuel mass fraction, (c) Root mean square (RMS) of filtered pressure (solid line, $T_{in} = 375^\circ K$ ; dashed line, $T_{in} = 475^\circ K$ ; long-dashed line, $T_{in} = 575^\circ K$ ; dashed-dot line, $T_{in} = 675^\circ K$ ; dashed-dot-dot line, $T_{in} = 775^\circ K$ ; dotted-delta line $T_{in} = 1100^\circ K$ ).	170
3.36	Axial variations of integrated droplet number density with various inlet temperature (solid line, $T_{in} = 375^\circ K$ ; dashed line, $T_{in} = 475^\circ K$ ; long-dashed line, $T_{in} = 575^\circ K$ ; dashed-dot line, $T_{in} = 675^\circ K$ ; dashed-dot-dot line, $T_{in} = 775^\circ K$ ; dotted-delta line $T_{in} = 1100^\circ K$ ).	171
3.37	Radial variations of various droplet quantities at axial location of $x/D = 3$ with various initial carrier gas temperatures; (a) Mean droplet temperature, (b) Mean droplet axial velocity (solid line, $T_{in} = 375^\circ K$ ; dashed line, $T_{in} = 475^\circ K$ ; long-dashed line, $T_{in} = 575^\circ K$ ; dashed-dot line, $T_{in} = 675^\circ K$ ; dashed-dot-dot line, $T_{in} = 775^\circ K$ ; dotted-delta line $T_{in} = 1100^\circ K$ ).	172
3.38	Iso-contours of the instantaneous of filtered temperature and fuel mass fraction as obtained by LES/FDMF with various turbulence forcing amplitudes; (a) $\sigma_{ref}$ , (b) $2 \times \sigma_{ref}$ , (c) $4 \times \sigma_{ref}$ .	173
3.39	Iso-surfaces of the instantaneous vorticity field as obtained by LES/FDMF with various turbulence forcing amplitudes; (a) $\sigma_{ref}$ , (b) $2 \times \sigma_{ref}$ , (c) $4 \times \sigma_{ref}$ .	174
3.40	Radial variations of various quantities at axial locations of $x/D = 3$ and $x/D = 6$ with various turbulence forcing amplitudes; (a) Instantaneous filtered temperature, (b) Instantaneous filtered fuel mass fraction, (c) Root mean square (RMS) of filtered pressure (solid line, $\sigma_{ref}$ ; dashed line, $2 \times \sigma_{ref}$ ; long-dashed line, $4 \times \sigma_{ref}$ ).	175
3.41	Axial variations of integrated droplet number density with various turbulence forcing amplitudes (solid line, $\sigma_{ref}$ ; dashed line, $2 \times \sigma_{ref}$ ; long-dashed line, $4 \times \sigma_{ref}$ ).	176
3.42	Radial variations of various droplet quantities at axial location of $x/D = 3$ with various turbulence forcing amplitudes; (a) Mean droplet temperature, (b) Mean droplet axial velocity (solid line, $\sigma_{ref}$ ; dashed line, $2 \times \sigma_{ref}$ ; long-dashed line, $4 \times \sigma_{ref}$ ).	177

# CHAPTER 1

## THE STRUCTURE OF PARTIALLY-PREMIXED METHANE FLAMES IN HIGH-INTENSITY TURBULENT FLOWS

### 1.1 Introduction

Accurate description of various flame regimes in practical combustion systems is difficult due to strong interactions between turbulence and combustion and the presence of a wide range of time and length scales. Understandably, the models developed for combustion systems often assume a certain type of reaction (e.g. slow, fast, premixed, non-premixed), even though most systems cannot be described based on just one type of reaction. Among the proposed numerical models for turbulent combustion (see [2–6] for example), the so called “flamelet” models are very popular due to their relative simplicity [7–12]. In these models, the smallest turbulent motions (often characterized by the Kolmogorov scale) are assumed to be much larger than the flame thickness. Thus, the inner structure of the flame is not affected by the turbulence [13].

Despite its limitations, the direct numerical simulation (DNS) method, has been widely employed for fundamental understanding of various type of turbulent flames [4, 12–18]. In many of the reported simulations, the flow is assumed to be two-dimensional [9, 19, 20]. This is based on the observation that the structure of the transported scalar is mainly two-dimensional, even though the turbulence itself is

three-dimensional [4, 19]. Along with the simplifications for the flow field, the chemistry is also often described by simpler (reduced) reaction models [21] in DNS.

Using DNS with simple chemistry, Poinso *et al.* [11] investigated the effects of partial fuel-air premixing on turbulent flames and have reported significant variations in the local flame burning rate with partial premixing. A similar investigation was conducted by Baum *et al.* [9] for premixed hydrogen flames in two-dimensional turbulence using DNS. Also, to better understand the effects of various flow/combustion parameters on turbulent premixed flames, Haworth *et al.* [22, 23] have conducted a series of simulations of two-dimensional, premixed, turbulent, propane-air flames. Their DNS results indicate that for the non-unity Lewis number, the local flame structure correlates more with the local flame curvature than with the tangential strain rate. Bell *et al.* [24] studied the effect of turbulence on a premixed methane flame with a more sophisticated 20-species, 84-reaction mechanism. Consistent with earlier studies conducted with simpler chemistry model, they have observed that the turbulence enhances the flame speed with a rate faster than the growth in flame surface area. Angoshtari [25] studied the strain and curvature effects on premixed methane flames in high-intensity two-dimensional isotropic turbulence with 1-step, 5-step and 12-step reaction models. It is shown that the 12-step mechanism is able to accurately predict the tear-offs, local extinction and flame pocket formations in an intense turbulence field.

The characteristics of triple flames in partially-premixed hydrogen-air mixtures, and the effects of unsteady strain rate on flame propagation in hydrogen-air and methane-air flames were investigated by Im *et al.* [26–28]. They indicated that the triple flame structure in a partially-premixed hydrogen-air flame is similar to that in a diffusion flame. Maas and Thévenin [20] also used data from two-dimensional DNS of turbulent non-premixed hydrogen-air flames for assessing the Intrinsic Low Dimensional Manifold (ILDM) model. The interactions between chemical reaction

and turbulence in homogeneous compressible turbulent flows have been studied by Jaber *et al.* [29–31]. Their results indicate the complexity of combustion effects on density, pressure, temperature and dilatational velocity fields.

The main objective of this study is to investigate the local and global behavior of partially-premixed and non-premixed (initially) laminar methane flames in high-intensity isotropic turbulent flows. The response of different types of flames to a high intensity turbulent field and the effects of various flow/flame parameters on the flame extinction and reignition are studied. The chemistry is modeled using a 10-step, 14-species reduced reaction mechanism, which has been proven to be accurate under various conditions [32]. A high-order finite difference method [33, 34] is used to integrate the governing equations with periodic and non-reflecting boundary conditions [35, 36] perpendicular and parallel to the flame. The results obtained by Eulerian [15, 37], and Lagrangian [38, 39] analysis of DNS data are discussed below.

## 1.2 Governing Equations

In this section, the governing equations for a compressible reacting flow are presented. For complete description of these equations the reader is referred to the textbooks on the subject [4, 40]. The standard equations representing the conservation of mass and momentum are:

$$\frac{\partial \rho}{\partial t} + \frac{\partial(\rho u_i)}{\partial x_i} = 0, \quad (1.1)$$

$$\frac{\partial(\rho u_i)}{\partial t} + \frac{\partial(\rho u_i u_j)}{\partial x_j} = -\frac{\partial p}{\partial x_i} + \frac{\partial \tau_{ij}}{\partial x_j} + \rho f_i \quad (i = 1, 2, 3), \quad (1.2)$$

where  $\rho$  is the density of mixture,  $u_i$  represents the velocity vector,  $p$  is the pressure,  $\tau_{ij}$  is the viscous stress tensor, and  $f_i$  is the external force in  $i$ th direction. In this

study, the total energy ( $e_t$ ) equation is solved,

$$\frac{\partial(\rho e_t)}{\partial t} + \frac{\partial(\rho u_i e_t)}{\partial x_i} = -\frac{\partial q_i}{\partial x_i} + \frac{\partial \Theta_{ij} u_i}{\partial x_j} + Q_e + \rho \sum_{s=1}^{N_s} [Y_s f_{s,i} (u_i + V_{s,i})], \quad (1.3)$$

where  $Q_e$  is the external energy source or sink,  $\Theta_{ij}$  is the total stress tensor, and  $f_{s,i}$  is the body force on species  $s$  in the  $i$ th direction. The mass fraction of reactive species are described by the following equations:

$$\frac{\partial(\rho Y_s)}{\partial t} + \frac{\partial(\rho u_i Y_s)}{\partial x_i} = -\frac{\partial(\rho Y_s V_{s,i})}{\partial x_i} + \dot{\omega}_s \quad (s = 1, \dots, N_s), \quad (1.4)$$

where  $Y_s$  indicates the mass fraction of species  $s$ , ( $N_s$  is the total number of species),  $V_{s,i}$  is the  $i$ th component of diffusion velocity for species  $s$ , and  $\dot{\omega}_s = W_s \sum_{r=1}^R \nu_{sr} w_r$  ( $\nu_{sr}$  is the difference between stoichiometric reaction constants as obtained by CHEMKIN [41]) is the rate of mass production/destruction per unit volume for species  $s$  with molecular weight of  $W_s$ .

The above system of partial differential equations (Eqs. 1.1 - 1.4) are closed by the equation of state for an ideal gas. The total energy and species enthalpy are expressed as:

$$e_t = \sum_{s=1}^{N_s} h_s Y_s - p/\rho + \frac{1}{2} u_i u_i, \quad h_s(T) = \int_{T_0}^T C_{p_s}(T) dT + \Delta h_{f,s}^0. \quad (1.5)$$

In Eq. 1.5,  $h_s$  is the enthalpy,  $C_{p_s}$  is the specific heat, and  $\Delta h_{f,s}^0$  is the enthalpy of formation of species  $s$ . Here, the enthalpy of formation and the specific heat coefficients are obtained via tables, polynomial functions and the CHEMKIN thermodynamic database [41]. The viscosity coefficient,  $\mu$  of the mixture in the definition of the fluid viscous stress tensor,  $\tau_{ij}$  is calculated based on the viscosity of species [42–44] and

the heat flux vector in Eq. 1.3 is given by:

$$q_i = -\lambda \frac{\partial T}{\partial x_i} + \sum_{s=1}^{N_s} [\rho h_s Y_s V_{s,i}]. \quad (1.6)$$

The first term in Eq. 1.6 represents the Fourier heat conduction term and the second term is the heat transport due to “differential diffusion”. The heat transfer due to radiation and Dufour effects has been neglected. The mixture-averaged thermal conductivity,  $\lambda$  is calculated from the thermal conductivities of individual species.

Computationally, it is very expensive to calculate the complete expression for the diffusion velocity,  $V_{s,i}$  in Eqs. 1.3 and 1.4. A less intensive, yet sufficiently accurate, model is used in this study. In this model, the diffusion velocity is assumed to be the opposite of the binary diffusion coefficient which is calculated from the mixture-averaged formula given by Hirschfelder et al. [45]. The modeled diffusion velocity does not satisfy the global mass conservation equation. To overcome this problem, a correction term is added to each species diffusion velocity.

### 1.3 Numerical Solution

Equations. 1.1 - 1.4 are integrated using the fourth order compact scheme [33, 34] with the periodic boundary conditions on the boundaries perpendicular to the flame and non-reflecting outflow conditions [35, 36] on the boundaries parallel to the flame (Figure 1.1). All simulations are conducted with  $512 \times 512$  uniformly distributed rectangular grid. The turbulence/flame statistics are monitored to assure the accuracy. Some of these statistics are calculated by averaging over all spatial directions, even though the flow is not homogeneous in one direction. The important statistical quantities for a 2D turbulent flow are the total energy  $\sigma_v$ , the vorticity magnitude  $\Omega$ , the dissipation rate of vorticity  $\eta$ , the (integral and micro) length scales  $L$ ,  $l$  and

the corresponding Reynolds numbers  $Re_L$ ,  $Re_l$  defined as

$$\sigma_v = \frac{1}{2} \langle u_i u_i \rangle, \quad \Omega = \frac{1}{2} \langle \omega_i \omega_i \rangle, \quad \eta = \nu \langle |\nabla \times \omega|^2 \rangle. \quad (1.7)$$

$$L = \sigma_v^{\frac{1}{2}} / \eta^{\frac{1}{3}}, \quad l = (\nu \Omega / \eta)^{\frac{1}{2}}, \quad Re_L = (2\sigma_v)^{\frac{1}{2}} L / \nu, \quad Re_l = (2\sigma_v)^{\frac{1}{2}} / \nu. \quad (1.8)$$

In turbulent combustion simulations, a significant part of the computational time is normally devoted to the calculation of molecular properties like viscosity and thermal conductivity [21, 25]. Evaluating the diffusion velocities could be also very expensive as it involves solution of a system of equations of  $3N_s^2$  unknowns ( $N_s$  is the number of species) at each grid point and time step. Our approach is to solve for the zeroth-order (or mixture-averaged) coefficients in the definition of diffusion velocity  $V_{s,i}$  [45] and to calculate the mixture viscosity as  $\mu \approx \sum_{s=1}^{N_s} X_s \mu_s$ . The variations of the species properties (e.g. gas constants) are also approximated by fourth-degree polynomials, which considerably reduces the computational time. The above approximations have been tested for turbulent flames and found to yield accurate results. Our analysis indicate that about 75% of total computational time will be spent for calculating the diffusion coefficients if these approximations are not made.

The chemical kinetics model is based on a reduced reaction mechanism [46, 47], which represents the combustion of methane with a 10-step and 14-species reaction. This mechanism has been reduced from a skeletal mechanism, which itself is derived from the GRI-Mech 2.11 [48] mechanism. The 10-step mechanism has been widely tested [32, 46, 47]. Mohammad [32] studied the effects of strain rate, fuel-air premixing, pressure, and preheating temperature on opposed-jet laminar methane-air flames via detailed and reduced mechanisms. For all of the tested flames, they have found the predictions of the reduced 10- and 12-step mechanisms to be in good agreement with those of the detailed GRI mechanisms.

## 1.4 Results and Discussion

In the simulations considered below, the initial turbulence field is generated by solving the governing equations and boundary conditions with an initially random, solenoidal, and Gaussian velocity field for sufficiently long time. The developed isotropic velocity field, described by a set of non-dimensional variables in Table 1.1, is multiplied by appropriate scale factors and is used as an initial velocity field in all of our reacting simulations. Additionally, the laminar flame data obtained by low-strain opposed-jet simulations are used for initialization of scalar (temperature and mass fraction) fields (Figure 1.1). Tables 1.2 and 1.3 list the initial and final values of some of the important flow/flame parameters for various simulations considered in this study. In Table 1.2,  $u'$  represents the root mean square (rms) of the velocity fluctuations and  $\tau_o$  is the eddy turn-over time. Also in Table 1.2,  $\hat{Da}$  is the Damköhler number which is the ratio of flow to chemical time scales. Damköhler values are relatively low due to high turbulent intensity. The chemical time scale (defined based on the laminar flame thickness, flame speed and the air viscosity at ambient temperature) is fixed.  $\hat{Da}$  is varied by changing the flow time scales. The effects of initial turbulent intensity, Reynolds number, Damköhler number, fuel-air premixing, and flame to turbulence length scale ratio are studied. Partial premixing of 0% (diffusion flame), 37.5%, and 75% air in the fuel stream are considered. Some of the flame parameters, such as the flame thickness, are listed in Table 1.3.

The results presented below are obtained by three different types of analysis (Figure 1.2). Our primary goal is to study the effects of turbulence on the flame structure and the flame dynamics in a “strong” turbulent field. The physical and compositional flame structures are examined with “standard Eulerian methods” [15] and the data at fixed grid points along and perpendicular to the flame. The flame dynamics is studied by a Lagrangian (particle) method. It is noted here that the images in the following sections of this dissertation are presented in color.

### 1.4.1 Physical Flame and Turbulence Structures

In this section, the effect of turbulence on the physical structure of the flame is studied through examination of “flame variables” like temperature, mixture fraction and species mass fractions. The effects of combustion on turbulent energy and vorticity are also investigated. Figures 1.3-1.5 show the iso-contours of several flame variables for case I-3. The temperature contours in Figure 1.3 are consistent with the (stoichiometric) mixture fraction contours in Figures 1.5 and 1.11, illustrating the physical flame structure at different times. Evidently, the initial laminar flame is highly distorted and stretched by the very strong strain field to the extent that the extinction becomes important. Structures similar to edge flames [49] appear on either side of the flame at locations where extinction is significant. Figure 1.4 shows that the contours of  $OH$  mass fraction follow those of the temperature as long as the flame extinction is not significant. However, there are some discontinuities in the  $OH$  mass fraction contours which are not observed in the temperature contours and are due to (local) flame extinction. It has been argued that the  $OH$  radical represents the flame behavior better than the temperature [25, 50]. It is to be noted that the flame is affected by an initially isotropic turbulent flow which has no mean flow convection.

The contours of other major and minor species exhibit similar patterns to those of temperature and  $Y_{OH}$ . This is shown in Figure 1.5, where the iso-contours of the mixture fraction,  $CO$  mass fraction,  $CO_2$  mass fraction and  $H$  mass fraction are considered. Clearly, the patterns in the mixture fraction and carbon monoxide iso-contours resemble those of temperature. However, there are some differences due to finite-rate chemistry and extinction effects. These effects are more pronounced in the carbon dioxide and hydrogen atom contours. The latter show similar behavior to that shown for  $OH$  radical in Figure 1.4.

To assess the effects of combustion on the turbulence, contours of vorticity and

other flow variables are also considered. Figure 1.6(a) shows the iso-contours of vorticity at  $t/\tau_o = 2.0$ . For an isotropic non-reacting flow, there is no preferred directional dependency. However, as the turbulence is affected more by the flame, small-scale, high intensity vorticity values are generated near the flame by the “baroclinic torque”. It is known that the turbulence is affected by the reaction because (i) heat of reaction induces volumetric expansion, which opposes the vorticity field, (ii) the temperature dependency of viscosity increases the dissipation of vorticity close to flame, (iii) vorticity is generated due to the “baroclinic” effect. The latest is very important in the simulated case considered here. This is evident in Figure 1.6(b), where it is shown that the high baroclinic and vorticity values are well correlated. The baroclinic torque ( $[-\omega \cdot (\nabla P \times \nabla \rho)]/\rho^2$ ) is dependent on vorticity and alignment of the pressure and density gradients. There seems to be also a good correlation between the high vorticity values and the flame temperature or the mixture fraction. However, the total kinetic energy (TKE) is not strongly correlated with the flame. The TKE mainly changes by the viscous-dissipation and the pressure-dilatation terms [30]. The viscous-dissipation always transfers energy from the kinetic energy to the internal energy, but the pressure-dilatation term may transfer energy from the internal energy to the kinetic energy at some locations. Our results (not shown) also indicate a very significant increase in the strain rate at regions close to the flame, where the vorticity magnitude is high. The increase in strain rate in turn promotes the scalar dissipation rate, mixing and reaction. However, it also enhances the finite-rate chemistry effects and in some regions even causes flame extinction.

## 1.4.2 Turbulence and Flame Statistics

Expectedly, with the non-periodic boundary condition in the flame-normal direction, the flow does not remain homogeneous in that direction. Nevertheless, the space-averaged statistics provide useful information on the overall flow behavior and

are considered in this section. For example, Figure 1.7 shows that the combustion increases the flow kinetic energy at small scales (or high wavenumbers of energy spectrum), which is understandable since the heat release is confined to narrow reaction zone. However, our results (not shown here) indicate that the kinetic energy decays on average at all times, even though the decay rate is affected significantly by the combustion. Similarly, the spectral density of temperature attains higher values at moderate and high wavenumbers in the reacting case. There are also some effects on the large-scale fluctuations of temperature and density.

Figure 1.8 shows the conditional PDFs of temperature and strain rate, conditioned on the mixture fraction being between  $0.21 < Z < 0.578$ . The conditional statistics have been widely employed in the analysis of both non-reacting [51, 52] and reacting [29, 53–56] turbulent flows. Figure 1.8(a) suggests that there is considerable difference between laminar and turbulent flames. For the turbulent flame, the PDF of temperature broadens in time due to finite-rate chemistry effects and local flame extinction, a clear indication of strong turbulence/strain rate effect. These results are consistent with those reported by Sripakagorn *et al.* [37]. Figure 1.8(b) shows that the strain field is also affected by the combustion. As the turbulence modifies the laminar flame and the local strain rate increases, the flame exhibits significantly more finite-rate chemistry effects and even extinction. Nevertheless, the maximum values of strain rate, scalar dissipation rate, and OH mass fraction continue to increase in time. This is consistent with the formation of separated flame pockets, as the  $OH$  contour plots in Figure 1.4 suggests.

The DNS data indicate that the correlation coefficient between temperature and scalar dissipation rate decreases as the reaction zone is significantly distorted by the turbulence and the flame experiences extinction. Early in the simulation,  $Y_{OH}$  is well correlated with the scalar dissipation rate in the thin laminar flame zones, where the scalar dissipation rate is relatively high. The correlations between the production

rates of  $OH$  and  $CO$  with the scalar dissipation rate are also significant at earlier times. Later on, however, with the significant increase in strain and scalar dissipation rate the flame exhibits signs of extinction and lower values of  $Y_{OH}$ . This lowers the overall correlation between the  $OH$  mass fraction and the scalar dissipation rate. Our results (not shown) also indicate lower correlation between the  $OH$  mass fraction and strain rate. The results for conditional averaged strain rate, conditioned on the scalar dissipation rate, indicate that the strain rate is strongly correlated with the scalar dissipation rate at high strain rate regions.

### 1.4.3 Compositional Flame Structure

Scatter plots of variables like temperature in the mixture fraction domain illustrate the overall state of flame/turbulence in the “flame coordinate system”. In this coordinate system, the temperature normally peaks somewhere near the stoichiometric mixture fraction for a flamelet-type combustion and closely follows the laminar profile depending on the local value of tangential strain rate. However, at locations where the tangential strain rate is very significant, deviations from laminar behavior is expected.

Figure 1.9 shows the scatter plots of temperature at different times in the mixture fraction domain for case I-3. The solid lines represent the initial laminar profiles. As the strong turbulent strain field affects the flame, the heat is transported away from the reaction zone with a rate much faster than the rate it is produced by the reaction. This effectively cools down the flame and leads to low flame temperature and extinction which are marked with considerable scatter in data and deviation from laminar flame. In some regions, the locally extinguished flame reignites due to lower strain rate at later times.

The scatter plots of some of the major and minor species in Figure 1.10 also indicate significant differences between the turbulent and laminar flames. Interest-

ingly, the maximum values of  $Y_{CO_2}$ , and  $Y_{CO}$  are lower than the corresponding laminar values, whereas those of  $Y_{OH}$  and  $Y_H$  are substantially higher in the turbulent flame. Such a behavior, termed the “superflamelet” behavior [57], has also been observed in the experimental [58–60] and large eddy simulation (LES) [57] data. The superflamelet behavior can be related to variable strain/scalar dissipation fields as the laminar flame calculations show similar behavior when a step change in scalar dissipation rate is imposed [61]. Consistent with the LES results of James and Jaber [57], the superflamelet behavior does not seem to be very significant for  $Y_{CO}$  (Figure 1.10(a)). This is in contrast to the experimental observations [58–60]. Additionally, the net  $Y_{CO}$  production rate in the turbulent case is different on the lean and rich sides of the flame, as the turbulence enhances  $Y_{CO}$  production on the lean side but has the tendency to decrease it on the rich side. Similarly,  $OH$  and  $H$  radicals exhibit different behaviors on the rich and lean flame sides (Figure 1.10(b) and Figure 1.10(d)). Experimental data of Barlow *et al.* [62] and DNS results of Mahalingam *et al.* [63] show similar trends for these species.

#### 1.4.4 Flame Normal Analysis

Despite being useful in the overall assessment of flame/turbulence behavior, the space-averaged statistics contain limited information concerning the local flame and turbulence structures. To better understand the turbulence effects on the flame and to directly compare the structures of turbulent and laminar flames, the variations of flow variables along the flame surface and normal to this surface are considered in this section. In our flame normal analysis, the flame surface is represented by the stoichiometric mixture fraction iso-surface (or iso-line in 2D flow). In the flamelet models, it is assumed that the structure of turbulent flame perpendicular to the stoichiometric mixture fraction ( $Z_{stoich}$ ) surface is laminar like, and flame state is characterized by the stoichiometric scalar dissipation rate ( $\chi_{stoich}$ ). For  $\chi_{stoich} > \chi_q$

( $\chi_q$  is the quenching limit of the scalar dissipation rate), flame extinction is possible. Here, we compare the structure of turbulent flame in the direction normal to the stoichiometric mixture fraction iso-surface with that of the laminar flame. Profiles of temperature, and other turbulent variables along and perpendicular to this surface are extracted from the DNS data and are compared with the laminar opposed-jet data. All the results discussed in this section are for case I-3.

Figure 1.11 shows the locations of several flame normal cross-sections along the stoichiometric mixture fraction surface and on the temperature contours. These cross-sections are selected in a way that various types of flames are represented. For instance, sections C and A are located at regions where the flame extinction is either very significant or not important. Additionally, section B-B' is selected for studying the interactions between two neighboring flames.

Figure 1.12 shows the variations of temperature,  $OH$  mass fraction,  $OH$  production rate, and  $CO$  mass fraction in the flame normal direction at sections A, B-B', C and D. Laminar results are also shown for comparison. It is observed in Figure 1.12(a) that the predicted turbulent and laminar temperatures are relatively close at section A. This suggests that the finite-rate chemistry effects and flame extinction are insignificant at section A. In contrast, the laminar and turbulent temperatures are very different in the flame normal direction at section C, where the flame is highly stretched and virtually turned off. At this location, the peak turbulent temperature is around 400 K.

The temperature profile along the flame normal direction at section B-B' (Figure 1.12(a)) can be divided into three different regions. The first region is the "main" flame region with the highest temperature around the stoichiometric mixture fraction point. The location of peak temperature in this region is close to that of the laminar flame, even though the magnitude of temperature is lower. Evidently, the flame is not strongly affected by the turbulence in this region. As we move along

the flame normal direction from B to B', we reach to the second region, where the temperature is considerably lower. In this region, the mixture is lean as the very low mixture fraction values indicate. In the third region, where the mixture fraction is close to stoichiometric and the temperature is normally expected to be comparable to the adiabatic flame temperature, the temperature is actually very low due to flame extinction. At section D, the flame still experiences extinction, yet the extent of it is not as significant as it is at sections B-B' and C. This is also consistent with the temperature iso-contours in Figure 1.11(b), where it is observed that the flame at section D is thicker than that at section C. The temperature profile in the fuel rich side at section D clearly shows the effects of two neighboring flames on each other.

Figures 1.12(b), 1.12(c), 1.12(d) show that the turbulent profiles of  $OH$  and  $CO$  mass fractions and  $OH$  production rate along the flame normal direction at sections A, B-B', C and D are different than the laminar ones, particularly where the strain rate is high. It is noted that the heat is transported away from the flame zone with a rate much faster than the rate it is produced in high strain rate regions, which cools down the flame and decreases the flame temperature. Expectedly, this will result in a decrease in rate of reaction and even local flame extinction. Consistent with the temperature results in Figure 1.12(a), the  $OH$  concentration in turbulent flame is shown to be higher than those in the laminar flame at section A. This "superflamelet" behavior is due to relatively weak but variable strain rate at this region. In contrast,  $Y_{OH}$  values are very small for all mixture fraction values at section C, confirming the flame extinction at this section. This is understandable as the production rate of  $OH$  is virtually zero at section C (Figure 1.12(c)). The profile of  $Y_{CO}$  along the flame normal direction at section C (Figure 1.12(d)) exhibits behavior closer to the temperature than to  $Y_{OH}$ . The non-zero (convex shape) values of  $Y_{CO}$  profile at section C suggests that there is still some reaction, even though the flame is strongly strained at this section.

Figures 1.13-1.15 show the spatial variation of several turbulent quantities along the stoichiometric mixture fraction iso-surface. The locations of flame normal cross sections A, B-B', C and D are also shown in these figures. All the reported variables display oscillatory behavior along the flame surface, consistent with the highly wrinkled flame structure shown in Figures 1.3 and 1.4. As the profiles of temperature and stoichiometric scalar dissipation rate,  $\chi_{stoich}$  in Figures 1.13(a) and (b) show, at section (or point) A the flame has its maximum temperature and minimum scalar dissipation rate; indicating a behavior similar to laminar flames. In contrast at point C, the temperature is the lowest, while the scalar dissipation rate is relatively high. Also at point C, the  $OH$  production rate is nearly zero (Figure 1.13(c)), an indication of flame extinction at this point. Interestingly, the maximum value of the scalar dissipation rate occur at point D and not at C. At point C, the scalar dissipation rate is significant because of lower diffusivity coefficient and stronger turbulent straining in the extinguished flame (Figure 1.11(b)). The flame extinction is also significant at point D. However, the temperature and consequently the molecular diffusivity and scalar dissipation rate are relatively higher at this section.

Our results (not shown) indicate that along the stoichiometric mixture fraction surface the vorticity is somewhat uncorrelated with the flame variables like temperature and  $OH$ . However, the scalar dissipation rate is found to be strongly correlated with the flame temperature, even at locations with noticeable flame extinction [37]. By comparing the strain rate and the scalar dissipation rates along the stoichiometric surface, one can examine the effect of the strain rate on the scalar dissipation rate and the flame. However, our analysis for the entire computational domain indicate that the local values of strain rate and scalar dissipation rate are not very well correlated. This suggests that the coupling between the scalar and turbulent fields is only significant in the "flame region".

Figure 1.14 shows the spatial variations of the total kinetic energy (TKE) and

the pressure-dilatation term in the kinetic energy equation along the stoichiometric mixture fraction surface. Direct numerical simulations of homogeneous reacting turbulent flows [29–31] have shown that the heat of reaction indirectly affects the mean turbulent kinetic energy mainly through the pressure-dilatation and viscous-dissipation terms. It is observed in Figure 1.14(a) that the TKE attains its lowest and highest values at locations where the temperature is high or low. However, there is a relatively weak correlation between TKE and flame temperature. On the other hand, comparison between Figures 1.13(d) and 1.14(a) indicates that the maximum values of TKE generally coincide with the maximum values of the strain rate except at point C. At this point, the strain rate is significant, but TKE is relatively small. The low values of TKE are due to several reasons, one being lack of energy transfer from the internal energy by the pressure-dilatation term. In the TKE equation, the terms that are responsible for production and destruction of TKE have different positive and negative contributions at different locations. For example, the pressure-dilatation term has a tendency to alternatively transfer energy between the internal energy and the kinetic energy [29, 30]. This is evident in Figure 1.14(b), where it is shown that the variations of pressure-dilatation along the flame surface generally coincide with that of TKE. However, as Figure 1.14(b) suggests the pressure-dilatation is insignificant at point C. On the other hand, there is a significant energy transfer from the internal energy to the kinetic energy by the pressure-dilatation term at point D (Figures 1.14(a) and 1.14(b)) which supports the high values of TKE at this location. The viscous-dissipation term in the TKE equation does not vary so much except close to point D. At this point, the turbulent scalar fluctuations, and the flame temperature/molecular diffusivity coefficient are significant (see the scalar dissipation and temperature plots in Figure 1.13). The high temperature values at point D is due to heat diffusion from the neighboring flames and transfer of energy from TKE as well as the heat of reaction.

To further examine the effects of combustion on turbulence, the variations of vorticity magnitude ( $\Omega$ ) along the stoichiometric mixture fraction surface are considered in Figure 1.15(a). The results in this figure indicates that  $\Omega$  peaks at locations where the flame stretching and/or curvature are significant. Evidently, the highest value of  $\Omega$  occurs at  $x/L_x \approx 0.8$ , where a highly distorted flame is located (Figure 1.11(b)). These results can be better explained by examining the baroclinic term in the vorticity equation [29, 30] in Fig. 1.15(b). The baroclinic term is composed of vorticity, pressure gradient and density gradient vectors; both the magnitude and relative alignment of which are important [30]. In two-dimensional flows, vorticity has only one component. The vorticity and density profiles along the stoichiometric mixture fraction surface (not shown) suggest that the high negative values of the baroclinic term are mainly due to negative vorticity, and low density values. Our results also indicate that along the stoichiometric mixture fraction surface the cosine of angle between the pressure and density gradient vectors is close to zero wherever the baroclinic term is significant (Figure 1.15(b)) and is close to one wherever the baroclinic term is insignificant. The contributions of the volumetric expansion term in the vorticity magnitude equation could be negative or positive depending on the flow being in expansion or in contraction [29, 30]. Our results (not shown) indicate that the highest vorticity values occur where the volumetric expansion term has its highest negative value or the flow is in strong contraction.

#### 1.4.5 Lagrangian Flame Analysis

In the Lagrangian method considered in this section, some of the fluid elements are marked with notional particles that are moved with the local fluid velocity and have the same local fluid properties. These particles cover several important flame zones

and are transported according to the following equation:

$$\frac{dX_i^{(n)}}{dt} = v_i^{(n)}, \quad (1.9)$$

where  $X_i$  is the displacement vector,  $v_i$  represents the fluid velocity interpolated to the particle position and  $n$  is the particle index. Equation 1.9 is integrated via an explicit finite difference method and the flow quantities at particle locations are evaluated by a high order interpolation scheme. The instantaneous and average (Lagrangian) particle results for cases I-3 and X-3 are discussed below.

Figure 1.16 shows the evolution of a set of Lagrangian particles originally located along the stoichiometric mixture fraction surface and perpendicular to this surface for the case X-3. As expected, the particle movement is directly related to the stretching and bending of the flame by the turbulent strain field and is very different at different sections. Also, as expected, particles in the left section (labeled (i) in Figure 1.16(a)) are affected less than those in the middle and right sections ((ii), (iii), (iv)) due to weaker strain field at this location (see Figure 1.3). The results at  $t/\tau_o = 0.5$  and  $t/\tau_o = 1.0$  suggest that the flame stretching in the right section (iv) is more than that in the left section (i), while the flames in the middle sections are strongly distorted by the turbulence. These observations are consistent with the vorticity and scalar dissipation rate contours.

Figure 1.17 shows the temporal variations of the turbulent flame temperature, mixture fraction and strain rate for several (sample) particles in case I-3. Different than those particles in the previous figure, these particles are initially located close to the stoichiometric mixture fraction surface, all with the same distance from this surface. Expectedly, the behaviors of particles are different as they follow different trajectories but the temperature of all of them decrease in time due to very low strain rate, endothermic reactions, and/or flame extinction. While some particles display

strong finite-rate chemistry effects and extinction, some are weakly affected by the turbulence. For instance, consider particle “A”, symbolized by “●”. Figures 1.17(c) and 1.17(a) show that with a sharp increase in the strain rate, the temperature of this particle decreases between times  $t/\tau_o = 0$  and  $t/\tau_o = 1.1$  to a very low value. Our results (not shown) also indicate a significant decline in the  $OH$  production rate for this particle. The temperature decline is mainly caused by high strain rate and finite rate chemistry effects. From  $t/\tau_o = 1.1$  to  $t/\tau_o = 1.5$ , the particle moves out of the flame zone to the fuel rich side as shown in Figure 1.17(b), resulting in an increase in its mixture fraction value. After  $t/\tau_o = 1.5$ , particle A again experiences an increase in temperature and consequently an increase in the viscosity coefficient and a decrease in the strain rate. As the low  $OH$  production rate values suggest, this increase in temperature is caused by movement of the particle closer to the flame and not the reignition. The particle B, symbolized by “▼”, shows similar behavior before  $t/\tau_o = 1.5$ . However, this particle does not move back to the flame zone after  $t/\tau_o = 1.5$  and its temperature continuously decreases. In contrast to those particles experiencing strong strain effects and even extinction, there are others that are not significantly affected by the turbulence. For instance, particle “C” (symbolized by “◇”) shows high temperature (Figure 1.17(a)) and  $OH$  production rate at all times since it stays in the flame zone and experiences relatively low strain rates. Interestingly, particle “D”, symbolized by “+”, also keeps its high temperatures before  $t/\tau_o = 1.0$ . However, after  $t/\tau_o = 1.0$ , the temperature of this particle decreases (Figure 1.17(a)) partly due to high strain rates (Figure 1.17(c)).

Figure 1.17(a) shows that the particle E, symbolized by “■,” experiences both the extinction and the reignition. In turbulent flames, the local extinction and reignition processes are primarily controlled by the turbulent strain, mixing and reaction at small scales. Figure 1.17(c) shows that the strain rate is initially high for this particle, leading to sharp decline in temperature before  $t/\tau_o = 0.8$ . Between times

$t/\tau_o = 0.8$  to  $t/\tau_o = 1.1$ , the temperature of particle E continues to decrease while the strain rate decreases and the particle moves out of the flame zone. Between  $t/\tau_o = 1.1$  and  $t/\tau_o = 1.4$ , the particle E stays in the fuel rich side, where it experiences high strain rates (Figure 1.17(c)), accompanied by low  $OH$  production rates. Between  $t/\tau_o = 1.4$  and  $t/\tau_o = 1.8$ , both the temperature and the  $OH$  production rate of particle E increase, suggesting reignition. However, as shown in Figures 1.17(a) and (b) the temperature of particle E again decreases after  $t/\tau_o = 1.8$ .

Figure 1.18 shows the conditional average values of the particle temperature for three different range of initial mixture fraction at different times. These conditional averages are obtained by averaging the temperature of a group of particles which have the same initial mixture fraction and (time) integrated strain rates. The averages are conditioned on the (initial) mixture fraction to study the collective behavior of particles that are initially at the same location with respect to the flame but follow different paths latter on. Also, the averages are conditioned on the integrated strain rate instead of instantaneous strain rate to include the turbulence history effects. The conditional mean temperature in the low mixture fraction (oxidizer) zone, stoichiometric (flame) zone, and high mixture fraction (fuel) zone are shown in Figures 1.18(a), (b), and (c), respectively. Evidently, in all cases the conditional mean temperature decreases. However, the decrease in temperature is more pronounced when the integrated strain rate is higher. A comparison between these results with those obtained based on conditioning with respect to instantaneous strain rate (not shown) suggests that the integrated strain rate represents the effect of turbulence on the flame better than the instantaneous strain rate.

Figure 1.18(d) shows the difference between average particle temperature when it is conditioned on the lowest and highest integrated strain rates. The mean temperature difference, represented by  $\Delta \langle\langle T \rangle\rangle$ , is obtained by subtracting the average particle temperature conditioned on high integrated strain rate from that

conditioned on low integrated strain rate for a range of mixture fraction values. The results for three different mixture fraction ranges are shown. Figure 1.18(d) shows that for all three mixture fraction ranges considered here, the average temperature significantly decreases at high strain rates due to finite-rate chemistry effects and flame extinction. At low strain rates, the flame temperature is generally higher. Nevertheless, the difference between the average temperatures evaluated at low and high integrated strain rates is the highest when the initial mixture fraction of the particles is in the stoichiometric mixture fraction range. The results for the conditional averaged values of  $OH$  production rate (not shown) are consistent with those shown for the temperature.

Figure 1.19 shows the conditional PDFs of the temperature and the strain rate at  $t/\tau_o = 2.0$ . The results at other times are similar and are not shown. These PDFs are calculated from the Eulerian grid points and Lagrangian particle data for  $Z \approx Z_{stoich}$ . Evidently, the PDFs obtained from the Lagrangian particles agree well with those obtained from the Eulerian grid points. This suggests the accuracy of Lagrangian particle analysis. Comparison between the PDFs at  $t/\tau_o = 2.0$  with those at earlier times (not shown) indicate that the initially narrow profile of the conditional PDFs of temperature of the laminar flame extends toward lower temperature values in time as a consequence of finite-rate chemistry/flame extinction. The flame also has a significant (local) effect on the turbulence as the conditional PDFs of the strain rate also broadens toward higher strain rate values in time due to combustion generated turbulence at small scales.

#### 1.4.6 Effects of Various Flow and Flame Parameters

In this section, the dependency of flame and turbulence behaviors on several different flow and flame parameters are examined by various simulations. Table 1.2 and 1.3 provide the relevant information on the cases considered. Cases II-3, III-3 and VIII-

3 have different turbulence intensities and case VIII-3 has been included to show the flame behavior under laminar like conditions. In cases IV-6 and V-7, turbulent Reynolds numbers are varied, while the Damköhler number is kept constant. In cases VI-6 and VII-7, the Damköhler number is changed by modifying the integral turbulent time scale and turbulent intensity, while the chemical time and Reynolds number are kept constant. Finally, cases I-1 and I-2 involve different premixing levels of the fuel with air and are considered to investigate the turbulence effects on various types of flames.

Table 1.3 shows the parameters of three flames with different initial premixing level. For these flames, the iso-contours of various turbulence and flame variables and the scatter plots of temperature and species mass fractions are compared. Figures 1.20(a), (b) and (c) show the scatter plots of temperature in the mixture fraction space for 75%, 37.5% and 0% air-fuel premixing levels, respectively. In all three cases, the flame temperature is considerably lower than the corresponding laminar temperature, similarly showing departure from the flamelet behavior in all flames. In Figure 1.20(d), it is shown that the 75% air-fuel premixed flame does not exhibit very different behavior than the flamelet behavior when turbulence is relatively weak. This confirms that the scatters in Figures 1.20(a), (b), (c) are due to strong turbulent strain field. The results in Figure 1.20 also indicate that the flame is thinner for lower premixing level, even though the peak values themselves are approximately the same in all flames. Moreover, the finite-rate chemistry effects and extinction do not seem to be much more significant in the non-premixed flame, in comparison to partially-premixed flames. Like temperature, the scatter plots of  $OH$  mass fraction indicate significant local flame extinction for all the three flames and again there is an “over-prediction” of the laminar  $OH$  concentration. This behavior, referred to as superflamelet behavior, has also been observed for the  $H$  radical and is consistent with the experimental and DNS results [57–60]. Laminar calculations conducted

with a step function scalar dissipation rate also show superflamelet behavior [61]. Further examination of the data indicate that distinct flame pockets with high  $Y_{OH}$  values are created by the strong turbulence field in all three flames. Additionally, our results indicate that the  $CO$  concentration increases when the amount of premixed air in the fuel stream is increased. However, similar to temperature, the maximum values of the scalar dissipation rate are found to be nearly the same in all flames.

Figure 1.21 shows the percentage of average temperature difference between turbulent and laminar flames for different levels of fuel-air premixing at  $t/\tau_o = 1.5$ . Consistent with the temperature plots shown in Figures 1.9 and 1.20, the maximum temperature difference, representing the extent of finite-rate chemistry effects, occurs close to the stoichiometric mixture fraction point in each flame. Also, the maximum difference between averaged turbulent and laminar temperatures is higher in the 37.5%-air flame in comparison to the other two. This suggests that the 37.5%-air flame is experiencing more extinction. In comparison to the 75%-air flame, the difference between the averaged turbulent and laminar temperatures is smaller in the 0%-air (non-premixed) flame.

The iso-contours of  $Y_{CO}$  in Figure 1.22 illustrates the physical structure of various flames as they are influenced by different flows. The temperature contours exhibit similar trend and are not shown. The effects of turbulence intensity are shown in Figure 1.22(a) and (b), where cases I-3 and IX-3 are considered. As expected, the flame tends to preserve its laminar structure in the lower intensity case IX-3, whereas it is strongly affected by the higher intensity turbulence case I-3, to a degree that turbulent and laminar flame structures become completely different at some locations. The  $Y_{CO}$  profiles are smoother in the flame zone in the low intensity case due to relatively higher temperature and molecular diffusion. The results for cases I-3, IV-6 and V-7 (not shown) indicate that the peak values of  $Y_{CO}$  are lower and the contours of radical species like  $OH$  are smoother in the flame region at lower

Reynolds numbers. Similarly, the  $OH$  concentration values are noticeably lower at lower Damköhler numbers. The magnitude of the scalar dissipation rate is found to increase with a decrease in Damköhler number.

In Figure 1.23, the percentage of grid points which are close to stoichiometric mixture fraction surface and have temperatures below  $1400K$  is shown for flames with different Reynolds and Damköhler numbers. These results quantify the effects of Reynolds and Damköhler number on the finite-rate chemistry and flame extinction. Evidently, there is more scatter in temperature at lower Reynolds number (Figure 1.23(a)), which is partly due to increased thermal diffusivity. Also, there seems to be slightly more scatter in the data for cases with lower Damköhler number (Figure 1.23(b)) which can be attributed to relatively higher turbulent intensity. The temperature iso-contours and the conditional PDFs of the temperature, conditioned on the mixture fraction being close to its stoichiometric value, exhibit trends similar to those shown in Figure 1.23.

## 1.5 Summary and Conclusions

Direct numerical simulations (DNS) are conducted to investigate the interactions of a methane-air laminar flame with a highly unsteady, and strained two-dimensional isotropic turbulent flow. The reaction is modeled with a 10-step, 14-species methane-air reduced mechanism. This mechanism has shown to reproduce the important features of laminar methane flames as obtained by the detailed mechanisms for various strain rates, premixing levels, pressures, and preheating temperatures.

The DNS data are analyzed by both grid-based “Eulerian” and particle-based “Lagrangian” methods. The results indicate that the local extinction frequently occurs at high strain and scalar dissipation rate regions. This is accompanied with the structures similar to edge flames on either side of the extinct flame and pockets

of isolated burning flames. Expectedly, the flame has a negative overall effect on the vorticity and kinetic energy due to reduced local Reynolds number and combustion-induced volumetric (dilatational) fluid motions. However, the flame was found to generate vorticity close to the reaction zone, mainly due to the baroclinic effects. The variations of vorticity and baroclinic torque along the flame surface confirm the vorticity generation by the baroclinic torque.

The strong strain field also makes the compositional turbulent flame structure very different than that of the laminar flame. Close to the stoichiometric mixture fraction surface, the flame exhibits very different temperatures between unburned and adiabatic values; demonstrating the significance of finite-rate chemistry effects and flame extinction. However, close examination of the data along the flame surface indicates that at some points the flame does not experience extinction, even though the strain and scalar dissipation rates are high. This is partly explained by considering the vorticity and kinetic energy variations along the stoichiometric mixture fraction (flame) surface. It is observed that in some locations with high scalar dissipation rate, the pressure-dilatation and viscous-dissipation terms in the kinetic energy equation transfer energy from the kinetic energy to the internal energy.

The two-way interactions between turbulence and combustion and the dynamical behavior of the flow/flame variables are shown to be well captured by the Lagrangian particle analysis. It is observed that the particles experience very different behavior, depending on their trajectories, even if they are initially at the same position within the flame. While some particles exhibit complete extinction, some are not virtually affected by the turbulence. It is concluded that the time integrated Lagrangian strain rate is a better parameter for characterization of the finite-rate chemistry effects and flame extinction than the strain rate itself.

The influences of (initial) turbulence intensity, Reynolds and Damköhler numbers, and air-fuel premixing on the flame properties and turbulence are also studied. It

is observed that by changing the flame-air premixing, the turbulence is not greatly affected, even though the flame always experiences extinction in an intense turbulence field. The  $CO$  concentration was found to increase and the flame thickness was found to decrease with an increase in the partial premixing of the fuel with oxidizer. Also, within the flame zone, the  $OH$  concentration was found to increase with an increase in Reynolds number or Damköhler number.

## 1.6 Tables and Figures

Table 1.1: Various non-dimensional statistics of the developed initial turbulence field.

$\sigma_v$	$\Omega$	$\eta$	$l$	$L$	$Re_l$	$Re_L$
0.359	8.94	2.75	0.06	0.427	9.71	230.32

Table 1.2: Turbulence parameters in various simulations.

Case	$u' (cm \cdot s^{-1})$	$l (cm)$	$\tau_o (s)$	$Re_l$		$\hat{Da}$
	$t_i$	$t_i$	$t_i$	$t_i$	$t_f$	$t_i$
<i>I</i> – *	2256	0.021	6.63e-5	293	103	5.04e-03
<i>II</i> – *	3000	0.021	4.98e-5	390	135	3.79e-03
<i>III</i> – *	4800	0.021	3.11e-5	624	257	2.37e-03
<i>IV</i> – *	1641	0.015	6.63e-5	152	90	5.04e-03
<i>V</i> – *	1026	0.010	6.63e-5	63	46	5.04e-03
<i>VI</i> – *	3102	0.015	3.51e-5	293	144	2.67e-03
<i>VII</i> – *	4963	0.010	1.85e-5	293	138	1.04e-03
<i>VIII</i> – *	6	0.021	2.49e-2	0.8	2.1	1.89e+00
<i>IX</i> – *	226	0.021	6.63e-4	30	24	5.04e-02
<i>X</i> – *	4800	0.029	4.13e-5	846	357	3.14e-03

\* Flame conditions/parameters are different and are provided in Table 1.3.

Table 1.3: Flame parameters in various simulations.

No.	Premixing (%)	$\delta (cm)$	$\delta/L$	Turbulence cases considered
* – 1	0	0.327	2.19	I
* – 2	37.5	0.250	1.67	I
* – 3	75	0.263	1.76	I, II, III, VIII, IX
* – 4	75	0.353	2.36	I
* – 5	75	0.443	2.97	I
* – 6	75	0.191	1.76	IV, VI
* – 7	75	0.119	1.76	V, VII
* – 8	75	0.349	1.76	X

\* Turbulence conditions/parameters are presented in Table 1.2.

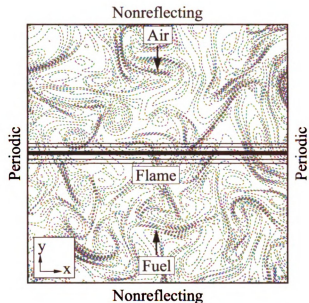


Figure 1.1: Computational domain, boundary conditions, and initial vorticity and flame fields.

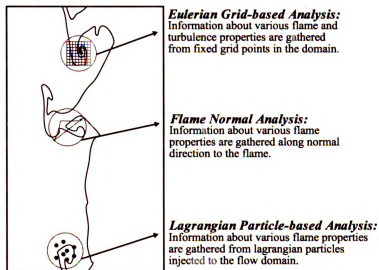


Figure 1.2: A schematic view of the flame surface, illustrating various methods employed for the analysis of DNS data.

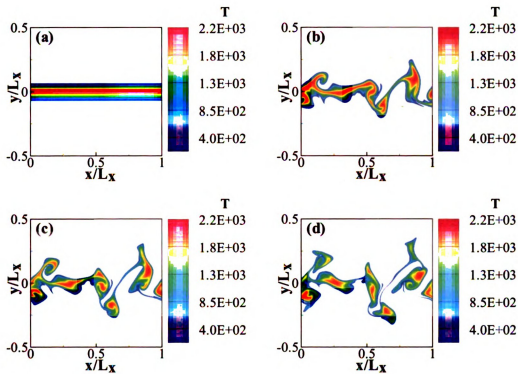


Figure 1.3: Instantaneous contours of temperature for case I-3 at different times; (a)  $t/\tau_o = 0.0$ , (b)  $t/\tau_o = 1.0$ , (c)  $t/\tau_o = 1.5$  and (d)  $t/\tau_o = 2.0$ .

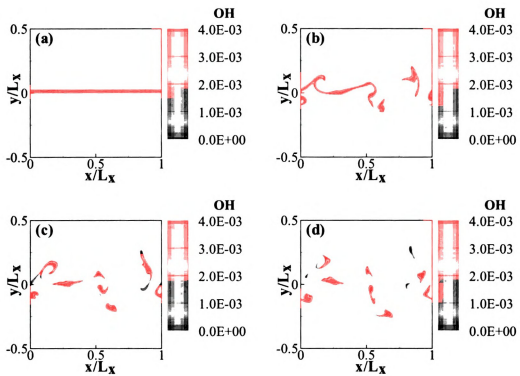


Figure 1.4: Instantaneous contours of  $OH$  mass fraction for case I-3 at different times; (a)  $t/\tau_o = 0.0$ , (b)  $t/\tau_o = 1.0$ , (c)  $t/\tau_o = 1.5$  and (d)  $t/\tau_o = 2.0$ .

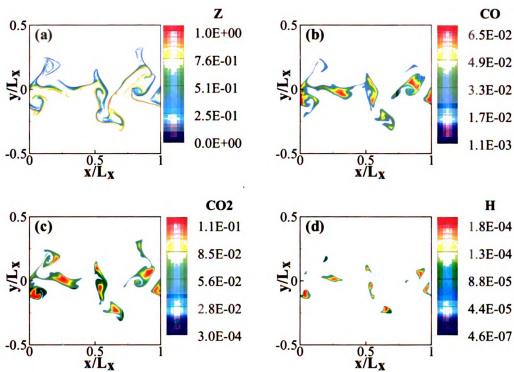


Figure 1.5: Instantaneous contours of various scalars for case I-3 at  $t/\tau_0 = 2.0$ ; (a) mixture fraction, (b)  $CO$  mass fraction, (c)  $CO_2$  mass fraction and (d)  $H$  mass fraction.

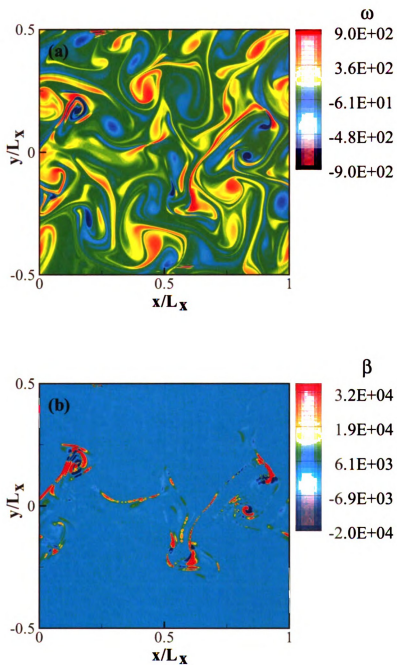


Figure 1.6: Instantaneous contours of various flow variables for case I-3 at  $t/\tau_o = 2.0$ ; (a) vorticity and (b) baroclinic torque.

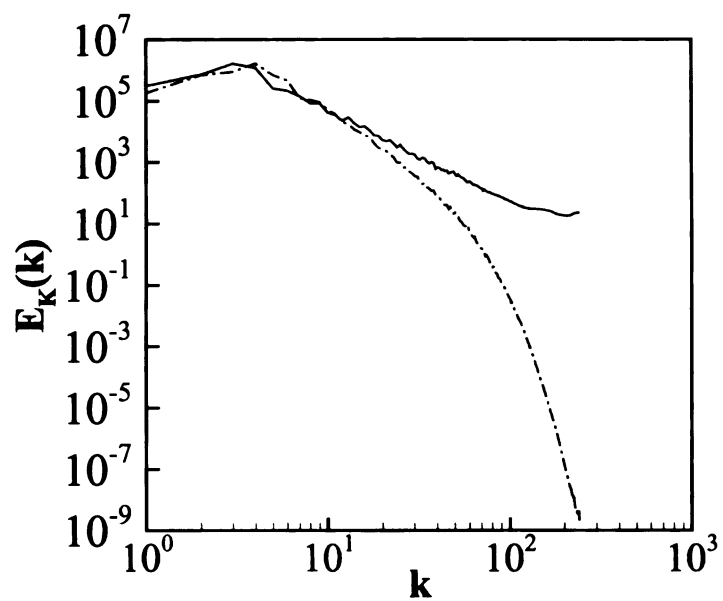


Figure 1.7: Two-dimensional energy spectral density function in reacting case I-3 at different times;  $t/\tau_o = 0.0$ , (dashed-dot line),  $t/\tau_o = 2.0$  (solid line).

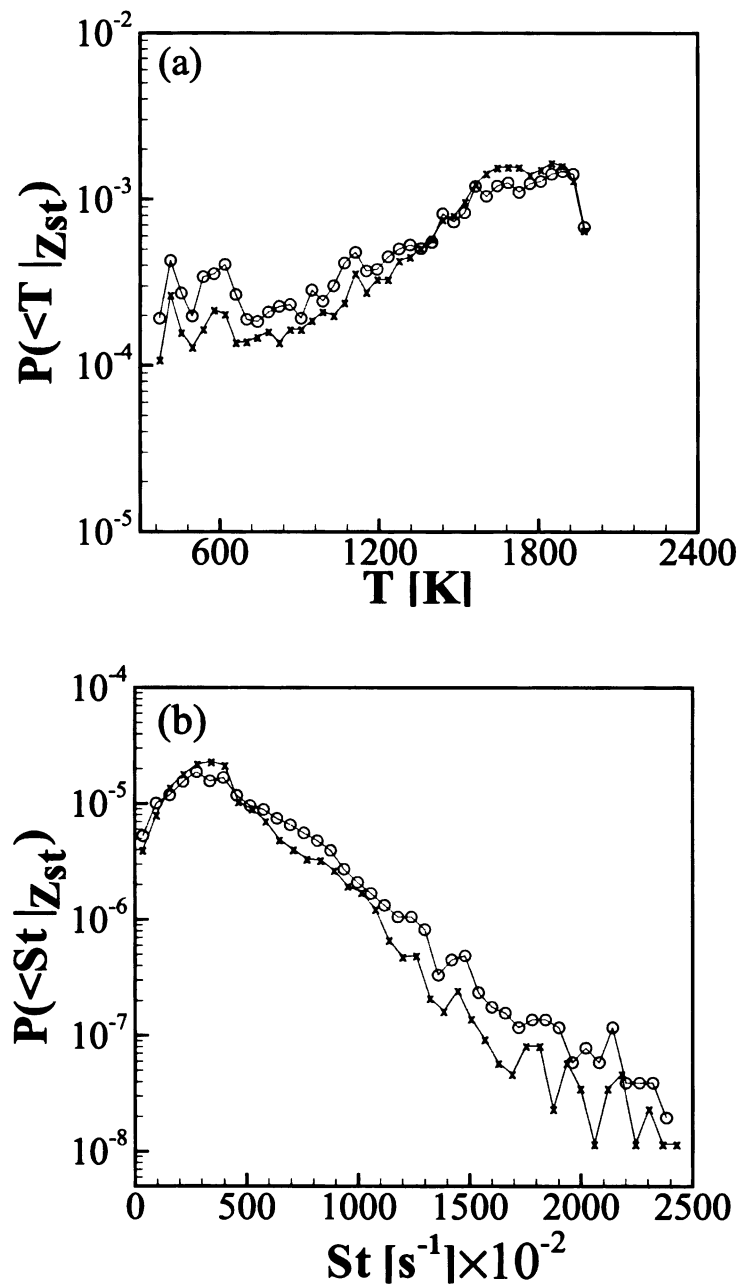


Figure 1.8: The conditional probability density function (PDF) of (a) temperature and (b) strain rate, conditioned on the mixture fraction being between  $0.21 < Z < 0.578$ . The PDFs are calculated from the Eulerian data at  $t/\tau_0 = 0.5$  (solid line),  $t/\tau_0 = 1.0$  (dotted line) and  $t/\tau_0 = 2.0$  (dashed-dot line).

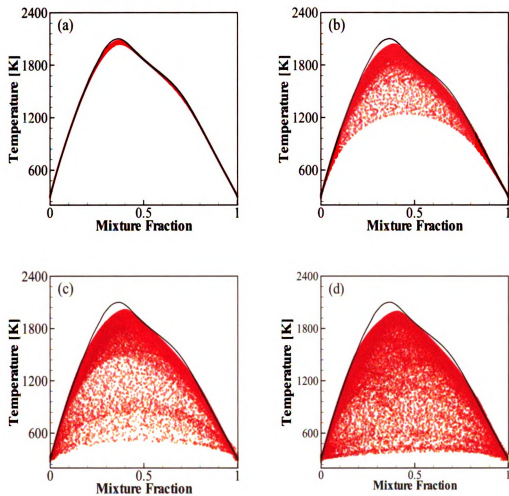


Figure 1.9: Scatter plots of the temperature in the mixture fraction space for case I-3 at (a)  $t/\tau_o = 0.25$ , (b)  $t/\tau_o = 1.0$ , (c)  $t/\tau_o = 1.5$  and (d)  $t/\tau_o = 2.0$ . Solid lines show the initial laminar profiles.

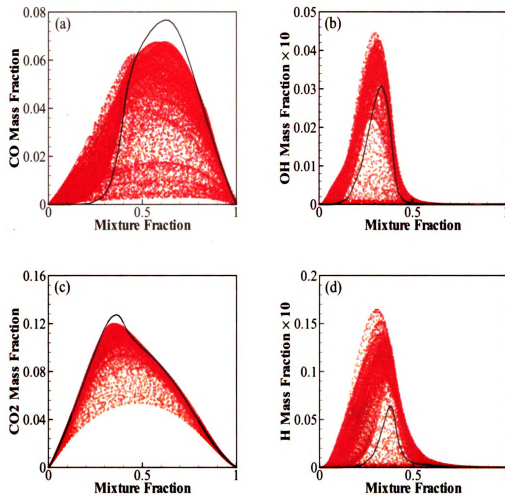


Figure 1.10: Scatter plots of different species mass fractions in the mixture fraction space for case I-3 at  $t/\tau_D = 1.0$ ; (a) *CO* mass fraction, (b) *OH* mass fraction, (c) *CO<sub>2</sub>* mass fraction and (d) *H* mass fraction. Solid lines show the initial laminar profiles.

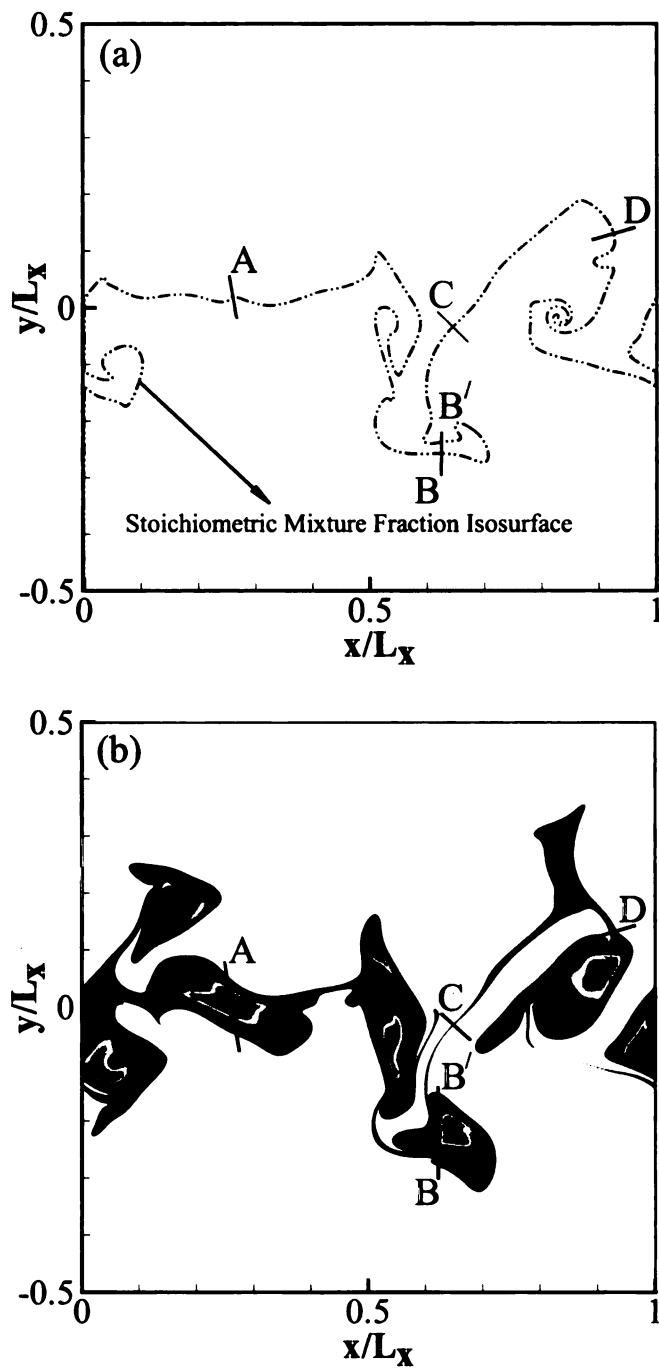


Figure 1.11: Positions of the flame normal cross-sections on the (a) stoichiometric mixture fraction iso-surface and (b) temperature contours. Flame normal A is at node 425, B is at node 1109, B' is at node 1265, C is at node 1425 and D is at node 1715.

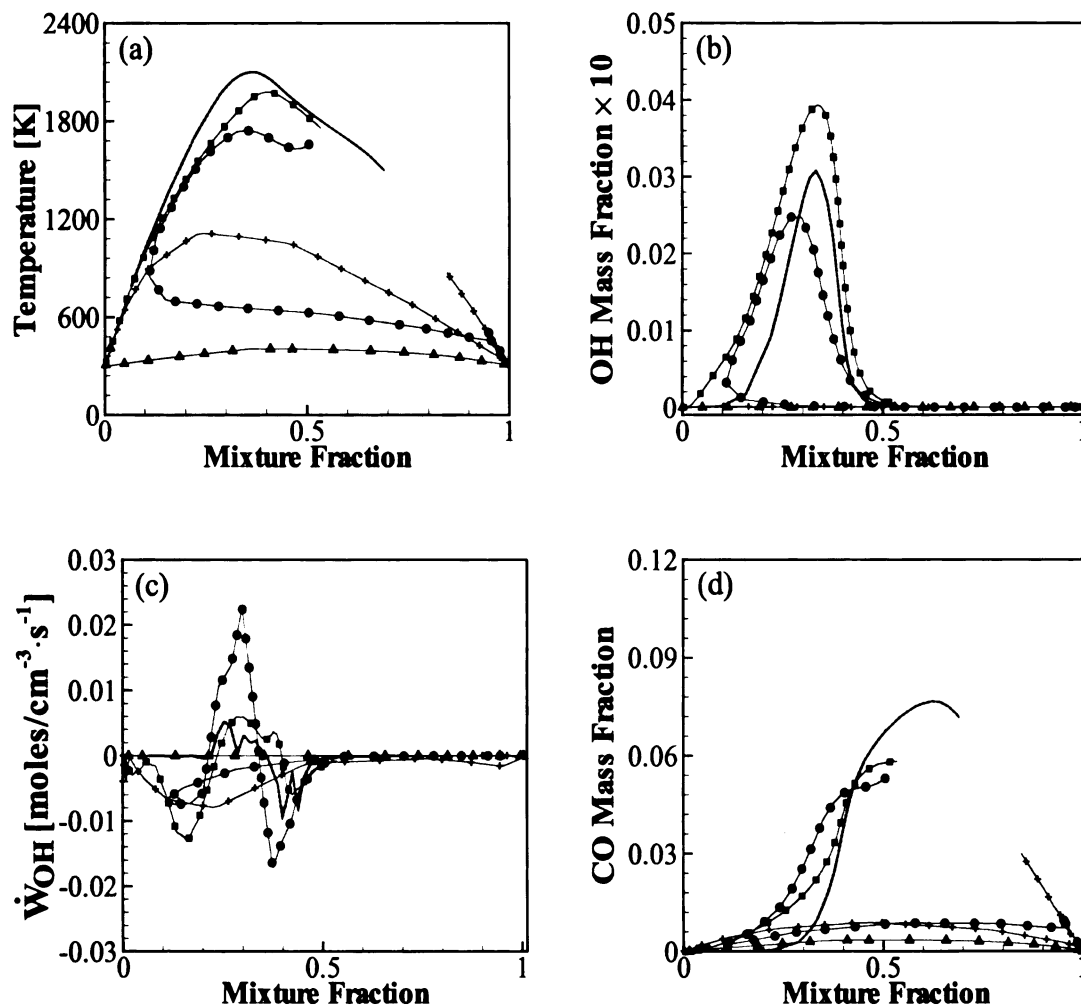


Figure 1.12: Comparison of various turbulent variables along the flame normal direction with the corresponding laminar values at different locations and at normalized time of  $t/\tau_o = 2.0$  for case I-3; (a) temperature, (b)  $OH$  mass fraction, (c) production rate of  $OH$ , and (d)  $CO$  mass fraction. Laminar profiles; dashed line, turbulent profiles along flame normal A; squared line, B-B'; circled line, C; triangled line; D; plused line.

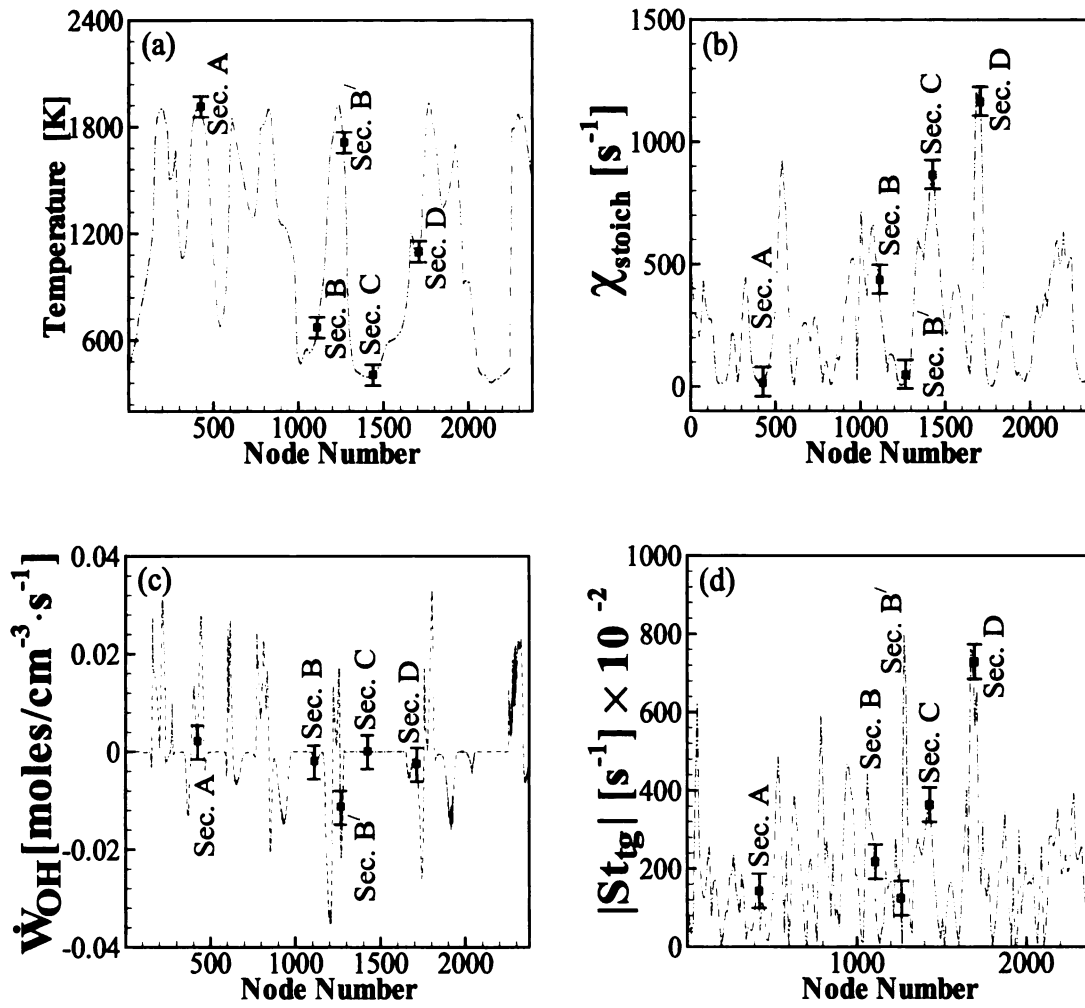


Figure 1.13: Variations of various turbulence and flame variables along the stoichiometric mixture fraction iso-surface at  $t/\tau_0 = 2.0$  for case I-3; (a) temperature, (b) scalar dissipation rate, (c)  $OH$  production rate, and (d) tangential strain rate.

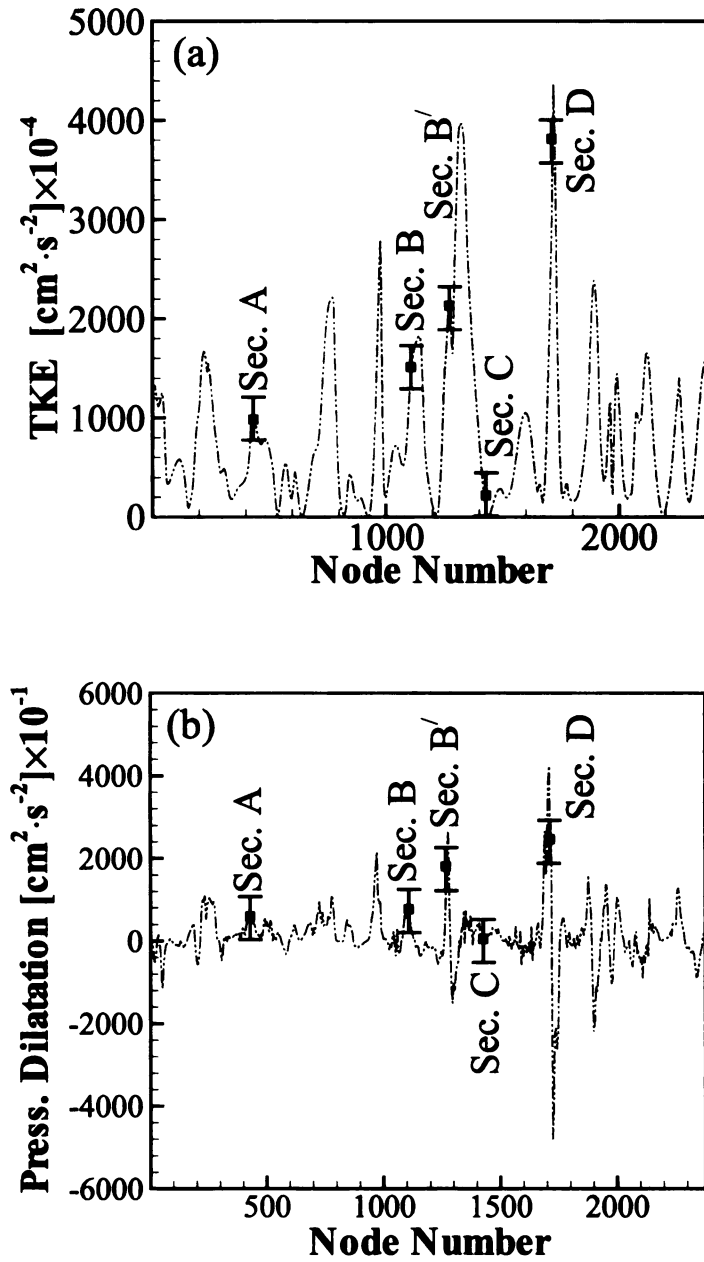


Figure 1.14: Variations of (a) total kinetic energy, and (b) pressure-dilatation term in the kinetic energy equation along the stoichiometric mixture fraction iso-surface at  $t/\tau_0 = 2.0$  for case I-3.

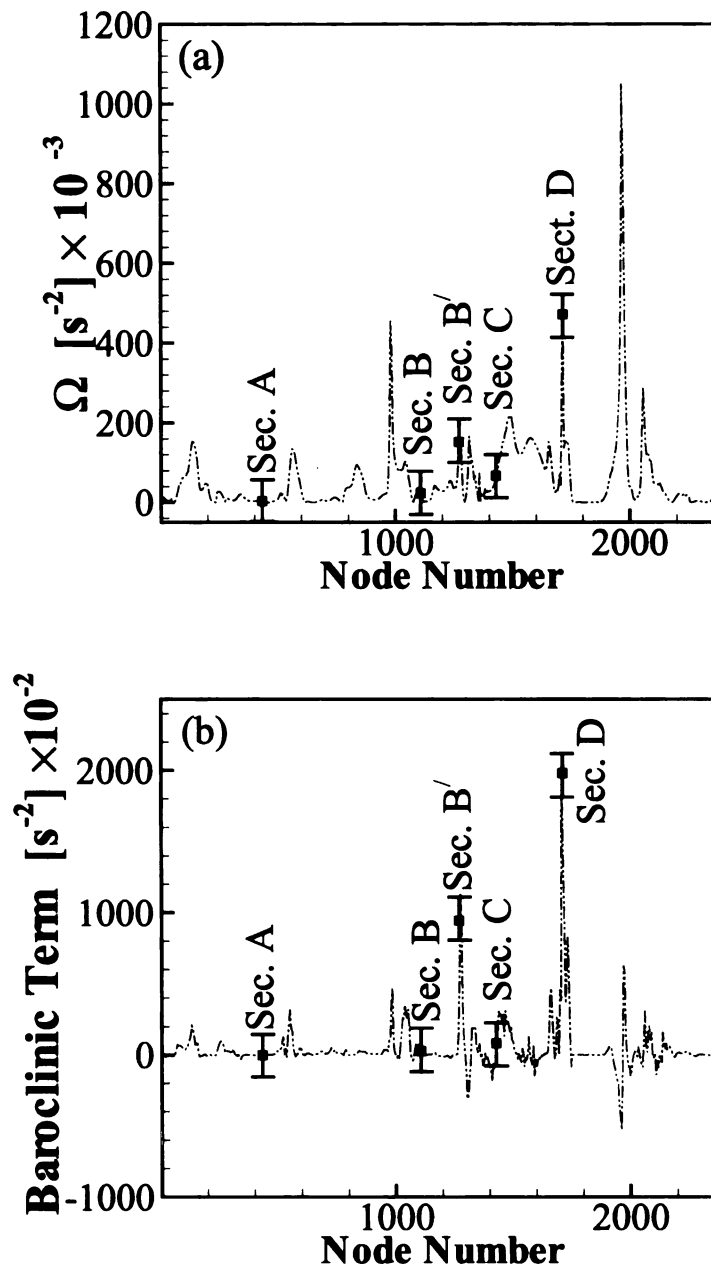


Figure 1.15: Variations of (a) vorticity magnitude, and (b) baroclinic term in the vorticity equation along the stoichiometric mixture fraction iso-surface at  $t/\tau_0 = 2.0$  for case I-3.

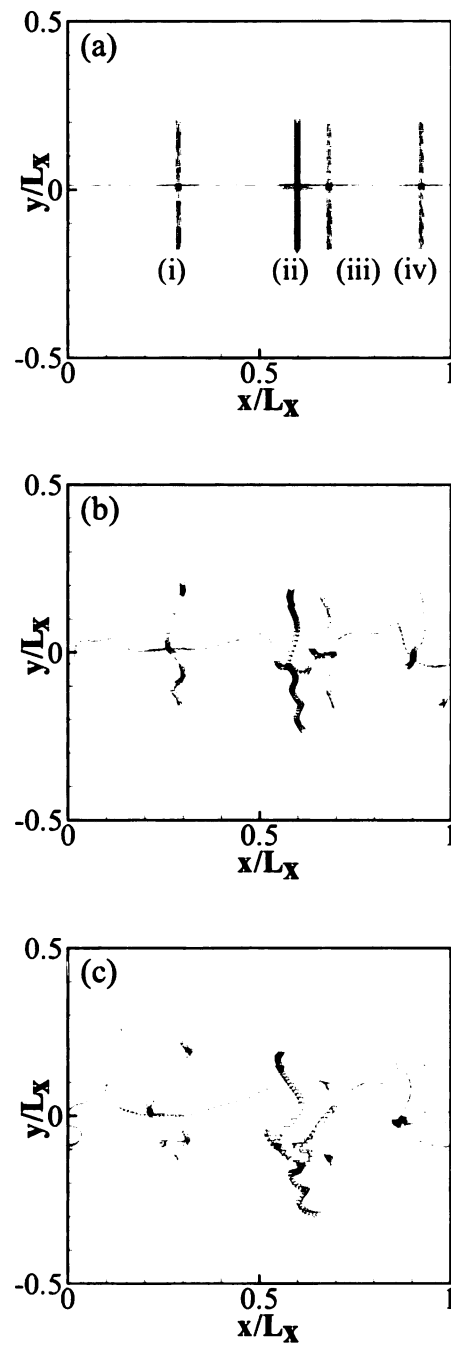


Figure 1.16: The location of Lagrangian particles at different sections on the stoichiometric mixture fraction iso-surface or perpendicular to this surface for case X-3; (a)  $t/\tau_0 = 0.0$ , (b)  $t/\tau_0 = 0.5$  and (c)  $t/\tau_0 = 1.0$ .

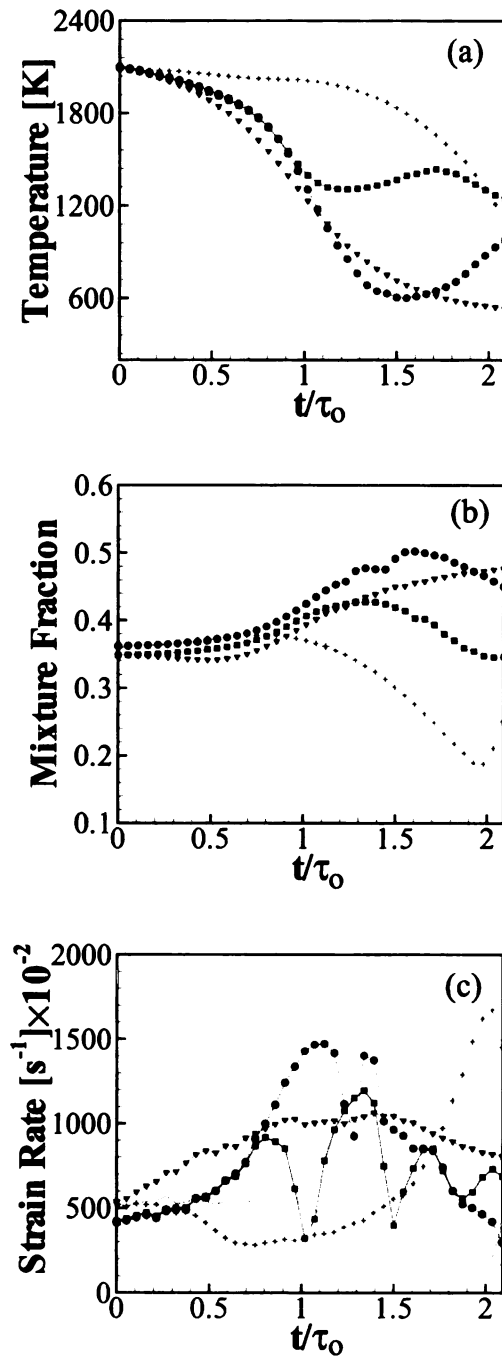


Figure 1.17: Temporal variations of the Lagrangian particle properties; (a) temperature, (b) mixture fraction, and (c) strain rate. Each symbol represents a particle initially located at different positions in the domain. Particle A is represented with “●”, particle B with “▼”, particle C with “◇”, particle D with “+” and particle E with “■”. Initially the relative distance of the particles with respect to the stoichiometric mixture fraction surface is the same.

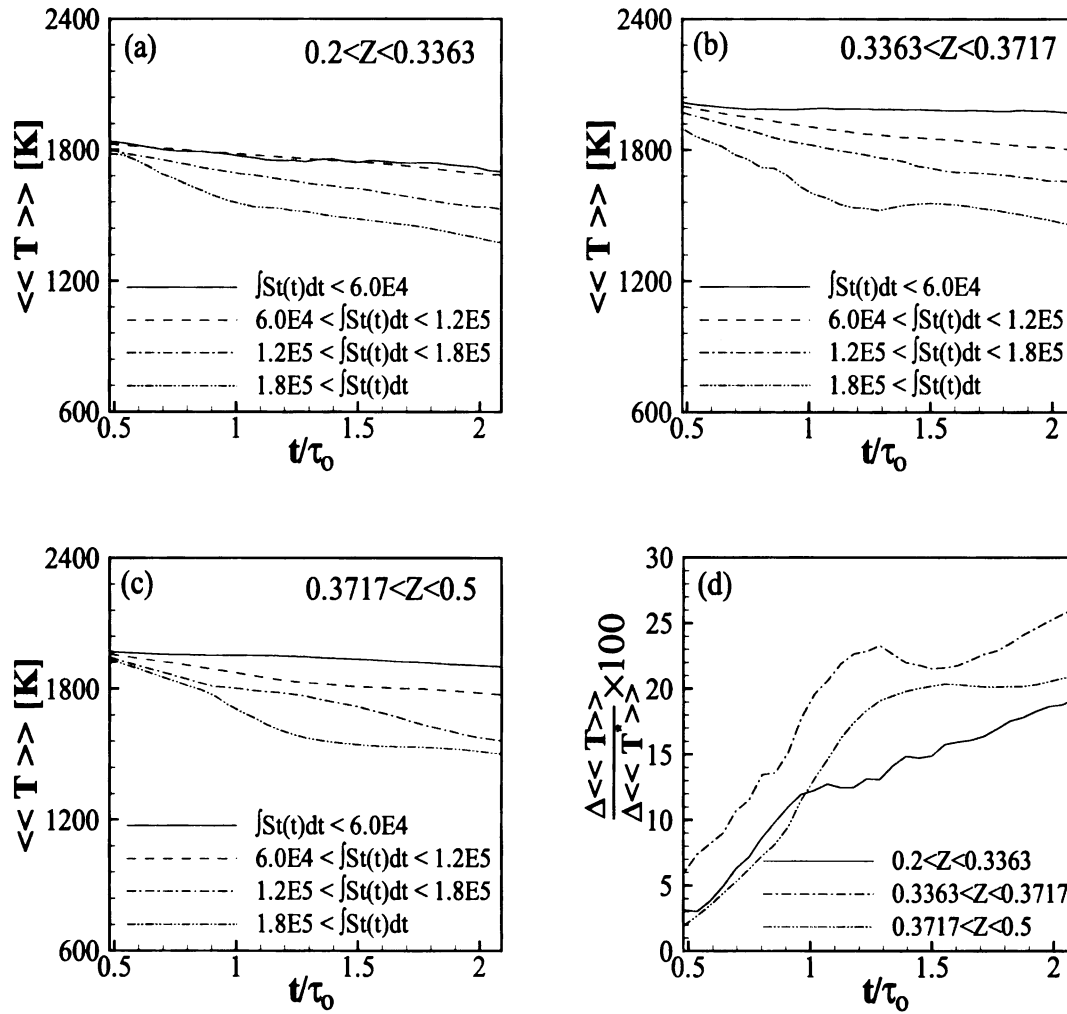


Figure 1.18: Temporal variations of the conditional mean temperature conditioned on the strain rate and mixture fraction; (a) low mixture fraction range, (b) stoichiometric mixture fraction range, (c) high mixture fraction range. (d) Percentage of the difference of the conditional average values of the particle temperature.

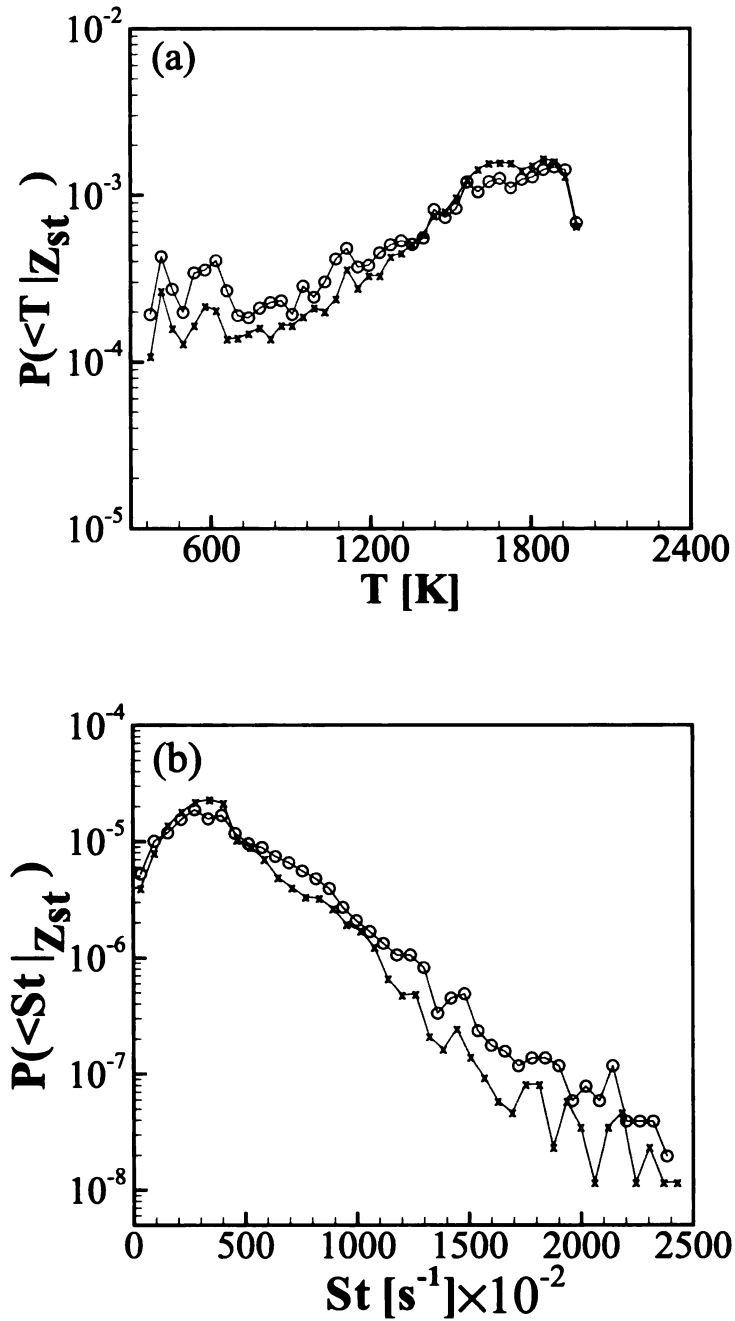


Figure 1.19: Temporal variations of the probability density function (PDF) of the temperature and the strain rate conditioned on  $Z = Z_{stoich}$  at  $t/\tau_o = 2.0$ . The crosses refer to Eulerian (grid) data, the circles refer to Lagrangian (particle) data; (a) PDF of temperature, (b) PDF of strain rate.

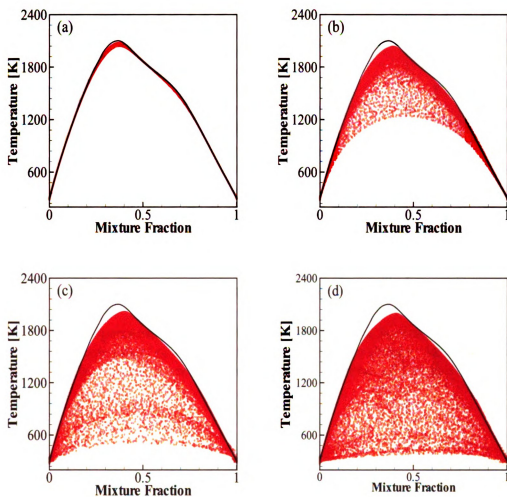


Figure 1.20: The scatter plots of temperature in the mixture fraction space for different cases at  $t/\tau_o = 1.5$ ; (a) case I-3, (b) case I-2 and (c) case I-1. (d) The scatter plot of temperature for low strain rate case, case VIII-3. Solid lines show the initial laminar profiles.

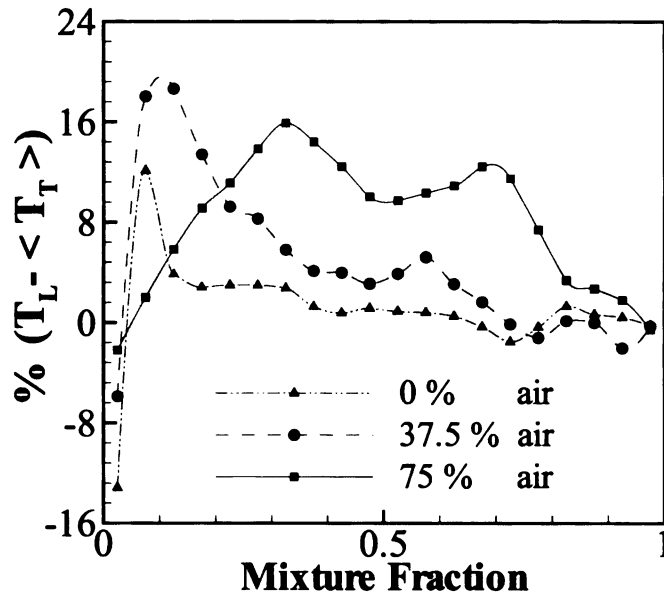


Figure 1.21: The percentage of the difference between the laminar and average turbulent temperatures at  $t/\tau_o = 1.5$  in the mixture fraction domain for various fuel-air premixing levels. The data are gathered from the Eulerian grid points.

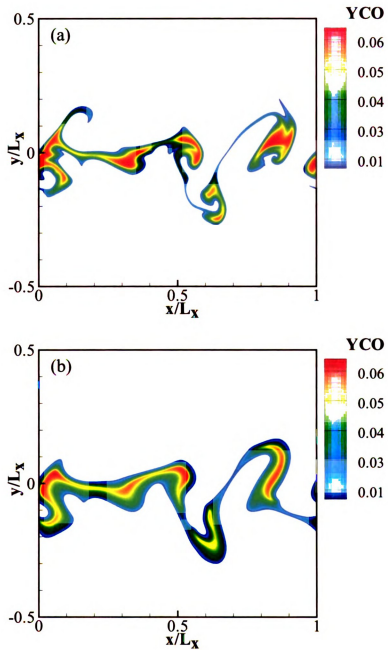


Figure 1.22: Instantaneous contours of the  $CO$  mass fraction for (a) case I-3 and (b) case IX-3 at  $t/\tau_o = 1.5$ .

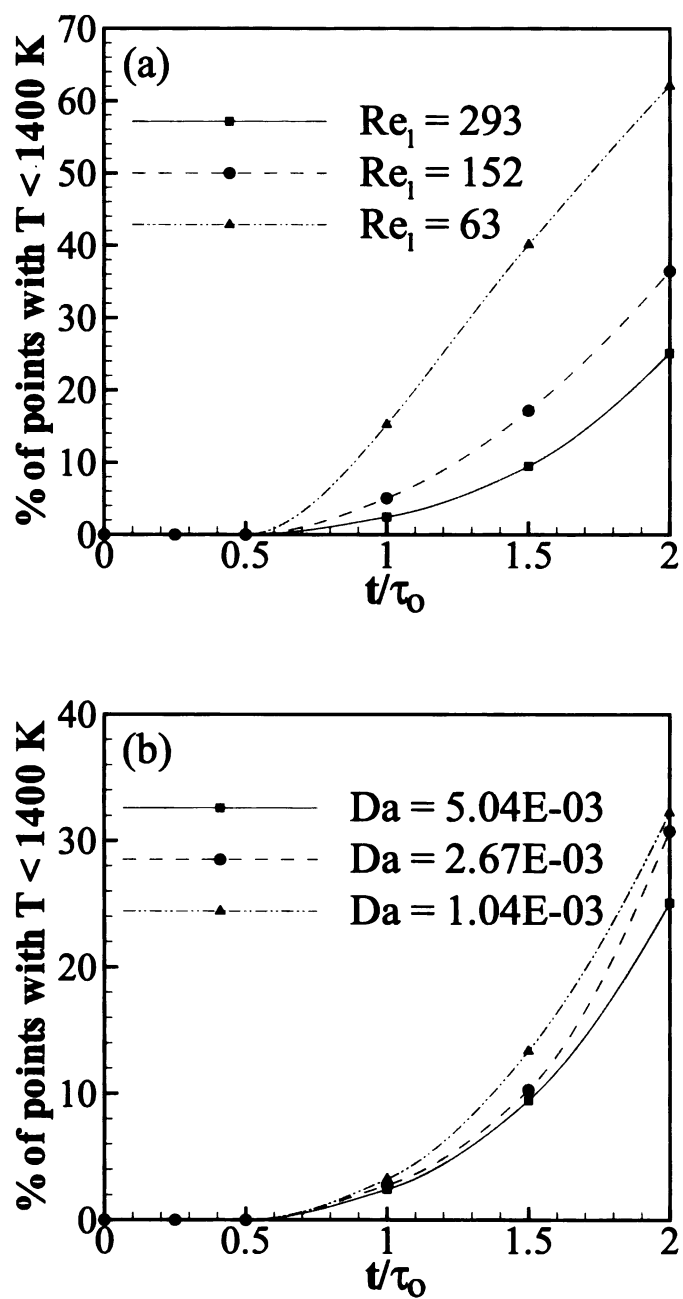


Figure 1.23: Temporal variations of the percentage of grid points in the vicinity of the flame surface ( $Z \approx Z_{stoich}$ ) with temperatures less than 1400 K; (a) various Reynolds numbers, and (b) various Damköhler numbers. The data are gathered from the Eulerian grid points.

# CHAPTER 2

## LARGE-EDDY SIMULATIONS OF TURBULENT METHANE JET FLAMES WITH FILTERED MASS DENSITY FUNCTION

### 2.1 Introduction

The well documented experimental data generated by the Sandia National Laboratory researchers and their collaborators for turbulent jet flames [58, 59, 64] have been widely employed for assessment of numerical models. Both Reynolds-Averaged Simulation (RAS) and Large-Eddy Simulation (LES) models have been evaluated [65–68]. For example, Jones and Kakhi [69] used the RAS based probability density function (PDF) method with linear mean square estimation (LMSE) and Curl’s coalescence-dispersion (CCD) mixing closures, standard turbulence models and 4-step kinetics mechanisms to simulate non-piloted non-premixed jet flames at various jet speeds. Their results indicate that at lower jet speed of  $41\text{m/s}$  (flame L), there is no significant extinction, but at higher speed of  $48\text{m/s}$  (flame B), there are some. In the extinction-reignition region ( $15 \leq x/D \leq 35$ ) of the flame B, the predicted temperature by the LMSE model is shown to be smaller than the experimental values, while CCD model overpredicts the experimental data at the same region. Muradoglu *et al.* [70] have conducted similar jet simulations with a flamelet based chemistry and interaction by exchange with the mean (IEM) mixing model and have found good agreement with the low-speed equilibrium flame L data.

The assumed PDF method with a reduced kinetics mechanism was used by Landefeld *et al.* [66] to simulate the Sandia’s piloted jet flame (flame D). The intrinsic low-dimensional manifolds (ILDM) algorithm [71, 72] was implemented along with reaction progress variables in these calculations. Additionally, transport equations for the mean and variance of mixture fraction and species mass fractions are solved, together with a Beta PDF for the mixture fraction and a Reynolds stress closure for the turbulence. Generally, the results were found to compare well with the low-speed piloted jet flame D data.

Xu and Pope [65] have simulated the piloted jet flames at various jet speeds with a joint velocity-composition-turbulent frequency RAS/PDF model. The 16 species augmented methane mechanism [73, 74] have been implemented with the *in situ* adaptive tabulation (ISAT) [75] algorithm for the chemistry. The Euclidian minimum spanning tree (EMST) model [76], which treats the mixing locally in the composition space, is used for the mixing model. Overall, the results were found to be in good agreement with the experimental data.

The models based on LES have also been used for prediction of Sandia’s jet flames [67, 77]. Different subgrid-scale (SGS) models have been employed. One of them is based on the filtered density function (FDF) methodology [78]. This method is the counterpart of the PDF method in RAS [4, 5, 78–81]. The fundamental advantage of the LES/FDF is that it accounts for the effects of chemical reaction exactly while calculating the resolved turbulence field, thus allowing a more reliable prediction of turbulent flames. The literature on SGS closures via the FDF method has been growing at a relatively fast pace since its first introduction [78]. The scalar FDF is considered in Refs. [82–85], the scalar filtered mass density function (FMDF) in Refs. [86–90], the velocity FDF in Ref. [91] and the velocity-scalar FDF in Ref. [92]. Some recent data on experimental validation of FDF are also available [93].

In the present work, the scalar FMDF methodology is employed as a SGS closure

in LES of turbulent methane jet flames. The main objectives are (1) to further assess the applicability and the extent of validity of the FMDF method for SGS closure of complex turbulent flames when local flame extinction is important, (2) to investigate the accuracy of various ways of implementing the mixing model, (3) to study the effects of chemical kinetics on LES predictions for both near-equilibrium and non-equilibrium flames. The chemistry is implemented following two different approaches. In the first approach, all reactive species are obtained by direct solution of an appropriate kinetics mechanism. In the second approach, only the FMDF of the mixture fraction is considered; the temperature and species concentrations are obtained from a set of flamelet tables. The tables are generated by solving the steady-state one-dimensional opposed jet equations with detailed (GRI) mechanism. Considering the steady-state flamelet assumption in the second approach, it is expected that the extinction would not be predicted correctly in this approach. However, it would be useful to evaluate the overall performance of the FMDF/flamelet method for near-equilibrium flames and show its limitations in non-equilibrium flames.

The Sandia's "high speed" piloted turbulent methane jet flames D and F [64] are considered in this study. Flame D involves limited regions of local extinction, while flame F tends towards total extinction. The existence of different level of local extinction in these flames provides a good means of assessing the capabilities of the models to predict realistic combustion systems. The geometrical configurations in these two flames is the same (see Fig. 2.1), but the jet inlet velocity in flame F is twice of that in flame D. The formulation of LES/FMDF methodology is reviewed in section 2.2, followed by section 2.3 which describes the consistency issues, the parallelization algorithm, the implementation of chemistry, and the computational parameters. Results obtained by the LES/FMDF for flames D and F are discussed in section 2.4, and the main conclusions are stated in 2.5.

## 2.2 Formulation

In the hybrid Eulerian-Lagrangian LES/FMDF methodology, the filtered velocity equations are solved together with the joint scalar FMDF equation. These equations are described in two different sections. The variables are listed in the nomenclature section. The resolved variables are obtained by application of the spatial filtering operator [94],

$$\langle f(\mathbf{x}, t) \rangle_\ell = \int_{-\infty}^{+\infty} f(\mathbf{x}', t) \mathcal{H}(\mathbf{x}', \mathbf{x}) d\mathbf{x}', \quad (2.1)$$

where  $\mathcal{H}$  denotes the filter function,  $\langle f(\mathbf{x}, t) \rangle_\ell$  represents the filtered value of the transport variable  $f(\mathbf{x}, t)$  and  $\mathbf{x} = (x, y, z)$  denotes the spatial coordinates, with  $x$  axis parallel to the jet and  $y, z$  perpendicular to  $x$ . In variable density flows it is more convenient to consider the Favre filtered quantity,  $\langle f(\mathbf{x}, t) \rangle_L = \langle \rho f \rangle_\ell / \langle \rho \rangle_\ell$ . For spatially & temporally invariant and localized filter functions,  $\mathcal{H}(\mathbf{x}', \mathbf{x}) \equiv H(\mathbf{x}' - \mathbf{x})$  with the properties[94],  $H(\mathbf{x}) = H(-\mathbf{x})$ , and  $\int_{-\infty}^{\infty} H(\mathbf{x}) d\mathbf{x} = 1$ .

### 2.2.1 The Filtered Transport Equations

With the application of the filter function to the transport equations [95] one can derive the following filtered equations,

$$\frac{\partial \langle \rho \rangle_\ell}{\partial t} + \frac{\partial \langle \rho \rangle_\ell \langle u_i \rangle_L}{\partial x_i} = 0 \quad (2.2)$$

$$\frac{\partial \langle \rho \rangle_\ell \langle u_j \rangle_L}{\partial t} + \frac{\partial \langle \rho \rangle_\ell \langle u_i \rangle_L \langle u_j \rangle_L}{\partial x_i} = -\frac{\partial \langle p \rangle_\ell}{\partial x_j} + \frac{\partial \langle \tau_{ij} \rangle_\ell}{\partial x_i} - \frac{\partial \mathcal{I}_{ij}}{\partial x_i} \quad (2.3)$$

$$\frac{\partial \langle \rho \rangle_\ell \langle \phi_\alpha \rangle_L}{\partial t} + \frac{\partial \langle \rho \rangle_\ell \langle u_i \rangle_L \langle \phi_\alpha \rangle_L}{\partial x_i} = -\frac{\partial \langle J_i^\alpha \rangle_\ell}{\partial x_i} - \frac{\partial \mathcal{M}_i^\alpha}{\partial x_i} + \langle \rho S_\alpha \rangle_\ell, \quad \alpha = 1, 2, \dots, \sigma. \quad (2.4)$$

In these equations, the scalar (composition and energy) field is denoted by  $\phi_\alpha \equiv Y_\alpha$ ,  $\alpha = 1, 2, \dots, N_s$ ,  $\phi_\sigma \equiv h = \sum_{\alpha=1}^{N_s} h_\alpha \phi_\alpha$ , in which  $h_\alpha = h_\alpha^0 + \int_{T_0}^T c_{p\alpha}(T') dT'$ .

Equations 2.2-2.4 are closed by the following constitutive relations

$$\langle p \rangle_\ell \approx \langle \rho \rangle_\ell R^0 \langle T \rangle_L \sum_1^{N_s} \frac{\langle \phi_\alpha \rangle_L}{W_\alpha} \quad (2.5)$$

$$\langle \tau_{ij} \rangle_\ell \approx \langle \mu \rangle_L \left( \frac{\partial \langle u_i \rangle_L}{\partial x_j} + \frac{\partial \langle u_j \rangle_L}{\partial x_i} - \frac{2}{3} \delta_{ij} \frac{\partial \langle u_k \rangle_L}{\partial x_k} \right), \quad \langle \mu \rangle_L = Pr \langle k / c_p \rangle_L \quad (2.6)$$

$$\langle J_i^\alpha \rangle_\ell \approx -\langle \rho \rangle_\ell \langle D \rangle_L \frac{\partial \langle \phi_\alpha \rangle_L}{\partial x_i}, \quad \langle D \rangle_L = \frac{1}{\langle \rho \rangle_\ell Le} \langle \frac{k}{c_p} \rangle_L. \quad (2.7)$$

In Eqs. 2.2 - 2.4, the hydrodynamic SGS closure problem is associated with [96]  $\mathcal{T}_{ij} = \langle \rho \rangle_\ell (\langle u_i u_j \rangle_L - \langle u_i \rangle_L \langle u_j \rangle_L)$  and  $\mathcal{M}_i^\alpha = \langle \rho \rangle_\ell (\langle u_i \phi_\alpha \rangle_L - \langle u_i \rangle_L \langle \phi_\alpha \rangle_L)$  denoting the SGS stresses and the SGS scalar fluxes, respectively. In reacting flows, an additional model is required for the filtered reaction rates  $\langle \rho S_\alpha \rangle_\ell = \langle \rho \rangle_\ell \langle S_\alpha \rangle_L$ . It will be shown in the next section that both  $\langle \rho \rangle_\ell$  and  $\langle S_\alpha \rangle_L$  are determined exactly with the knowledge of the FMDF. For  $\mathcal{T}_{ij}$ , the model used by Jaberi *et al.* [97] is considered:

$$\mathcal{T}_{ij} = -2 \langle \rho \rangle_\ell \nu_t \left( \langle \mathcal{S}_{ij} \rangle_L - \frac{1}{3} \langle \mathcal{S}_{kk} \rangle_L \delta_{ij} \right) + \frac{2}{3} C_I \langle \rho \rangle_\ell E \delta_{ij}, \quad (2.8)$$

where  $\langle \mathcal{S}_{ij} \rangle_L$  is the resolved strain rate and  $E = |\langle u_i^0 \rangle_L \langle u_i^0 \rangle_L - \langle \langle u_i^0 \rangle_{L'} \langle \langle u_i^0 \rangle_{L'} \rangle_{L'}|$ ,  $\nu_t = C_R \Delta_H \sqrt{\bar{E}}$ ,  $u_i^0 = u_i - \mathcal{U}_i$  ( $\mathcal{U}_i$  is a reference velocity in the  $x_i$  direction and the subscript  $\ell'$  denotes filtering at the secondary level with a characteristic size larger than that at grid level). We have found the performance of this model to be better than the Smagorinsky type closures [98–100], and we did not even have to implement the “dynamic” procedure [101, 102] for evaluation of the model coefficients.

For the closure of the subgrid mass flux  $\mathcal{M}_i^\alpha$ , the model most often used in LES of non-reacting flows [103–105] is used

$$\mathcal{M}_i^\alpha = -\langle \rho \rangle_\ell D_t \frac{\partial \langle \phi_\alpha \rangle_L}{\partial x_i}, \quad \alpha = 1, 2, \dots, \sigma. \quad (2.9)$$

It must be indicated here that this model is not used directly in the FMDF approach but modeled FMDF transport equation is constructed to be consistent with it as discussed below.

## 2.2.2 The Filtered Mass Density Function (FMDF)

The scalar filtered mass density function (FMDF) is defined as [84, 85, 88, 97]

$$F_L(\boldsymbol{\psi}, \mathbf{x}; , t) \equiv \int_{-\infty}^{+\infty} \rho(\mathbf{x}', t) \zeta[\boldsymbol{\psi}, \boldsymbol{\phi}(\mathbf{x}', t)] H(\mathbf{x}' - \mathbf{x}) d\mathbf{x}' \quad (2.10)$$

$$\zeta[\boldsymbol{\psi}, \boldsymbol{\phi}(\mathbf{x}, t)] = \delta[\boldsymbol{\psi} - \boldsymbol{\phi}(\mathbf{x}, t)] \equiv \prod_{\alpha=1}^{\sigma} \delta[\psi_{\alpha} - \phi_{\alpha}(\mathbf{x}, t)] \quad (2.11)$$

where  $\delta$  denotes the delta function and  $\boldsymbol{\psi}$  denotes the composition domain of the scalar array  $\boldsymbol{\phi}(\mathbf{x}, t)$ . The term  $\zeta[\boldsymbol{\phi}, \boldsymbol{\psi}(\mathbf{x}, t)]$  is the “fine-grained” density [5, 106], and Eq. 2.10 implies that the FMDF is the *mass weighted spatially filtered* value of the fine-grained density. To ensure that the FMDF has all the properties of the PDF, we will only consider “positive” filter functions [107] for which all the moments  $\int_{-\infty}^{\infty} x^m H(x) dx$  exist for  $m \geq 0$ . The following exact deterministic equation describes the variations of FMDF in space and time

$$\begin{aligned} \frac{\partial F_L}{\partial t} + \frac{\partial \langle u_i \rangle_L F_L}{\partial x_i} &= \frac{\partial}{\partial x_i} \left\langle \rho D \frac{\partial \zeta}{\partial x_i} \right\rangle_{\ell} - \frac{\partial^2}{\partial \psi_{\alpha} \partial \psi_{\beta}} \left[ \left\langle \rho D \frac{\partial \phi_{\alpha}}{\partial x_i} \frac{\partial \phi_{\beta}}{\partial x_i} | \boldsymbol{\psi} \right\rangle_{\ell} F_L / \hat{\rho} \right] \\ &- \frac{\partial [\langle u_i | \boldsymbol{\psi} \rangle_{\ell} - \langle u_i \rangle_L] F_L}{\partial x_i} - \frac{\partial [\hat{S}_{\alpha}(\boldsymbol{\psi}) F_L]}{\partial \psi_{\alpha}}. \end{aligned} \quad (2.12)$$

In Eq. 2.12,  $\langle \mathcal{A} | \mathcal{B} \rangle_{\ell}$  denotes the filtered value of the variable  $\mathcal{A}$ , “conditioned” on  $\mathcal{B}$ , and the hat is used for the quantities which are dependent only on the scalar field. In Eq. 2.12, the last term on the right-hand side represents the effects of chemical reaction and is in a closed form. The second and the third terms on the right-hand side are unclosed. They represent the effects of SGS mixing and convection,

respectively. The convective flux is modeled here as

$$[\langle u_i | \psi \rangle_\ell - \langle u_i \rangle_L] F_L = -\langle \rho \rangle_\ell D_t \frac{\partial (F_L / \langle \rho \rangle_\ell)}{\partial x_i}, \quad D_t = \nu_t / S_{c_t} \quad (2.13)$$

where  $\nu_t$  is the SGS viscosity and is to be determined by hydrodynamic LES and  $S_{c_t}$  is the SGS Schmidt number. The first “moment” of Eq. 2.13 recovers the model given in Eq. 2.9.

The closure for the SGS mixing can be via any of the ones used in RAS/PDF methods [108–110]. The simplest one is the LMSE model, [106, 111]

$$\frac{\partial^2}{\partial \psi_\alpha \partial \psi_\beta} \left[ \left\langle \rho D \frac{\partial \phi_\alpha}{\partial x_i} \frac{\partial \phi_\beta}{\partial x_i} | \psi \right\rangle_\ell F_L / \hat{\rho} \right] = -\frac{\partial}{\partial \psi_\alpha} [\Omega_m (\psi_\alpha - \langle \phi_\alpha \rangle_L) F_L], \quad (2.14)$$

where  $\Omega_m(\mathbf{x}, t)$  is the frequency of mixing within the subgrid. This frequency is modeled as  $\Omega_m = C_\Omega (\langle D \rangle_L + D_t) / (\Delta_H^2)$ , where  $C_\Omega$  is the mixing model coefficient and  $\Delta_H$  is the characteristic size of the filter. The mixing model coefficient  $C_\Omega$  represents the velocity-to-scalar timescale ratio [65]. It needs to be either empirically specified [65, 112–118] or directly obtained via a dynamic model [89, 90, 119–121]. In the present work, a range of constant empirical values and two different dynamic models are employed to calculate  $C_\Omega$ :

1. In this approach, the LMSE model is used in its standard form, while the mixing model coefficient  $C_\Omega$  is assumed to be constant [112–114]. Here,  $C_\Omega = 5$  is used as the base value for the reference case since it generates the closest predictions to the experimental data. However, other values of  $C_\Omega$  are also considered.
2. In this approach, the mixing coefficient  $C_\Omega$  is computed as a function of time and space by a dynamic method. The dynamic method is based on

the generalized subgrid variance,  $\sigma_\alpha^2 = \langle \phi_{(\alpha)}^2 \rangle_L - \langle \phi_{(\alpha)} \rangle_L^2$  and the total subgrid scalar dissipation rate,  $\epsilon_\alpha$ . The latter is defined as

$$\epsilon_\alpha = 2\langle \rho \rangle_\ell (\langle D \rangle_L + D_t) \left[ \frac{\partial \langle \phi_{(\alpha)} \rangle_L}{\partial x_i} \frac{\partial \langle \phi_{(\alpha)} \rangle_L}{\partial x_i} \right] = 2\Omega_m \langle \rho \rangle_\ell (\langle \phi_{(\alpha)}^2 \rangle_L - \langle \phi_{(\alpha)} \rangle_L^2), \quad (2.15)$$

$$\Omega_m = C_\Omega (\langle D \rangle_L + D_t) / (\Delta_H^2)$$

where the subscripts in parentheses are excluded from the summation convention. The model for  $\epsilon_\alpha$  in Eq. 2.15 is obtained by assuming that the dissipation term balances the production term in the generalized subgrid variance equation citepCJGP98,raman1. By using  $\Omega_m$ ,  $\sigma_\alpha^2$  and  $\epsilon_\alpha$ , the model coefficient can be computed locally as

$$C_\Omega = \frac{\Delta_H^2 \nabla \langle \phi_{(\alpha)} \rangle_L \cdot \nabla \langle \phi_{(\alpha)} \rangle_L}{\sigma_\alpha^2}, \quad \alpha = 1, 2, \dots, N_s. \quad (2.16)$$

Evidently, this formulation allows different coefficients for different species, meaning ‘‘Differential diffusion’’ effects may be included. However, the computational time needed for the calculation of  $C_\Omega$  could become extensive when realistic chemistry models with numerous species are employed. Therefore, to reduce the computational overhead, a modified version of Eq. 2.16 is considered in which mixture fraction variable  $Z$  is used,

$$C_\Omega = \frac{\Delta_H^2 \nabla \langle Z \rangle_L \cdot \nabla \langle Z \rangle_L}{\langle Z^2 \rangle_L - \langle Z \rangle_L^2}. \quad (2.17)$$

In the numerical implementation of the model, the gradient of the favre-filtered mixture fraction  $\nabla \langle Z \rangle_L$  is calculated from the fixed finite difference grid points with a purpose of decreasing the numerical noise, while the subgrid scalar variance is determined from the Monte Carlo particles. An

additional statistical averaging over the homogeneous (azimuthal) direction is also performed to prevent numerical instabilities. In the discussion below, this dynamic model is referred to as DM1.

3. In this approach, a dynamic method proposed by Raman and Pitsch [90] is employed for calculating the coefficient  $C_\Omega$ . This model is referred to as DM2. In the DM2 model, the subgrid scale mixing frequency  $\Omega_m$  is again directly evaluated from the subgrid scalar variance and the dissipation rate. However, in contrast to DM1, the subgrid scalar variance in DM2 is obtained by a model. The equations [90] describing the conserved scalar variance  $\widetilde{Z''^2}$  and dissipation rate  $\chi$  are

$$\widetilde{Z''^2} = C_Z \Delta_H^2 \nabla \widetilde{Z} \cdot \nabla \widetilde{Z}, \quad (2.18)$$

$$\chi = 2(\widetilde{D} + D_t) \nabla \widetilde{Z} \cdot \nabla \widetilde{Z}, \quad (2.19)$$

where the operator “ $\widetilde{(\dots)}$ ” denotes the favre-filtering operator  $\langle \dots \rangle_L$ . Based on these equations, the scalar mixing timescale  $\tau_\phi$  (which is the inverse of subgrid mixing frequency ( $1/\Omega_m$ )) is computed as

$$\tau_\phi = \widetilde{Z''^2} / \chi = \frac{C_Z \Delta^2}{2(\widetilde{D} + D_T)}, \quad (2.20)$$

where the model coefficient  $C_Z = 2/C_\Omega$  is obtained by a dynamic procedure [120].

The IEM model has some limitations [108, 109] which are not discussed here, but per results obtained in previous studies [5, 78, 109, 110, 122–127], it can be safely indicated that while the IEM is not quite satisfactory in RAS/PDF, it functions reasonably well in LES/FMDF, and its numerical implementation is computationally

convenient.

With the closures for the SGS convection and mixing, the modeled FMDF transport equation may be written as

$$\frac{\partial F_L}{\partial t} + \frac{\partial[\langle u_i \rangle_L F_L]}{\partial x_i} = \frac{\partial}{\partial x_i} \left[ \langle \rho \rangle_\ell (\langle D \rangle_L + D_t) \frac{\partial(F_L / \langle \rho \rangle_\ell)}{\partial x_i} \right] + \quad (2.21)$$

$$\frac{\partial}{\partial \psi_\alpha} [\Omega_m(\psi_\alpha - \langle \phi_\alpha \rangle_L) F_L] - \frac{\partial[\hat{S}_\alpha F_L]}{\partial \psi_\alpha}.$$

The transport equations for the SGS moments can be obtained by direct integration of the above FMDF equation over the composition domain. The equations for the first subgrid Favre moment,  $\langle \phi_\alpha \rangle_L$  is identical with that in Eq. 2.4.

## 2.3 Numerical Solution

The numerical method used for LES/FMDF has two components. For the solution of the hydrodynamic field, a high-order accurate finite difference (FD) method which has proven effective for LES [4] is employed. The FD discretization procedure is based on the “compact parameter” scheme [128] which yields up to 6th order spatial accuracy. All the finite difference operations for obtaining the filtered values are performed on fixed and uniform grid points.

The SGS empirical “constants” are  $C_I$ ,  $C_R$ ,  $Sc_t$ . Based on our experience, in which a variety of different flows (2D and 3D, constant and variable density, different chemistry schemes, *etc.*) are considered, we have determined  $C_I \approx 0.01$ ,  $C_R \approx 0.02$ ,  $Sc_t \approx 0.4 - 0.7$ . Interestingly, the range of some of these values is the same as that typically used in equivalent models in RAS [79]. The magnitudes of the molecular parameters are the same as those typically used for hydrocarbon-air flames [129, 130]. For methane  $\langle k/c_p \rangle_L \approx 2.58 \times 10^{-5} (\langle T \rangle_L / 298)^{0.7}$ ,  $Pr \approx 0.75$  and  $c_{p_\alpha}$  is specified through polynomial fits as functions of the temperature.

### 2.3.1 The Lagrangian Monte Carlo Method

The most convenient means of solving the FMDF transport equation is via the “Lagrangian Monte Carlo” procedure [5, 131]. The basis of this procedure is the same as that described in recent papers [70, 84, 88, 91, 97, 132–134]. Therefore, here only the basic features of the procedure are described. With the Lagrangian procedure, the FMDF is represented by an ensemble of computational “stochastic elements” (or “particles”) which are transported in the “physical space” by the combined actions of large scale convection and diffusion (molecular and subgrid). In addition, transport in the “composition space” occurs due to chemical reaction and SGS mixing. In doing so, the notional particles evolve via a “stochastic process,” described by the set of stochastic differential equations (SDEs) [135, 136]

$$dX_i(t) = \mathcal{D}_i(\mathbf{x}(t), t)dt + \mathcal{E}(\mathbf{X}(t), t)d\mathcal{W}_i(t), \quad d\phi_\alpha^+(t) = \mathcal{R}_\alpha(\phi^+, t)dt. \quad (2.22)$$

where  $X_i$  is the Lagrangian position of the particles,  $\mathcal{D}$  and  $\mathcal{E}$  are known as the “drift” and “diffusion” coefficients, and  $\mathcal{W}_i$  denotes the Wiener-Lévy process [137].  $\phi_\alpha^+$  denotes the scalar value of the particle with the Lagrangian position vector  $X_i$ . Eq. 3.28 defines what is known as the general “diffusion” process [136–138]; thus the PDFs of the stochastic processes  $(X_i(t), \phi_\alpha^+(t))$  are governed by the Fokker-Planck equation. A comparison between the standard Fokker-Planck equation corresponding to Eq. 3.28 with the FMDF equation (Eq. 2.21) under consideration identifies the parameters of Eq. 3.28,

$$\mathcal{E} \equiv \sqrt{2(\langle D \rangle_L + D_t)}, \quad \mathcal{D}_i \equiv \langle u_i \rangle_L + \frac{1}{\langle \rho \rangle_\ell} \frac{\partial[\langle \rho \rangle_\ell (\langle D \rangle_L + D_t)]}{\partial x_i}, \quad (2.23)$$

$$\mathcal{R}_\alpha \equiv -\Omega_m(\phi_\alpha^+ - \langle \phi_\alpha \rangle_L) + \hat{S}_\alpha(\phi^+).$$

With this analogy, the FMDF is represented by an ensemble of Monte Carlo particles, each with a set of scalars  $\phi_\alpha^{(n)}(t) = \phi_\alpha(\mathbf{X}^{(n)}(t), t)$  and Lagrangian position vector  $\mathbf{X}^{(n)}$ . A splitting operation then can be employed in which the transports in physical and compositional domains are treated separately. The simplest means of simulating the spatial transport in Eq. 3.28 is via the Euler-Maruyamma approximation [139]. The transfer of information from the fixed finite difference points to the location of the Monte Carlo particles are conducted via (fourth and second order) interpolation. The filtered scalar quantities are calculated by weighted averaging of the particle values over space with average volumetric size of  $\Delta_E$ . Ideally,  $\Delta_E$  has to be very small.

### 2.3.2 Consistency

As stated before, the equation governing the first subgrid Favre-moment of the scalar  $\phi_\alpha$  obtained from the FMDF equation is identical with the filtered scalar Eq. 2.4, indicating that the filtered temperature, scalar and density may be alternatively obtained from the Eulerian, finite difference (FD) or Lagrangian, Monte Carlo (MC) solutions. This implies a mathematical consistency between FD and MC parts of the hybrid scheme. However, due to finite grid size in FD and limited number of MC particles, consistency may not be achieved in practice. In the following, the possible sources of inconsistency are identified and conditions leading to a consistent solution are discussed.

Four preliminary simulations with constant values of  $C_\phi = 2C_\Omega = 8, 16$  and  $\Delta_E = \Delta$  ( $\Delta$  is grid spacing) and  $\Delta_E = 2\Delta$  have been performed to study the consistency of LES/FMDF for conditions of Sandia's piloted jet flames. The reaction is turned off in these simulations but the variable density/temperature effects are still important due to strong pilot at inflow. The instantaneous temperature profiles for cases with  $\Delta_E = 2\Delta$  and  $\Delta_E = \Delta$  are compared in Fig. 2.2. It is observed that

the difference between the MC and FD solutions becomes negligible when  $\Delta_E = \Delta$ . Moreover, the mixing model coefficient, which does not appear explicitly in the Favre-filtered equation, does not seem to have a significant effect on the filtered temperature when  $\Delta_E = 2\Delta$ , even though the temperature profiles seem to be slightly more diffused for higher  $C_\phi$  (compare results for  $C_\phi = 16$  with those for  $C_\phi = 8$  in Fig. 2.2a). For the reacting simulations considered in the next section,  $\Delta_E$  was chosen to be equal to  $2\Delta$ . In all of these simulations we have found the difference between the FD and MC solutions to be less than 3 percent for instantaneous temperatures and even lower for time averaged values.

### 2.3.3 Parallelization

As mentioned before, in the hybrid LES/FMDF methodology the filtered continuity, momentum and energy equations (Eqs. 2.2-2.4) are solved by a finite difference (FD) method over a fixed Eulerian grid system. On the other hand, all scalars are obtained from the FMDF by solving its transport equation with a Lagrangian stochastic Monte Carlo MC method. The employed MC method involves grid-free particles interacting with the fixed background Eulerian grid. However, there is no inter-particle interactions, suggesting that MC calculations are potentially efficient in a parallel environment. However, the particle transport and mixing require interactions with the FD field. Moreover, the source term in the FD energy equation should be calculated by averaging the particle reaction source terms. Consequently, the MC calculations can not be performed independent from the FD calculations.

To obtain a good statistical representation, a significant number of particles are required within each FD cell. Typically, about ten particles are required for each FD grid for  $\Delta_E = 2\Delta$ . A typical hybrid (FD - MC) simulation with ten particles per cell is about 5 times more expensive than its corresponding FD simulation with no MC particles. Hence, the usage of “complex” multi-step kinetics mechanisms in

these simulations would only be possible by proper application of parallel processing techniques. Two different parallelization schemes may be used:

1. In the first approach, all processors are solving the same FD equations for the whole domain. Consequently no speed-up is gained in the FD part. However, since the FD calculations are small fraction of total calculations in the hybrid scheme for reacting simulations, it is theoretically possible to achieve relatively high parallel efficiencies. In the MC part, particles are equally divided among the processors. Since the particles are not transferred between the processors, there is no communication load for the MC calculations and the load distribution is exactly uniform. Inter-processor communications are only required in the averaging process, where a local ensemble average value of particles is calculated on each FD cell. Since each processor is dealing with particles traversing the whole domain, global communications are required for calculating the summation and broadcasting the outcome back to the processors. For  $nf$  number of FD grid points and  $np$  number of processors, the averaging calculations require a summation of  $np$  arrays of size  $nf$  and  $2 \times nf \times np$  times transfer of data between the processors. On distributed memory architecture, this amount of data transfer can be prohibitive, since the network speed is normally much slower than the memory transfer rate. The main drawback is the linear increase in the number of operations and communications with the number of processors.
2. The second approach is considerably more complex than the first one. However, it is proven to be scalable and much more efficient. In this approach, both the FD domain and the MC particles are distributed among the processors. A limited number of communications are required when the

subgroup of particles are located in the boundaries of the FD subdomain defined for each processor. With this, the communications required for the averaging process described in the first parallelization method is eliminated. However, since each processor needs to keep track of the particles located in its own FD subdomain, particles that exit the subdomain have to be transferred to its respective processor. For keeping the same load on every processor, it is necessary to have the same number of particles per processor at all times. Indeed, our analysis indicate that about one percent of the particles traverse the boundaries of the subdomains ate each time step, suggesting very little communication load. Limited communications are also required for calculating the ensemble averages on the boundary points. Inter-processor communications are also required for interpolating a FD quantity on a particle location and for differencing and filtering FD operations.

To evaluate the difference between the above parallel processing methods, a benchmarking simulation with 1.2 million FD grid points and 7 million MC particles was conducted. Single-processor simulations were not possible due to the hardware structure, thus the speedups reported are relative to a 2-processor simulation. The speedups obtained for the 4-, 8-, and 16-processor simulations are plotted in Fig. 2.3. For 4- and 8- processor simulations, superlinear speedups are obtained, since the problem size for each processor becomes smaller and the higher speed cache is used more efficiently. For the 2-, 4-, and 8-processor simulations, only one processor per node is used. However, for the 16-processor simulation, 2 processors per node are used, which have to share the memory and network bandwidth, resulting in a sublinear speedup in this case. It is clear that despite apparent complexity of the second parallel processing method, it is a very efficient method.

### 2.3.4 Chemistry

In quantitative comparison with laboratory data, the role that the chemical kinetics model plays may become important. In this work, the chemistry model is based on (i) non-equilibrium (finite-rate) and (ii) near-equilibrium models.

In (i), the finite rate kinetics effects are modeled with a one-step global mechanism [140], or a 12-step reduced mechanism. In (ii), the transport equation of FMDF for the mixture fraction is solved together with a set of flamelet tables, generated by laminar opposed jet flame simulations and detailed kinetics model. All other thermochemical variables are constructed from the flamelet data. Additionally, in (i), the transport equation for the sensible enthalpy ( $h_s = \int_{T_0}^T c_p(T')dT'$ ) is solved

$$\frac{\partial \langle \rho \rangle_\ell \langle h_s \rangle_L}{\partial t} + \frac{\partial \langle \rho \rangle_\ell \langle u_i \rangle_L \langle h_s \rangle_L}{\partial x_i} = -\frac{\partial \langle J_i^\sigma \rangle_\ell}{\partial x_i} - \frac{\partial \mathcal{M}_i^\sigma}{\partial x_i} + \langle \rho S_\alpha h_\alpha^0 \rangle_\ell, \quad (2.24)$$

where

$$\langle J_i^\sigma \rangle_\ell \approx -\frac{1}{Le} \langle \frac{k}{c_p} \rangle_L \frac{\partial \langle h_s \rangle_L}{\partial x_i}, \quad \mathcal{M}_i^\sigma = -\langle \rho \rangle_\ell D_t \frac{\partial \langle h_s \rangle_L}{\partial x_i} \quad (2.25)$$

and the term  $\langle \rho S_\alpha h_\alpha^0 \rangle_\ell$  is obtained from FMDF and Monte Carlo particles. In (ii), a transport equation for the  $\langle E \rangle_L = \langle RT \rangle_L$  is solved (in the flamelet table  $RT$  is a function of mixture fraction). This equation, as derived by multiplying the modeled FMDF equation by  $E$  and integrating over the mixture fraction space, is

$$\frac{\partial \langle \rho \rangle_\ell \langle E \rangle_L}{\partial t} + \frac{\partial \langle \rho \rangle_\ell \langle u_i \rangle_L \langle E \rangle_L}{\partial x_i} = -\frac{\partial \langle J_i^\sigma \rangle_\ell}{\partial x_i} - \frac{\partial \mathcal{M}_i^\sigma}{\partial x_i} + \langle \rho \rangle_\ell \Omega_m [\langle ZG \rangle_L - \langle Z \rangle_L \langle G \rangle_L] \quad (2.26)$$

where

$$G = \frac{dE(Z)}{dZ}, \quad \langle J_i^\sigma \rangle_\ell \approx -\frac{1}{Le} \langle \frac{k}{c_p} \rangle_L \frac{\partial \langle E \rangle_L}{\partial x_i} \quad \mathcal{M}_i^\sigma = -\langle \rho \rangle_\ell D_t \frac{\partial \langle E \rangle_L}{\partial x_i}. \quad (2.27)$$

The reduced mechanism considered in (i) is the 12-step mechanism of Sung *et al.* [141].

This mechanism is developed from the GRI 1.2 detailed mechanism and involves 16 species ( $H_2$ ,  $H$ ,  $O_2$ ,  $OH$ ,  $H_2O$ ,  $HO_2$ ,  $H_2O_2$ ,  $CH_3$ ,  $CH_4$ ,  $CO$ ,  $CO_2$ ,  $CH_2O$ ,  $C_2H_2$ ,  $C_2H_4$ ,  $C_2H_6$ ,  $N_2$ ). It contains more unsteady intermediates than the conventional 4 and 5-steps mechanisms, and it has proven effective in a range of applications including auto-ignition, laminar flame propagation [74], and variety of premixed, non-premixed and partially-premixed laminar opposed jet flames [32]. In all these applications, the 12-step results were found to be almost indistinguishable from the GRI results. The detailed mechanism in (ii) is based on GRI-3.

### 2.3.5 Jet Parameters and Boundary Conditions

Figure 2.1 shows a schematic view of the Sandia's piloted methane jet flame, and the coordinate system used in our simulations. For these simulations, a FD mesh with  $160 \times 161 \times 161$  grid points was considered for a domain of  $16 \times 12 \times 12$  jet diameters in the x, y, and z directions, respectively. The approximate number of MC elements per each FD cell is 8 and  $\Delta_E = 2\Delta$ . The main jet composition is 25%  $CH_4$  and 75% air with a Reynolds number of 22400 in Flame D. Flame F has the same parameters, except the jet speed or Reynolds number, which is doubled. Detailed specifications of the flames and measurement methods are available elsewhere [142, 143], and are not discussed here. However, for convenience the main parameters of flames D and F are listed in table 2.1.

Non-reflecting boundary conditions [144] are considered for the outlet boundary and zero-gradient conditions are used for the lateral boundaries. For the inflow, non-reflecting boundary conditions are used with a prescribed velocity based on experiment. It should be noted that the temperature is not measured at the nozzle exit, and  $x/d = 1$  is the closest distance to the nozzle where such measurements are conducted. The sensitivity of the model predictions to the uncertainty in the pilot boundary conditions is an important consideration [145], specially with regards to

flame F, which is at a state very close to global extinction. Here, we use the values close to those suggested by Barlow [142].

## 2.4 Results and Discussion

The isosurfaces and isocontours of the instantaneous vorticity magnitude, and temperature for flame D and flame F simulations are shown in Figs. 2.4 - 2.5. These figures indicate that there is a transition to turbulence at  $x/D \approx 5$  in both flames. Nevertheless, the flow field in flame F appears to be more turbulent due to increased jet speed, and lesser overall heat release effects particularly when 12-step chemistry is employed. The results (not shown) for flame D indicate that the flow field is not very different when flamelet and 1-step chemistry are used but the turbulence is stronger when 12-step chemistry is employed. This is due to damping effect of reaction on turbulence, which is more significant in our 1-step and flamelet simulations. The temperature isosurfaces in flame D, as obtained by 1-step and flamelet models (not shown) seem to be continuous without a noticeable sign of extinction. This is consistent with the nature of 1-step reaction and flamelet models which do not allow significant or any local extinction. However, the temperature isosurface as obtained by the 12-step mechanism in flame D (Fig. 2.5a) exhibits discontinuities at  $x/D \approx 5$  and  $x/D \approx 15$ ; suggesting limited (local) extinction at some regions of the flame. For flame F, the local extinction is much more significant and clearly visible in Fig. 2.5b, where the temperature isosurfaces are shown to be severely broken after  $x/D \approx 5$  when 12-step model is used. This is consistent with Fig. 2.4b that shows stronger turbulent flow in flame F and lesser effect of combustion on turbulence due to enhanced local flame extinction. In contrast, the local extinction is not so important when 1-step model is used or is not present when flamelet model is used. These are also consistent with the results shown below. It is noted here that the images in the

following sections of this dissertation are presented in color.

### 2.4.1 Turbulence and Flame Statistics

Figure 2.6 shows the radial variations of the time-averaged mean axial velocity and RMS of axial velocity for flames D and F at  $x/D = 15$ . In this figure, the LES predicted Favre-averaged results obtained with flamelet, 1-step and 12-step chemistry models are compared to Favre-averaged experimental data. The measurement error is estimated to be below 5% for the mean velocity and about 10% for the RMS [143]. In general, the agreement between the calculated and the measured mean values is good for both flames for all of the tested chemistry models, suggesting that the chemistry effects on the mean axial velocity is not significant.

For both flames, the predicted RMS values are lower and higher than the experimental values at  $r/D \approx 1$  and  $x/D \approx 0$ , respectively. The agreement between the numerical and measured values is better at  $r/D > 1$ . For flame D, the predictions with 12-step model are higher at  $r/D < 1$  while the predicted RMS values with 1-step, flamelet and 12-step models are close at  $r/D > 1$ . This is understandable since in the jet core region the effect of combustion on turbulence is more significant. In this region, the turbulence damping is less when 12-step model is used. The 1-step and flamelet models predict higher heat release and mean temperature (Fig. 2.7a). Similar trend is observed in flame F (Fig. 2.6d). For this flame, the predicted values by the flamelet model are the lowest due to highest heat release effects. The results in Fig. 2.6 are consistent with those shown in Figs. 2.5 and 2.7.

The favre-averaged mean values of the temperature for flames D and F are shown in Figs. 2.7a and 2.7b, respectively. The measured temperatures in flame F are much lower than those in flame D; at  $x/D = 15$ , the peak temperature is about 1100K in flame F compared to 1750K in flame D. Nevertheless, the radial variation of the mean temperature is observed to be reasonably well predicted by the LES/FMDF

when 12-step model is employed. The predicted mean temperatures are higher than the corresponding experimental values for both flames when 1-step or flamelet model is used. The 1-step model is based on an irreversible and fast reaction that generally overpredicts the flame temperature, particularly in the rich side of the flame. However, the mean temperatures calculated by the flamelet model are higher than those via 1-step in flame F, since the flamelet model does not allow extinction. These results show the importance of chemical kinetics model particularly when flame F is simulated. It is possible to improve the 1-step model predictions by adjusting the reaction parameters. However, we have decided to use the same original values for these parameters.

Figs. 2.7c and 2.7d show the predicted and measured values of the RMS of temperature. Overall, the computed results for flames D and F are not very different than the experimental data in the jet core region when 12-step model is used. The difference is much more significant away from centerline at  $r/D > 1.5$ . This can be attributed to the differences in the physical structure of turbulence. The results shown below indicate a better comparison between experiment and LES when temperature RMS is plotted in the mixture fraction domain. The RMS of temperature is affected by the combined effects of turbulence and heat conduction on one hand, and the chemical heat release on the other.

The axial variations of the mean temperature, mixture fraction and axial velocity along the jet centerline (not shown) are found to be in good agreement with the experimental data for both flames D and F when 12-step model is used. The 1-step and flamelet model predictions are less accurate, as expected. Also, the mean temperature and mixture fraction profiles as obtained from the finite difference part of LES/FMDF are found to be close with those calculated from the Monte-Carlo part, indicating the insignificance of the numerical error.

Radial profiles of the  $CO_2$  mass fraction for flames D and F as obtained by the

12-step model are shown in Fig. 2.8a. There is again good agreement between the computed and measured values in both flames, particularly at the jet core region. The agreement is less away from the centerline. Again, this can be primarily attributed to the differences in the turbulence structure. The radial profiles of the intermediate species  $H_2$ ,  $CO$  and  $OH$  in Figs. 2.8b, 2.8c, 2.8d also indicate a good agreement between LES/FMDF and experiment when 12-step model is employed. The results for other species (e.g.  $CH_4$  and  $O_2$ ) are similar to those shown in Fig. 2.8 and are not shown. In comparison with the experimental data, the LES/FMDF predictions with 1-step and flamelet models exhibit considerable differences, specially for flame F.

The radial variation of the mean heat release in the energy equation at  $x/D = 7.5$  as calculated by the flamelet and 12-step models are shown in Fig. 2.9. The results at  $x/D = 15$  exhibit similar trends and are not shown. For flame D, the LES/FMDF results for 12-step and flamelet models are relatively close which is consistent with the isosurfaces and statistics of the temperature. However, for flame F, the predicted heat release with flamelet model is substantially higher than that with the 12-step model. This is consistent with the mean and the isocontours of temperature in Figs. 2.7b and 2.5b.

## 2.4.2 Compositional Flame Structure

The measured and computed conditional average and RMS values of various flame variables conditioned on the mixture fraction, in Figs. 2.10 and 2.11, show the structure of the piloted jet flames D and F [142]. The numerical results are obtained by the LES/FMDF with the 12-step chemistry model and  $C_\phi = 10$ . As commonly done in experimental and computational studies [65, 89, 90, 112–115, 117–121], the conditional averages and RMS are computed by using the data in a plane perpendicular to the jet axis at several different times. Figs. 2.10a and 2.10c show that for

flame D the peak values of conditional mean temperature are slightly overpredicted by the LES/FMDF at both locations from the nozzle, which is consistent with the underprediction of  $O_2$  mass fraction. The slightly higher predicted values of mean temperature at both locations for flame D in Figs. 2.10a and 2.10c are consistent with less scatter in the temperature data shown below in Figs. 2.12c and 2.12d. This could be due to SGS stress, SGS scalar flux, or mixing models. The conditional RMS of temperature, as shown in Figs. 2.10a and c, are also slightly underpredicted by LES/FMDF.

Figs. 2.10b and 2.10d show the conditional mean mass fractions of the  $CO$  and  $H_2$  species for flame D. Evidently, the  $H_2$  concentration is very well predicted at both lean and rich sides of the flame away from the stoichiometric location, where it is over predicted. The predicted  $CO$  mass fraction also agree well with the experimental data on the lean side of the flame, but they tend to be higher than the measured data on the rich side. For flame D, the reported conditional averages of the temperature,  $O_2$ ,  $CO$  and  $H_2$  mass fractions exhibit trends similar to those appeared in the literature [67, 89, 90, 146, 147].

The conditional mean and RMS of the temperature and the  $O_2$  mass fraction as obtained by LES/FMDF with the 12-step kinetics model for flame F are shown in Figs. 2.11a and 2.11c. At  $x/D = 7.5$ , the LES/FMDF results are in good agreement with the experimental data. However, the conditional average temperature is slightly overpredicted on the rich side of the flame at  $x/D = 15$ , which is again consistent with the underestimation of the  $O_2$  mass fraction. Interestingly, the (conditional) RMS values of the temperature are well predicted at  $x/D = 15$ . The increase in the magnitude of the temperature RMS in flame F is due to stronger strain field in this flame in comparison to that for flame D. However, the higher level of local extinction in flame F leads to the conditional mean temperature in this flame to be lower than that in flame D.

The conditional  $CO$  and  $H_2$  mass fraction for flame F are shown in Figs. 2.11b and 2.11d. Again, the experimental results are well predicted for all mixture fraction values at  $x/D = 7.5$ , while there is a slight discrepancy between the experimental and computational data for  $Z \geq 0.45$  at  $x/D = 15$ . Despite some uncertainty in the flow conditions, the predictions of the flame F by the LES/FMDF are in overall good agreement with the experimental data when 12-step chemistry model is employed. The error in the conditional mean  $CO$  mass fraction and temperature on the rich side of the flame are consistent with those reported by others [65, 113, 115, 148, 149].

The scatter plots of temperature in the mixture fraction space as obtained by the LES/FMDF with the 12-step mechanism for both flames D and F are compared with the experimental data in Figs. 2.12 and 2.13. The steady-state results obtained from low-strain laminar opposed jet flame simulations are also shown for comparison. For flame D, as Figs. 2.12a and 2.12b indicate, there is a limited scatter in the experimental data at  $x/D = 7.5$  and at  $x/D = 15$ , suggesting that the local extinction is insignificant [64]. For flame F, there is considerable local extinction and significant scatter in the data at  $x/D = 7.5$ , and 15 (Figs. 2.13a and 2.13b). Also at both locations, the LES/FMDF results for flame F are considerably lower than the laminar flamelet results, while they are close to the laminar flamelet results for flame D. Overall, the computed temperatures show a reasonably good agreement with the experimental data at different locations. For flame D, there are some finite-rate effects in the experimental data that is not fully captured by the LES/FMDF. This could be due to SGS turbulence and mixing models. At  $x/D = 7.5$ , a limited local extinction is predicted by the LES/FMDF for flame F when 1-step model is employed, which is consistent with the isosurface contours of the temperature. Our results (not shown) indicate that the temperatures are significantly overpredicted by the 1-step model in the rich side of the flame.

Fig. 2.14 shows the predicted favre time-averaged mean and RMS of temperature,

and the predicted Favre mean values of  $O_2$ ,  $CO$  and  $H_2$  mass fractions in flames D and F as a function of the mean mixture fraction in comparison to the corresponding experimental data. These values are obtained by cross-referencing the radial mean and rms values of the temperature and species mass fractions with the radial mixture fraction. The computed data are obtained by the LES/FMDF with the 12-step chemistry model and mixing model constant of  $C_\phi = 10$ .

For flame D, both the peak and shape of scalar and temperature profiles for mean and RMS are well predicted by the LES/FMDF (Fig. 2.14a). At axial location of  $x/D = 15$ , the RMS of temperature appears to be slightly underpredicted for  $\langle Z \rangle_L \leq 0.125$ . Considering the highly sensitive and oscillatory behavior of flame F, the Favre-averaged mean and RMS of temperature, and the Favre-averaged mean mass fraction of  $O_2$  are actually well predicted by LES/FMDF (Fig. 2.14b), even though the mean temperature is somewhat underpredicted on the rich side of the flame. The RMS of temperature for flame F exhibit similar trend to that for flame D. As shown in Fig. 2.14c and d, the mean mass fractions of  $CO$  and  $H_2$  are also in overall good agreement with those of experiment for both flames at  $x/D = 15$ . However, there are some discrepancies in the  $CO$  profile for flame F at  $x/D = 7.5$  on the rich side (not shown), mainly due to finite rate effects. This is consistent with the underpredictions of  $CO$  in the rich side of the flame that has been reported in the literature [146]. Additional error might be resulted from the constant mixing coefficient in the LMSE mixing model. However, similar trends have been observed in the calculated mean profiles of  $Y_{CO}$  by Pitsch *et al.* [90, 146], who used a dynamic method to compute the IEM mixing model coefficient. This issue is discussed further in the following section.

### 2.4.3 Subgrid-Scale Mixing

In this section we focus on the sensitivity of the LES/FMDF calculations to the mixing model coefficient  $C_\phi$  which is either empirically prescribed or dynamically evaluated in the simulations considered below. All of the following simulations are conducted with the 12-step reaction model.

Fig. 2.15a and b show radial profiles of the mean (favre-averaged) temperature for flames D and F as obtained by the LES/FMDF with various  $C_\phi$ . The mean species mass fractions exhibit similar trends to that of temperature and not shown. For flame F, a comparison between the results obtained with constant values of  $C_\phi = 6, 8, 10$  indicates that by increasing  $C_\phi$  the mixing/combustion enhances and the average temperature increases, albeit not linearly, which is expected and consistent with the previous studies [65, 113, 116]. However, the influences of  $C_\phi$  on the temperature profiles of flame D do not seem to be very significant. This is because of the less sensitivity of flame D, which is close to equilibrium, to the molecular mass and thermal diffusivity coefficients. The mean temperatures predicted by the dynamic models DM1 and DM2 are also shown in Fig. 2.15a, b to be close to those obtained by constant  $C_\phi$  for flame D. However, comparison of the results obtained with DM1 and DM2 with those of  $C_\phi = 6, 8, 10$  for flame F indicates that the physical flame structure is affected more by the mixing model in this flame. The higher mean temperature values observed with DM2 for flame F is due to higher level of mixing. With DM1, the predicted mixing is relatively lower than that obtained with constant coefficient of  $C_\phi = 10$ . Consistently, the predicted temperature RMS by DM1 is found to be higher than those calculated with  $C_\phi = 10$ . The dynamic model DM2 predicts the highest RMS temperature. The results for constant mixing coefficients (not shown) indicate that the mean heat release is significantly lower for  $C_\phi = 6, 8$  in comparison with  $C_\phi = 10$  in flame F simulations. Combined with the stronger turbulence in flame F, these lower heat release values yields substantially lower mean temperature

profiles (Fig. 2.15b). Also, consistent with the mean temperature profiles shown in the preceding figures, substantially higher mean heat release values are observed when DM2 model is employed, particularly for flame F.

The effects of mixing model on the compositional structure of flames D and F are shown in Figs. 2.16 - 2.17, where the variations of various flame variables in the mixture fraction domain for different mixing model coefficients are considered. In Figs. 2.16a and 2.16c, the conditional profiles of the mean temperature and RMS of temperature for flame D with different constant  $C_\phi$  and dynamic models at axial locations of  $x/D = 7.5$  and  $x/D = 15$  are compared with the experimental data. Overall, the mean temperature is well predicted by the LES/FMDF. However, at  $x/D = 7.5$ , the peak values of the conditional temperature are observed to be slightly overestimated for all  $C_\phi$  coefficients. The conditional RMS of temperature is shown to be also well captured with LES/FMDF when  $C_\phi = 6, 8$  or DM1 is used, while it is underestimated with the DM2 model at all mixture fraction values. The inaccuracy of simulations with DM2 model is mainly due to local equilibrium assumption in the dynamic model as Raman and Pitch [90] suggested. Consistent with our earlier results and with those obtained by others [65, 113, 116], the RMS of temperature decreases and the mean temperature increases as  $C_\phi$  increases. The results at  $x/D = 15$  are somewhat similar to those at  $x/D = 7.5$ , but more visibly, the conditional mean temperature are overestimated by the LES/FMDF in the stoichiometric and the fuel-rich regions. Also, the deviations between the experimental and LES/FMDF values of the temperature RMS are higher at  $x/D = 15$ , mainly due to stronger turbulence at downstream locations.

Figs. 2.16b and 2.16d show the conditional averages of species  $CO$  and  $H_2$  for flame D at two different downstream locations. At  $x/D = 7.5$ , the predicted values are generally in agreement with the reported experimental data at all mixture fraction values for all  $C_\phi$  values. There seems to be a slight overprediction of the experimental

data around the stoichiometric point when  $C_\phi = 8, 10$  or DM2 is used, which is mainly due to differences in heat release. As expected this effect is more noticeable at further downstream locations (Fig. 2.16d). The experimental profiles of  $H_2$  mean mass fraction at both axial locations are overpredicted by the LES/FMDF in the stoichiometric region but are well captured at all other mixture fractions by the simulations.

Figs. 2.17a and 2.17c show the computed and measured conditional mean and RMS of temperature for flame F at two downstream locations. At  $x/D = 7.5$ , the local extinction and conditional mean temperature and the extend of local extinction present in flame F are well predicted for  $C_\phi = 6, 8$  and DM1 model. However, the DM2 model overpredicts the peak temperature, even though the predictions on the lean and rich sides of the flame are still in fairly good agreement with the experiment. Also at this location, the RMS fluctuations of the conditional mean temperature are well predicted for all  $C_\phi$ 's. At further downstream location of  $x/D = 15$ , where the effects of turbulence is more significant, the conditional mean temperature is underpredicted at stoichiometric and lean side of the flame by the LES/FMDF when mixing coefficient is constant  $C_\phi = 6, 8$ . The simulations conducted with the dynamic models of DM1 and DM2 overpredict the measured mean temperatures for the mixture fraction values of  $Z \geq 0.25$ . The poorest agreement is for DM2 model, mainly a result of higher heat release. At  $x/D = 15$ , the computed conditional RMS of temperatures are also in good agreement with the experimental data for  $C_\phi = 6, 8$  and DM1. With the DM2 model, there is an underprediction of data at lean side of the flame, possibly due to sensitivity of the flame F to the oscillations in the dynamic model coefficient. Similar to what have been shown for flame D, the  $CO$  and  $H_2$  mass fractions profiles agree well with the experimental data for flame F at  $x/D = 7.5$  as observed in Fig. 2.17b. Only the peak values of these species are overestimated when DM2 is used, which is consistent with the expository temperature profiles in

Fig. 2.17a. Similar results have been observed at lower jet speed for the (piloted jet) flame E by Raman and Pistch [90]. Close examination of the mass fraction profiles at  $x/D = 15$  (Fig. 2.17d) indicates that the LES/FMDF results with constant mixing coefficients of  $C_\phi = 6, 8$  are better than those with DM1 and DM2 models. Both dynamic models tend to underpredict the rate of change of the mean  $CO$  mass fraction profile with the Reynolds number, which is consistent with the results obtained by others for jet flames [65, 115, 147–149]. Nevertheless, the strong influences of the turbulence on the flame and the level of local flame extinction as seen in the conditional variables seem to be well captured by the LES/FMDF, not only with constant mixing coefficients but also with the dynamically computed, composition dependent, mixing coefficients.

For flame D, the computed time-averaged mean temperature with different  $C_\phi$  models (not shown) are found to be close to each other, and generally in agreement with the experimental data. Similarly, the predicted values of mean mass fraction of  $CO$  and  $H_2$  for different  $C_\phi$ 's agree well with the experimental data. Again, by increasing the SGS mixing coefficient  $C_\phi$  the peak mean temperature are found to increase.

The mean values of the temperature and species mass fractions are more sensitive to  $C_\phi$  for flame F. However, the measured mean temperature profiles and the level of local flame extinction seem to be well predicted by the simulations when  $C_\phi = 10$ . There are some minor differences between LES/FMDF and experiment when DM2 is employed. This is consistent with the overprediction of  $CO$  mass fraction by DM2 model in flame F.

The scatter plots of temperature in the mixture fraction domain for various mixing models and for both flames D and F are shown in Figs. 2.18 - 2.19. These results obtained, similar to experiment, by collecting the data from the cells that are at radial distance of  $x/d = 0.83$ . Only the results at  $x/D = 7.5$  are shown. The trends

are similar at different axial locations. The solid lines in Figs. 2.18 - 2.19 show the temperature for a low-strain ( $10/s$ ) laminar opposed jet flame profile.

Figs. 2.18 shows the scatter plots of temperature for flame D. In general, the computed temperature for flame D are in reasonably good agreement with the measurements. Evidently, the number of data points with relatively low temperature is lowest for case DM2, which is consistent with the overestimation of the peak conditional mean temperature in Fig. 2.16a by this model. Simulations with the dynamic model DM1 and with constant coefficients of  $C_\phi = 6, 8, 10$  exhibit a more significant finite rate chemistry effect, making the prediction of the conditional mean temperature closer to experiment for these cases. The results at  $x/D = 15$  (not shown) exhibit similar trends, even though the distribution of the scattered temperature points is narrower in the fuel-rich side [65, 145].

For flame F, it can be safely stated that the challenging task of representing the increasing level of local extinction is fairly accomplished by the LES/FMDF when 12-step model is employed. As shown in Fig. 2.19, the results calculated with different  $C_\phi$  coefficients are somewhat similar and are in quite good agreement with the reported experimental data; this is consistent with the accurate predictions of conditional mean temperatures in Fig. 2.17a. The predictions of the dynamic models DM1 and DM2 tend to show less number of “low temperature” data points and consequently higher average temperature, nevertheless, they seem to well capture the “two banded structure” observed in the experimental data (Fig. 2.13).

## 2.5 Summary and Conclusions

This paper is concerned with the application and assessment of the filtered mass density function (FMDF) for large-eddy simulation (LES) of Sandia’s “high speed” piloted turbulent methane jet flames [64]. The LES/FMDF calculations are con-

ducted with both finite-rate and flamelet-type reaction models. The flamelet model employs detailed (GRI-3) kinetics mechanism. The finite-rate model employs 1-step and 12-step mechanisms. Various subgrid-scale mixing models are also used and tested. A scalable algorithm for parallelization of the hybrid (Eulerian-Lagrangian) LES/FMDF methodology is presented and the consistency of its Monte Carlo - finite difference solutions were discussed. The parallel algorithm was shown to yield superlinear speedups with respect to single node calculations. The Favre-averaged temperatures for the two jet speeds (referred to as flames D and F) were found to be in fairly good agreement with the experimental data. For the lower speed jet (flame D), the numerical results are consistent with the experiment exhibiting near-equilibrium flame structure with limited local extinction. The higher degrees of local extinction observed in the higher speed jet (flame F) is successfully captured and reproduced with the LES/FMDF when 12-step chemistry model is employed. As expected, the flamelet and 12-step chemistry models generate results close to each other and comparable to experiment for flame D. For flame F, only the 12-step model predictions are comparable to experiment. For this flame, the higher heat release predicted by the 1-step and flamelet models suppress the effects of turbulence on the flame. The sensitivity of the calculations to the subgrid mixing model coefficient  $C_\phi$  is also inspected by performing simulations with different model coefficients and with two dynamic models. The LES/FMDF results seem to be much more sensitive to the mixing model (and the way model coefficient is evaluated) in flame F than in flame D. Even though, the results with different mixing coefficients and models are not that much different for flame D, the calculations conducted with constant coefficient of  $C_\phi = 10$  yield the most accurate overall agreements for both flames. Further improvements in the predictions might be possible with better mixing and subgrid stress/scalar flux closures.

## 2.6 Tables and Figures

Table 2.1: Important parameters of Sandia's piloted turbulent methane jet flames D and F.

	Flame D	Flame F
$Re_{jet}$	22400	44800
Main jet diameter	7.2 mm	7.2 mm
Pilot jet diameter	18.2 mm	18.2 mm
Main jet bulk velocity	49.6 m/s	99.2 m/s
Main jet peak velocity	63.1 m/s	126.2 m/s
Main jet temperature	300 K	300 K
Pilot bulk velocity	11.4 m/s	22.8 m/s
Pilot temperature	1880 K	1880 K
Pilot mixture fraction	0.27	0.27
Co-flow bulk velocity	0.9 m/s	0.9 m/s

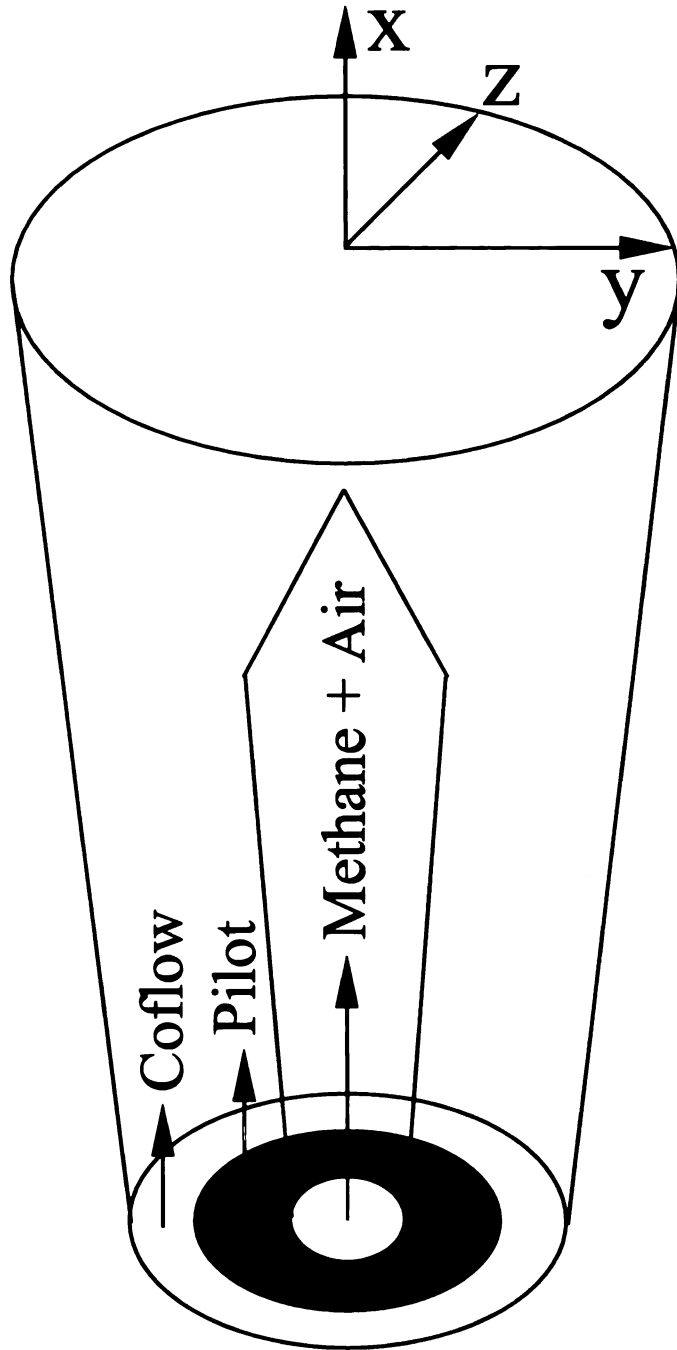


Figure 2.1: Schematic view of the Sandia's piloted methane jet flame. Main jet and pilot jet diameters are  $7.2\text{mm}$  and  $18.2\text{mm}$ , respectively.

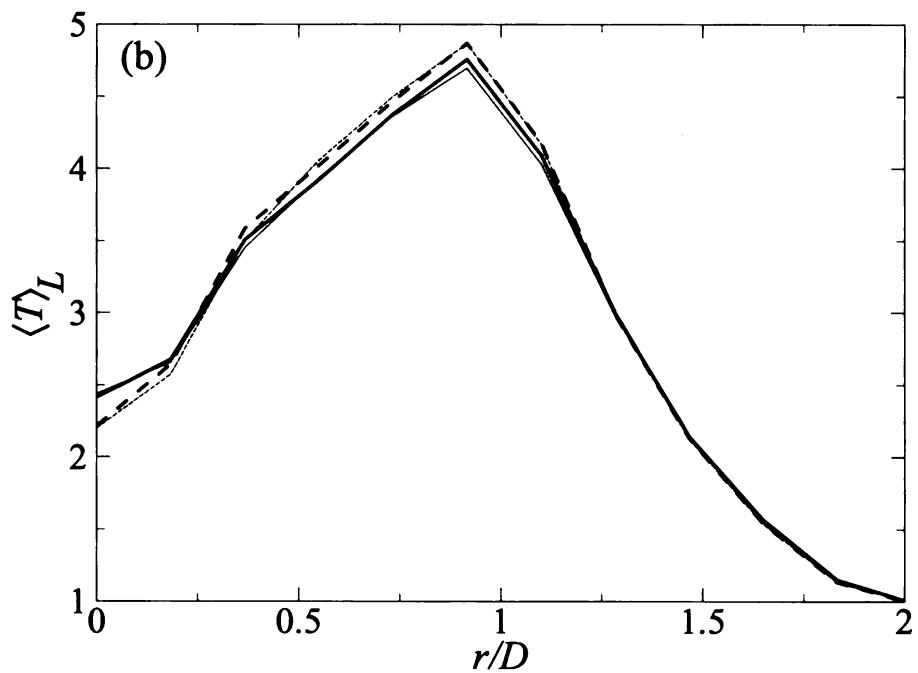
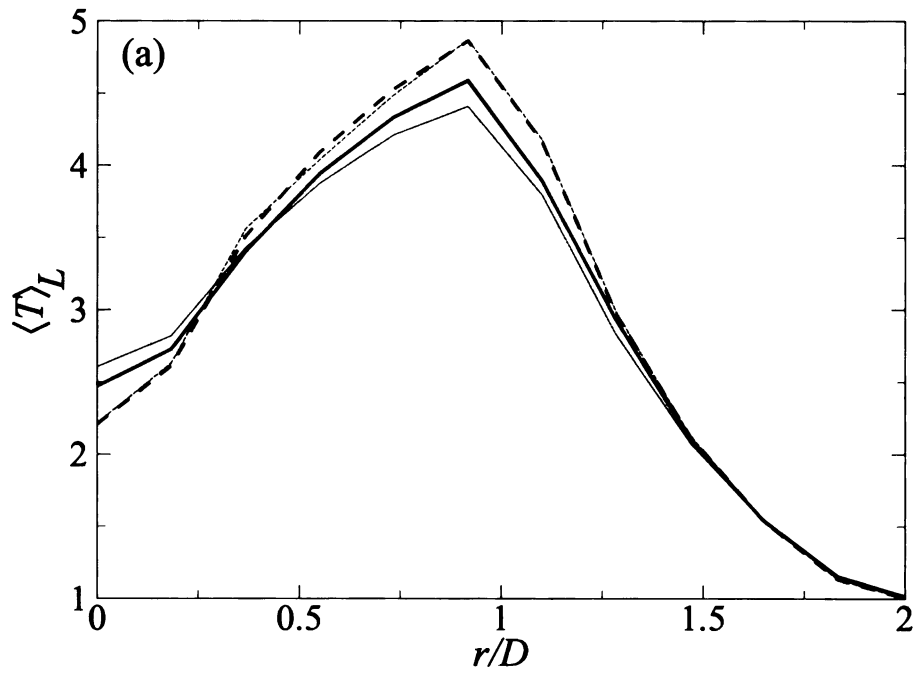


Figure 2.2: Comparison between Monte Carlo (MC) and finite difference (FD) values of the normalized instantaneous filtered temperature; (a)  $\Delta_E = 2\Delta$ , and  $C_\phi = 8, 16$ , (b)  $\Delta_E = \Delta$ , and  $C_\phi = 8, 16$ . MC with  $C_\phi = 8$ ; thick solid line, FD with  $C_\phi = 8$ ; thick dashed line, MC with  $C_\phi = 16$ ; solid line, FD with  $C_\phi = 16$ ; dashed line.

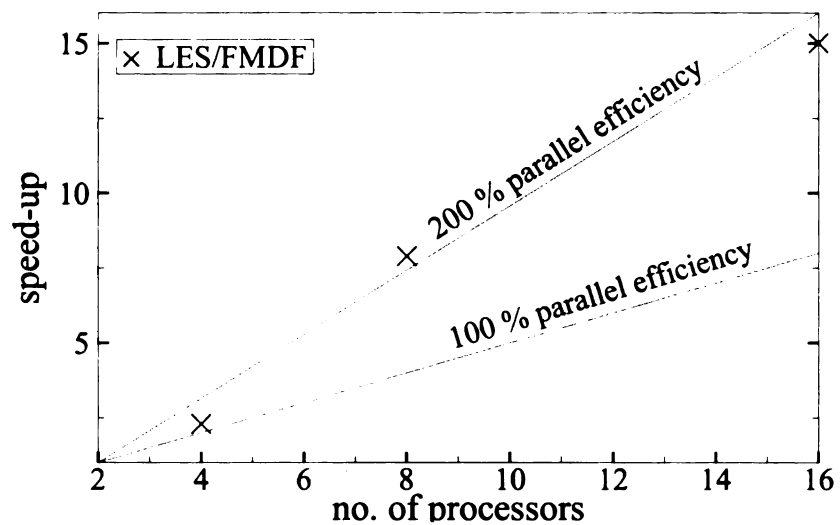


Figure 2.3: Speed-up of the parallelized LES/FMDF calculations relative to those conducted on a 2-processor node.

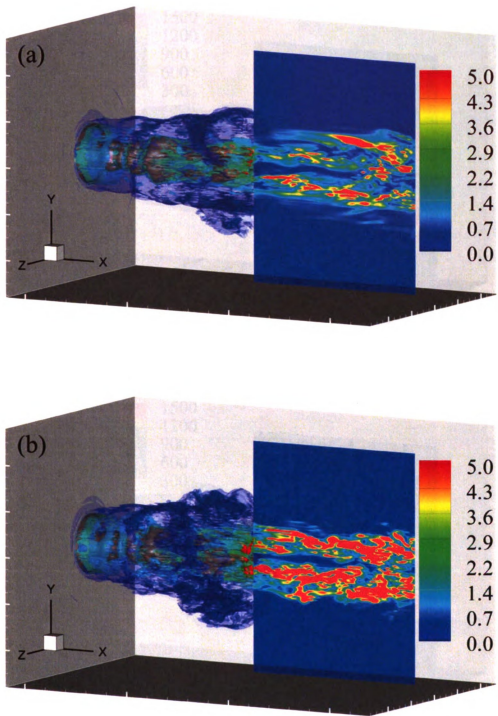


Figure 2.4: Isosurfaces and isocontours of vorticity magnitude,  $\Omega$ , obtained by LES/FMDF with the 12-step chemistry model; (a) flame D and (b) flame F.

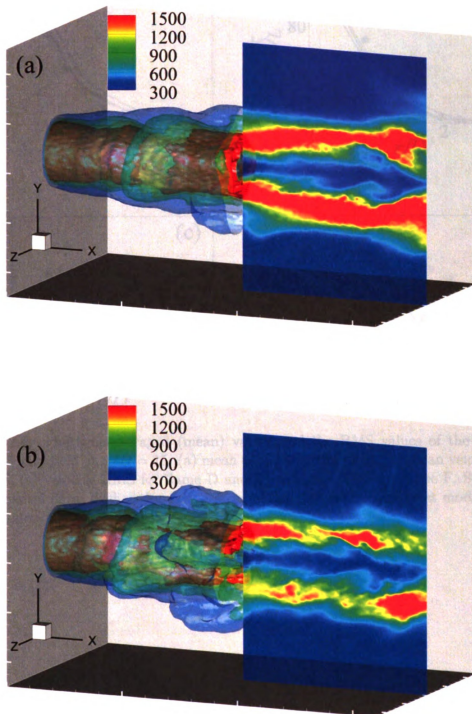


Figure 2.5: Isosurfaces and isocontours of filtered temperature,  $\langle T \rangle_L$ , obtained by LES/FMDF with the 12-step chemistry model; (a) flame D and (b) flame F.

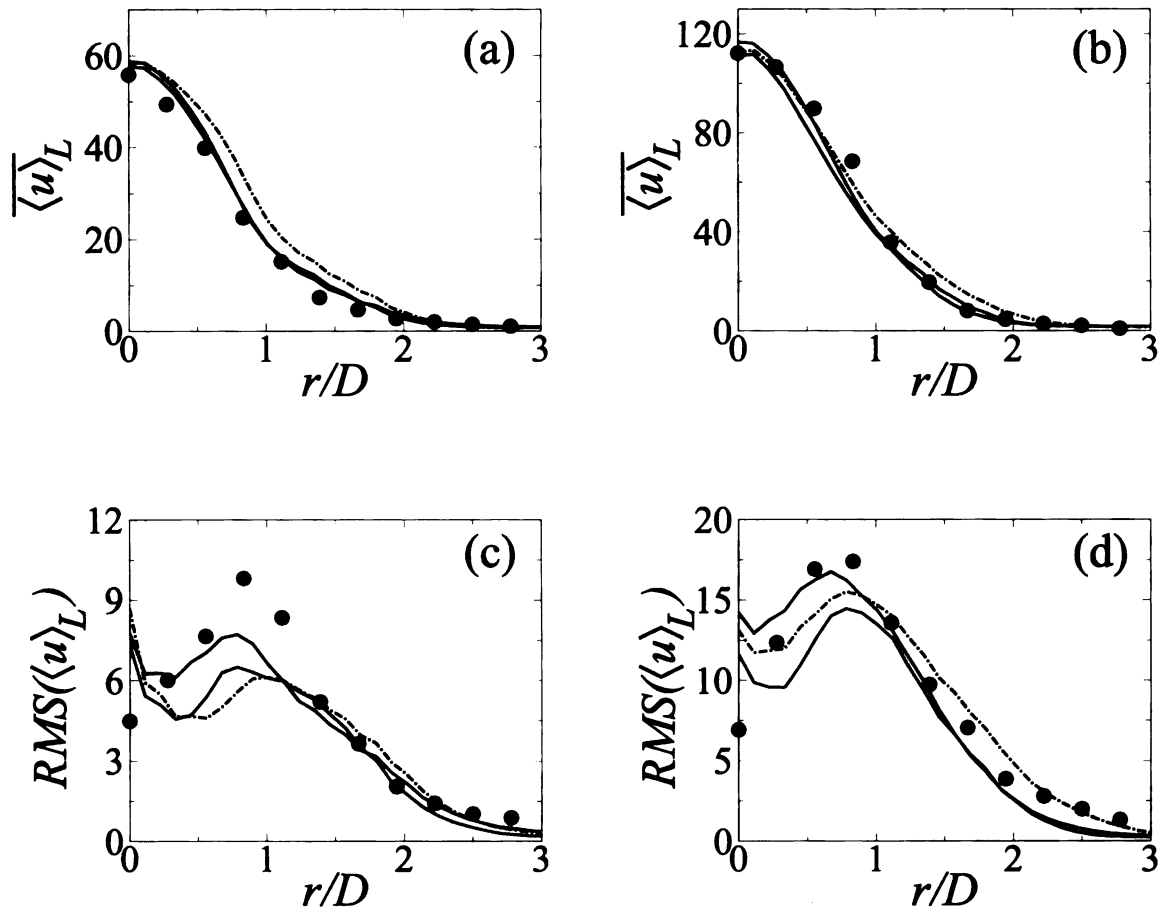


Figure 2.6: The time-averaged (mean) values and the RMS values of the filtered axial velocity field at  $x/D = 15$ ; (a) mean velocity for flame D, (b) mean velocity for flame F, (c) velocity RMS for flame D and (d) velocity RMS for flame F. Symbols, experimental data; dashed-dot line, 1-step model; dashed line, flamelet model; solid line, 12-step model.

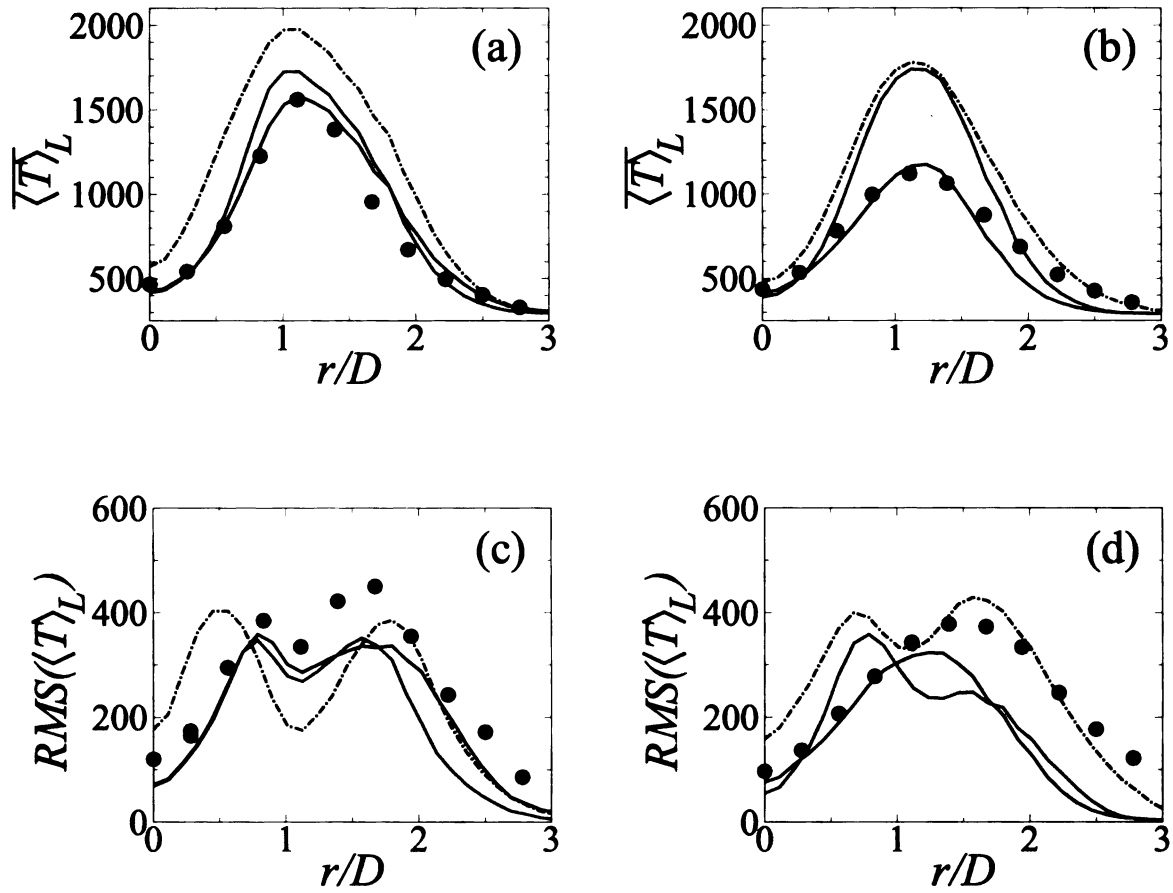


Figure 2.7: The time-averaged (mean) temperature and RMS of temperature at  $x/D = 15$ ; (a) mean temperature for flame D, (b) mean temperature for flame F, (c) RMS of temperature for flame D and (d) RMS of temperature for flame F. Symbols, experimental data; dashed-dot line, 1-step model; dashed line, flamelet model; solid line, 12-step model.

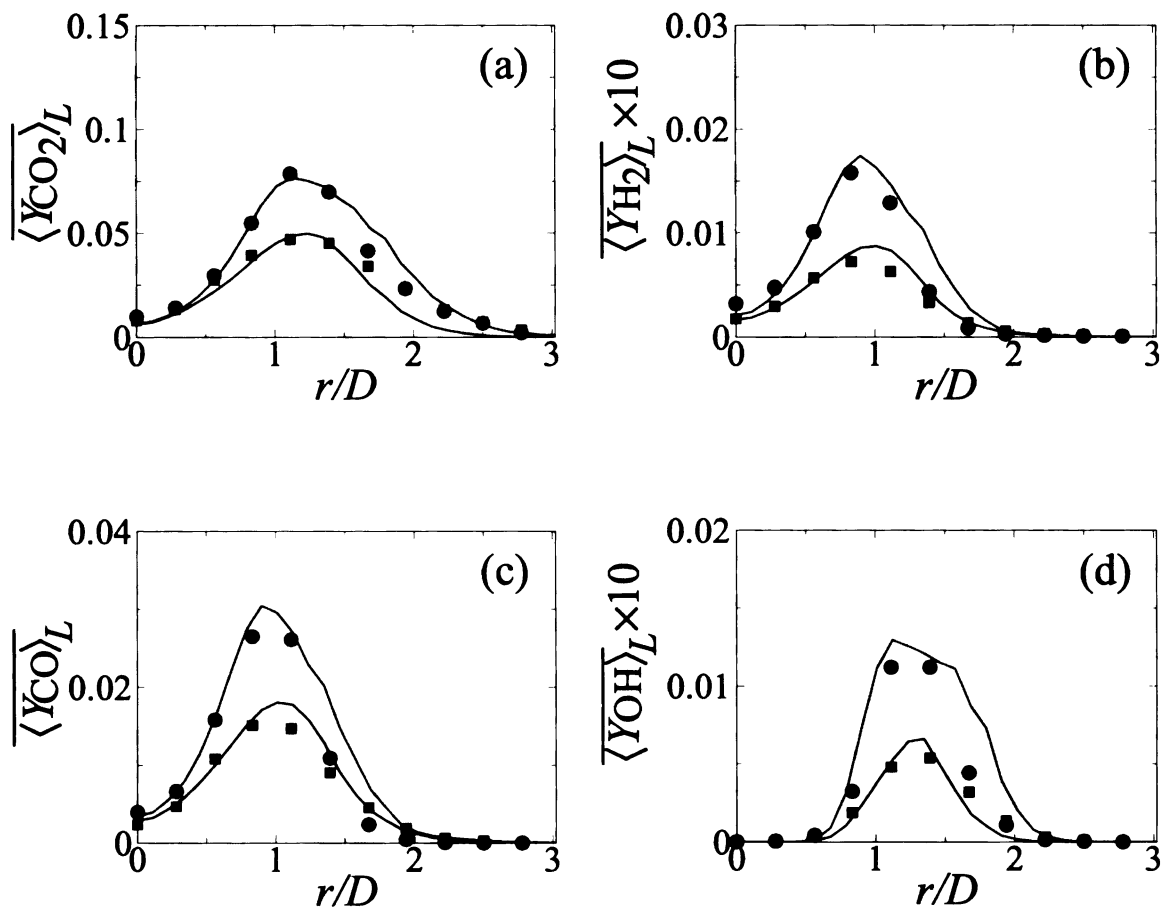


Figure 2.8: Profiles of various species mass fractions as predicted by LES/FMDF with the 12-step model at  $x/D = 15$ ; (a)  $CO_2$  (b)  $H_2$ , (c)  $CO$ , (d)  $OH$ . Circles, measured flame D; squares, measured flame F; dashed line, computed flame D; solid line, computed flame F.

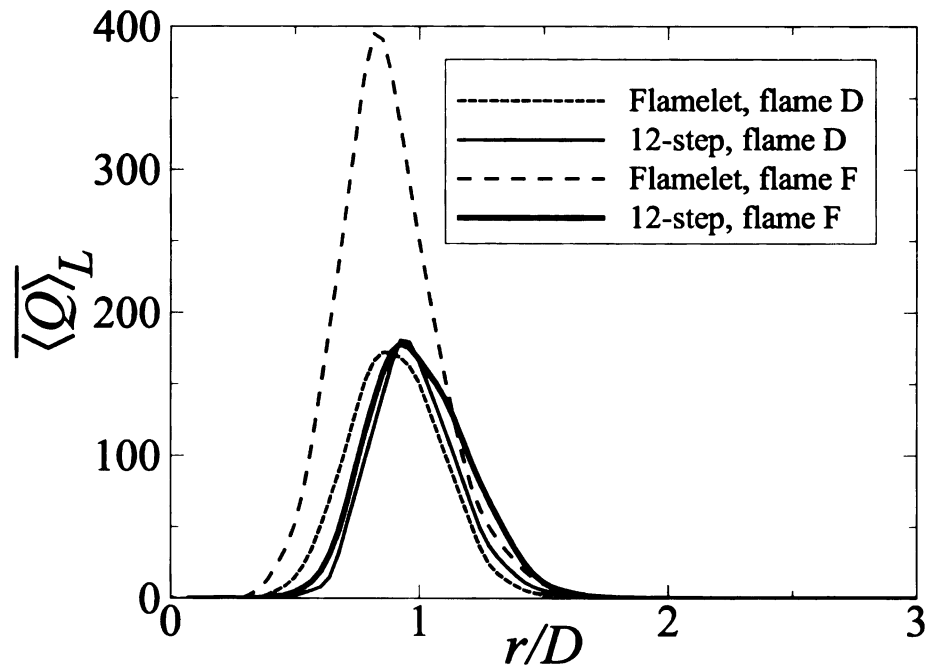


Figure 2.9: Profiles of mean heat release for the flamelet and 12-step models in flame D (dashed line, flamelet; solid line, 12-step) and in flame F (long dashed line, flamelet; dashed-dot line, 12-step) at  $x/D = 7.5$ .

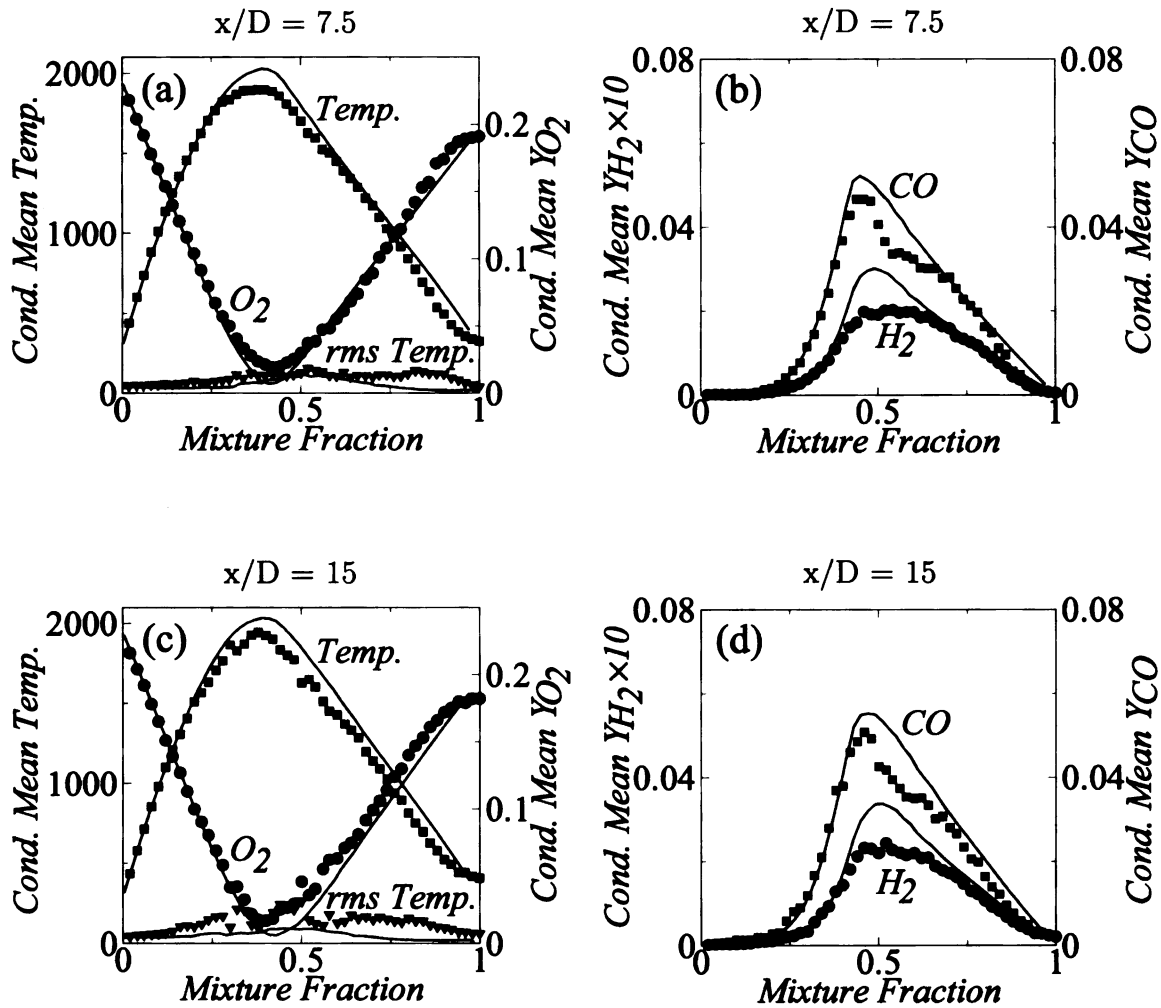


Figure 2.10: Conditional mean temperature and  $O_2$ ,  $CO$ ,  $H_2$  mass fractions for flame D as predicted by LES/FMDF with 12-step kinetics mechanism and with  $C_\phi = 10$ ; (a) and (b) show the results, at  $x/D = 7.5$ ; (c) and (d) show the results, at  $x/D = 15$  (lines, calculations; symbols, measurements).

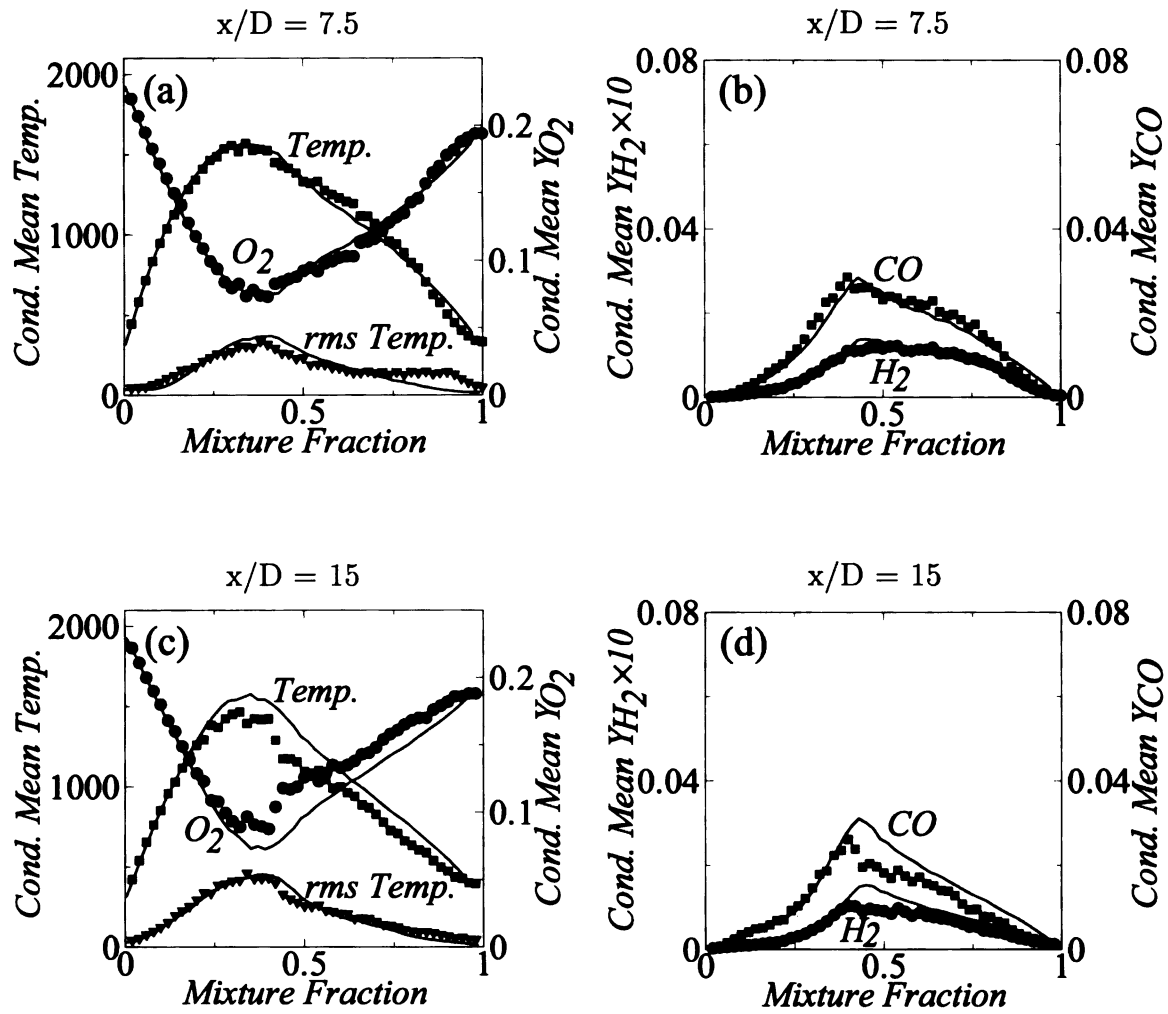


Figure 2.11: Conditional mean temperature and  $O_2$ ,  $CO$ ,  $H_2$  mass fractions for flame F as predicted by LES/FMDF with 12-step kinetics mechanism and with  $C_\phi = 10$ ; (a) and (b) show the results, at  $x/D = 7.5$ ; (c) and (d) show the results, at  $x/D = 15$  (lines, calculations; symbols, measurements).

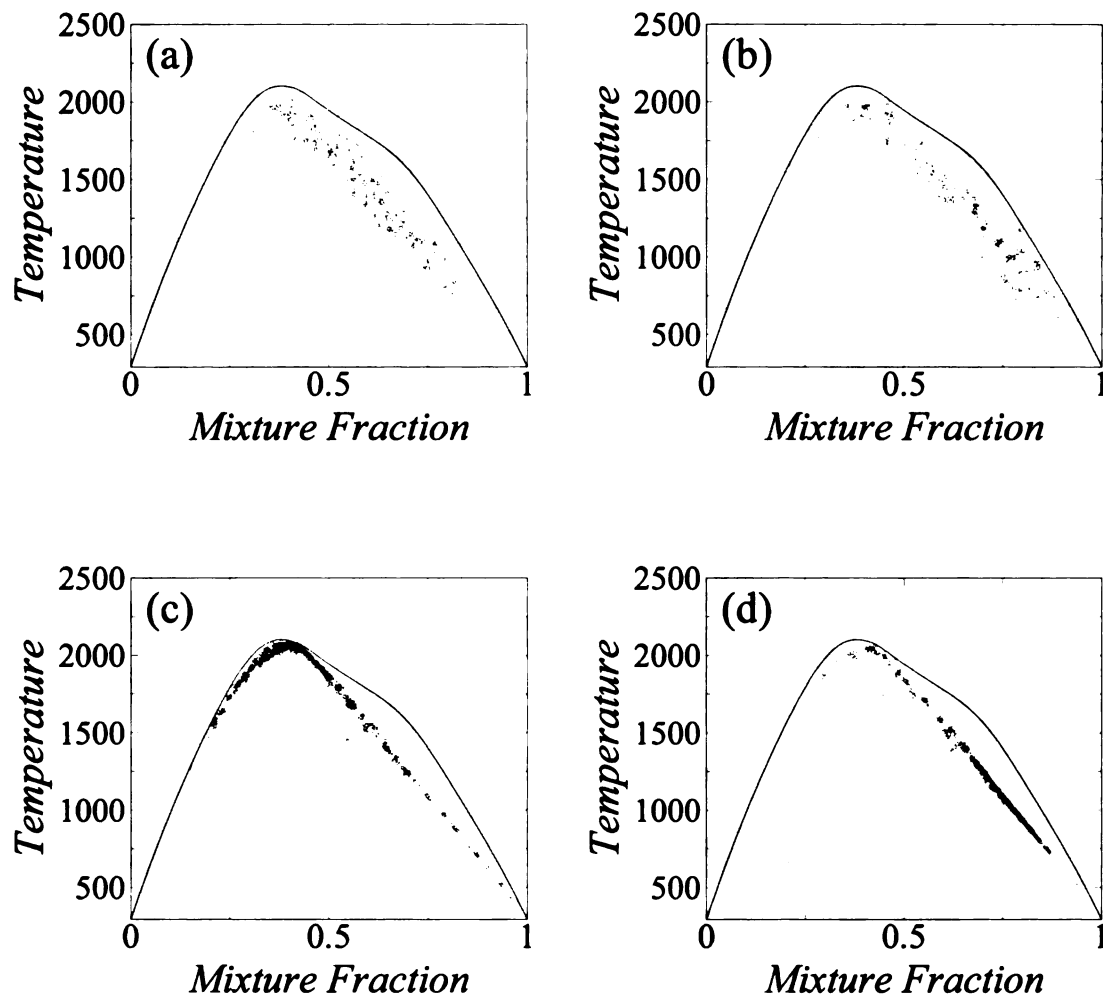


Figure 2.12: Scatter plots of temperature vs. mixture fraction at  $r/D = 0.83$  for flame D; (a) measurements at  $x/D = 7.5$  (975 sample points); (b) measurements at  $x/D = 15$  (780 sample points); (c) calculations with LES/FMDF and 12-step mechanism at  $x/D = 7.5$  (973 sample points); (d) calculations with LES/FMDF and 12-step mechanism at  $x/D = 15$  (762 sample points).

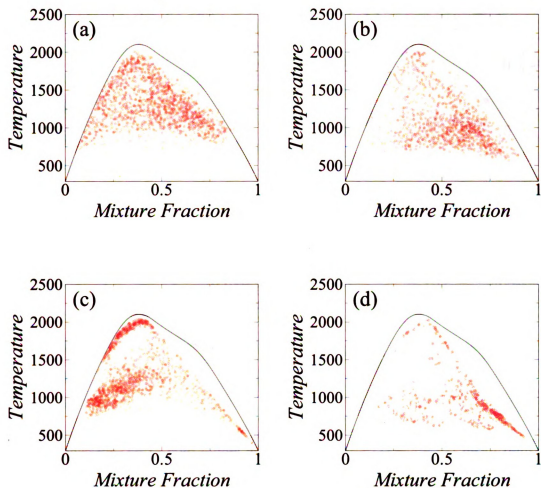


Figure 2.13: Scatter plots of temperature vs. mixture fraction at  $r/D = 0.83$  for flame F; (a) measurements at  $x/D = 7.5$  (1550 sample points); (b) measurements at  $x/D = 15$  (976 sample points); (c) calculations with LES/FMDF and 12-step mechanism at  $x/D = 7.5$  (1347 sample points); (d) calculations with LES/FMDF and 12-step mechanism at  $x/D = 15$  (1097 sample points).

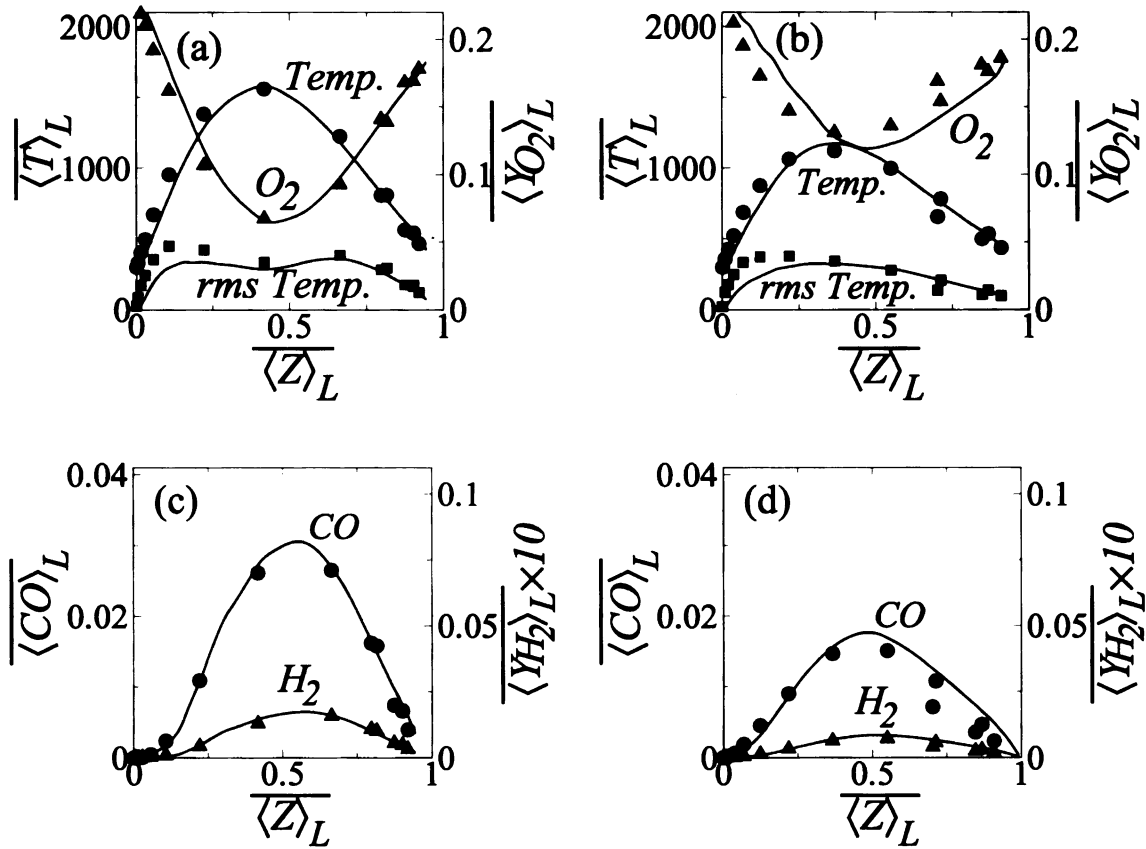


Figure 2.14: Comparison between LES/FMDF and experimental data in the mixture fraction space for the 12-step model with  $C_\phi = 10$  at  $x/D = 15$ ; (a) mean temperature and  $O_2$  mass fraction for flame D; (b) mean temperature and  $O_2$  mass fraction for flame F; (c) mean  $CO$  and  $H_2$  mass fractions for flame D; (d) mean  $CO$  and  $H_2$  mass fractions for flame F (lines, calculations; symbols, measurements).

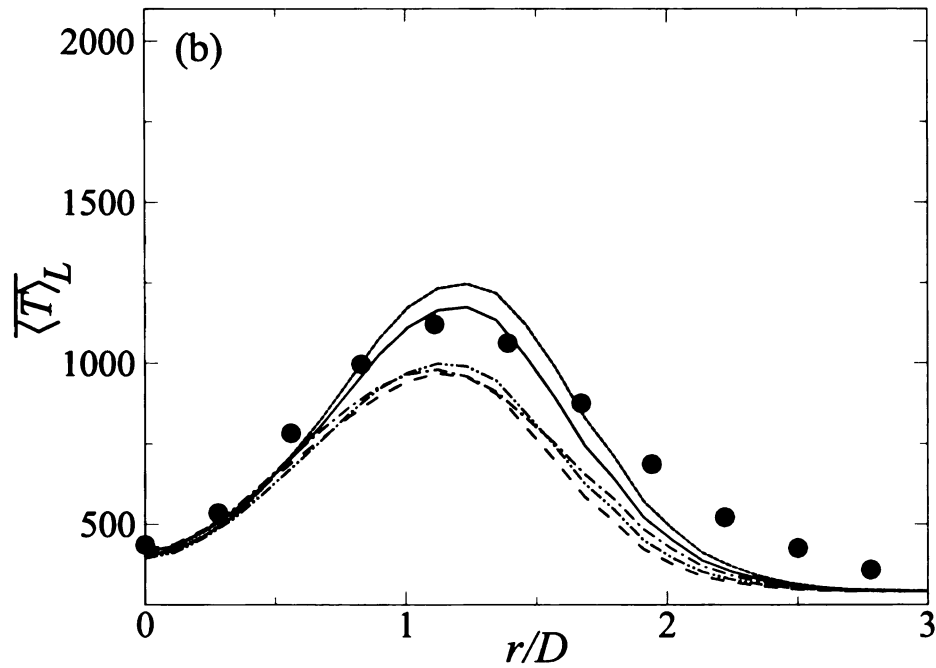
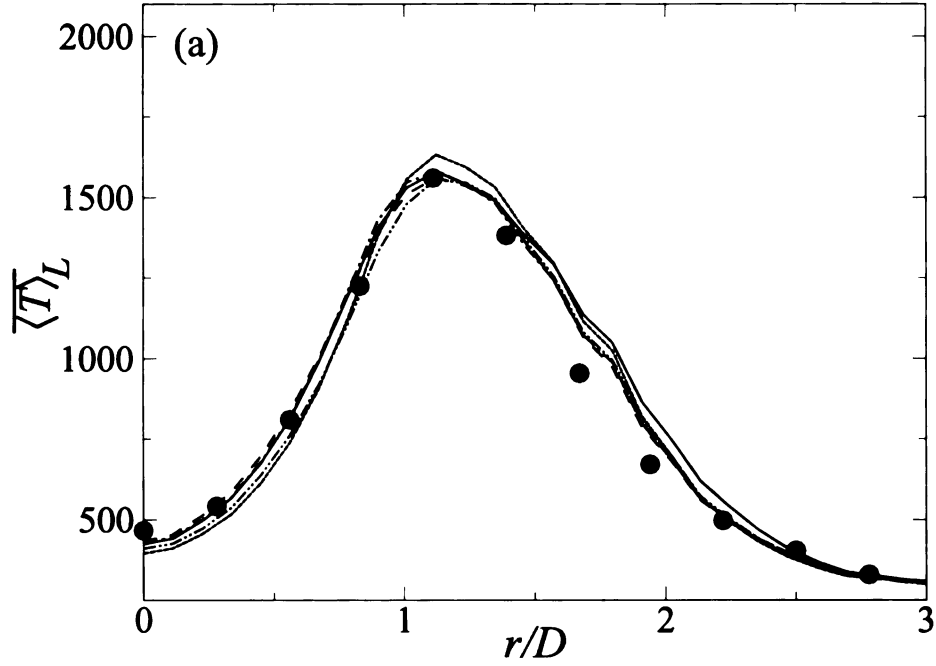


Figure 2.15: The radial variations of the mean temperature as obtained by LES/FMDF with 12-step model and different  $C_\phi$  values at  $x/D = 15$ ; (a) flame D and (b) flame F (symbols, measurements; long-dashed line,  $C_\phi = 6$ ; dashed-dot line,  $C_\phi = 8$ ; solid line,  $C_\phi = 10$ ; dashed-dot-dot line,  $C_\phi = DM1$ ; dashed line,  $C_\phi = DM2$ ).

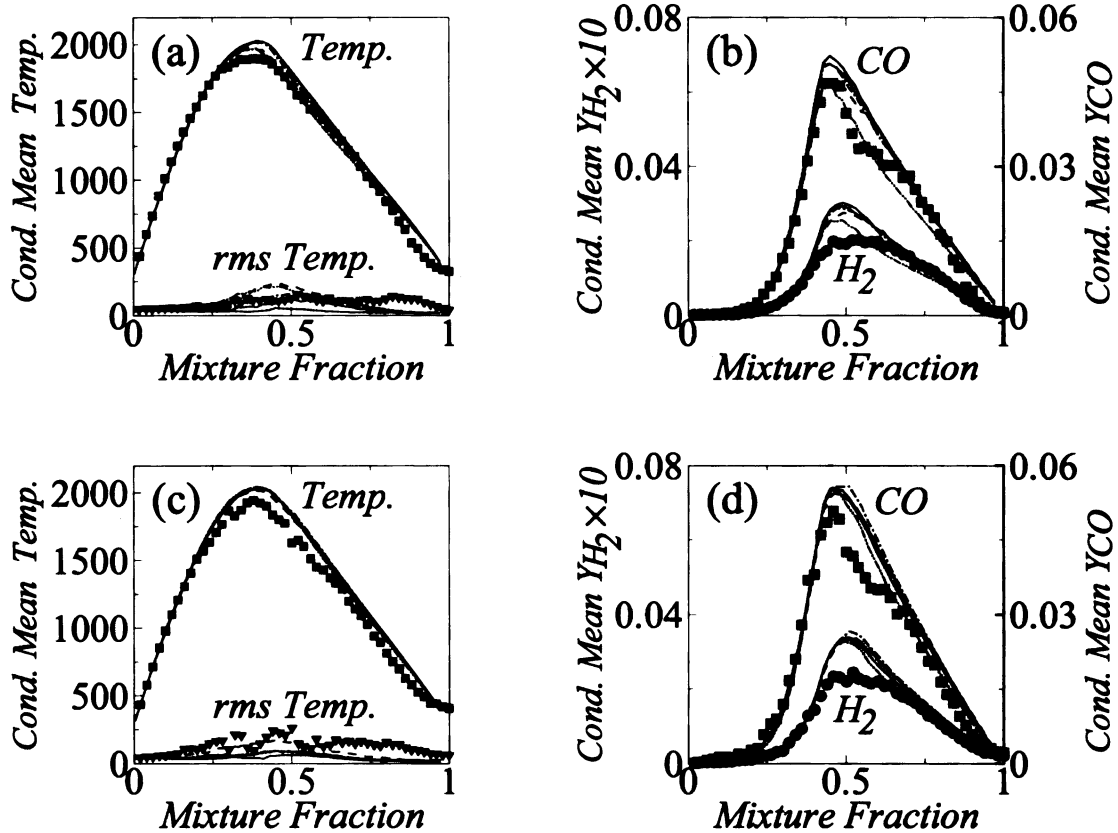


Figure 2.16: Conditional mean and RMS of various flame variables as obtained by LES/FMDF with the 12-step model and different  $C_\phi$  values for flame D; (a) mean and RMS of temperature at  $x/D = 7.5$ ; (b) mean of  $CO$  and  $H_2$  mass fractions at  $x/D = 7.5$ ; (c) mean and RMS of temperature at  $x/D = 15$ ; (d) mean of  $CO$  and  $H_2$  mass fractions at  $x/D = 15$  (symbols, measurements; long-dashed line,  $C_\phi = 6$ ; dashed-dot line,  $C_\phi = 8$ ; solid line,  $C_\phi = 10$ ; dashed-dot-dot line,  $C_\phi = DM1$ ; dashed line,  $C_\phi = DM2$ ).

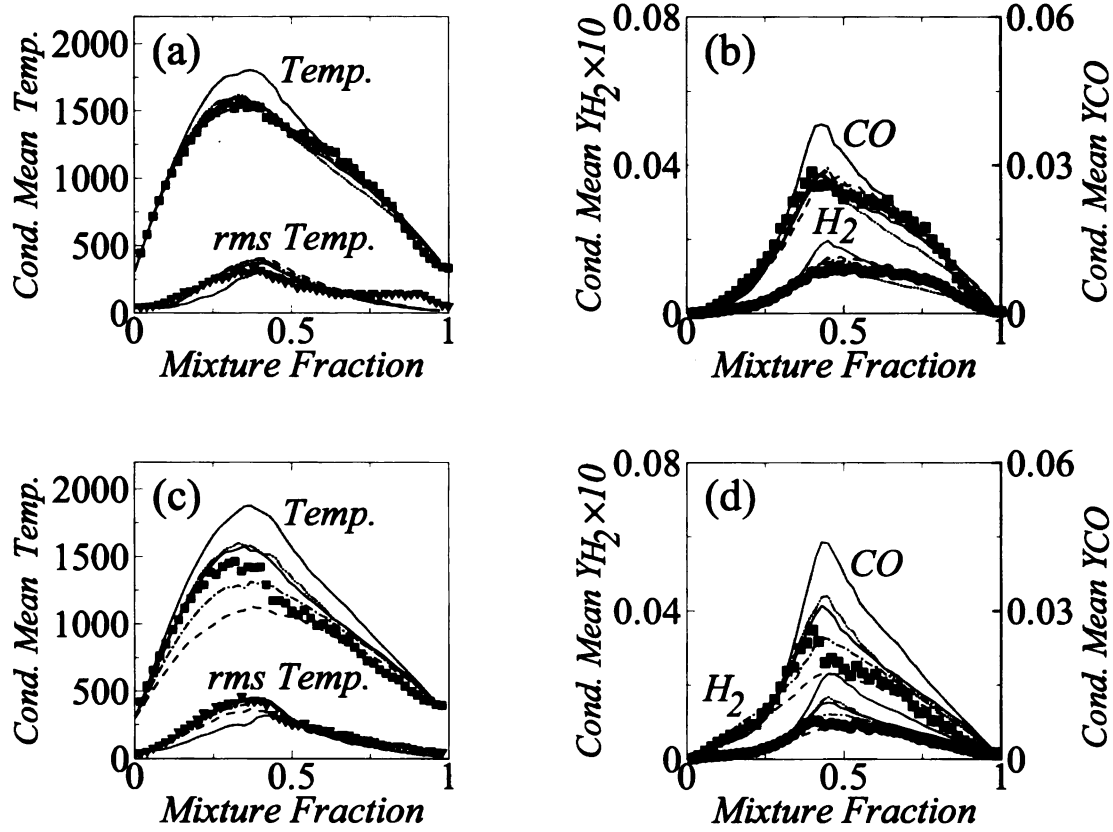


Figure 2.17: Conditional mean and RMS of various flame variables as obtained by LES/FMDF with the 12-step model and different  $C_\phi$  values for flame F; (a) mean and RMS of temperature at  $x/D = 7.5$ ; (b) mean of  $CO$  and  $H_2$  mass fractions at  $x/D = 7.5$ ; (c) mean and RMS of temperature at  $x/D = 15$ ; (d) mean of  $CO$  and  $H_2$  mass fractions at  $x/D = 15$  (symbols, measurements; long-dashed line,  $C_\phi = 6$ ; dashed-dot line,  $C_\phi = 8$ ; solid line,  $C_\phi = 10$ ; dashed-dot-dot line,  $C_\phi = DM1$ ; dashed line,  $C_\phi = DM2$ ).

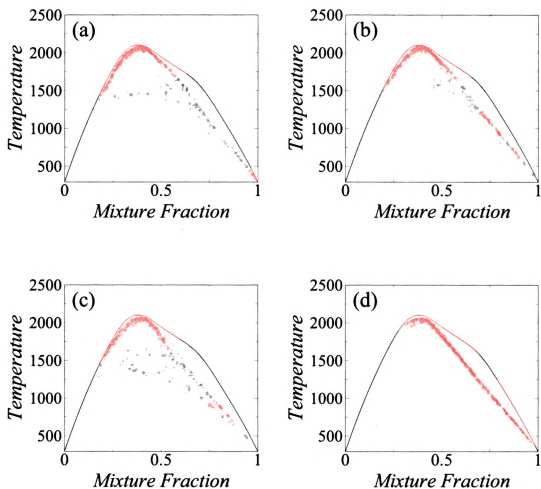


Figure 2.18: Scatter plots of temperature vs. mixture fraction as obtained by LES/FMDF with the 12-step model and different  $C_\phi$  values for flame D at  $x/D = 7.5$ , and  $r/D = 0.83$ ; (a)  $C_\phi = 6$  (1102 sample points); (b)  $C_\phi = 8$  (1022 sample points); (c)  $C_\phi = DM1$  (1042 sample points); (d)  $C_\phi = DM2$  (973 sample points).

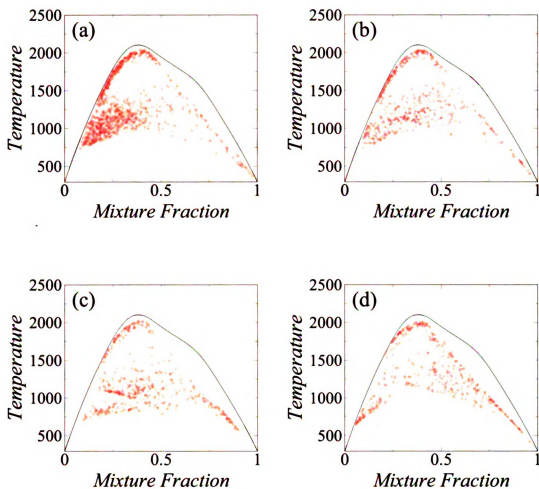


Figure 2.19: Scatter plots of temperature vs. mixture fraction as obtained by LES/FMDF with the 12-step model and different  $C_\phi$  values for flame F  $x/D = 7.5$ , and  $r/D = 0.83$ ; (a)  $C_\phi = 6$  (1418 sample points); (b)  $C_\phi = 8$  (1350 sample points); (c)  $C_\phi = DM1$  (1376 sample points); (d)  $C_\phi = DM2$  (1134 sample points).

# CHAPTER 3

## LARGE-SCALE SIMULATIONS OF TURBULENT SPRAY COMBUSTION IN A DUMP COMBUSTOR VIA TWO-PHASE FMDF

### 3.1 Introduction

Detailed experimental measurements and numerical simulations of multiphase turbulent flows continue to be important but challenging [150–155]. An important subcategory of two-phase flows is the flow of dispersed droplets in fluids that occurs in spray combustion in various energy conversion and propulsion devices such as internal combustion engines, gas-turbine combustors, oil-fired industrial furnaces, liquid-fueled rocket engines, etc. The efficiency and the stability of turbulent combustion and the emissions in such liquid-fuel combustion systems are dependent on the coupled and complicated effects of various parameters such as the fuel spray characteristics, the fuel type, the geometry, and the input/output flow conditions. It is often very difficult to predict the flow and combustion behaviors in such systems under various operating conditions. Considering the fact that turbulence itself has remained as an "unsolved" problem, one may expect the two-phase turbulent reacting flows to be almost unpredictable! In fact, with the addition of evaporating and reacting liquid droplets, the additional physical complexities due to multi-phase transport including the couplings between the phases, make the analytical/numerical description of the problem very difficult. A major challenge is to develop affordable

and accurate computational fluid dynamics (CFD) models which can describe the complicated interactions among turbulence, combustion and spray in a wide range of time and length scales.

This chapter presents a brief description of a novel two-phase large eddy simulation (LES) model (that we have developed for the numerical simulation of two-phase turbulent reacting flows based on the two-phase filtered mass density function (FMDF) methodology. A comprehensive analysis of the turbulent combustion in a spray-controlled lean, premixed dump combustor is also presented. Among the theoretical, experimental and numerical studies appeared in the literature for modeling/understanding of two-phase turbulent reacting flows [156–167], we refer to a class of Lagrangian statistical methods which dates back to Taylor [168] method of relating the fluid particle dispersion to the Lagrangian auto-correlation of fluid elements. Taylor’s theory has been the basis of many other theoretical investigations involving the dispersion of fluid and light tracer particles [169–171].

Experimental studies of spray combustion in turbulent flows may be classified into two groups; (i) studies concerning a single droplet evaporation and combustion in turbulent flow conditions, (ii) studies concerning spray development under conditions comparable to real-life applications. For the latter, numerous studies of evaporating and combusting sprays have been motivated by a wide variety of practical applications; see, for example, Ref. [172–193] and references cited therein. As a geometrically simple problem but relevant to those used in air-breathing propulsion systems, the spray combustion in a dump combustor is one of the most commonly employed configurations in gas turbine and ramjet engine combustors. An example is the experimental work of El Banhawy *et al.* [177] that includes a cylindrical combustion chamber equipped with a rotating cup atomizer, producing near-monosized droplets. The results for this experiment indicate that an increase in the mean droplet diameter reduces the combustion intensity in the regions away from the centerline

for both high and low swirl flames. The results obtained with different degrees of air swirl, but the same mean droplet diameter, indicates that with the reduction in swirl, the reaction rate within the initial part of the combustor and close to the center line decreases. Khalil *et al.* [178] also investigated the effect of swirl on the flow pattern and spray combustion air in a cylindrical furnace. They indicated that by increasing the swirl intensity increases the size and strength of the central recirculation zone, and there are linear relations between the swirl intensity and both the average and maximum recirculated mass flow rate. Gupta *et al.* [188] examined the spray flame characteristics of kerosene and methanol spray flames in a co-annular, swirl-stabilized combustor. They found that when the airflow field and the amount of heat released by the fuel are similar, the structure and the dynamics will also be similar. Sommerfeld *et al.* [182] studied the droplet dispersion and evaporation in a heated turbulent air stream and the effects they have on the flow in a sudden expansion by measuring the droplet size distribution, the correlations between droplet size and velocity, and the droplet mass flux. They found that air velocities and turbulence have significant effect on droplet evaporation rate. Among the other available experimental studies on spray combustion in dump combustors, the experimental studies of Yu *et al.* [189–193] are of particular interest since various combustion and spray parameters were investigated. They showed that with the pulse injection, synchronized with the large-scale shedded vortices, the spatial distribution of fuel droplets in the flow field, and therefore the combustion instability can be controlled. They also showed that the basic flame characteristics, in particular the flame length and intensity could be controlled by controlling fuel spray injection.

From a mathematical/computational point of view, the turbulent spray combustion is generally studied with three different methods [194, 195]: (i) Eulerian-Eulerian methods [155, 196–205], (ii) Eulerian-Lagrangian methods [151, 153, 196, 206–214], and (iii) Lagrangian-Lagrangian methods [195, 211, 215, 216]. In the first group,

the continuum transport equations for both phases are solved. These equations are somewhat similar and are often obtained by some sort of volume averaging which is conceptually different than the ensemble averaging in Reynolds-averaged simulation (RAS) or space averaging in large-eddy simulation (LES). In the second group, the carrier fluid continuum equations are solved in its "instantaneous" form in direct numerical simulation (DNS) or in its "averaged" form in RAS and LES over a fixed Eulerian grid system. However, the "dispersed" phase (droplets) is described by a set of modeled Lagrangian equations which determine the position, velocity, temperature, and other properties [153, 196, 207, 208] of the dispersed phase. In the third group, both phases are described in the Lagrangian context.

Eulerian-Eulerian and Eulerian-Lagrangian methods have been widely employed in DNS, LES or RAS of turbulent spray combustion [217–229]. In comparison, there have been limited number of simulations conducted based on Lagrangian-Lagrangian method [195]. One may also consider some of the joint probability density function (PDF) and the joint mass density function (MDF) models [211, 215] as Lagrangian-Lagrangian models. Here, we do not discuss the Eulerian-Eulerian and Eulerian-Lagrangian models, rather we refer the interested reader to review articles and books on subject [151, 153, 155, 164, 196, 207].

Despite known benefits of LES-based models, specially their ability to capture the unsteady physical features of complex turbulent flows [155, 196, 208, 230, 231], they have not widely used for numerical simulations of turbulent spray combustion [228, 232–235]. Among the limited number of LES studies involving turbulent spray combustion we refer the reader to the papers by Cuenot *et al.* [198]; Sankaran *et al.* [212]; Ying-wen *et al.* [214]; Ham *et al.* [228]; Okong'o *et al.* [236]; Leboissetier *et al.* [237]; Patel *et al.* [238]; Mahesh *et al.* [239]; Afshari *et al.* [240].

Cuenot *et al.* [198] simulated turbulent spray combustion in different geometric configurations with Eulerian-Eulerian LES models. Then the solver is applied to the

Vesta combustor of Turbomeca, composed of 18 main burners ignited by two pilot flames, which illustrated the capacity of LES to compute complex two-phase reacting flows in transient regimes. The two-phase reacting LES model employed in Refs. [212, 238] is based on the Eulerian-Lagrangian method. In this model, the carrier gas equations are solved on fixed Eulerian grid. However, the mixing and reaction are implemented in one-dimensional (1D) domain via linear eddy model (LEM). The spray is represented by Lagrangian droplets employing empirical evaporation and secondary break-up submodels. A similar hybrid Eulerian-Lagrangian approach is employed in Refs. [228, 239], where the zero Mach number Navier-Stokes equations are solved on an unstructured grid and the spray is modeled with Lagrangian droplets. In the studies conducted by Okong'o *et al.* [236] and Leboissetier *et al.* [237], the DNS data for a temporal mixing layer laden with evaporating droplets are used to assess different subgrid-scale (SGS) models for carrier gas, droplet and evaporated vapor. It is shown that with the SGS scale-similarity models the predicted droplet distribution by LES is comparable to that of DNS. However, the mass, momentum and heat transfer between droplet and carrier gas phases shown to not be accurately represented by the proposed deterministic closures. The LES models in Ref. [209, 212, 214, 228, 239] have been applied to realistic (complex) gas turbine combustors with various level of success.

In this work, a new two-phase LES model and a new Lagrangian-Eulerian-Lagrangian numerical scheme [240] are developed for two-phase turbulent reacting flows in complex geometrical configurations. The model is applied to high Reynolds number turbulent combustion in a spray-controlled lean premixed dump combustor [191]. The velocity field is obtained solving the filtered Eulerian equations with a high-order compact finite difference method. The spray model is based on a Lagrangian mathematical/computational methodology that allows two-way mass, momentum and energy coupling between phases. The subgrid gas-liquid combustion is modeled

with the two-phase filtered mass density function (FMDF). The new LES/FMDF is used for systematic study of the effects of various spray, fuel/air and flow parameters on turbulence and combustion.

The remainder of this chapter is organized as follows: first the governing equations for velocity, scalar and droplets are presented in Section 2. Followed by the description of numerical solution procedure in Section 3. The two-phase LES/FMDF results are presented in Section 4 and the chapter is completed by a summary and some concluding remarks in Section 5.

## 3.2 Two-Phase LES/FMDF Model Equations

In this section, the governing equations for two-phase compressible turbulent reacting flows, as solved in the LES/FMDF model are presented. The two-phase LES/FMDF model is based on a Lagrangian-Eulerian-Lagrangian mathematical/computational methodology in which a combined set of strongly coupled Eulerian finite-difference (FD) gas-phase, Lagrangian liquid/droplet-phase, and Lagrangian stochastic Monte Carlo (MC) particle equations are solved.

### 3.2.1 Eulerian Gas-Phase LES Equations

The carrier phase is considered to be a compressible and Newtonian, and ideal gas with zero bulk viscosity. The LES equations describing the carrier gas, as obtained by filtering the Navier-Stokes, energy and scalar equations, are

$$\frac{\partial \langle \rho \rangle_l}{\partial t} + \frac{\partial \langle \rho \rangle_l \langle u_i \rangle_L}{\partial x_i} = \langle S_\rho \rangle_l \quad (3.1)$$

$$\frac{\partial \langle \rho \rangle_l \langle u_i \rangle_L}{\partial t} + \frac{\partial \langle \rho \rangle_l \langle u_i \rangle_L \langle u_j \rangle_L}{\partial x_j} = -\frac{\partial \langle P \rangle_l}{\partial x_i} + \frac{\partial \langle \tau_{ij} \rangle_l}{\partial x_j} - \frac{\partial \Gamma_{ij}}{\partial x_j} + \langle \rho \rangle_l g_i + \langle S_{u_i} \rangle_l \quad (3.2)$$

$$\frac{\partial \langle \rho \rangle_l \langle H \rangle_L}{\partial t} + \frac{\partial \langle \rho \rangle_l \langle u_i \rangle_L \langle H \rangle_L}{\partial x_i} = -\frac{\partial \langle q_i \rangle_l}{\partial x_i} - \frac{\partial N_i}{\partial x_i} + \langle S_H \rangle_l \quad (3.3)$$

$$\frac{\partial \langle \rho \rangle_l \langle \phi_\alpha \rangle_L}{\partial t} + \frac{\partial \langle \rho \rangle_l \langle u_i \rangle_L \langle \phi_\alpha \rangle_L}{\partial x_i} = -\frac{\partial \langle J_i^\alpha \rangle_l}{\partial x_i} - \frac{\partial M_i^\alpha}{\partial x_i} + \langle \rho S_\alpha \rangle_l + \langle S_\rho^\alpha \rangle_l \quad (3.4)$$

where  $\langle f(\mathbf{x}, t) \rangle_l$  and  $\langle f(\mathbf{x}, t) \rangle_L = \langle \rho f \rangle_l / \langle \rho \rangle_l$  represent the filtered and the Favre-filtered values of the transport variable  $f(\mathbf{x}, t)$  and  $\rho$ ,  $u_i$ ,  $P$ ,  $T$  and  $H$  are the fluid density, velocity, pressure, temperature, and total enthalpy, respectively. The species' mass fractions are represented in a side equation with  $\phi_\alpha \equiv Y_\alpha$ ,  $\alpha = 1, 2, \dots, N_s$ . Equations 3.1-3.4 are closed by the following constitutive relations

$$\langle p \rangle_\ell \approx \langle \rho \rangle_\ell R^0 \langle T \rangle_L \sum_{\alpha=1}^{N_s} \frac{\langle \phi_\alpha \rangle_L}{W_\alpha} \quad (3.5)$$

$$\langle \tau_{ij} \rangle_\ell \approx \langle \mu \rangle_L \left( \frac{\partial \langle u_i \rangle_L}{\partial x_j} + \frac{\partial \langle u_j \rangle_L}{\partial x_i} - \frac{2}{3} \delta_{ij} \frac{\partial \langle u_k \rangle_L}{\partial x_k} \right), \quad \langle \mu \rangle_L = Pr \langle \kappa / C_p \rangle_L \quad (3.6)$$

$$\langle J_i^\alpha \rangle_\ell \approx -\langle \rho \rangle_\ell \langle D \rangle_L \frac{\partial \langle \phi_\alpha \rangle_L}{\partial x_i}, \quad \langle D \rangle_L = \frac{1}{\langle \rho \rangle_\ell Le} \langle \frac{\kappa}{C_p} \rangle_L. \quad (3.7)$$

In Eqs. 3.5 - 3.7,  $W_\alpha$  is the molecular weight of species  $\alpha$ ,  $\mu$  is the dynamic viscosity and  $\kappa$  is the thermal conductivity coefficient.

The SGS closures that appear in the filtered equations include the SGS stress  $\Gamma_{ij} = \langle \rho \rangle_l [\langle u_i u_j \rangle_L - \langle u_i \rangle_L \langle u_j \rangle_L]$ , the SGS energy and the scalar flux terms [87, 88, 231, 241] that are usually modeled with similarity and diffusivity type closures [87, 240, 242–244]. Additional models are required for the filtered source/sink terms. These are described in the next section, where the governing equations for the two-phase FMDF is presented.

It must be indicated here that diffusivity type closures are not used directly in the FMDF approach but the modeled FMDF transport equation is constructed to be consistent with them as discussed below.

### 3.2.2 Lagrangian Liquid/Droplet-Phase Equations

The dispersed droplet field equations are derived based on the assumptions that the droplets are fine and heavy, and the mixture is dilute. Under these conditions, the droplet collisions are infrequent and one may ignore the droplet-droplet interactions. Also, the droplets are assumed to be spherical and their movement are governed by an empirically corrected Stokesian drag force. There are numerous studies on the transport properties of spherical droplets/particles in turbulent flows [231, 245–249]. The density of droplets is considered to be much larger than the density of the carrier gas such that the dominant force on the droplets is the drag force. In addition, heat transfer due to radiation is neglected. Consequently, the following set of governing equations employed in a Lagrangian frame to describe the droplet displacement vector ( $X_i$ ), the droplet velocity vector ( $v_i$ ), the droplet temperature ( $T_d$ ), and the droplet mass ( $m_d$ ) are used.

$$\frac{dX_i}{dt} = v_i, \quad (3.8)$$

$$\frac{dv_i}{dt} = \frac{F_i}{m_d}, \quad (3.9)$$

$$\frac{dT_d}{dt} = \frac{Q_{conv} + \dot{m}_d L_V}{m_d C_L}, \quad (3.10)$$

$$\frac{dm_d}{dt} = \dot{m}_d = -m_d \left( \frac{1}{\tau_d} \right) \left( \frac{Sh}{3Sc} \right) \ln [1 + B_M], \quad (3.11)$$

where  $F_i$  and  $Q_{conv}$  are the modified Stokes drag force, and the heat flux to the surrounding gas, defined as

$$F_i = m_d \left( \frac{f_1}{\tau_d} \right) (u_i^* - v_i), \quad (3.12)$$

$$Q_{conv} = m_d \left( \frac{f_2}{\tau_d} \right) \left( \frac{Nu}{3\zeta Pr} \right) (T^* - T_d). \quad (3.13)$$

The subscript  $d$  indicates the droplet property, and the asterisk refers to the local fluid variables which are interpolated to the droplet location.  $L_V = h_V^0 - (C_L - C_{p,V})T_d$  is the droplet latent heat of vaporization,  $h_V^0$  is the enthalpy of formation of the evaporated vapor,  $C_L$  is the heat capacity of the droplet, and  $C_{p,V}$  is the constant pressure specific heat of the evaporated vapor. Also,  $\zeta$  is the ratio of the heat capacity of the droplet  $C_L$  to constant pressure specific heat of the gas mixture  $C_p^* = \sum_{\alpha} Y_{\alpha} C_{p,\alpha}$ , where the dependency of the specific heat of species  $C_{p,\alpha}$  to temperature is approximated via high degree polynomials. The gas-phase Prandtl (Pr) and Schmidt (Sc) numbers, on the other hand, are both set to be constant. Additionally, the empirically corrected droplet Nusselt number  $Nu = 2 + 0.552Re_d^{1/2}Pr^{1/3}$  and Sherwood number  $Sh = 2 + 0.552Re_d^{1/2}Sc^{1/3}$ , where  $Re_d$  is empirically corrected droplet Reynolds number,  $Re_d = D_d\rho^*|u_i^* - v_i|/\mu^*$ , defined based on the droplet diameter  $D_d$  and local slip velocity. The mass transfer number  $B_M$  for evaporating droplets is calculated as  $B_M = (Y_{v,s} - Y_v)/(1 - Y_{v,s})$  in which the subscript “s” denotes a droplet surface parameter.

In Eq. 3.12,  $\tau_d$  is the droplet time constant,

$$\tau_d = \frac{\rho_d D_d^2}{18\mu^*}, \quad (3.14)$$

and  $f_1$  is the empirical correction function to the Stokes drag which is obtained by the following correlation

$$f_1 = \frac{1 + 0.0545Re_d + 0.1Re_d^{1/2}(1 - 0.03Re_d)}{1 + a|Re_b|^b}, \quad (3.15)$$

$$a = 0.09 + 0.077\exp(-0.4Re_d) \quad b = 0.4 + 0.77\exp(-0.04Re_d),$$

where  $Re_b = \rho^*U_b D_d/\mu^*$  is based on the blowing velocity. Also, in Eq. 3.13  $f_2$  is the

empirical correction factor to the evaporative heat transfer and is defined as

$$f_2 = \frac{\beta}{e^\beta - a}, \quad (3.16)$$

with the normalized evaporation parameter,  $\beta = -1.5Pr\tau_d\dot{m}_d/m_p$  [250].

Finally, the vapor mass fraction at droplet surface is calculated from the surface molar fraction using the Langmuir-Knudsen evaporation model [251], which takes into account both equilibrium (subscript *eq*) and non-equilibrium (subscript *neq*) effects:

$$Y_{v,s} = \frac{\chi_{neq,s}}{\chi_{neq,s} + (1 - \chi_{neq,s})W_C/W_V}, \quad (3.17)$$

where  $W_C$  and  $W_V$  are the molecular weights of the carrier gas and evaporated liquid vapor, respectively. In Eq. 3.17, the equilibrium and non-equilibrium vapor mole fractions at droplet surface are defined as

$$\chi_{neq,s} = \chi_{eq,s} - \left( \frac{2L_K}{D_d} \beta \right), \quad (3.18)$$

$$\chi_{eq,s} = \frac{P_{atm}}{P^*} \exp \left\{ \frac{L_V}{R^0/W_V} \left( \frac{1}{T_{B,L}} - \frac{1}{T_d} \right) \right\}, \quad (3.19)$$

where  $P_{atm}$  is atmospheric pressure,  $R^0$  is the universal gas constant and  $T_{B,L}$  is the liquid boiling temperature. The term  $L_K$  in the definition of non-equilibrium mole fraction is the Knudsen layer thickness and is defined as

$$L_K = \frac{\mu^*(2\pi T_d(R^0/W_V))^{1/2}}{ScP^*} \quad (3.20)$$

The integrated effects of droplets on the carrier gas mass, momentum, energy and species mass fraction are expressed through several source/sink terms (i.e.  $S_\rho$ ,  $S_{u_i}$ ,  $S_H$ ,  $S_\alpha$ ,  $S_\rho^\alpha$  in Eqs. 3.1- 3.4). The mass source term,  $S_\rho$  represents the mass

contribution of droplets via evaporation, the momentum source term,  $S_{u_i}$  represents the momentum transfer between two phases due to drag force, and the heat source term,  $S_H$  represents the exchange of the internal and kinetic energy by convective heat transfer and particle drag. These terms represent the two-way coupling of the Lagrangian droplets on the Eulerian field by localized volume averaging and are defined as:

$$S_\rho = -\frac{1}{\delta V} \sum^{nd} \dot{m}_d, \quad (3.21)$$

$$S_{u_i} = -\frac{1}{\delta V} \sum^{nd} (F_i + \dot{m}_d v_i), \quad (3.22)$$

$$S_H = S_E - u_i^* S_{u_i} + \frac{u_i^* u_i^*}{2} S_\rho, \quad (3.23)$$

$$S_E = -\frac{1}{\delta V} \sum^{nd} \left( \mathcal{Q} + F_i v_i + \dot{m}_d \left( h_{v,s} + \frac{v_i v_i}{2} \right) \right), \quad (3.24)$$

where the summation is taken over all droplets in a volume  $\delta V = \delta x^3$  centered at each Eulerian (grid) point and  $h_{v,s} = C_{p,v} T_d + h_V^0$  is the evaporated vapor enthalpy at droplet surface.

### 3.2.3 Two-Phase FMDF Formulation

In conventional LES methods developed for the reacting flows, the filtered equation for the scalars (i.e. Eq. 3.4) are solved together with the mass, momentum and energy equations. In the scalar equation, the filtered chemical source/sink terms are not closed and need modeling. In this study, the subgrid combustion model is based on the FMDF methodology and the temperature and species mass-fractions are obtained from the FMDF. The chemical source/sink terms are also determined exactly from the FMDF.

The scalar FMDF is the joint probability density function of the scalars at subgrid-level [84, 252–254], defined as:

$$P_L(\boldsymbol{\psi}, \mathbf{x}; , t) \equiv \int_{-\infty}^{+\infty} \rho(\mathbf{x}', t) \xi[\boldsymbol{\psi}, \boldsymbol{\phi}(\mathbf{x}', t)] \mathcal{H}(\mathbf{x}' - \mathbf{x}) d\mathbf{x}' \quad (3.25)$$

$$\xi[\boldsymbol{\psi}, \boldsymbol{\phi}(\mathbf{x}, t)] = \delta[\boldsymbol{\psi} - \boldsymbol{\phi}(\mathbf{x}, t)] \equiv \prod_{\alpha=1}^{\sigma} \delta[\psi_{\alpha} - \phi_{\alpha}(\mathbf{x}, t)] \quad (3.26)$$

where  $\mathcal{H}$  and  $\delta$  denote the filter and delta functions, respectively, and  $\xi[\boldsymbol{\phi}, \boldsymbol{\psi}(\mathbf{x}, t)]$  is the “fine-grained” density [88]. Equation 3.25 indicates that the FMDF is the *mass weighted spatially filtered* value of the fine-grained density. To ensure that the FMDF has all the properties of the PDF, we will only consider “positive” filter functions [107] for which all the moments  $\int_{-\infty}^{\infty} x^m \mathcal{H}(x) dx$  exist for  $m \geq 0$ .

The variable  $\boldsymbol{\psi}$  in Eqs. 3.25 and 3.26 represents the composition space of the scalar (species mass fractions and specific enthalpy) array  $\boldsymbol{\phi}(\mathbf{x}, t)$  that is denoted by  $\phi_{\alpha} \equiv Y_{\alpha}$ ,  $\alpha = 1, 2, \dots, N_s$ ,  $\phi_{\sigma} \equiv h_s = \sum_{\alpha=1}^{N_s} h_{s,\alpha} \phi_{\alpha}$ ,  $h_{s,\alpha} = \int_{T_0}^T C_{p,\alpha}(T') dT'$ . The deterministic equation describes the variations of FMDF in space and time is derived from the original (unfiltered) governing equations and has the following final form:

$$\begin{aligned} \frac{\partial P_L}{\partial t} + \frac{\partial [\langle u_i \rangle_L P_L]}{\partial x_i} &= \frac{\partial}{\partial x_i} \left[ \langle \rho \rangle_l (\langle D \rangle_L + D_t) \frac{\partial (P_L / \langle \rho \rangle_l)}{\partial x_i} \right] \\ &+ \sum_{\alpha=1}^{\sigma} \frac{\partial}{\partial \psi_{\alpha}} [\Omega_m (\psi_{\alpha} - \langle \phi_{\alpha} \rangle_L) P_L] - \sum_{\alpha=1}^{\sigma} \frac{\partial}{\partial \psi_{\alpha}} [\hat{S}_{\alpha} P_L] \\ &+ \frac{\partial}{\partial \psi_{\alpha}} P_L \left[ \frac{\psi_{\alpha} \langle S_{\rho} | \boldsymbol{\psi} \rangle}{\langle \rho \rangle_l} - \frac{\langle S_{\rho}^{\alpha} | \boldsymbol{\psi} \rangle}{\langle \rho \rangle_l} \right] + \frac{\langle S_{\rho} | \boldsymbol{\psi} \rangle P_L}{\langle \rho \rangle_l} \end{aligned} \quad (3.27)$$

In Eq 3.27,  $\langle \mathcal{A} | \mathcal{B} \rangle$  denotes the filtered value of the variable  $\mathcal{A}$ , “conditioned” on  $\mathcal{B}$ , and the hat is used for the quantities which are dependent only on the scalar field.  $S_{\alpha}$  and  $\Omega_m$  denote the production rate of species  $\alpha$  and the SGS mixing frequency, respectively. The molecular and SGS diffusivity coefficients are denoted by  $D$  and  $D_t$ . The effects of molecular/SGS mixing and SGS convection are modeled with

closures similar to those used in RANS/PDF methods [88]. The last three terms on the right-hand side represents the effects of droplets and combustion.

### 3.3 Numerical Solution

As illustrated in Fig. 3.1, the numerical method used for solving the Eulerian and Lagrangian equations in the two-phase LES/FMDF methodology has three main components. For the carrier gas velocity and pressure, a high-order accurate finite difference (FD) method [4] is employed. The discretization of the filtered Eulerian gas-phase LES equations (Eqs. 3.1-3.4) is based on the “compact parameter” finite difference scheme [128], which yields up to sixth order spatial accuracies. The time differencing is based on a third order low storage explicit Runge-Kutta method [255]. All the finite difference operations are performed on fixed and uniform grid points. For the solution of spray and dispersed droplet-phase, the Lagrangian Eqs. 3.8-3.11, are solved with a point particle method [256]. Time advancement in the Lagrangian droplet (spray) equations is performed using an explicit second order accurate Adams-Bashforth scheme. The Eulerian carrier gas-phase variables at the droplet locations are obtained by a fourth-order Lagrangian interpolation scheme.

Finally, a Lagrangian monte carlo particle method is used for the solution of gas-phase scalar (species and temperature) FMDF [70, 84, 88, 91, 97, 132–134, 240, 252]. Here only the basic features of the FMDF solution procedure are described. With the Lagrangian procedure, the FMDF is represented by an ensemble of computational “stochastic elements” (or “particles”) which are transported in the “physical space” by the combined actions of large scale convection and diffusion (molecular and subgrid). In addition, transport in the “composition space” occurs due to chemical reaction and SGS mixing. In doing so, the notional particles evolve via a “stochastic

process,” described by a set of stochastic differential equations (SDEs) [135, 136],

$$dX_i(t) = \mathcal{D}_i(\mathbf{x}(t), t)dt + \mathcal{E}(\mathbf{X}(t), t)d\mathcal{W}_i(t), \quad d\phi_\alpha^+(t) = \mathcal{R}_\alpha(\phi^+, t)dt. \quad (3.28)$$

where  $X_i$  is the Lagrangian position of the particles,  $\mathcal{D}$  and  $\mathcal{E}$  are known as the “drift” and “diffusion” coefficients, and  $\mathcal{W}_i$  denotes the Wiener-Lévy process [137].  $\phi_\alpha^+$  denotes the scalar value of the particle with the Lagrangian position vector  $X_i$ . Eq. 3.28 defines what is known as the general “diffusion” process [136–138]; thus the PDFs of the stochastic processes  $(X_i(t), \phi_\alpha^+(t))$  are governed by the Fokker-Planck equation. A comparison between the standard Fokker-Planck equation corresponding to Eq. 3.28 with the FMDF equation (Eq. 3.27) under consideration identifies the parameters of Eq. 3.28,

$$\mathcal{E} \equiv \sqrt{2(\langle D \rangle_L + D_t)}, \quad \mathcal{D}_i \equiv \langle u_i \rangle_L + \frac{1}{\langle \rho \rangle_\ell} \frac{\partial[\langle \rho \rangle_\ell (\langle D \rangle_L + D_t)]}{\partial x_i}, \quad (3.29)$$

$$\mathcal{R}_\alpha \equiv -\Omega_m(\phi_\alpha^+ - \langle \phi_\alpha \rangle_L) + \widehat{S}_\alpha(\phi^+).$$

With this analogy, the FMDF is represented by an ensemble of Monte Carlo particles, each with a set of scalars  $\phi_\alpha^{(n)}(t) = \phi_\alpha(\mathbf{X}^{(n)}(t), t)$  and Lagrangian position vector  $\mathbf{X}^{(n)}$ . A splitting operation then can be employed in which the transports in physical and compositional domains are treated separately. The simplest means of simulating the spatial transport in Eq. 3.28 is via the Euler-Maruyamma approximation [139]. The transfer of information from the fixed finite difference points to the location of the Monte Carlo particles are conducted via (fourth and second order) interpolation. The filtered scalar quantities are calculated by weighted averaging of the particle values over space with average volumetric size of  $\Delta_E$ . Ideally,  $\Delta_E$  has to be very small. In this study, the chemical reaction is modeled by a “simple” non-equilibrium (finite-rate) one-step global mechanism [140]. However, all the reaction terms in the

FMDF equation are calculated exactly with no SGS model.

### 3.3.1 Consistency of FMDF

As stated before, the equation governing the first subgrid Favre-moment of the scalar  $\phi_\alpha$  as obtained from the FMDF equation (Eq. 3.25) is identical with the filtered scalar equation (Eq. 3.4). This indicates that the filtered temperature, scalar and density may be alternatively obtained from the Eulerian, finite difference (FD) or Lagrangian, Monte Carlo (MC) solutions, implying a mathematical consistency between FD and MC parts of the hybrid scheme. However, due to finite grid size in FD and limited number of MC particles, absolute consistency may not be achieved in practice. Nevertheless, various simulation results (i.e. non-reacting non-isothermal, reacting without spray, reacting with spray) are presented below to demonstrate the consistency and the accuracy of the two-phase FMDF formulation and its Lagrangian MC method with the conventional LES models and its Eulerian FD method. For this, the instantaneous filtered temperature and fuel mass fraction variables as calculated by LES/FD and FMDF/MC models are compared.

#### **Non-reacting non-isothermal simulations without spray**

First we consider non-reacting non-isothermal case without spray. In this case, there are significant density and temperature variations in the combustor between the inlet temperature  $1100K$  and initial temperature of  $300K$ . However, the pressure variations remain small at all times.

Fig. 3.2 shows the iso-contours of the instantaneous filtered temperature and fuel mass fraction at relatively long time as obtained by FD and MC. The FD values are obtained directly from the finite-difference grid points and the MC variables are obtained from the Monte Carlo particles and are interpolated to finite-difference grid points for plotting. The results in Fig. 3.2 indicate that the Monte Carlo predictions

of the temperature and fuel mass fraction are almost the same as the finite difference results. Although the temperature/density effects on molecular and turbulent mixing are significant, the data indicate very good consistency between FD and MC suggesting that the finite difference and Monte Carlo solvers are both reliable and accurate.

### **Reacting simulations without spray**

The results obtained by FMDF/MC and LES/FD for reacting case without spray are compared in this section. The reaction is for a lean-premixed n-heptane-air mixture with the equivalence ratio of 0.7, which is modeled with a one-step global mechanism [257]. The incoming cold fuel-air mixture is ignited by the preheated gas mixture within the combustor.

As Fig. 3.3 indicates, the predictions of instantaneous temperature and fuel mass fraction as by FMDF/MC for reacting flow case without spray fairly well agree with those of LES/FD. Evidently, the values obtained by the FD and MC methods are very close at all locations, indicating a good consistency between two methods in the reacting case without spray.

### **Reacting simulations with spray**

The consistency between LES/FD and FMDF/MC results for reacting flows cannot be established unless the nonlinear reaction source/sink terms are calculated from the FMDF method and used in the conventional LES/FD equations. The reason that these nonlinear terms have to be modeled in conventional LES/FD equations, while they are closed in the FMDF/MC equations.

Fig. 3.4 shows the comparison between the instantaneous filtered temperature and fuel mass fraction obtained with the two-phase FMDF/MC and LES/FD for reacting case with the spray. The spray is injected towards the centerline jet at the

inlet. The turbulent scalar mixing is very well captured by both models. There are some negligible oscillations at the shear layer in the MC particle predictions, which is mainly due to the restrictions in the MC particle averaging process and transfer of Lagrangian data to Eulerian grids as discussed above.

In Fig. 3.5, the radial variations of the instantaneous temperature and mass fraction of the evaporated fuel are plotted at axial locations of  $x/D = 2$  and  $x/D = 4$  for all three cases discussed above. Evidently, the Monte-Carlo particle values are generally in good agreement with the finite difference ones, even in the case with reaction and spray. The differences in the case with spray are primarily due to averaging of the Lagrangian droplets that is intentionally conducted in an inconsistent manner to show the significance of the droplet averaging procedure. In this procedure, the droplet source terms are first calculated by averaging over finite-difference cells and then the averaged values are interpolated to the Monte Carlo particle locations. A better approach is to first interpolate the droplet values to the particle location then calculate the droplet/source terms in the finite difference equations from the particles. It is to be noted that in reacting and/or two-phase flows the reaction and droplet source/sink terms in the finite difference equations are obtained from the Monte Carlo particles. This is for the testing of the numerical methods and for showing the consistency. Such information is not available in standard finite difference methods.

### **3.3.2 Combustor Parameters And Boundary Conditions**

In Fig. 3.6, a picture of the axisymmetric dump combustor and experimental setup [1] are shown along with the computational and spray. Numerical simulations are performed on a grid of  $121 \times 51 \times 51$  for a domain of  $8 \times 5 \times 5$  jet diameters in the x, y, and z directions, respectively. The approximate number of MC particles is 1800000. The flow Reynolds number, calculated based on the inlet diameter and mean bulk

inlet velocity is 38580 in both experiment and LES. The flow Mach number is 0.18. We tried to keep the spray parameters are close to those suggested by Ken Yu *et al.* [191], even though the spray is not well characterized.

For the inflow, non-reflecting boundary conditions [258] are used with a prescribed inflow gas velocity based on experiment. First zero derivative boundary conditions are considered for all variables on the combustor wall. For the outlet boundary, non-reflecting boundary conditions are used.

## 3.4 Results and Discussion

The results of LES/FMDF for two-phase reacting simulations of Ken Yu's spray-controlled laboratory-scale lean dump combustor [191] are presented and discussed in this section. The effects of various combustion and spray parameters similar to those studied by Ken Yu *et al.* [191] have been investigated.

Table 3.1 summarizes the spray/flow parameters for all cases considered. Cases I-V are to considered to study the effects of the initial Sauter mean diameter (SMD), spray angle  $\alpha$ , spray injection angle  $\beta$ , liquid fuel to gas mass loading ratio  $\Gamma$ , and droplet injection velocity  $u_p$ . Case VI is considered to asses the effects of pulsative spray with different values of droplet injection frequency  $\psi$  on the combustion. Finally, the effects of flow parameters such as the inflow equivalence ratio  $\phi$  of the premixed heptane/air mixture, inlet temperature  $T_{in}$  and the amplitude of turbulent fluctuations  $\sigma_{ref}$  are investigated by considering cases VII-IX. It is noted here that the images in the following sections of this dissertation are presented in color.

### 3.4.1 Effect of Sauter Mean Diameter (SMD)

To examine the effect of initial droplet size on turbulent spray combustion, five different cases with initial Sauter mean diameter (SMD) of 30, 45, 60, 90 and 120  $\mu\text{m}$

are considered. SMD is an important spray parameter that has been commonly considered in spray studies [259]. The mass loading ratio of droplets,  $\Gamma$  is kept constant around  $\approx 0.1$  when SMD changes by changing the number of injected droplets. The other spray and flow parameters are also kept constant as evident in Table 3.1.

Fig. 3.7 shows the iso-contours of instantaneous filtered temperature and filtered fuel mass fraction as obtained by two-phase LES/FMDF with various Sauter Mean Diameter. The relative amount of n-heptane fuel distribution in the combustor is strongly affected by SMD as droplets follow trajectories depending on their initial size. The droplets are injected at an initial temperature of  $298K$ . For the n-heptane, the boiling temperature is  $T_{boil} \approx 371K$ . The results in Fig. 3.7 indicate that for smaller values of SMD most droplets closely follow the flow due to their small inertia. As shown in Fig. 3.7(a), (b), and (c), the small droplets even reach to the locations close to exit, where they are finally vaporized. There are high levels of fuel mass fraction in the center of the combustor, suggesting that most particles completely evaporate before they reach to exit nozzle. In contrast to small droplets, large droplets are found to have high enough inertia to cross “high vorticity” and “high temperature” areas, and reach to the side walls of the combustor. Even though the life times of larger droplets are more than those of small ones, they quickly evaporate in the high temperature regions, resulting in an increase in the fuel mass fraction as shown in Fig. 3.7. The instantaneous filtered temperature clearly indicate the thermal effects of evaporating droplets on the gas. First, the droplets warm up to their boiling temperature by the heat transfer from the carrier gas. The evaporation starts when the dynamic equilibrium between the carrier gas and droplets is reached. The gas temperature may finally rise due to the added vapor internal energy and combustion.

The instantaneous radial values of the filtered temperature, the filtered fuel mass fraction and the RMS of pressure as obtained by two-phase LES/FMDF are shown

in Fig. 3.8 at axial locations of  $x/D = 3$  and  $x/D = 6$ . Consistent with the former iso-contour plots, higher values of fuel mass fraction are observed at locations close to side walls of the combustor for large SMD. Nevertheless, the results for  $SMD = 45, 60\mu m$  show that for  $r/D < 0.5$  as the droplet size decreases the fuel concentration increases. However, for  $SMD = 30\mu m$  the fuel concentration is relatively low at nearly all  $r/D$  values and both axial locations, which indicates that a relatively small number of droplets survive at downstream locations. Fig. 3.8 also shows the cooling effect of vaporizing droplets. This is especially significant for  $r/D < 0.5$  at  $x/D = 3$  and for  $r/D > 0.5$  at  $x/D = 6$ , where the drop in gas temperature is evident. It is also quite clear in Fig. 3.8 that for suppressing the pressure instabilities smaller droplets are more desirable as the radial variations of the RMS of pressure is higher for larger droplets, consistent with the experimental observations. However, as the results with  $SMD = 30\mu m$  and  $SMD = 45\mu m$  indicate, injection of small droplets damps the pressure oscillations due to lack of homogeneous combustion.

Fig. 3.9 shows the axial variations of the integrated droplet number density within the combustor for various SMD values. At locations close to the spray injectors and the combustor inlet, the integrated droplet number is approximately the same for all SMD values with a peak indicating the droplet injection. Consistent with Fig. 3.7 which shows the injected droplets, the integrated droplet number values decay to zero at locations closer to inlet for the sprays with  $SMD = 30, 45\mu m$ , in comparison to those with higher SMD of 90 and  $120\mu m$ . At  $x/D \approx 2$ , the results for  $SMD = 90, 120\mu m$  show peak values of droplet number, indicating the accumulation of unburned droplets closed to the side walls of the combustor (Fig. 3.7). However, the droplet number is still significant at  $x/D \approx 5$  for the spray with  $SMD = 60\mu m$  since the droplets with this average size are neither large enough to cross the high velocity main gas stream nor small enough to vaporize earlier.

The simulated values of the mean droplet temperature and the axial velocity

versus  $r/D$  for various SMD are shown in Fig. 3.10 at axial locations of  $x/D = 3$  and  $x/D = 6$ . It is shown in Fig. 3.10a that the mean droplet temperature is generally below the n-heptane liquid boiling temperature  $T_{boil} \approx 1.25$  for all SMD at both downstream locations, indicating the accuracy of the droplet evaporation model. At  $x/D = 3$  and close to combustor axis ( $r/D < 0.5$ ), the mean temperature is relatively high as a result of low droplet evaporation for all cases with SMD values greater than  $30\mu m$  but decreases with the initial SMD values at locations away from the combustor axis. The profiles of mean droplet axial velocity in Fig. 3.10b indicate that the axial velocity of the smaller droplets decrease rapidly by the momentum interactions with the carrier gas. The reason for higher mean droplet axial velocities at  $x/D = 3$  in the centerline region for cases with  $SMD = 45, 60, 90, 120\mu m$  is the reduced response to fluid motions of larger droplets.

### 3.4.2 Effect of Spray Angle ( $\alpha$ )

Another important spray parameter considered in the present study is the spray angle  $\alpha$ . Four different cases with different spray cone angles from  $0^\circ$  (mono-dispersed) to  $80^\circ$  (widely-dispersed) are considered. The initial Sauter mean diameter is set to  $45\mu m$  in all cases. Sample results are shown below.

Fig. 3.11 shows the effects of spray angle  $\alpha$  on the instantaneous iso-surfaces of density, and iso-contours of fuel mass fraction. Overall, the central region of the combustor is dominated by high density gas due to relatively small droplet size for all spray angles. Nevertheless, the density is higher close to the combustor side walls for wider sprays (Fig. 3.11d). As the spray angle is increased, droplets penetrate less in the axial direction causing lower fuel mass fraction values within the main fuel stream. The instantaneous values of  $CO_2$  mass fraction (not shown) also suggests that a better droplet dispersion leads to more homogeneous and faster reaction.

Fig. 3.12 shows that for all spray angles the instantaneous filtered temperature

are relatively close and the cooling effect of droplets is not very significant away from the combustor centerline. This is primarily due to small initial droplet SMD. Nevertheless, the radial profiles of fuel mass fraction in Figure 3.12b are consistent with the mass fraction iso-contours, indicating a higher fuel evaporation for smaller spray angle close combustor centerline ( $r/D < 0.3$ ). What also shown in Fig. 3.12 is the radial variations of the RMS of pressure for different values of  $\alpha$ . At locations close to the walls, the RMS of pressure increases as the spray angle increases. However, for the smaller spray angle of  $\alpha \approx 20^\circ$ , the pressure variations are relatively high suggesting that other factors are important.

The integrated droplet number density plots in Fig. 3.13 indicate that more unburned droplets exist within the combustor for smaller spray angle, which is due to non-uniform droplet dispersion. Since the droplets for smaller spray angles mostly reside within the relatively cold main flow stream, droplet evaporation takes longer time.

The radial variations of mean droplet temperature and axial velocity for various  $\alpha$  at  $x/D = 3$  and  $x/D = 6$  are shown in Fig. 3.14. The results indicate that the mean droplet temperature is higher for  $\alpha \approx 20^\circ$ ,  $40^\circ$  and  $60^\circ$  compared to that for  $\alpha \approx 0^\circ$  at  $x/D = 3$  due to higher heat transfer. Similarly, the mean droplet velocities are higher for wider spray angles, partly because of momentum interactions between the droplets and the carrier gas. Since the initially large droplets get smaller by evaporation, which is more significant for wider sprays, they get affected more by the main flow motions. At  $x/D = 6$ , both the mean droplet temperature and axial velocity attain their highest values for  $\alpha \approx 80^\circ$  close to combustor axis. By getting away from the combustor axis the shear layer in the regions between the cold and hot regions, the mean droplet temperature and axial velocity start to increase, suggesting higher fuel evaporation and combustion at higher spray angles.

### 3.4.3 Effect of Injection Angle ( $\beta$ )

The spray injection angle  $\beta$  is defined as the angle between the spray axis and the combustor axis. The location of injectors and the angle of injection has direct effect on the evaporation and burning of the liquid fuel. In this section, LES/FMDF results obtained for  $\beta \approx 0^\circ$ ,  $30^\circ$ ,  $45^\circ$  and  $60^\circ$  are presented and discussed.

The iso-surfaces and iso-contours of instantaneous filtered gas density and temperature and droplet dispersion for different  $\beta$  are shown in Fig. 3.15. As observed in the filtered density iso-surfaces, the density variations in the combustor is more significant for straight injection or  $\beta = 0^\circ$ . This can be related to the interactions of the droplet with the shear layer and turbulence. Also, for  $\beta \approx 0^\circ$ , the droplet cooling effect is clearly observed at the points close to combustor side walls. This effect is less significant at other injection angles except at locations close to the combustor exit, which can be explained based on the interactions of sprays. As the injection angle increases, the incoming droplets from two separate sprays disperse less, interact more and act like a single spray inside the main incoming carrier gas stream, which penetrates farther in the combustor.

Fig. 3.16 shows the radial variations of the instantaneous filtered temperature and fuel mass fraction at axial locations of  $x/D = 3, 6$  as obtained by LES/FMDF. Consistent with the iso-contours of filtered temperature (Fig. 3.15) and the fuel mass fraction (not shown), the results with  $\beta = 30^\circ, 45^\circ$  and  $60^\circ$  are found not to be significantly different than each other. From the radial variations of fuel mass fraction, it can be stated that the injection angle increases the fuel concentration in the main stream ( $r/D < 0.5$ ). As one moves outward radially to the sidewalls ( $r/D > 0.5$ ), however, the fuel mass fraction values become higher for  $\beta = 0^\circ$ . The radial variations of the RMS of filtered pressure (Fig. 3.16c) indicate that the pressure variations have significantly higher values when  $\beta = 0^\circ$  not only at  $x/D = 3$  but also at  $x/D = 6$ . There are discrepancies among the results obtained with different  $\beta$  at

$r/D < 0.5$ .

The axial variations of the integrated number of droplets are presented in Fig. 3.17 for different injection angles. Consistent with the visualized droplet distribution in Fig. 3.15, there are less number of unburned droplets in the combustor for the case with the injection angle of  $\beta = 0^\circ$ . Since all of the droplets are injected only into the main carrier gas stream, the rate of evaporation of droplets and their integrated numbers of droplets are pretty much the same for  $\beta = 30^\circ$ ,  $45^\circ$  and  $60^\circ$ .

The radial variations of the mean droplet temperature and axial velocity for various injection angles are shown in Fig. 3.18 at axial location of  $x/D = 3$ . Our results (not shown here) indicate that a small fraction of droplets survive at far downstream locations when  $\beta = 45^\circ$ .

#### **3.4.4 Effect of Mass Loading Ratio ( $\Gamma$ )**

One of the important parameters that modify the turbulence/combustion structure is the mass loading ratio  $\Gamma$  which is the ratio of liquid fuel mass to carrier gas mass. To further examine and understand the impact of this parameter on a spray driven axisymmetric dump combustor, a set of simulations is performed with five different mass loading ratios ( $\Gamma = 0.01, 0.055, 0.11, 0.22$  and  $0.44$ ). Fig. 3.19 shows the instantaneous iso-contours of the filtered temperature and fuel mass fraction for different  $\Gamma$ . Here, the mass flow rate of the liquid spray is controlled by multiplying the droplet source terms in Eqs. 3.1-3.4 with a correction coefficient rather than changing the actual number of droplets in simulations due to computational cost. The iso-contours of temperature for very high mass loading ratio (Fig.3.19c) indicate a significant cooling effect of the droplets on the gas temperature, along with local flame extinction close to combustor exit. The absence of sufficient oxygen is another factor, which prevents the complete combustion and causes local flame extinction. It is also observed in Fig. 3.19 that the gas temperature diffusion in the central

region of the combustor increases with the loading ratio; high temperature values are observed for  $r/D < 0.5$ . Nevertheless, it seems that the temperature distributions are not very different for mass loading ratios of  $\Gamma = 0.055, 0.11$  and  $0.22$ . For very low mass loading ratios (Fig.3.19a), lower temperature values are observed in the “thermal shear layer zone” mainly due to insufficient fuel for combustion and not the cooling effect of droplets as the fuel mass fraction iso-contours suggest. An interesting observation is that by increasing the mass loading ratio, the sprays interact more and the droplet scattering is decreased.

Figs. 3.20a and 3.20b show the radial variations of the instantaneous filtered temperature and fuel mass fraction at different axial locations. The general observation is that the cooling effect of droplets is significant only for  $\Gamma = 0.01$  at  $x/D = 3$ . For higher values of  $\Gamma$ , the radial profiles of the filtered temperature for different  $\Gamma$  are close to each other. At  $x/D = 6$ , the increase in mass loading ratio decreases the carrier gas temperature at  $r/D > 0.5$  due to combustion and added mass for  $\Gamma = 0.01$ . Since the relatively cold carrier gas stream gradually mixes and warms up along the combustor centerline the temperature at  $r/D < 0.5$  increase in the case with  $\Gamma = 0.01$ . However, the reason for the higher filtered temperature values observed in the cases with  $\Gamma = 0.44$  at points  $r/D < 0.5$  could be attributed to diffusion of the hot combustion products from the outer burning zone to the central region of the combustor as the vaporized cold fuel partly react and partly pushes the gas to the center. The effect of dispersed droplet phase on the instantaneous filtered pressure for different mass loading ratios is shown in Fig. 3.20c. As expected, the effect of droplets on the instantaneous mean gas pressure is significantly different for different mass loading ratios. An important observation is that by decreasing droplet mass loading ratios from a very high value to a very low value the mean gas pressure increases. There seems to be an optimum mass loading ratio for the lowest pressure oscillations in the combustor.

In Fig. 3.21, the axial variations of the integrated droplet number density are shown for different  $\Gamma$ . It appears that by increasing the droplet mass loading ratio, the number of unburned droplets at locations close to combustor inlet and exit increases. This indicates that the increase of the mass loading ratio decreases the relative rate of the evaporation of individual fuel droplets, which is due to an increase in fuel vapor mass fraction, since  $Y_{v,s} - Y_v$  determines the rate of evaporation [260].

The droplet statistics are also effected by the two-way coupling effects in a non-linear way for various  $\Gamma$ . Fig. 3.22 shows the radial variations of the mean droplet temperature and axial velocity at axial location of  $x/D = 3$ . Even though the deviations between the results with low and moderate values of  $\Gamma$  are not very pronounced, the LES/FMDF results with  $\Gamma = 0.44$  seems to be very different. At  $x/D = 3$ , the mean droplet temperature is high, where the mean droplet axial velocity is low due to the significantly increased thermal and momentum couplings between the carrier gas-phase and the dispersed liquid-phase. Consistent with the results in Fig 3.19, the droplet results (not shown here) indicate that a few unburned droplets survive within the relatively cold main flow stream along the centerline  $\Gamma = 0.11, 0.22$ .

### 3.4.5 Effect of Droplet Injection Velocity ( $u_p$ )

This section investigates the effects of droplet injection velocity  $u_p$  on both the carrier gas and turbulence, combustion and spray. Three different droplet injection velocities,  $u_p = 15, 30$  and  $60$   $m/s$  are considered, while other spray and mean flow parameters remain as those given in Table 3.1.

Fig. 3.23 presents the iso-contours of the instantaneous filtered temperature and fuel mass fraction for different  $u_p$ . It is observed that droplets are able to cross the carrier gas stream as the injection velocity is increased (Fig. 3.23c). As a result of this, the carrier gas temperature eventually decreases where the droplets are vaporized. The axial distance beyond which no droplets could be detected is much smaller for

higher injection velocities, since the droplets penetrate towards the sidewalls rather than the central carrier gas stream. This trend is clearly seen in the fuel mass fraction iso-contours in Fig. 3.23c where the elevated fuel mass fraction values, due to droplet evaporation, are observed at the upper and the lower sides of the central gas stream. Comparison of the results for  $u_p = 15 \text{ m/s}$  and  $u_p = 30 \text{ m/s}$  indicates that the droplet evaporation increases as the injection velocity increases since the convective heat transfer to the droplets is enhanced by the increased relative velocity between the carrier gas and droplets.

In Fig. 3.24, the axial variations of the integrated droplet number density are presented for different droplet injection velocities. Overall, the number of unburned droplets decreases by increasing the injection velocity as argued above. Nevertheless, at some locations (e.g.  $x/D \approx 2$ ) the number of unburned droplets are found to be still less for  $u_p = 15 \text{ m/s}$  in comparison to those for  $u_p = 30 \text{ m/s}$ .

The radial profiles of the instantaneous filtered temperature, fuel mass fraction and total kinetic energy (TKE) at two different axial locations are shown in Fig. 3.25, where TKE is defined as  $(\langle u_i \rangle_L \langle u_i \rangle_L)/2$ . For both axial locations, the filtered temperature is considerably lower for  $u_p = 60 \text{ m/s}$  than those for  $u_p = 15, 30 \text{ m/s}$  at  $r/D > 0.5$ , indicating the significance of the cooling effect of droplets. The lower temperature for  $u_p = 15 \text{ m/s}$  is mainly due to turbulence-droplet thermal interactions as Fig. 3.23a suggests. A comparison of the corresponding TKE profiles shown in Fig. 3.25c demonstrates that the mean total kinetic energy increases as the droplets are injected with higher velocities, which is again a consequence of momentum coupling between phases.

### 3.4.6 Effect of Injection Frequency ( $\psi$ )

Pulsating liquid-fuel sprays are commonly used in active control of the combustion. Suppressing the pressure oscillations via creating controlled out-of-phase heat release

oscillations is the basic idea behind the active control strategies [189]. Ken Yu *et al.* [191] have showed that the pressure oscillation amplitude reached the minimum value when the start of the pulsed fuel injection was synchronized with the inlet vortex shedding process. They achieved up to a 15-dB reduction in sound pressure level with phasing of fuel injection and pressure.

In pulsating sprays, the droplet injection frequency  $\psi$  is defined as the total number of openings and closings of the fuel actuators in one second. In other words, the number of times the liquid-fuel is injected per second. Our study is motivated by the desire to better understand the effects of droplet injection frequency on two-phase turbulent reactive flows. Simulations with various injection frequencies ( $\psi = 38Hz \sim 1kHz$ ) are conducted. For all cases studied, approximately 4200 droplets are injected when the fuel actuators are opened.

Fig. 3.26 shows a series of 2D plots of the instantaneous filtered temperature and fuel mass fraction at different frequencies. Expectedly, the extent of spatial fuel modulation become more evident at higher injection frequencies [189]. This is attributed to shortening of the time gap between two pulses. Before the droplets that are concentrated in some locations either evaporate or leave the combustor, the liquid-fuel actuator are opened for next the injection. The cooling effect of evaporated droplets is quite clear at these locations, as the temperature and the evaporated fuel mass fraction contours show. However, it is observed that for low frequencies the locations with high fuel concentration are rare, but their size is relatively larger. From the comparison of both temperature and fuel mass fraction images at different frequencies, it can be concluded that by increasing the droplet injection frequency the large-scale discontinuities observed at very low frequencies in the main carrier gas stream disappear.

In Fig. 3.27, the iso-surfaces of the instantaneous mean gas pressure are shown. Comparison of the results with different injection frequencies indicates that in general

by an increase in the injection frequency, the mean gas pressure increases. The results for  $\psi = 38Hz$ ,  $500Hz$  show that the mean gas pressure at locations close to inlet is lower than that at the rest of combustor. Furthermore, significant local pressure drops are observed for  $\psi = 1kHz$ . These results suggest that the effect of spray on the pressure field is rather complicated and is strongly dependent on the injection frequency. A systematic parametric study certainly needed for the selection of the optimum operation conditions.

The radial variations of the instantaneous filtered fuel mass fraction are shown in Fig. 3.28 at axial locations of  $x/D = 3, 6$ . Expectedly, the fuel mass fraction values are lower for lower injection frequency. Fig. 3.28 shows the effect of pulsating spray on the mean gas pressure through radial variations of the RMS of pressure. The pressure fluctuations are lower for  $\psi = 1kHz$  in comparison to those for other frequencies, indicating that the damping effect of spray is more significant at this particular frequency. As mentioned before, the damping of pulsating sprays is primarily modified by creating out-of-phase heat release oscillations. Therefore, as Fig. 3.28 shows the pulsating spray is not that effective in suppressing the pressure oscillations at other frequencies.

### 3.4.7 Effect of Equivalence Ratio ( $\phi$ )

The effect of initial equivalence ratio of the carrier gas on combustion flow variables are here by changing the initial fuel-air equivalence ratio from  $\phi = 0.01$  through to  $\phi = 2.0$ , while the other flow and spray parameters are kept constant (Table 3.1).

The instantaneous temperature and fuel mass fraction iso-contours in Fig. 3.29 indicate that the structure of the temperature and turbulence fields is changed by altering the equivalence ratio. As the initial equivalence ratio of the carrier gas decreases, the intensity of large-scale turbulent motions increases. As a result, the relatively cold incoming main stream become more turbulent, causing locally reduced

temperature zones within the hot surrounding fluid. In addition to its effect on temperature, the enhanced turbulent mixing affects the distribution of the heptane mass fraction within the combustor, also evident in high concentration fuel zones throughout the combustor. Nevertheless, the spatially averaged values of the temperature and fuel concentration (not shown here) increases and decreases, respectively, which is expected since by an increase in fuel-air ratio in a lean combustor the reaction rate and heat release increase.

Fig. 3.30 illustrates how the initial equivalence ratio of the carrier gas stream affects the instantaneous vorticity field. Evidently, as the initial equivalence ratio decreases regions with high vorticity values start to appear in the combustor, which promotes the formation rich detached elements from the tip of the main gas stream.

In Fig. 3.31, the radial variations of the instantaneous filtered temperature, fuel mass fraction and the RMS of pressure are presented at different axial locations. The results at  $x/D = 3$  show that the centerline temperature is somewhat similar for all values of  $\phi$ . Nevertheless, the structure of the temperature field appear to be very different in different fuel-lean and fuel-rich cases. The results with  $\phi = 0.01, 0.1$  and  $0.4$  at  $x/D = 6$  suggest that the high temperature field engulfs more cold fluid from the central stream as  $\phi$  increases, which is an indirect effect of equivalence ratio on the temperature through turbulence. As shown in Fig. 3.31b, the radial profiles of instantaneous filtered fuel mass fraction for  $\phi = 0.01$  and  $0.4$  are observed to have higher values at points close to combustor sidewalls in comparison to those for  $\phi = 0.7 - 2.0$ . Fig. 3.31(c) shows that the pressure fluctuations are also significantly affected by  $\phi$  and are the highest when the equivalence ratio is  $2.0$ . However, the magnitude of the pressure fluctuations does not seem to vary linearly and monotonically with  $\phi$ , as the RMS for  $\phi = 0.01$  are generally higher compared to those for  $\phi = 0.1 - 1.0$ .

Fig. 3.32a shows the radial variations of mean droplet temperature with different

values of  $\phi$  at axial location  $x/D = 3$ . It is observed from that at  $r/D < 0.3$ , the mean droplet temperature attains higher values as the equivalence ratio increases, indicating more heat transfer from the carrier gas to the droplets. At  $0.3 < r/D < 0.6$ , the mean droplet temperature decreases as the equivalence ratio increases since the relatively cold central main stream becomes thicker as  $\phi$  increases. The radial profiles of the droplet number density in Fig. 3.32b show that by increasing the initial equivalence ratio of the incoming premixed gas stream, the droplet evaporation rate may increase or decrease. By increasing the equivalence ratio of a lean mixture, heat release increases resulting in more convective heat transfer to the droplets and faster evaporation on one hand, and smaller difference of  $Y_{v,s} - Y_v$  and lower droplet vaporization rate on the other..

### 3.4.8 Effect of Inlet Gas Temperature ( $T_{in}$ )

In this section, a series of numerical experiments were conducted with different inlet gas temperatures to quantify the dependence of turbulence/spray interactions on the flow preheating. The heated inlet flow simulations were performed at inlet temperatures of  $375K$ ,  $475K$ ,  $575K$ ,  $675K$ ,  $775K$  and  $1100K$ . The initial equivalence ratio of the heptane-air gas mixture was fixed at  $\phi = 0.7$ .

Comparison of the instantaneous filtered temperature and fuel mass fraction iso-contours for various inlet temperatures in Fig. 3.33 indicates that a significantly smaller number of unburned droplets survive at downstream locations, which is expected. The cooling effect of droplet vaporization is, however, more significant in the results with higher inlet temperature, especially when the inlet gas temperature is higher than the liquid boiling temperature. The iso-contours of fuel mass fraction indicates that droplets tend to accumulate more as the inlet temperature decreases. Additionally, the diffusion of the vaporized fuel increases as the inlet temperature increases, which results in significantly higher fuel concentration close to combustor

inlet.

The vorticity field and how it is affected by the inlet gas temperature is shown in Fig. 3.34. Apparently, as the inlet gas temperature decreases regions with high vorticity values are created, particularly at  $x/D < 4$ . Compared to the cases with  $T_{in} = 675, 775K$ , the vorticity values seem to be higher in case with  $T_{in} = 1100K$  at  $x/D > 5$ . Since the reaction significantly affects the density and pressure distribution, the higher inlet temperature alters the vorticity generation through the baroclinic term in the vorticity equation [261].

Fig. 3.35 shows the radial variations of the instantaneous filtered temperature, fuel mass fraction and the RMS of gas field pressure at axial locations of  $x/D = 3, 6$ . At both axial locations, the filtered temperature increases as the inlet temperature increases, which is expected. However, the temperature for the case with  $T_{in} = 375K$  seems to be higher at  $x/D = 6$  close to the combustor centerline. The radial profiles of fuel mass fraction shown in Fig. 3.35b indicate that for relatively lower  $T_{in}$  the mass fraction of heptane in the main gas stream increases as the inlet temperature increases due to the droplet vaporization. However, it decreases for highly heated flows as a result of significant fuel consumption in the combustion process. The radial variations of the pressure RMS in Fig. 3.35c demonstrate variations of pressure fluctuations with the inlet temperature. It is observed that in general for very high or very low  $T_{in}$  the pressure fluctuations are pronounced by high heat release or lack of substantial droplet evaporation.

In Fig. 3.36, the axial variations of the integrated unburned droplet number density are shown for the cases with different inlet temperatures. Expectedly, the number of droplets that still survive within the combustor decreases as the inlet temperature of the carrier gas increases. Some droplets seem to be able to leave the combustor without evaporation in the simulations with  $T_{in} = 375K$  and  $475K$ , which is not desirable.

The mean temperature and axial velocity values of the droplets are plotted versus the radial location of the droplets in Fig. 3.37 at axial location of  $x/D = 3$ . Expectedly, the mean droplet temperature increases as the inlet carrier gas temperature increases due to enhanced convective heat transfer. However, for very high inlet temperatures (e.g.  $T_{in} \geq 675K$ ) where all of the droplets reach to the boiling temperature point, the full evaporation of fuel droplets is unavoidable before they reach to farther downstream locations. Analysis of the mean droplet axial velocity (Fig. 3.37) for different inlet gas temperatures suggests that as the fuel droplets pass through the flame and start to evaporate due to convective heat transfer, the axial velocity of the smaller droplets is decreased due to momentum interactions with the carrier gas.

### 3.4.9 Effect of Inflow Turbulence

To investigate the effects of the inlet turbulence forcing amplitude on spray combustion and on heat and mass transfer rate of dispersed droplets, simulations with different magnitudes of  $\sigma_{ref}$  (inlet turbulence forcing amplitude) are conducted in this section.

Fig. 3.38 shows the iso-contours of instantaneous filtered temperature and fuel mass fraction for three different turbulence  $\sigma_{ref}$ . These iso-contours indicate that as the forcing amplitude increases, there is more temperature and fuel vapor diffusion within the combustor. The relatively cold and rich central gas stream is observed to be totally broken in the case with strong inlet turbulence ( $4 \times \sigma_{ref}$ ), where the formation of concentrated droplet regions is quite clear. These “isolated droplet islands” at some locations may cause local flame extinction. The results also show that “the burn-out” time of droplets becomes shorter as they escape from the relatively cold central flow stream and are significantly exposed to hot gas regions.

In Fig. 3.39, the iso-contours of instantaneous vorticity field for different turbu-

lence forcing are presented. Expectedly, the vortex structures which are primarily responsible for the altered “circulation” and mixing of fuel and oxidizer seem to be augmented by increasing the turbulence forcing. Interestingly, the high magnitude vorticity contours are observed to be in the upper side of the combustor close to spray injection regions. This suggests that the evaporating droplet mass and energy transfer to the carrier gas can be also considered as mechanisms responsible for vortex formation.

The radial variations of the instantaneous filtered temperature, fuel mass fraction and RMS of pressure at  $x/D = 3$  and  $x/D = 6$  are shown in Fig. 3.40. It is observed that at both axial locations the temperature iso-contour values are higher at  $r/D < 0.5$  for higher turbulence forcing. On the other hand, the gas temperature is observed to decrease as one moves out radially. This is mainly due to better mixing of the hot products and cold fuel-rich mixture. This is also quite clear in the profiles of the fuel mass fraction shown in Fig. 3.40b, where the fuel concentration is higher for higher turbulence forcing at locations close to combustor axis and lower at locations close to side walls. Thus, by increasing the forcing amplitude more homogeneous droplet evaporation and combustion is expected. Nevertheless, as shown in the radial profiles of the RMS of mean pressure (Fig. 3.40c), the pressure fluctuations seem to be much higher for high  $\sigma_{ref}$  ( $4 \times \sigma_{ref}$ ). On the other hand, the results with moderate turbulence forcing ( $2 \times \sigma_{ref}$ ) indicate that the pressure fluctuations are better suppressed compared to those in cases with the lowest  $\sigma_{ref}$ .

The axial variations of the integrated droplet number density for different turbulence forcing are shown in Fig. 3.41. It is observed that the droplets completely burn-out earlier as the turbulence forcing increases. Further integration of the droplet number density profile along the x-axis (not shown) indicates that the highest droplet evaporation ratio is achieved in the results with a moderate inlet turbulence intensity ( $2 \times \sigma_{ref}$ ). Consequently, there seems to be no clear correlation between the droplet

evaporation rate and the inlet turbulence intensity, even though by increasing  $\sigma_{ref}$  the combustion becomes more homogeneous.

The effects of inlet turbulence on droplets are illustrated in Fig. 3.42 via the radial variations of the mean droplet temperature and axial velocity at  $x/D = 3$ . Both the droplet temperature and velocity are observed to be lower for the highest simulated inlet turbulent intensity ( $4 \times \sigma_{ref}$ ). Our other results (not shown) indicate that this can be attributed to the droplet size. Due to evaporation delay, larger droplets survive at this particular location, which tend to preserve more their initial temperature and velocity.

### 3.5 Summary and Conclusions

Large eddy simulations (LES) of two-phase turbulent reacting flows in a spray-controlled axisymmetric dump combustor are conducted to investigate the effects various spray properties and ambient flow conditions on the droplet and carrier gas temperature, pressure, and velocity. A hybrid Lagrangian-Eulerian-Lagrangian methodology is developed and implemented for solving the Lagrangian spray, Eulerian finite-difference (FD) velocity, and Lagrangian-Monte Carlo (MC) gas scalar equations via conventional numerical models and a PDF-based two-phase subgrid combustion model, termed the filtered mass density function (FMDF). Full two-way mass, momentum and energy coupling between the evaporating droplets and the carrier lean-premixed heptane-air gas mixture are considered. Different initial values of droplet Sauter mean diameter, spray and injection angles, liquid fuel to gas mass loading ratio, droplets injection velocity, pulsative spray injection frequency, carrier gas equivalence ratio, inlet temperature and turbulence intensity are considered.

The results for non-reacting, reacting without spray and spray-controlled combustion cases show that the LES/FD and FMDF/MC are consistent in all tested flow

conditions. In a qualitative agreement with experimental observations [262, 263], the LES/FMDF results indicate that the initial droplet size has a strong influence on the flow dynamic and thermal characteristics of the carrier gas and the evaporating droplets. For example, with an increase in initial droplet size, the rate of evaporation decreases. The mass, momentum and energy of the evaporating droplets decrease the mean gas temperature and increase combustion of lean mixture. Consistent with experimental data [250], smaller droplets closely follow the flow structure, while large droplets are found to cross high vorticity areas and reach to the wall where they go through a complicated interaction process.

The results indicate that as the spray angle is increased the penetration of the droplets decreases. Therefore, droplets are vaporizing at upstream locations, which yields higher fuel mass fraction and combustion at those locations. It is also observed that the burn-out ratio of the injected droplets decreases as the spray cone angle decreases. Similarly, the results with different injection angles indicate that the droplet penetrate more in the axial direction as the injection angle increases. Except for zero degree injection angle, where the injection is parallel to the combustor axis, the total number of vaporized droplets seems to be close to each other for different injection angles since the droplets are injected into the core carrier gas stream. Nevertheless, our results (not shown) indicate that the effect of injection angle is more significant when larger droplets are dispersed. Both for large spray and injection angles, the pressure fluctuations are observed to be significantly suppressed.

The effect of droplet mass loading ratio is investigated in several cases, ranging from highly dilute to highly dense sprays. It is shown that by increasing the droplet mass loading the rate of evaporation of individual droplets decrease. Local flame extinctions are also observed for very high mass loading ratios due to significant droplet cooling effect and insufficient oxidizer to sustain the combustion.

By comparing the results with different droplet injection velocities, it is found

that droplets with higher injection velocities are able to cross the high vorticity regions and reach to high temperature reacting zones, resulting in an increase in the droplet evaporation. Furthermore, it is found that the mean total kinetic energy of the carrier gas and the vorticity are both enhanced when droplets are injected with higher velocities. Our results (not shown) also indicate that the pressure fluctuations could be decreased beyond a certain point by injecting faster droplets. The results with different injection frequencies demonstrate that the damping effect of spray is quite significant at a certain high injection frequency. This suggests that by creating out of-phase heat release oscillations the pressure fluctuations can be well managed.

Investigation of the effects of carrier gas properties on combustion indicates that the physical structure of mean gas is modified differently by the spray for different initial equivalence ratio, inlet temperature and turbulence intensity. As the inlet equivalence ratio decreases or the inlet turbulence intensity increases, the large-scale turbulent motions are observed to become more pronounced, resulting in very different spray effects on the combustion. The radial variations of droplet properties indicate that by increasing the initial equivalence ratio the droplet evaporating rate tends to increase due to higher heat release. Comparison between the cases with different turbulence intensity indicates that even though the stronger turbulence causes more homogeneous combustion, there seems to be no significant change in the total number of vaporized droplets.

Our results reveal several important physical effects of different spray/flow parameters on two-phase turbulent reacting flows and indicate that the numerical simulations via hybrid Lagrangian-Eulerian-Lagrangian two-phase LES/FMDF methodology is affordable, consistent and reliable for turbulent spray combustion in complex systems.

## 3.6 Tables and Figures

Table 3.1: Spray parameters of various tested cases.

Case No.	SMD ( $\mu m$ )	Spr. Angle ( $\alpha^\circ$ )	Inj. Angle ( $\beta^\circ$ )	MLR ( $\Gamma$ )	Inj. Velocity ( $u_p$ m/s)	Inj. Freq. ( $\psi$ Hz.)	EQR ( $\phi$ )	Inlet Temp. ( $T_{in}$ °K)	Turb. Intensity ( $\sigma_{ref}$ )
I	30-120	40	45	0.11	15	0	0.7	575	$1 \times \sigma_{ref}$
II	45	0-80	45	0.11	15	0	0.7	575	$1 \times \sigma_{ref}$
III	45	40	0-60	0.11	15	0	0.7	575	$1 \times \sigma_{ref}$
IV	45	40	45	0.01-0.44	15	0	0.7	575	$1 \times \sigma_{ref}$
V	45	40	45	0.11	15-60	0	0.7	575	$1 \times \sigma_{ref}$
VI	45	40	45	0.11	15	0-1000	0.7	575	$1 \times \sigma_{ref}$
VII	45	40	45	0.11	15	0	0.01-2.0	575	$1 \times \sigma_{ref}$
VIII	45	40	45	0.11	15	0	0.7	375-1100	$1 \times \sigma_{ref}$
IX	45	40	45	0.11	15	0	0.7	575	$1.4 \times \sigma_{ref}$

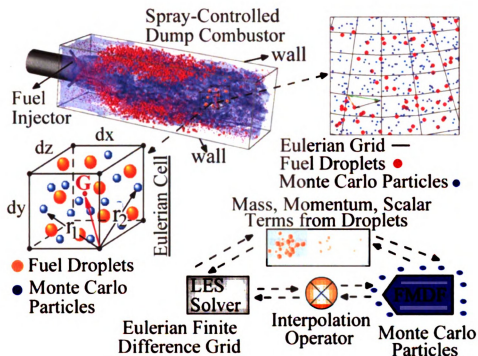


Figure 3.1: The Eulerian and the Lagrangian fields of the two-phase LES/FMDF methodology.

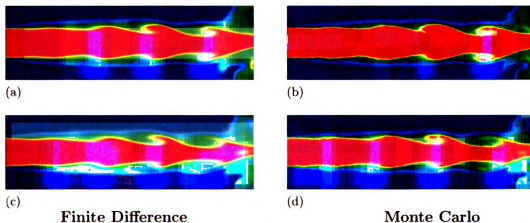


Figure 3.2: Iso-contours of the instantaneous filtered temperature and fuel mass fraction in the non-reacting axisymmetric dump combustor without spray as obtained by LES/FMDF; (a) FD values of temperature, (b) MC values of temperature, (c) FD values of fuel mass fraction, and (d) MC values of fuel mass fraction.

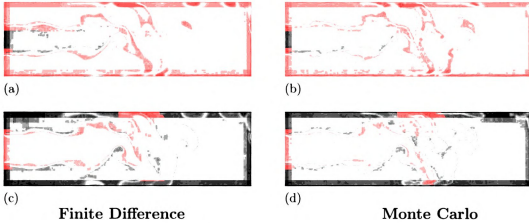


Figure 3.3: Iso-contours of the instantaneous filtered temperature and fuel mass fraction in the reacting axisymmetric dump combustor without spray as obtained by LES/FDMF; (a) FD values of temperature, (b) MC values of temperature, (c) FD values of fuel mass fraction, and (d) MC values of fuel mass fraction.

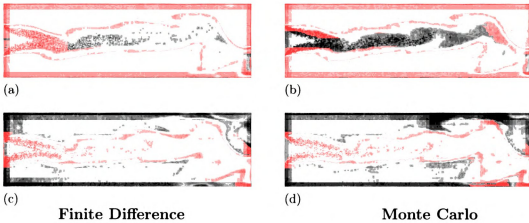
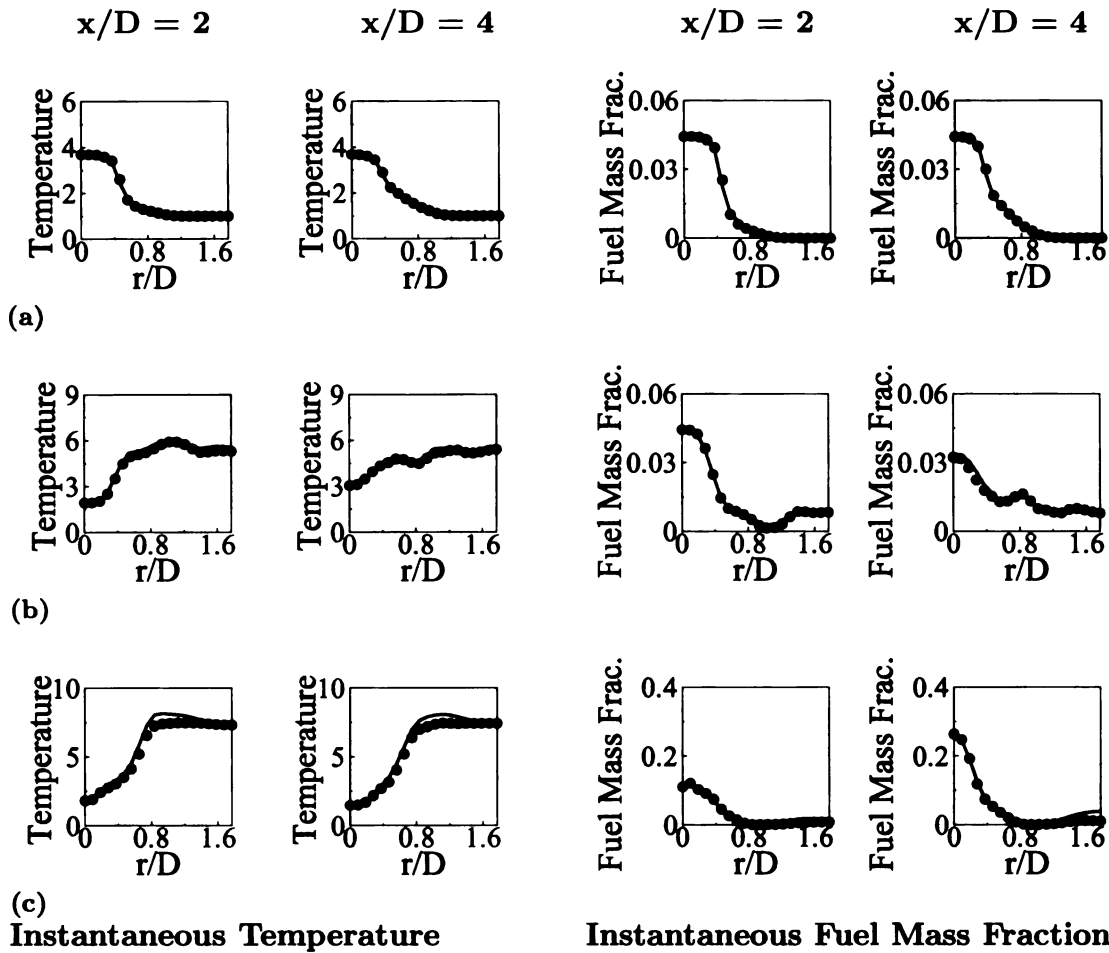
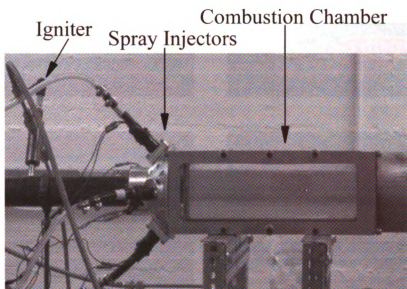


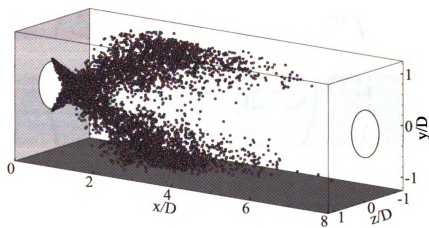
Figure 3.4: Iso-contours of the instantaneous filtered temperature and fuel mass fraction in the reacting axisymmetric dump combustor with spray as obtained by LES/FDMF; (a) FD values of temperature, (b) MC values of temperature, (c) FD values of fuel mass fraction, and (d) MC values of fuel mass fraction.



**Figure 3.5:** Radial variations of the instantaneous filtered temperature and fuel mass fraction at axial locations of  $x/D = 2$  and  $x/D = 4$ ; (a) Non-isothermal non-reacting case without spray, (b) Non-isothermal reacting case without spray, (c) Non-isothermal reacting case with spray. The results are obtained by averaging the instantaneous data in the azimuthal direction and not in time.



(a)



(b)

Figure 3.6: Images of the axisymmetric dump combustor; (a) Picture of experimental setup [1] and (b) Illustration of computational domain and droplet injection.

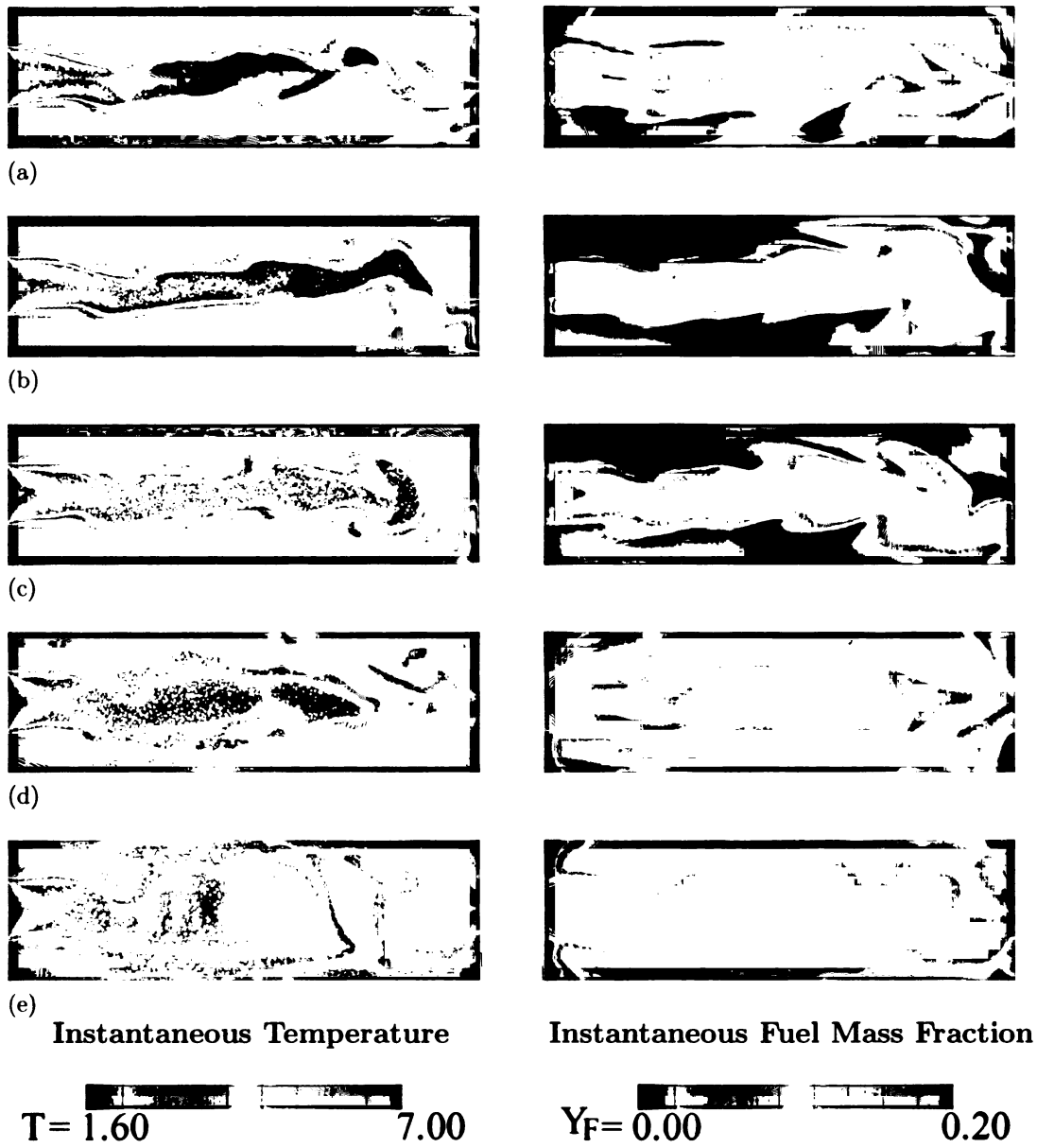


**Figure 3.7:** Iso-contours of the instantaneous of filtered temperature and fuel mass fraction as obtained by LES/FDMF with various SMD values; (a)  $SMD = 30\mu m$ , (b)  $SMD = 45\mu m$ , (c)  $SMD = 60\mu m$ , (d)  $SMD = 90\mu m$ , (e)  $SMD = 120\mu m$ .

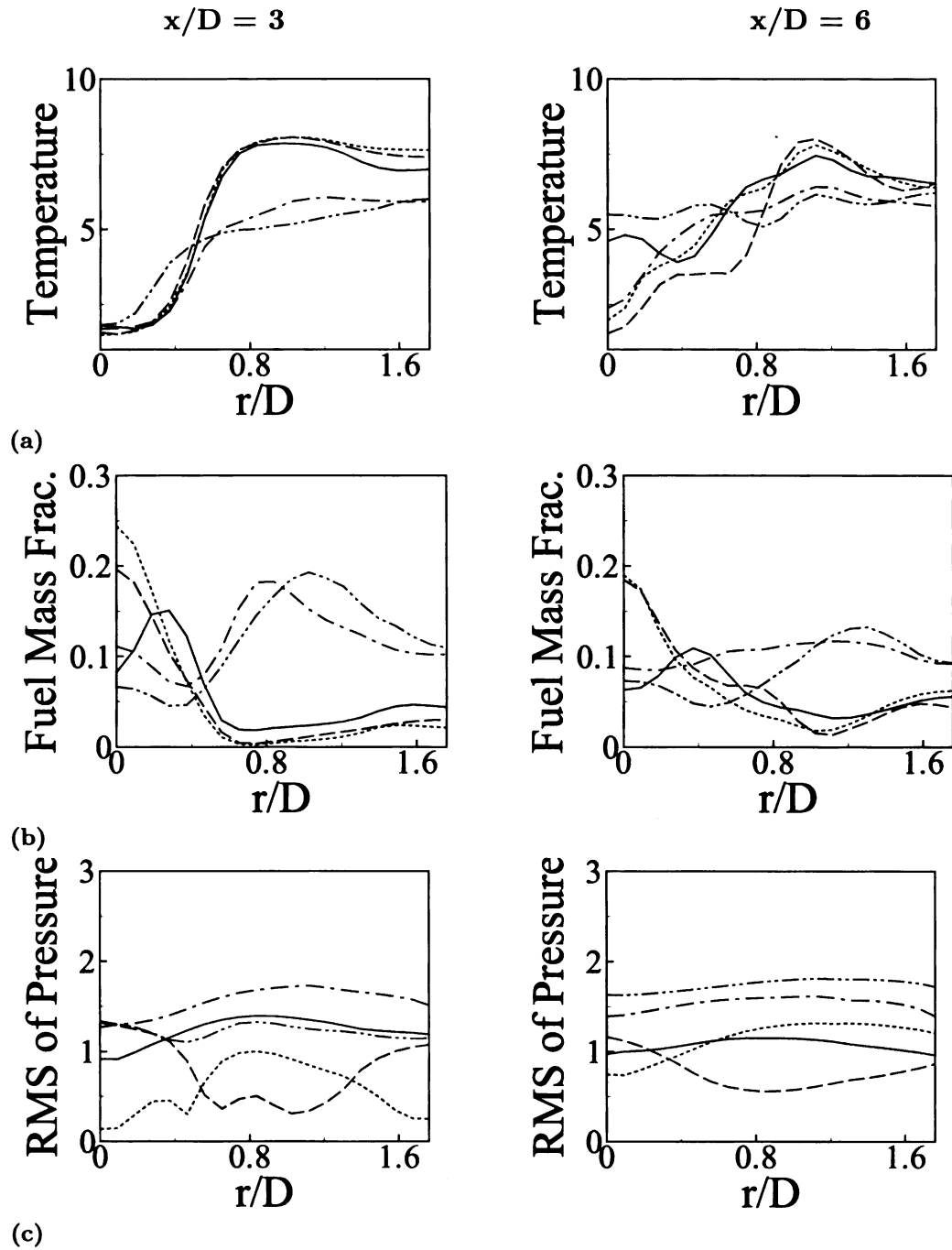


Figure 3.8: Radial variations of various quantities at axial locations of  $x/D = 3$  and  $x/D = 6$  with various SMD values; (a) Instantaneous filtered temperature, (b) Instantaneous filtered fuel mass fraction, (c) Root mean square (RMS) of filtered pressure (solid line,  $30\mu m$ ; dashed line,  $45\mu m$ ; long-dashed line,  $60\mu m$ ; dashed-dot line,  $90\mu m$ ; dashed-dot-dot line,  $120\mu m$ ).

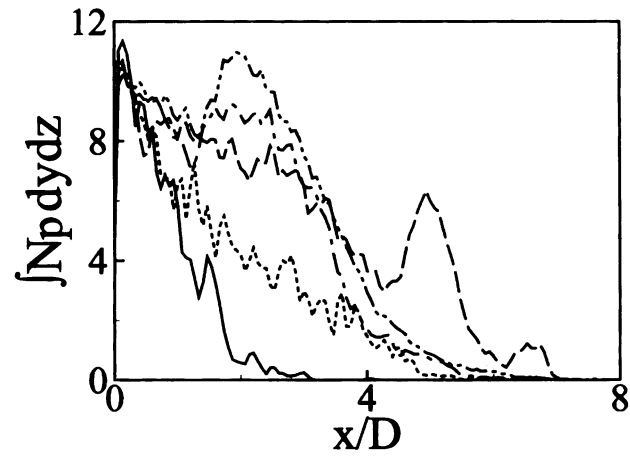
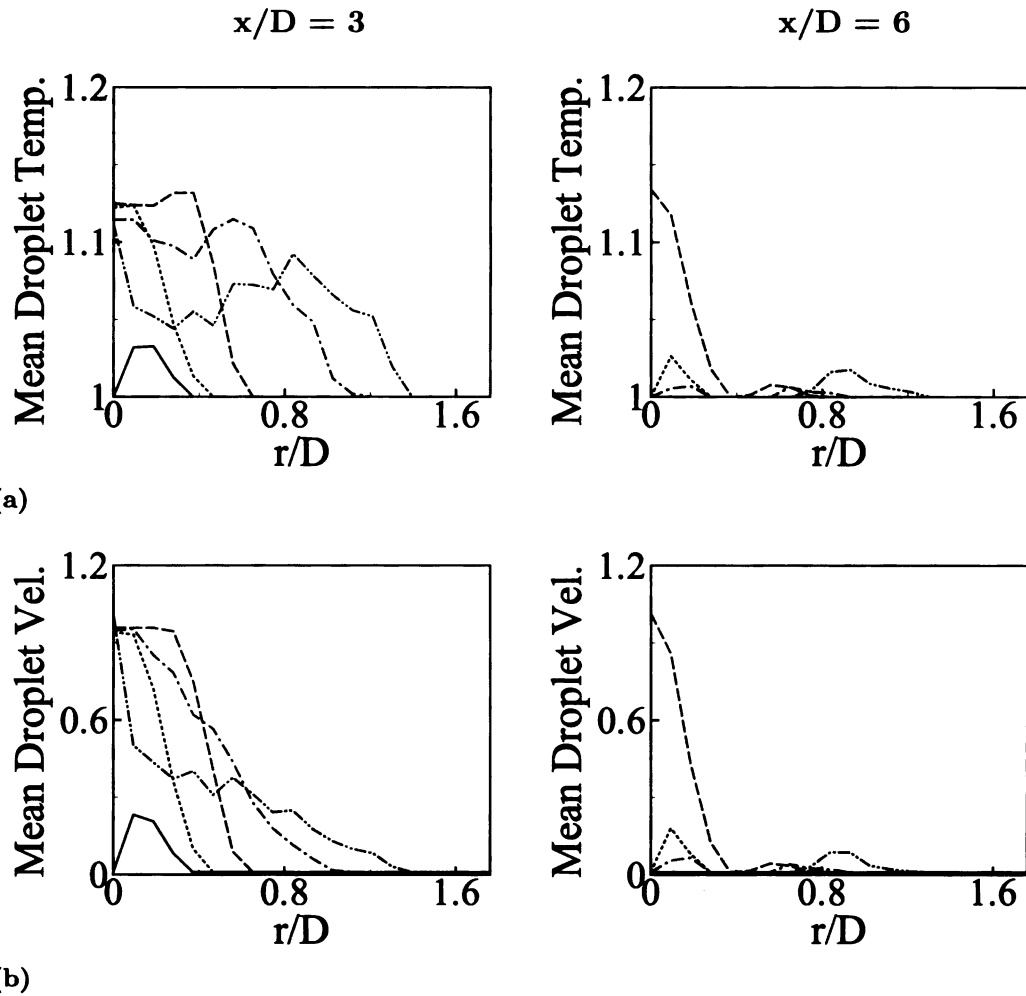


Figure 3.9: Axial variations of integrated droplet number density with various SMD values (solid line,  $30\mu m$ ; dashed line,  $45\mu m$ ; long-dashed line,  $60\mu m$ ; dashed-dot line,  $90\mu m$ ; dashed-dot-dot line,  $120\mu m$ ).



**Figure 3.10: Radial variations of various droplet quantities at axial locations of  $x/D = 3$  and  $x/D = 6$  with various SMD values; (a) Mean droplet temperature, (b) Mean droplet axial velocity (solid line,  $30\mu m$ ; dashed line,  $45\mu m$ ; long-dashed line,  $60\mu m$ ; dashed-dot line,  $90\mu m$ ; dashed-dot-dot line,  $120\mu m$ ).**

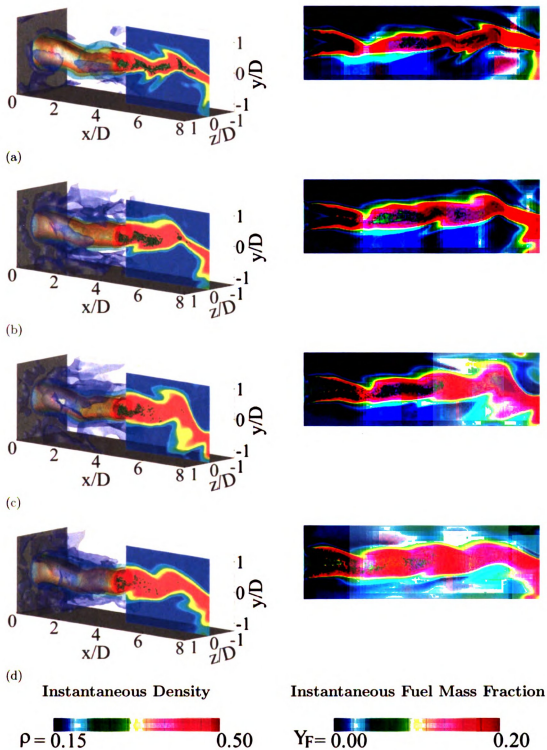
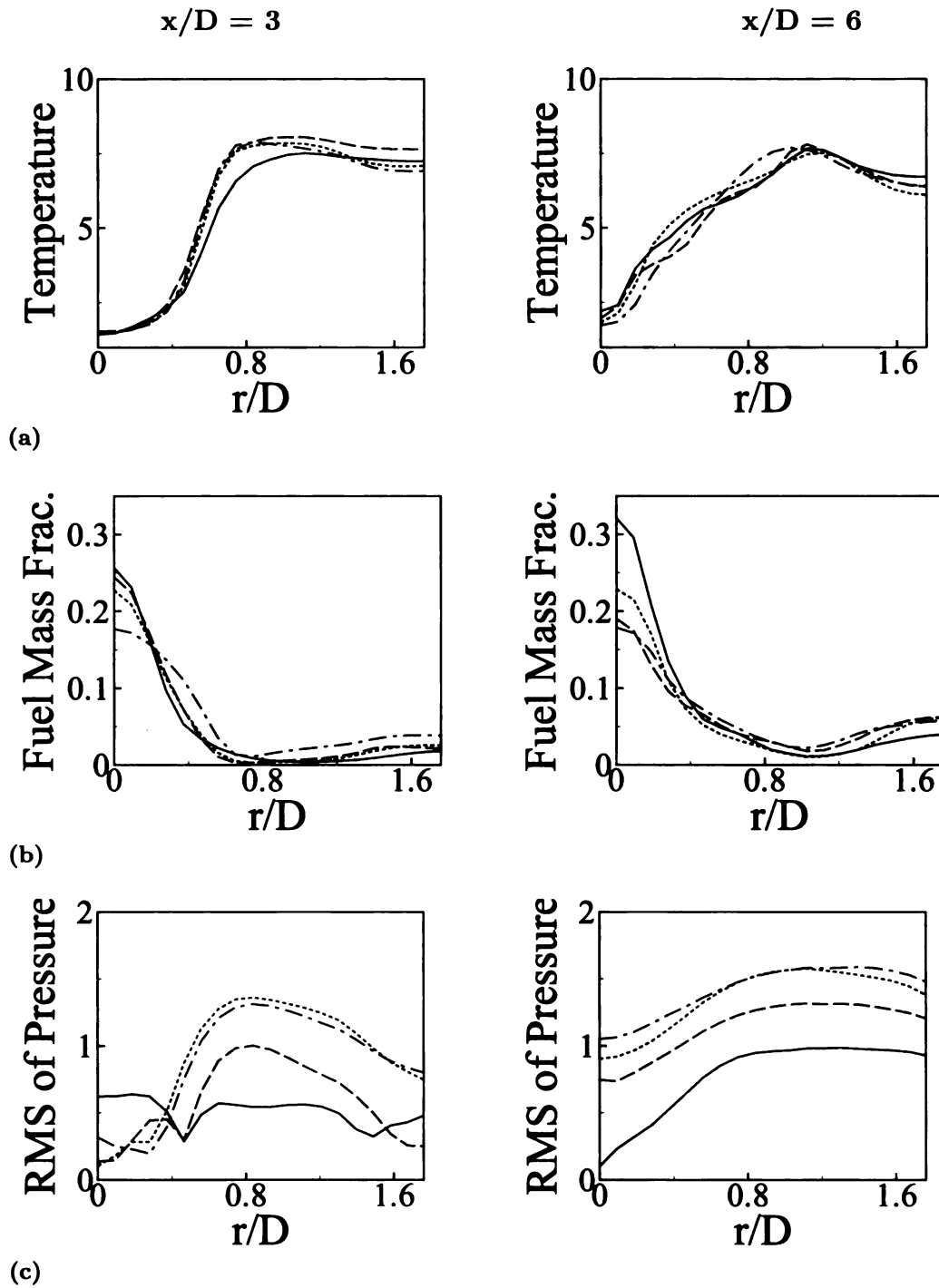


Figure 3.11: Iso-contours of the instantaneous filtered density and fuel mass fraction as obtained by LES/FDMF with various spray angles; (a)  $\alpha \approx 0$ , (b)  $\alpha \approx 20$ , (c)  $\alpha \approx 40$ , (d)  $\alpha \approx 80$ .



**Figure 3.12:** Radial variations of various quantities at axial locations of  $x/D = 3$  and  $x/D = 6$  with various spray angles; (a) Instantaneous filtered temperature, (b) Instantaneous filtered fuel mass fraction, (c) Root mean square (RMS) of filtered pressure (solid line,  $\alpha \approx 0$ ; dashed line,  $\alpha \approx 20$ ; long-dashed line,  $\alpha \approx 40$ ; dashed-dot line,  $\alpha \approx 80$ ).

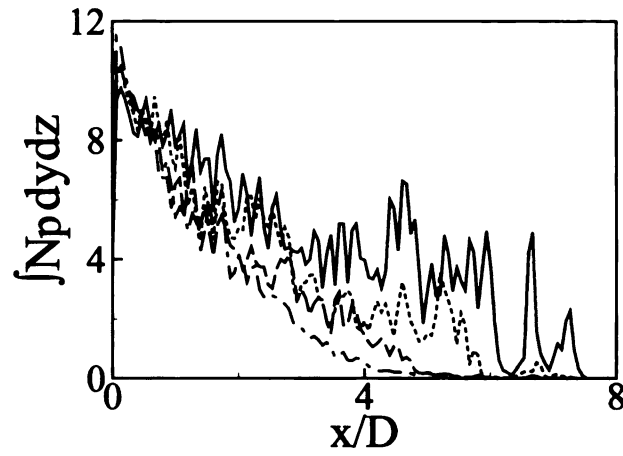
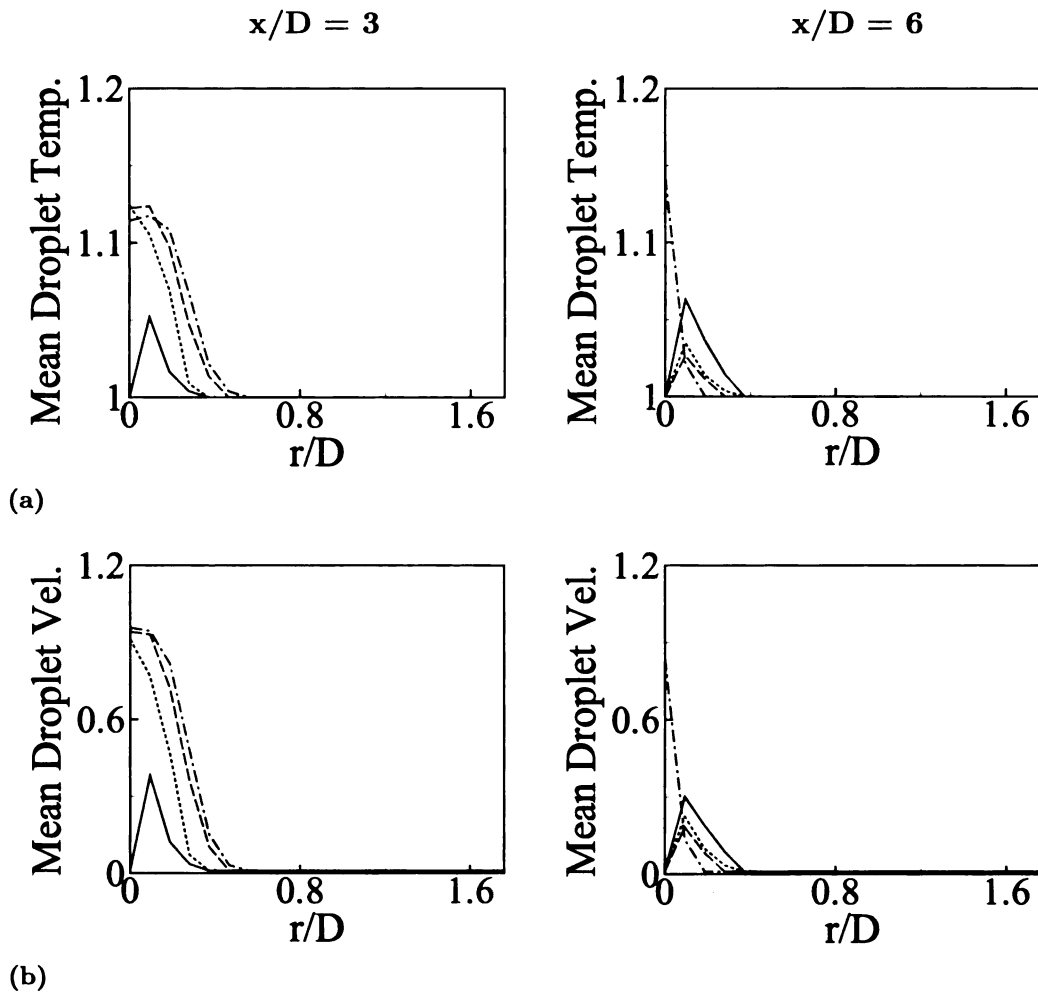


Figure 3.13: Axial variations of integrated droplet number density with various spray angles (solid line,  $\alpha \approx 0$ ; dashed line,  $\alpha \approx 20$ ; long-dashed line,  $\alpha \approx 40$ ; dashed-dot line,  $\alpha \approx 80$ ).



**Figure 3.14: Radial variations of various droplet quantities at axial locations of  $x/D = 3$  and  $x/D = 6$  with various spray angles; (a) Mean droplet temperature, (b) Mean droplet axial velocity (solid line,  $\alpha \approx 0$ ; dashed line,  $\alpha \approx 20$ ; long-dashed line,  $\alpha \approx 40$ ; dashed-dot line,  $\alpha \approx 80$ ).**

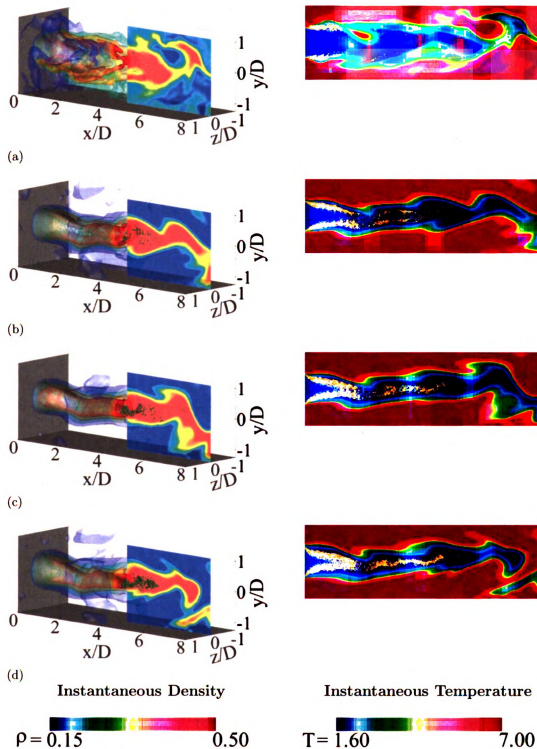
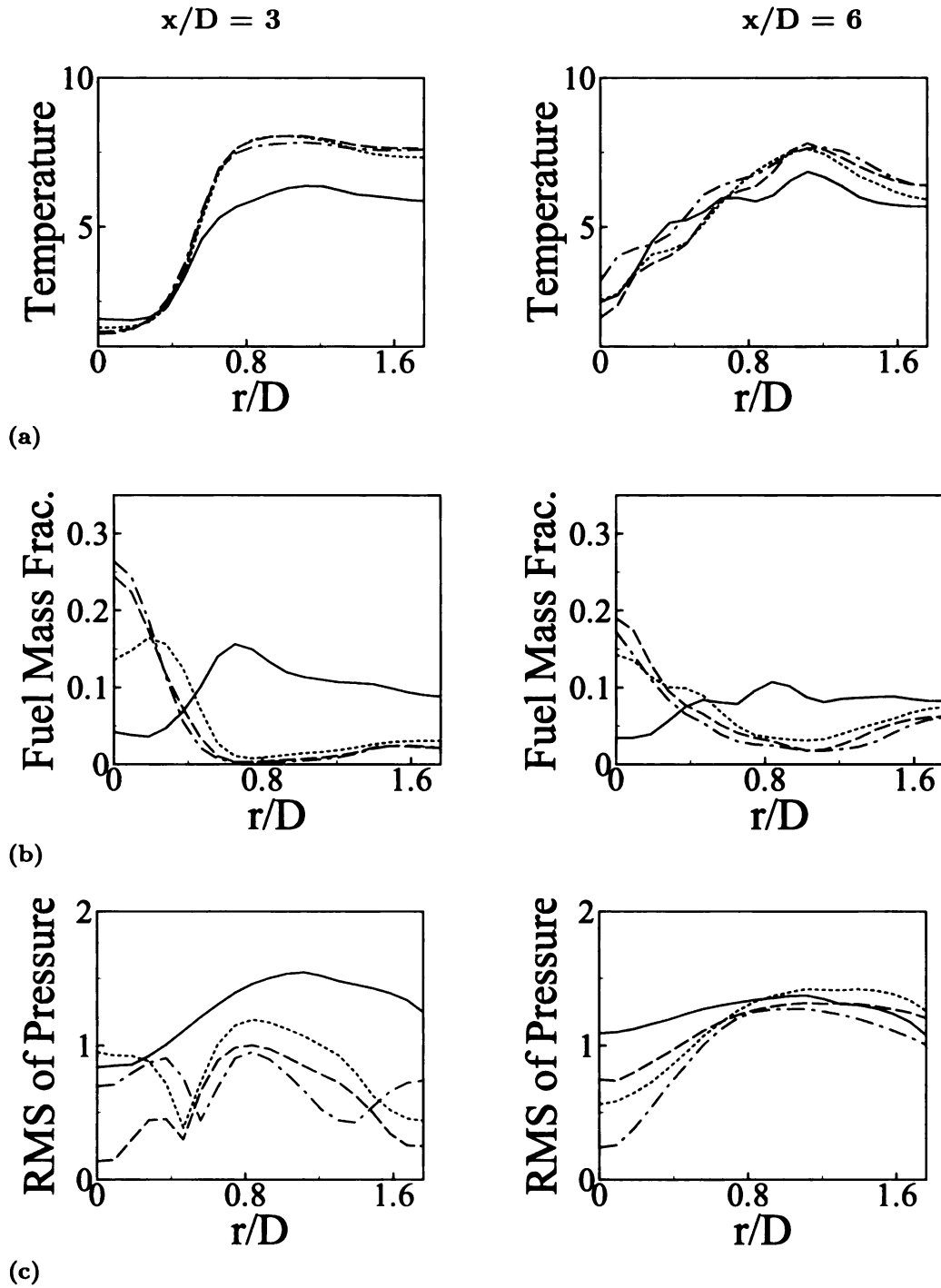


Figure 3.15: Iso-contours of the instantaneous filtered density and temperature as obtained by LES/FDMF with various injection angles; (a)  $\beta \approx 0$ , (b)  $\beta \approx 30$ , (c)  $\beta \approx 45$ , (d)  $\beta \approx 60$ .



**Figure 3.16: Radial variations of various quantities at axial locations of  $x/D = 3$  and  $x/D = 6$  with various injection angles; (a) Instantaneous filtered temperature, (b) Instantaneous filtered fuel mass fraction, (c) Root mean square (RMS) of filtered pressure (solid line,  $\beta \approx 0$ ; dashed line,  $\beta \approx 30$ ; long-dashed line,  $\beta \approx 45$ ; dashed-dot line,  $\beta \approx 60$ ).**

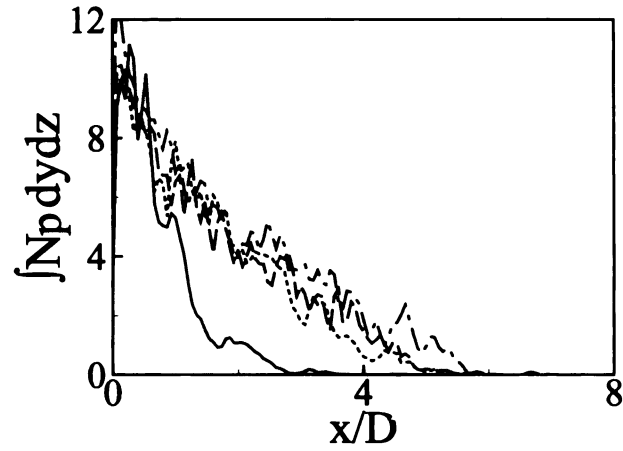
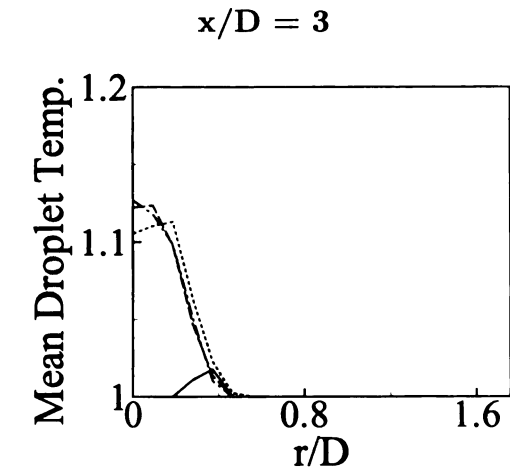
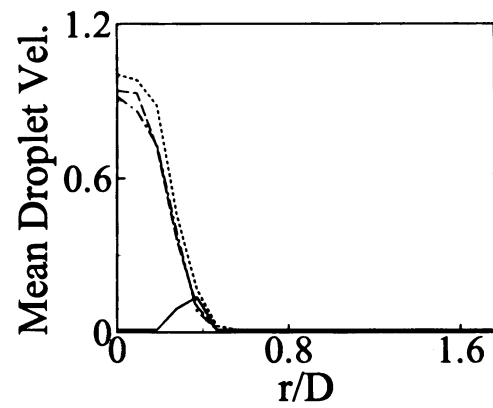


Figure 3.17: Axial variations of integrated droplet number density with various injection angles (solid line,  $\beta \approx 0$ ; dashed line,  $\beta \approx 30$ ; long-dashed line,  $\beta \approx 45$ ; dashed-dot line,  $\beta \approx 60$ ).



(a)



(b)

**Figure 3.18: Radial variations of various droplet quantities at axial location of  $x/D = 3$  with various injection angles; (a) Mean droplet temperature, (b) Mean droplet axial velocity (solid line,  $\beta \approx 0$ ; dashed line,  $\beta \approx 30$ ; long-dashed line,  $\beta \approx 45$ ; dashed-dot line,  $\beta \approx 60$ ).**

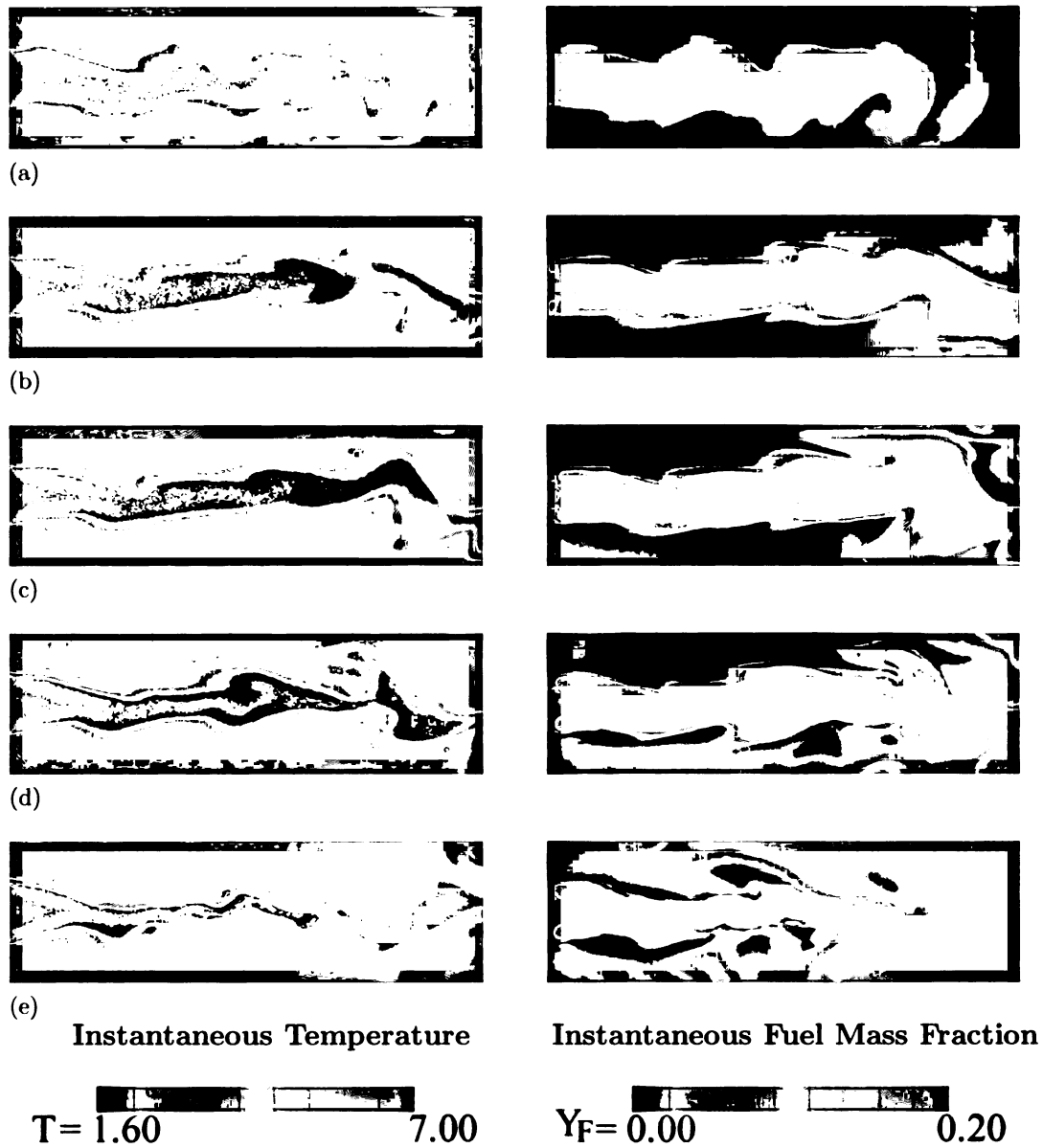


**Figure 3.19:** Iso-contours of the instantaneous of filtered temperature and fuel mass fraction as obtained by LES/FDMF with various droplet mass loading ratios; (a)  $\Gamma = 0.01$ , (b)  $\Gamma = 0.055$ , (c)  $\Gamma = 0.11$ , (d)  $\Gamma = 0.22$ , (e)  $\Gamma = 0.44$ .

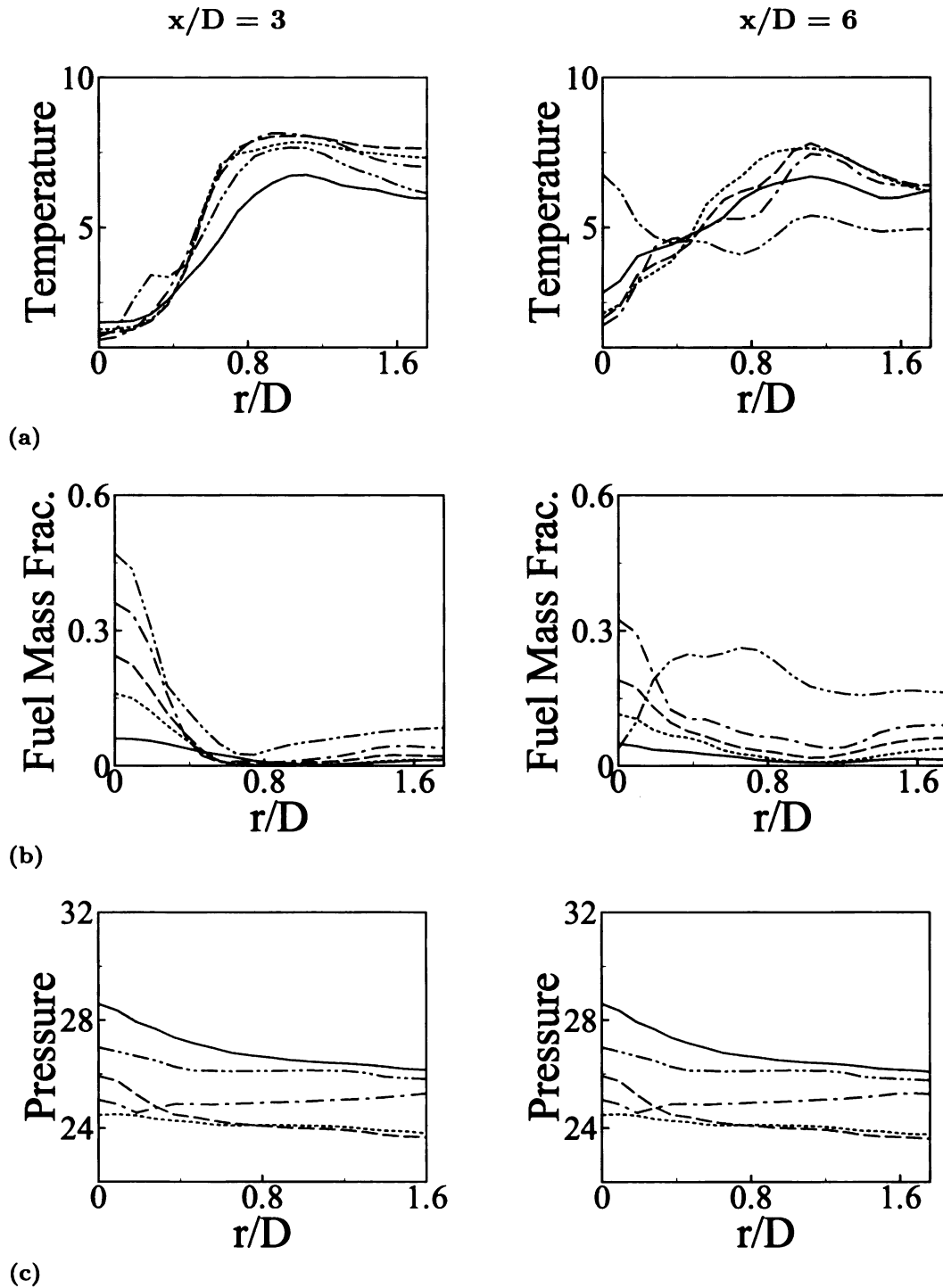


**Figure 3.20:** Radial variations of various quantities at axial locations of  $x/D = 3$  and  $x/D = 6$  with various droplet mass loading ratios; (a) Instantaneous filtered temperature, (b) Instantaneous filtered fuel mass fraction, (c) Instantaneous filtered pressure (solid line,  $\Gamma = 0.01$ ; dashed line,  $\Gamma = 0.055$ ; long-dashed line,  $\Gamma = 0.11$ ; dashed-dot line,  $\Gamma = 0.22$ ; dashed-dot-dot line,  $\Gamma = 0.44$ ).

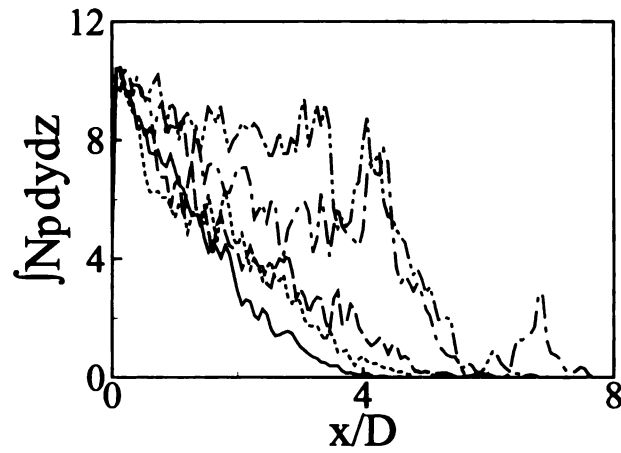
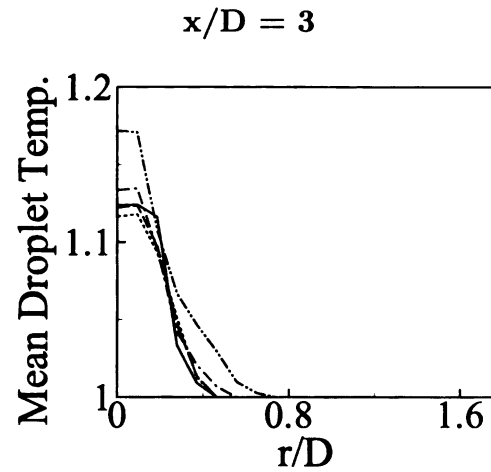
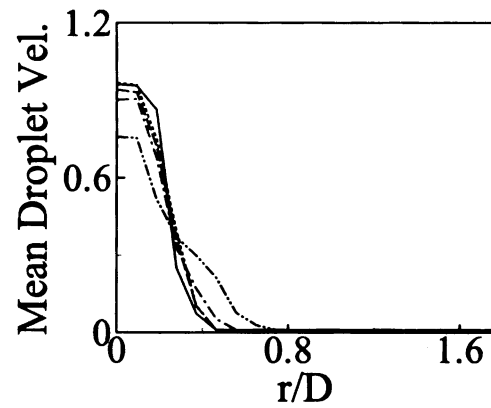


Figure 3.21: Axial variations of integrated droplet number density with various droplet mass loading ratios (solid line,  $\Gamma = 0.01$ ; dashed line,  $\Gamma = 0.055$ ; long-dashed line,  $\Gamma = 0.11$ ; dashed-dot line,  $\Gamma = 0.22$ ; dashed-dot-dot line,  $\Gamma = 0.44$ ).



(a)



(b)

**Figure 3.22:** Radial variations of various droplet quantities at axial location of  $x/D = 3$  with various droplet mass loading ratios; (a) Mean droplet temperature, (b) Mean droplet axial velocity (solid line,  $\Gamma = 0.01$ ; dashed line,  $\Gamma = 0.055$ ; long-dashed line,  $\Gamma = 0.11$ ; dashed-dot line,  $\Gamma = 0.22$ ; dashed-dot-dot line,  $\Gamma = 0.44$ ).

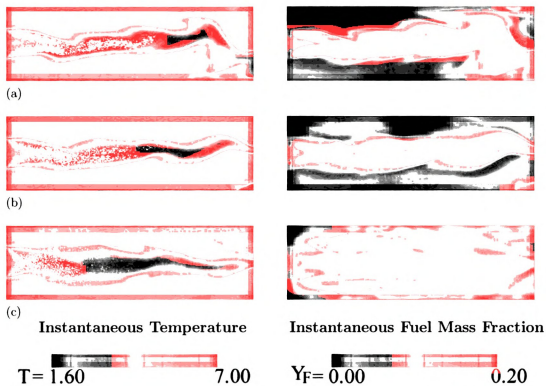


Figure 3.23: Iso-contours of the instantaneous of filtered temperature and fuel mass fraction as obtained by LES/FDMF with various droplet injection velocities; (a)  $u_p = 15\text{m/s}$ , (b)  $u_p = 30\text{m/s}$ , (c)  $u_p = 60\text{m/s}$ .

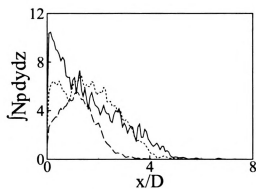
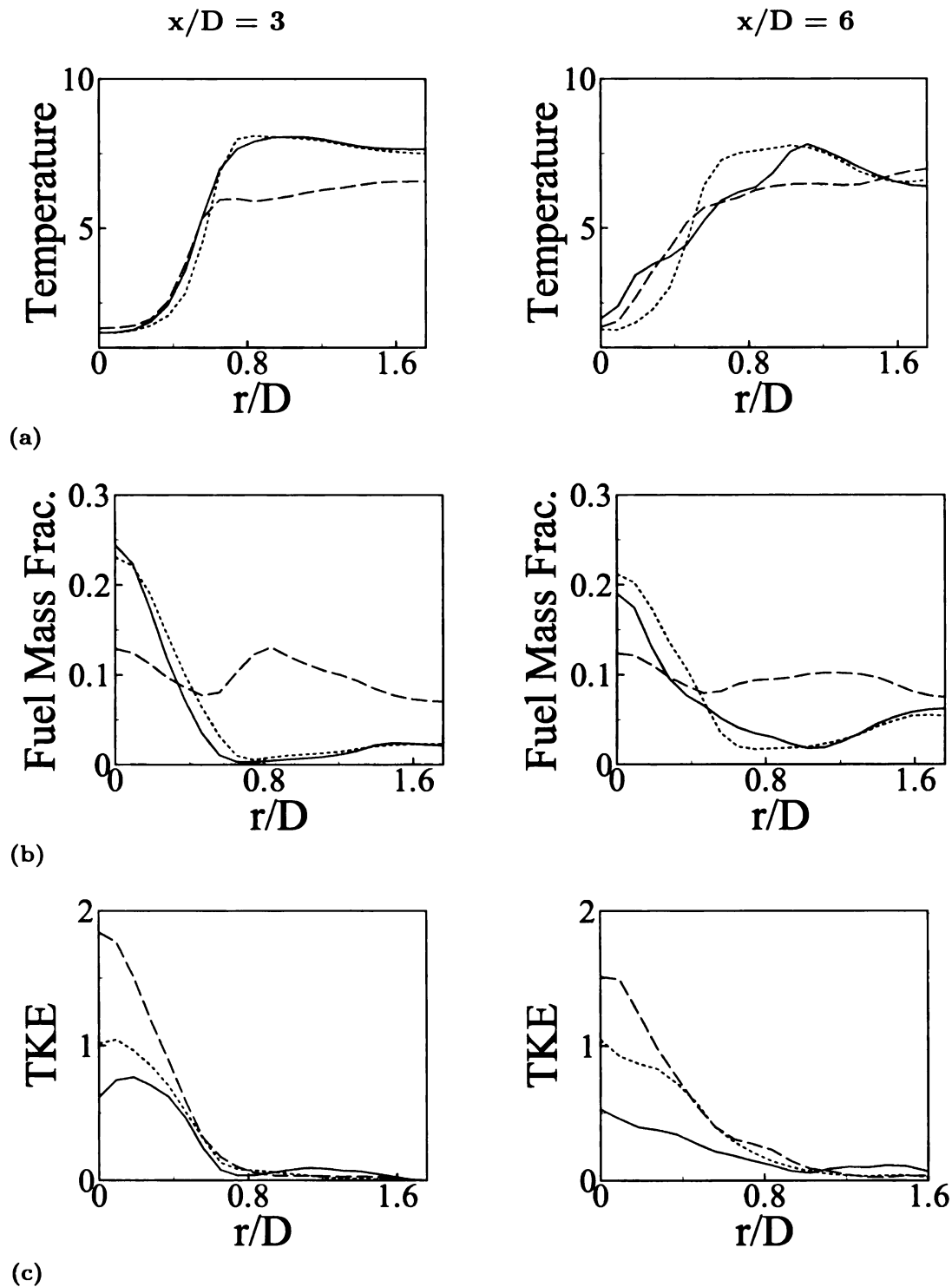


Figure 3.24: Axial variations of integrated droplet number density with various droplet injection velocities (solid line,  $u_p = 15\text{m/s}$ ; dashed line,  $u_p = 30\text{m/s}$ ; long-dashed line,  $u_p = 60\text{m/s}$ ).



**Figure 3.25: Radial variations of various quantities at axial locations of  $x/D = 3$  and  $x/D = 6$  with various droplet injection velocities; (a) Instantaneous filtered temperature, (b) Instantaneous filtered fuel mass fraction, (c) Instantaneous filtered total kinetic energy (TKE) (solid line,  $u_p = 15\text{ m/s}$ ; dashed line,  $u_p = 30\text{ m/s}$ ; long-dashed line,  $u_p = 60\text{ m/s}$ ).**

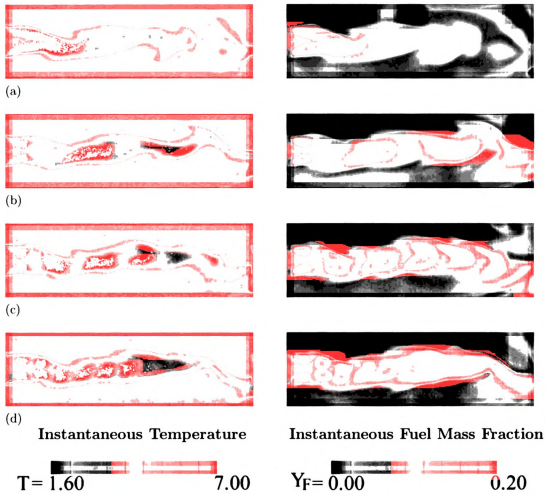


Figure 3.26: Iso-contours of the instantaneous filtered temperature and fuel mass fraction as obtained by LES/FDMF with various injection frequencies; (a)  $\psi = 38Hz$ , (b)  $\psi = 250Hz$ , (c)  $\psi = 500Hz$ , (d)  $\psi = 1kHz$ .

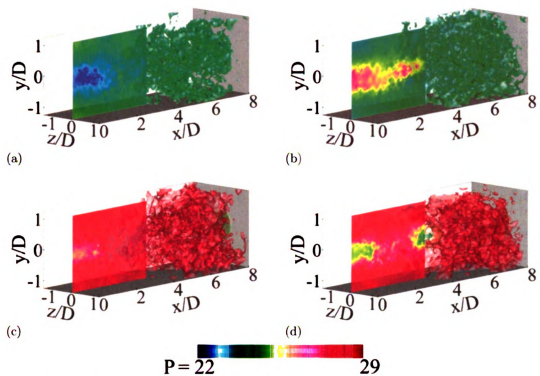
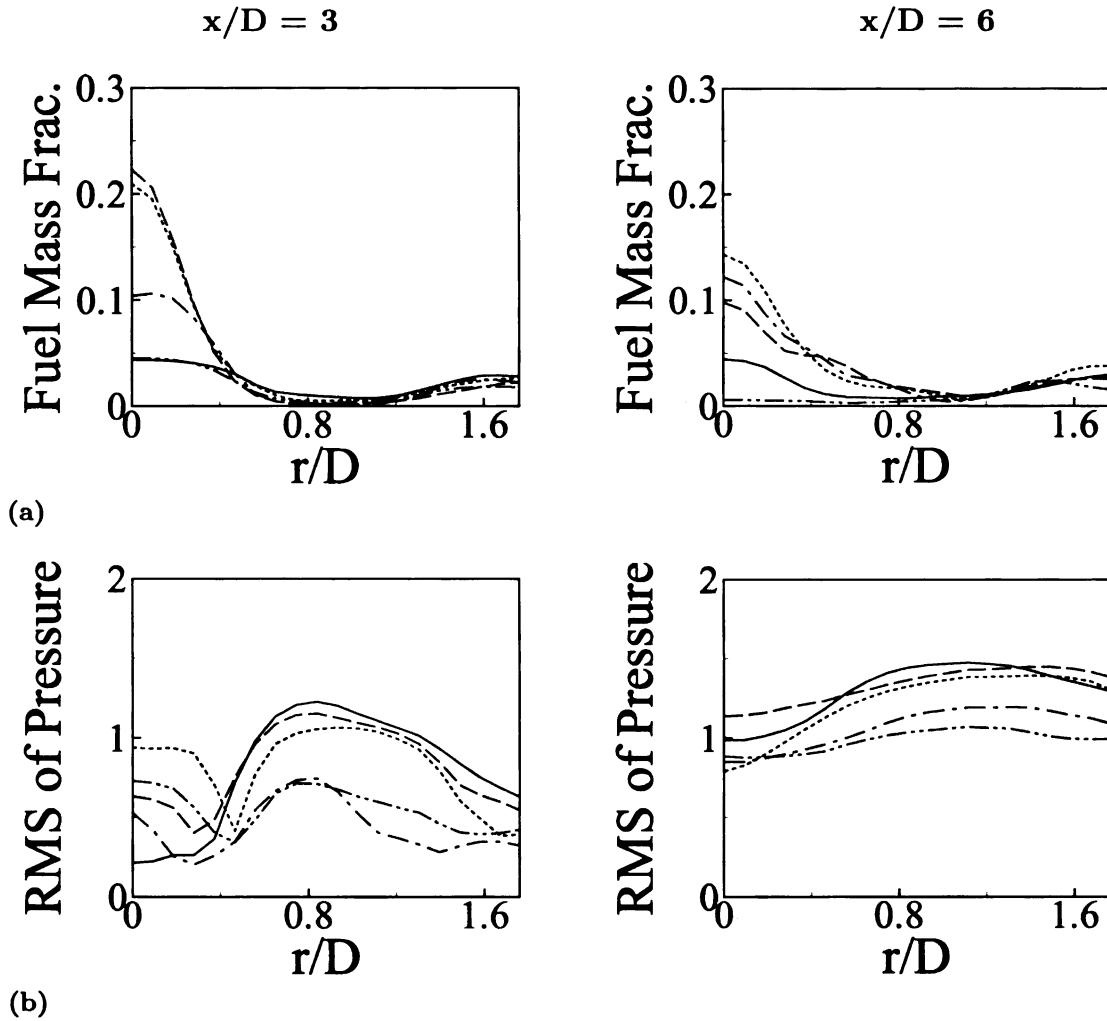


Figure 3.27: Iso-surfaces of the instantaneous filtered pressure as obtained by LES/FDMF with various injection frequencies; (a)  $\psi = 38Hz$ , (b)  $\psi = 250Hz$ , (c)  $\psi = 500Hz$ , (d)  $\psi = 1kHz$ .



**Figure 3.28:** Radial variations of various quantities at axial locations of  $x/D = 3$  and  $x/D = 6$  with various injection frequencies; (a) Instantaneous filtered fuel mass fraction, (b) Root mean square (RMS) of filtered pressure (solid line,  $\psi = 38\text{Hz}$ ; dashed line,  $\psi = 250\text{Hz}$ ; long-dashed line,  $\psi = 500\text{Hz}$ ; dashed-dot line,  $\psi = 1\text{kHz}$ ).

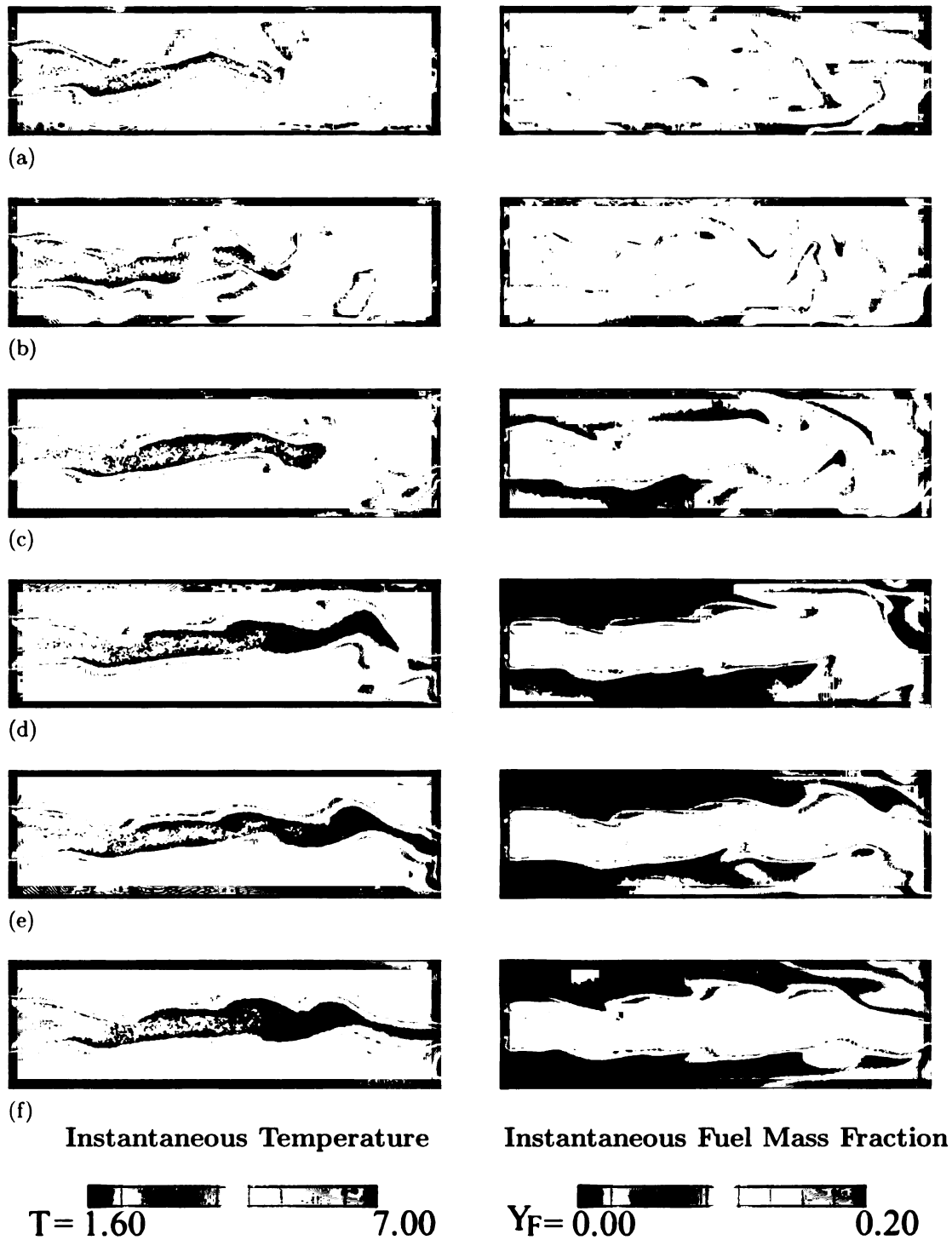


Figure 3.29: Iso-contours of the instantaneous of filtered temperature and fuel mass fraction as obtained by LES/FDMF with various initial equivalence ratios; (a)  $\phi = 0.01$ , (b)  $\phi = 0.1$ , (c)  $\phi = 0.4$ , (d)  $\phi = 0.7$ , (e)  $\phi = 1.00$ , (f)  $\phi = 2.00$ .

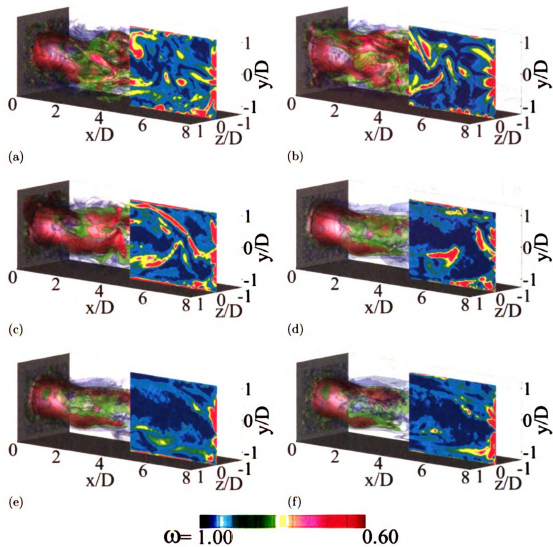
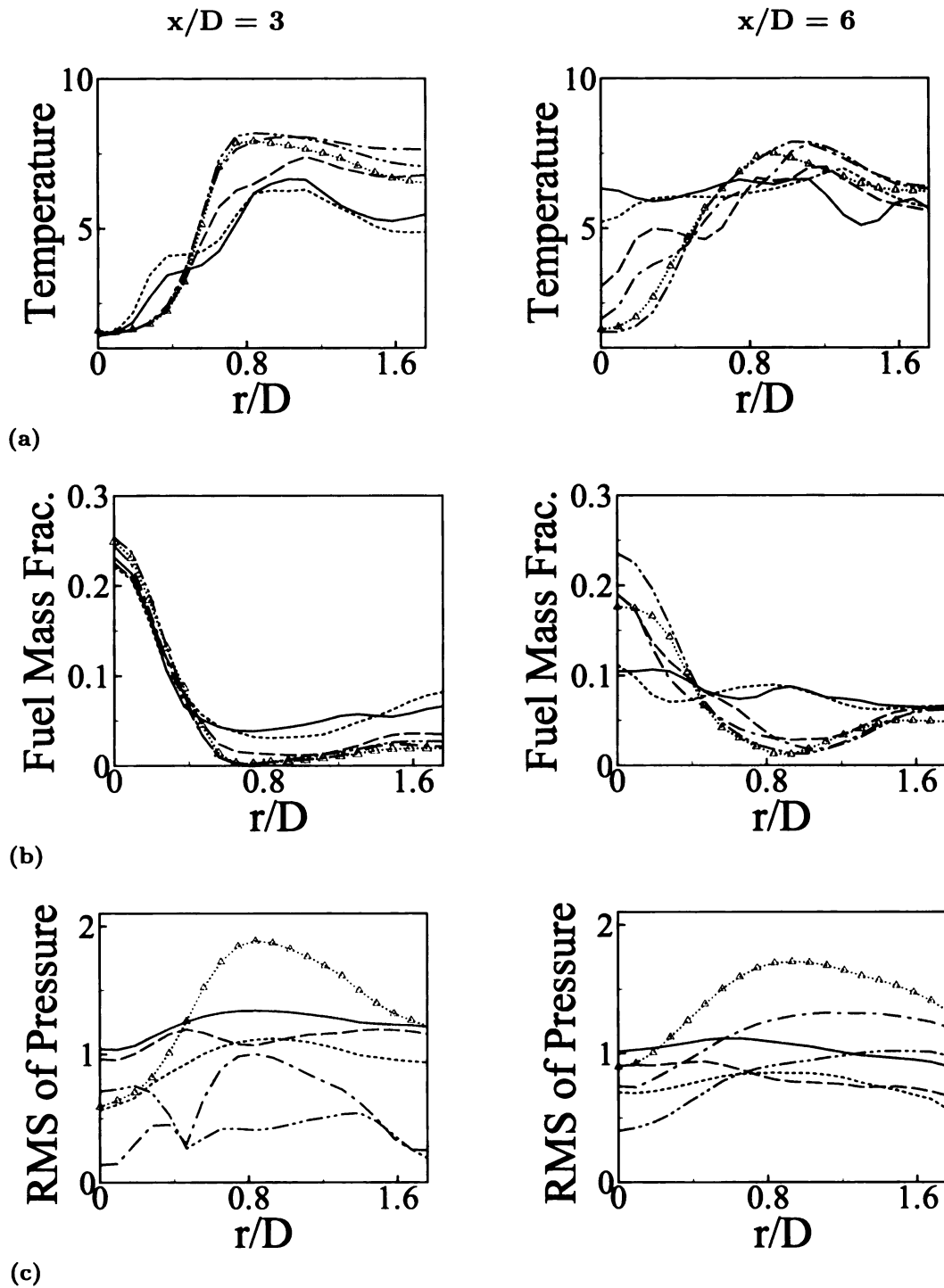
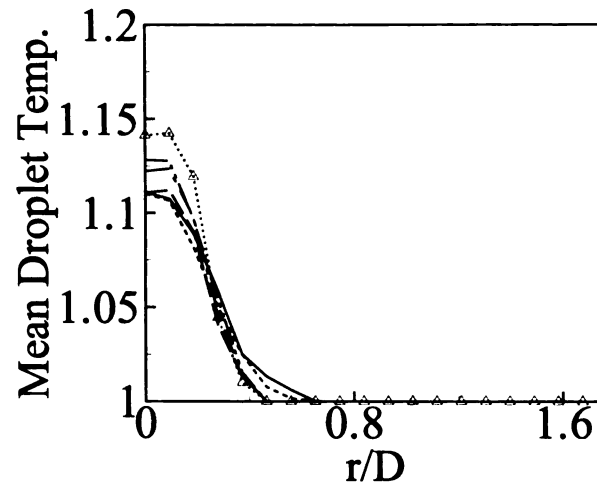


Figure 3.30: Iso-surfaces of the instantaneous vorticity field as obtained by LES/FDMF with various initial equivalence ratios; (a)  $\phi = 0.01$ , (b)  $\phi = 0.1$ , (c)  $\phi = 0.4$ , (d)  $\phi = 0.7$ , (e)  $\phi = 1.00$ , (f)  $\phi = 2.00$ .

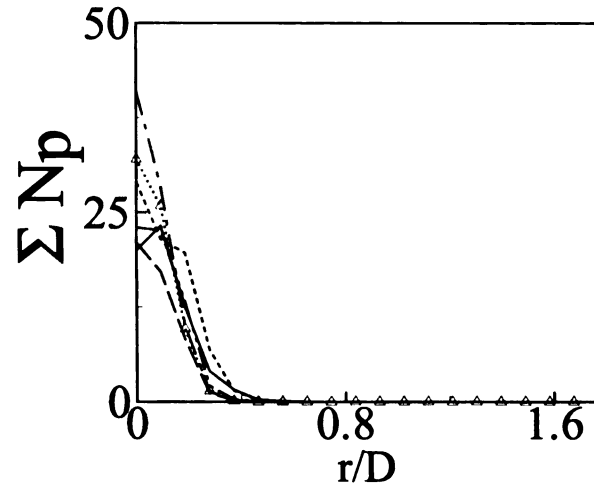


**Figure 3.31:** Radial variations of various quantities at axial locations of  $x/D = 3$  and  $x/D = 6$  with various initial equivalence ratios; (a) Instantaneous filtered temperature, (b) Instantaneous filtered fuel mass fraction, (c) Root mean square (RMS) of filtered pressure (solid line,  $\phi = 0.01$ ; dashed line,  $\phi = 0.1$ ; long-dashed line,  $\phi = 0.4$ ; dashed-dot line,  $\phi = 0.7$ ; dashed-dot-dot line,  $\phi = 0.1$ ; dotted-delta line  $\phi = 0.2$ ).

$$x/D = 3$$



(a)



(b)

**Figure 3.32: Radial variations of various droplet quantities at axial location of  $x/D = 3$  with various initial equivalence ratios; (a) Mean droplet temperature, (b) Total droplet number (solid line,  $\phi = 0.01$ ; dashed line,  $\phi = 0.1$ ; long-dashed line,  $\phi = 0.4$ ; dashed-dot line,  $\phi = 0.7$ ; dashed-dot-dot line,  $\phi = 0.1$ ; dotted-delta line  $\phi = 0.2$ ).**

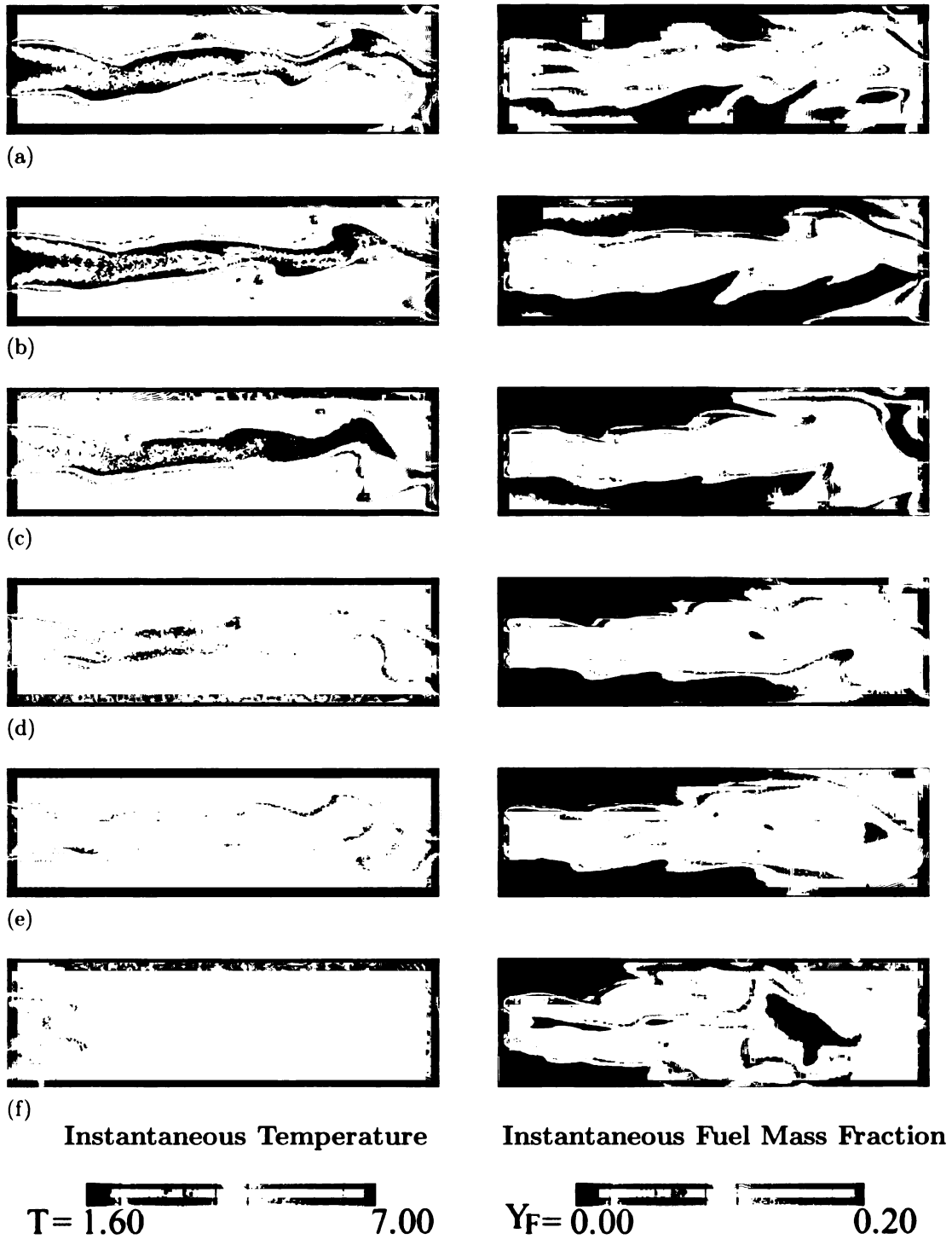


**Figure 3.33:** Iso-contours of the instantaneous of filtered temperature and fuel mass fraction as obtained by LES/FDMF with various inlet temperatures; (a)  $T_{in} = 375^\circ K$ , (b)  $T_{in} = 475^\circ K$ , (c)  $T_{in} = 575^\circ K$ , (d)  $T_{in} = 675^\circ K$ , (e)  $T_{in} = 775^\circ K$ , (f)  $T_{in} = 1100^\circ K$ .

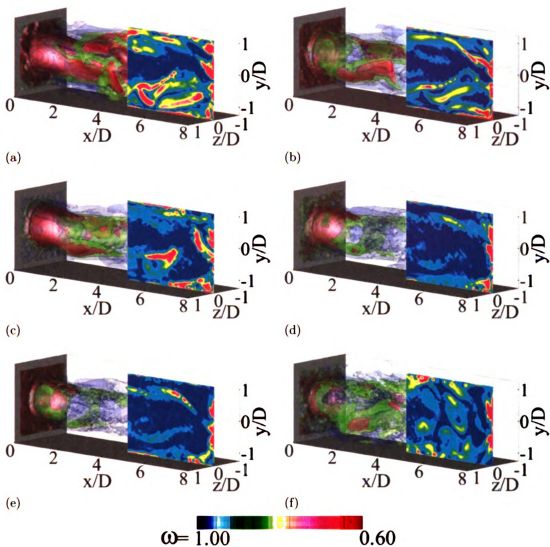


Figure 3.34: Iso-surfaces of the instantaneous vorticity field as obtained by LES/FDMF with various inlet temperatures; (a)  $T_{in} = 375^\circ K$ , (b)  $T_{in} = 475^\circ K$ , (c)  $T_{in} = 575^\circ K$ , (d)  $T_{in} = 675^\circ K$ , (e)  $T_{in} = 775^\circ K$ , (f)  $T_{in} = 1100^\circ K$ .

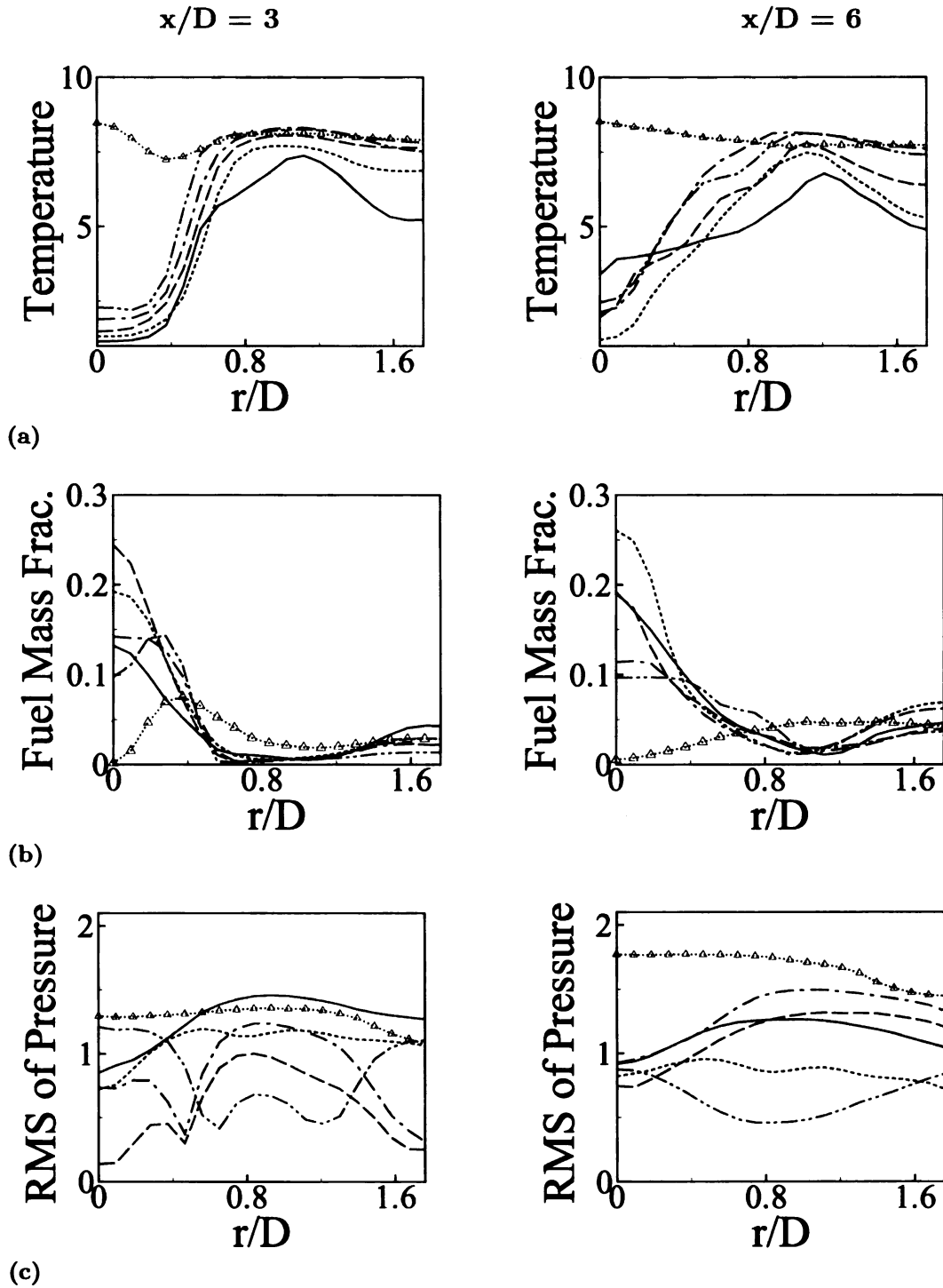


Figure 3.35: Radial variations of various quantities at axial locations of  $x/D = 3$  and  $x/D = 6$  with various inlet temperatures; (a) Instantaneous filtered temperature, (b) Instantaneous filtered fuel mass fraction, (c) Root mean square (RMS) of filtered pressure (solid line,  $T_{in} = 375^\circ K$ ; dashed line,  $T_{in} = 475^\circ K$ ; long-dashed line,  $T_{in} = 575^\circ K$ ; dashed-dot line,  $T_{in} = 675^\circ K$ ; dashed-dot-dot line,  $T_{in} = 775^\circ K$ ; dotted-delta line  $T_{in} = 1100^\circ K$ ).

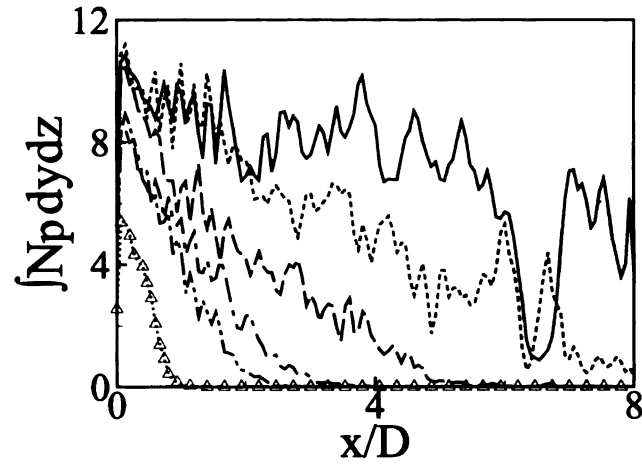
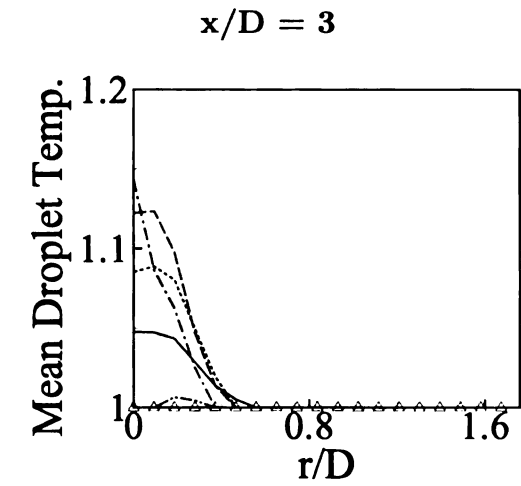
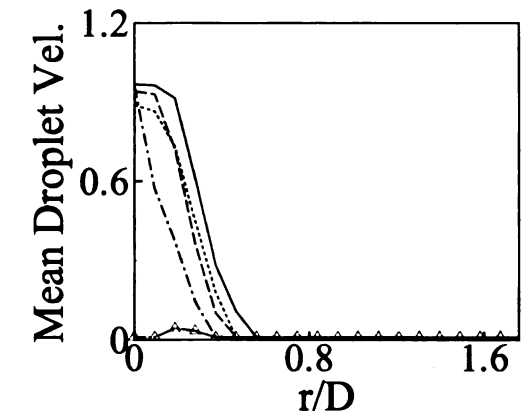


Figure 3.36: Axial variations of integrated droplet number density with various inlet temperature (solid line,  $T_{in} = 375^{\circ}K$ ; dashed line,  $T_{in} = 475^{\circ}K$ ; long-dashed line,  $T_{in} = 575^{\circ}K$ ; dashed-dot line,  $T_{in} = 675^{\circ}K$ ; dashed-dot-dot line,  $T_{in} = 775^{\circ}K$ ; dotted-delta line  $T_{in} = 1100^{\circ}K$ ).



(a)



(b)

**Figure 3.37: Radial variations of various droplet quantities at axial location of  $x/D = 3$  with various initial carrier gas temperatures; (a) Mean droplet temperature, (b) Mean droplet axial velocity (solid line,  $T_{in} = 375^{\circ}K$ ; dashed line,  $T_{in} = 475^{\circ}K$ ; long-dashed line,  $T_{in} = 575^{\circ}K$ ; dashed-dot line,  $T_{in} = 675^{\circ}K$ ; dashed-dot-dot line,  $T_{in} = 775^{\circ}K$ ; dotted-delta line  $T_{in} = 1100^{\circ}K$ ).**

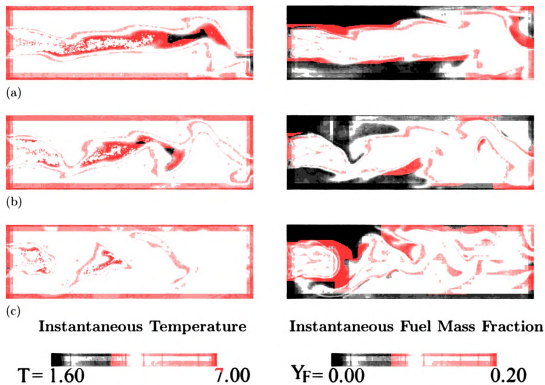


Figure 3.38: Iso-contours of the instantaneous of filtered temperature and fuel mass fraction as obtained by LES/FDMF with various turbulence forcing amplitudes; (a)  $\sigma_{ref}$ , (b)  $2 \times \sigma_{ref}$ , (c)  $4 \times \sigma_{ref}$ .

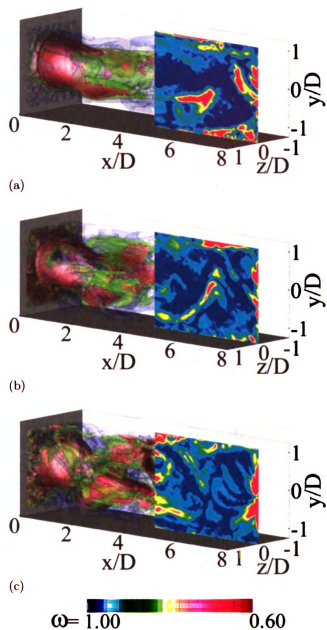


Figure 3.39: Iso-surfaces of the instantaneous vorticity field as obtained by LES/FDMF with various turbulence forcing amplitudes; (a)  $\sigma_{ref}$ , (b)  $2 \times \sigma_{ref}$ , (c)  $4 \times \sigma_{ref}$ .

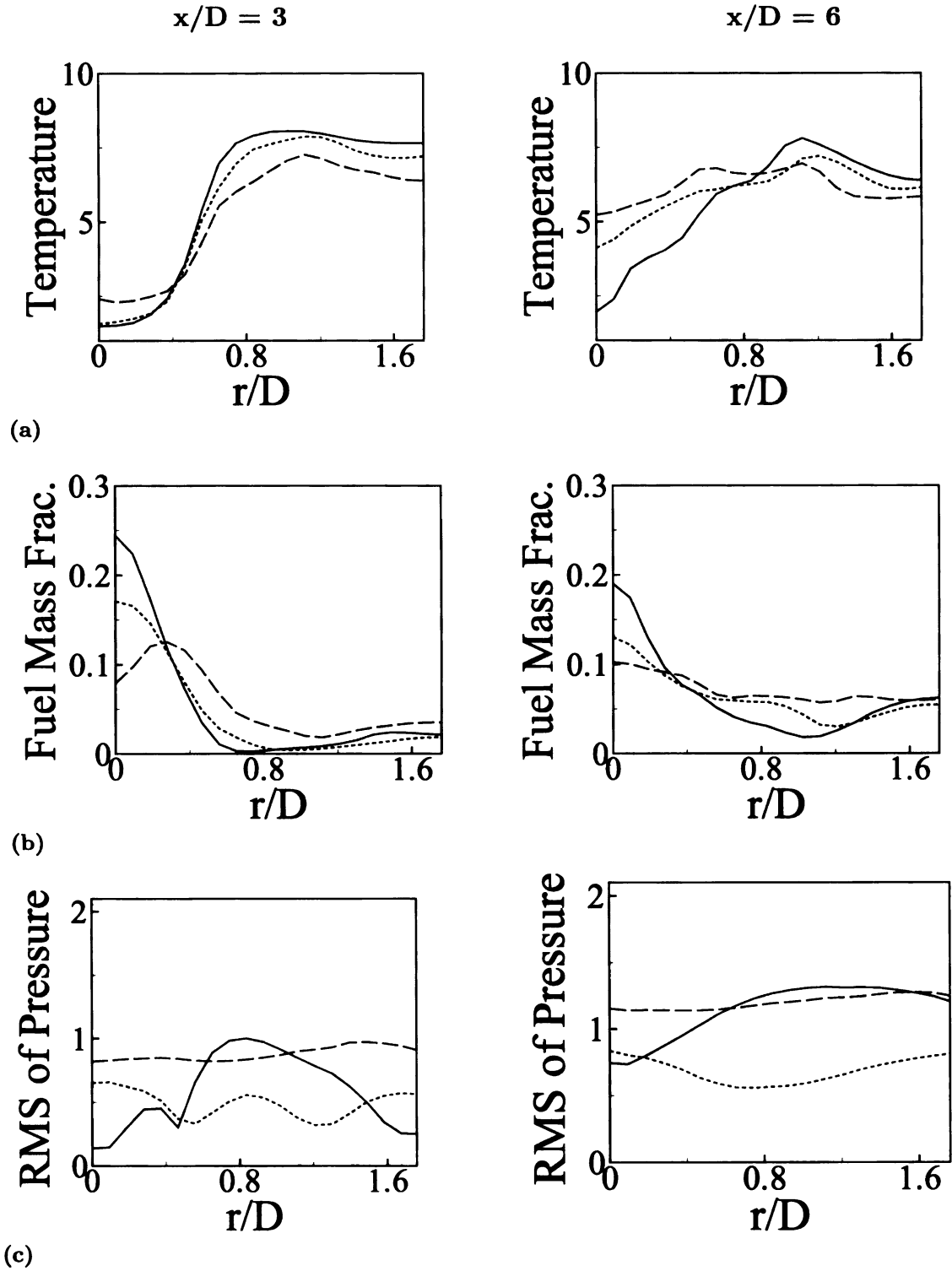


Figure 3.40: Radial variations of various quantities at axial locations of  $x/D = 3$  and  $x/D = 6$  with various turbulence forcing amplitudes; (a) Instantaneous filtered temperature, (b) Instantaneous filtered fuel mass fraction, (c) Root mean square (RMS) of filtered pressure (solid line,  $\sigma_{ref}$ ; dashed line,  $2 \times \sigma_{ref}$ ; long-dashed line,  $4 \times \sigma_{ref}$ ).

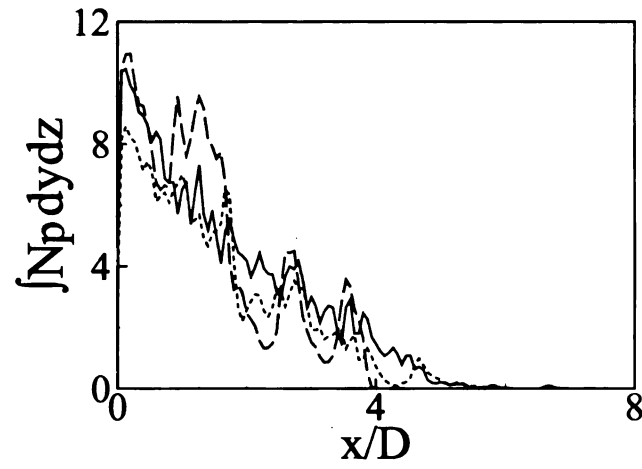
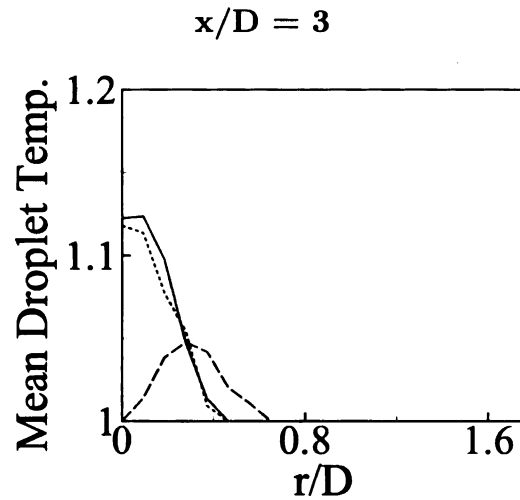
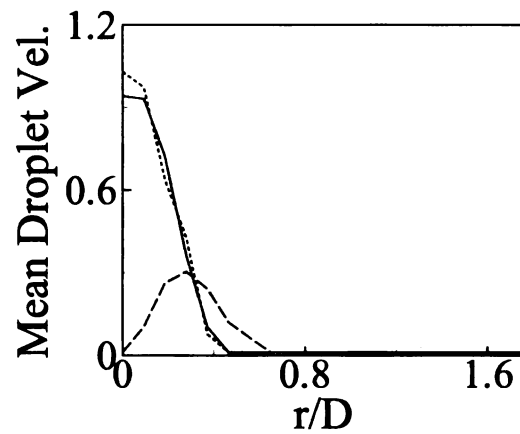


Figure 3.41: Axial variations of integrated droplet number density with various turbulence forcing amplitudes (solid line,  $\sigma_{ref}$ ; dashed line,  $2 \times \sigma_{ref}$ ; long-dashed line,  $4 \times \sigma_{ref}$ ).



(a)



(b)

**Figure 3.42:** Radial variations of various droplet quantities at axial location of  $x/D = 3$  with various turbulence forcing amplitudes; (a) Mean droplet temperature, (b) Mean droplet axial velocity (solid line,  $\sigma_{ref}$ ; dashed line,  $2 \times \sigma_{ref}$ ; long-dashed line,  $4 \times \sigma_{ref}$ ).

### 3.7 Nomenclature

$c_p$	: Specific heat of the mixture at constant pressure
$C_\Omega$	: Constant of the stochastic mixing closure
$C_R$	: Constant in the subgrid scalar stress
$C_I$	: Constant in the subgrid scalar stress
$D$	: Molecular diffusion coefficient
$D_t$	: Subgrid diffusion coefficient
$\mathcal{D}_i$	: Drift coefficient in the SDE
$\mathcal{E}$	: Diffusion coefficient in the SDE
$F_L$	: Joint scalars filtered mass density function
$H$	: Filter function
$\mathcal{H}$	: Filter function
$h$	: Enthalpy
$h_\alpha$	: Enthalpy of species $\alpha$
$h_\alpha^0$	: Enthalpy of formation of species $\alpha$
$J_i^\alpha$	: $i$ th component of the flux of scalar $\alpha$
$k$	: Thermal conductivity of the mixture
$Le$	: Molecular Lewis number
$M_i^\alpha$	: $i$ th component of the subgrid scalar flux of species $\alpha$
$N_s$	: Number of species
$Pr$	: Molecular Prandtl number
$R^0$	: Universal gas constant
$Re$	: Reynolds number
$Sc_t$	: SGS Schmidt number
$S_\alpha$	: Production rate of species $\alpha$
$S_{ij}$	: Strain rate tensor
$T$	: Temperature
$T_0$	: Reference temperature
$\mathcal{T}_{ij}$	: Subgrid scale stresses
$t$	: Time
$u_i$	: $i$ th component of the velocity vector
$\mathcal{U}_i$	: $i$ th component of the reference velocity in MKEV closure
$W_\alpha$	: Molecular weight of species $\alpha$
$\mathcal{W}_i$	: Wiener-Levy process
$\mathbf{x}$	: Position vector
$x_i$	: $i$ th component of the position vector
$X_i$	: Lagrangian position of the particles
$x$	: Streamwise coordinate
$Y_\alpha$	: Mass fractions of species $\alpha$
$y, z$	: Coordinates defining the plane normal to $x$
$Z$	: Mixture fraction

### Greek Symbols:

- $\nabla$  : Gradient operator
- $\Delta$  : Grid spacing in LES
- $\delta$  : Dirac delta function
- $\delta_{ij}$  : Kronecker delta
- $\Delta_E$  : Ensemble domain width
- $\Delta_H$  : Grid level filter width
- $\Delta_{H'}$  : Secondary level filter width
- $\mu$  : Molecular viscosity,  $\mu = \rho\nu$
- $\nu_t$  : Subgrid viscosity
- $\Omega_m$  : SGS mixing frequency
- $\psi$  : Composition space
- $\phi$  : Scalar field
- $\phi_\alpha$  : The compositional values of scalar  $\alpha$
- $\phi_\alpha^+$  : The compositional values of stochastic scalar  $\alpha$
- $\rho$  : Density
- $\sigma$  : Number of scalars,  $\sigma = N_s + 1$
- $\tau_{ij}$  : Molecular stresses
- $\tau_\phi$  : Scalar mixing timescale

### Symbols

- $\langle \rangle_\ell$  : Filtered value
- $\langle \rangle_L$  : Favre filtered value
- $\langle | \rangle_L$  : Conditional Favre filtered value
- $\hat{\phantom{x}}$  : Quantities which depend only on the scalar composition,  
*i.e.*  $\hat{S}(\phi, \mathbf{x}, t) \equiv S(\phi(\mathbf{x}, t))$
- $\infty$  : Ambient

### Subscripts

- $k$  : Dummy index

### Superscripts

- $+$  : Properties of the stochastic Monte Carlo particles
- $(n)$  : Index of the Monte Carlo particles

## References

- [1] Pang, B., Active Suppression of Vortex-Driven Combustion Instability Using Controlled Liquid-Fuel Injection., PhD Thesis, University of Maryland, College Park, MD, 2005.
- [2] Klimenko, A. Y. and Bilger, R. W., Conditional Moment Closure for Turbulent Combustion, *Prog. Energy Combust. Sci.*, **25**(6):595–687 (1999).
- [3] Peters, N., Laminar Diffusion Flamelet Models In Non-Premixed Turbulent Combustion, *Prog. Energy Combust. Sci.*, **10**:319–339 (1984).
- [4] Poinso, T. and Veynante, D., editors, *Theoretical and Numerical Combustion*, R.T. Edwards Inc., Philadelphia, PA, 2001.
- [5] Pope, S. B., PDF Methods for Turbulent Reacting Flows, *Prog. Energy Combust. Sci.*, **11**:119–192 (1985).
- [6] Pope, S. B., Turbulent Premixed Flames, *Ann. Rev. Fluid Mech.*, **19**:237–270 (1987).
- [7] Williams, F. A., Progress in Knowledge of Flamelet Structure And Extinction Combustion, *Prog. Energy Combust. Sci.*, **26**:657–682 (2000).
- [8] Givi, P., Filtered Density Function for Subgrid Scale Modeling of Turbulent Combustion, *AIAA Journal*, **44**(1):16–23 (2006).
- [9] Baum, M., Poinso, T., Haworth, D. C., and Darabiha, N., Direct Numerical Simulation of  $h_2/o_2/n_2$  Flames With Complex Chemistry in Two-Dimensional Turbulent Flows, *J. Fluid Mech.*, **281**:1–32 (1994).
- [10] Haworth, D. C., A Probability Density Function/Flamelet Method for Partially Premixed Turbulent Combustion, *Proceedings of the Summer Program 2000, Center for Turbulence Research*, pp. 145–156 (2000).
- [11] Poinso, T., Candel, S., Trouve, A., and Ruetsch, G., Turbulent Flame Propagation in Partially Premixed Flames, *Proceedings of the Summer Program 1996, Center for Turbulence Research*, pp. 111–141 (1996).
- [12] Poinso, T., Candel, S., and Trouve, A., Applications of Direct Numerical Simulations to Premixed Turbulent Combustion, *Prog. Energy Combust. Sci.*, **21**:531–576 (1995).
- [13] Peters, N., *Turbulent Combustion*, Cambridge University Pres., Cambridge, UK, 2000.
- [14] Moin, P. and Mahesh, K., Direct Numerical Simulation: A Tool in Turbulence Research, *Ann. Rev. Fluid Mech.*, **30**:539–578 (1998).

- [15] Vervisch, L. and Poinso, T., Direct Numerical Simulation of Non-Premixed Turbulent Flames, *Annu. Rev. Fluid Mech.*, pp. 655–691 (1998).
- [16] Veynante, D. and Vervisch, L., Turbulent Combustion Modelling, *Prog. Energy Combust. Sci.*, **28**:193–266 (2002).
- [17] Jaber, F. A., Mashayek, F., Madnia, C. K., Taulbee, D. B., and Givi, P., *Advances in Analytical Description of Turbulent Reacting Flows*, chapter 9, pp. 149–64, CRC Press LLC, Boca Raton, FL, 2002.
- [18] Givi, P., Model Free Simulations of Turbulent Reactive Flows, *Prog. Energy Combust. Sci.*, **15**:1–107 (1989).
- [19] Poinso, T., Veynante, D., and Candel, S., Diagrams of Premixed Turbulent Combustion Based on Direct Simulation, *Proc. Combust. Inst.*, **23**:613–619 (1990).
- [20] Maas, U. and Thévenin, D., Correlation Analysis of Direct Numerical Simulation Data of Turbulent Non-Premixed Flames, *Proc. Combust. Inst.*, **27**:1183–1189 (1998).
- [21] Hilbert, R., Tap, F., El-Rabii, H., and Thévenin, D., Impact of Detailed Chemistry And Transport Models on Turbulent Combustion Simulations, *Combust. Flame*, **121**:395–417 (2000).
- [22] Haworth, D., Blint, R., Cuenot, B., and Poinso, T., Numerical Simulation of turbulent propane-air combustion with nonhomogeneous reactants, *Combustion and Flame*, (2000).
- [23] Haworth, D. and Poinso, T., Numerical simulations of Lewis number effects in turbulent premixed flames, *J. Fluid Mech.*, **244**:405–436 (1992).
- [24] Bell, J. B., Day, M. S., and Grcar, J. F., Numerical Simulation of Premixed Turbulent Methane Combustion, *Report No. LBNL-49331, Lawrence Berkeley National Laboratory*, (2001).
- [25] Angoshtari, N., Direct Numerical Simulation of Premixed Turbulent Methane Flames Modeled with Various Reduced Mechanisms, Master’s thesis, Michigan State University, East Lansing, MI, 2003.
- [26] Im, H. G., Chen, J. H., and Chen, J. Y., Chemical Response of Methane/Air Diffusion Flames to Unsteady Strain Rate, *Combust. Flame*, **118**:204–212 (1999).
- [27] Im, H. G. and Chen, J. H., Structure And Propagation of Triple Flames in Partially Premixed Hydrogen-Air Mixtures, *Combust. Flame*, **119**:436–454 (1996).

- [28] Im, H. G. and Chen, J. H., Effects of Strain on Triple Flame Propagation, *Combust. Flame*, **126**:1384–1392 (2001).
- [29] Jaberri, F. A. and Madnia, C. K., Effects of Heat of Reaction on Homogeneous Compressible Turbulence, *J. Sci. Comp.*, **13**(2) (1998).
- [30] Jaberri, F. A., Livescu, D., and Madnia, C. K., Characteristics of Chemically Reacting Compressible Homogeneous Turbulence, *Physics of Fluids*, **12**(5):1189–1209 (2000).
- [31] Livescu, D., Jaberri, F. A., and Madnia, C. K., Effects of Heat Release on The Energy Exchange in Reacting Turbulent Shear Flow, *J. Fluid Mech.*, **450**:35–66 (2002).
- [32] Mohammad, H., Numerical Simulation of Partial Premixed Methane Combustion in Laminar and Turbulent Flows, *Masters Thesis, MSU*, (2004).
- [33] Kennedy, C. A. and Carpenter, M. H., Comparison of Several Numerical Methods for Simulation of Compressible Shear Layers, *Report No. 3484, NASA*, (1997).
- [34] Carpenter, M. H., *A High-order Compact Numerical Algorithm For Supersonic Flow*, pp. 254–258, Lecture Notes in Physics, Springer-Verlag, 1990.
- [35] Poinso, T. and Lele, S., Boundary Conditions for Direct Simulations of Compressible Viscous Flows, *J. Comput. Physics*, **101**(1):104–129 (1992).
- [36] Rudy, D. and Strikwerda, J., Boundary Conditions for Subsonic Compressible Navier-Stokes Calculations, *Comput. Fluids*, **9**:327–338 (1981).
- [37] Sripakagorn, P., Mitarai, S., Kosály, G., and Pitsch, H., Extinction And Reignition in A Diffusion Flame: A Direct Numerical Simulation Study, *J. Fluid Mech.*, **518**:231–239 (2004).
- [38] Taylor, G. I., Diffusion by Continuous Movements, *Proc. Lond. Math. Soc.*, **20**(1):196–211 (1921).
- [39] Mitarai, S., Kosly, G., and Riley, J. J., A New Lagrangian Flamelet Model for Local Flame Extinction And Reignition, *Combust. Flame*, **137**:306–319 (2004).
- [40] Williams, F. A., *Combustion Theory*, The Benjamin/Cummings Publishing Company, Inc., New York, 2 edition, 1985.
- [41] Kee, R. J., Rupley, F. M., and Miller, J. A., A Fortran Chemical Kinetics Package for The Analysis of Gas-Phase Chemical Kinetics, *Report No. SAND89-8009B, Sandia National Laboratories*, (1989).
- [42] Bird, R. B., Stewart, W. E., and Lightfoot, E. N., *Transport Phenomena*, Wiley, New York, 1960.

- [43] Kee, R. J., Dixon-Lewis, G., Warnatz, J., Coltrin, M. E., and Miller, J. A., A Fortran Computer Code Package for The Evaluation of Gas-Phase Multi-Component Transport Properties, *Report No. SAND86-8246, Sandia National Laboratories*, (1986).
- [44] Wilke, C. R., A Viscosity Equation for Gas Mixtures, *J. Chem. Phys.*, **18**(4):517–523 (1950).
- [45] Hirschfelder, J. O., Curtiss, C. F., and Bird, R. B., *Molecular Theory of Gases And Liquids*, Wiley, New York, 1954.
- [46] Chen, J. Y., Development of Reduced Mechanisms for Numerical Modeling of Turbulent Combustion, *Workshop on "Numerical Aspects of Reduction in Chemical Kinetics"*, (1997).
- [47] Chang, W. C. and Chen, J. Y., Reduced Mechanisms Based on Gri-Mech 1.2, <http://firebrand.me.berkeley.edu/griREDU.html>, (2008).
- [48] Bowman, C. T., Hanson, R. K., Davidson, D. F., Gardiner, W. C., Jr., V. L., Smith, G. P., Golden, D. M., Frenklach, M., and Goldenberg, M., GRI-Mech 2.11, <http://www.me.berkeley.edu/gri-mech>, (2008).
- [49] Bédard, B., Egolfopoulos, F. N., and Poinso, T., Direct Numerical Simulation of Heat Release And Nox Formation in Turbulent Nonpremixed Flames, *Combust. Flame*, **119**:69–83 (1999).
- [50] Rehm, J. E. and Clemens, N. T., The Relationship Between Vorticity/Strain And Reaction Zone Structure in Turbulent Non-Premixed Jet Flames, *Proc. Combust. Inst.*, **27**:1113–1120 (1998).
- [51] Miller, R. S., Passive Scalar, Magnetic Field, and Solid Particle Transport in Homogeneous Turbulence, Ph.D. Thesis, Department of Mechanical and Aerospace Engineering, State University of New York at Buffalo, Buffalo, NY, 1995.
- [52] Jaber, F. A., Miller, R. S., Mashayek, F., and Givi, P., Differential Diffusion in Binary Scalar Mixing and Reaction, *Combust. Flame*, **109**:561–577 (1997).
- [53] Mehravaran, K. and Jaber, F. A., Direct Numerical Simulation of Transitional And Turbulent Buoyant Planar Jet Flames, *Physics of Fluids*, **16**(12):4443–4461 (2004).
- [54] Barlow, R. S. and Frank, J. H., Effects of Turbulence on Species Mass Fractions in Methane/Air Jet Flames, *Proc. Combust. Inst.*, **27**:1087–1095 (1998).
- [55] XU, J. and Pope, S. B., PDF Calculations of Turbulent Nonpremixed Flames with Local Extinction, *Proc. Combust. Inst.*, **123**:281–307 (2000).

- [56] Cao, R. R. and Pope, S. B., The Influence of Chemical Mechanism on Pdf Calculations of Nonpremixed Piloted Jet Flames, *Combust. Flame*, **143**:450–470 (2005).
- [57] James, S. and Jaber, F. A., Large Scale Simulations of Two-Dimensional Nonpremixed Methane Jet Flames, *Combust. Flame*, **123**:465–487 (2000).
- [58] Masri, A., Bilger, R., and Dibble, R., Turbulent Nonpremixed Flames of Methane Near Extinction - Mean Structure from Raman Measurements, *Combustion and Flame*, **71**:245–266 (1988).
- [59] Masri, A., Bilger, R., and Dibble, R., Conditional-Probability Density-Functions Measured in Turbulent Nonpremixed Flames of Methane Near Extinction, *Combustion and Flame*, **74**:267–297 (1988).
- [60] Masri, A. R., Dibble, R. W., and Barlow, R. S., The Structure of Turbulent Nonpremixed Flames Revealed by Raman-Rayleigh-Rif Measurements, *Prog. Energy Comb. Sci.*, **22**:307–362 (1996).
- [61] Barlow, R. S. and Chen, J. Y., On Transient Flamelets And Their Relationship to Turbulent Methane Air Jet Flames, *Proc. Combust. Inst.*, **24**:231–237 (1992).
- [62] Barlow, R. S., Dibble, R. W., Starner, S. H., and Bilger, R. W., Piloted Diffusion Flames of Nitrogen-Diluted Methane near Extinction: OH Measurements, *Combust. Flame*, **23**:583–589 (1990).
- [63] Mahalingam, S., Chen, J. H., and Vervisch, L., Finite-Rate Chemistry and Transient Effects in Direct Numerical Simulations of Turbulent Nonpremixed Flames, *Combust. Flame*, **102**:285–297 (1995).
- [64] Barlow, R. and Frank, J., Effects of Turbulence on Species Mass Fractions in Methane/Air Jet Flames, *27th International symposium on combustion*, pp. 1087–1095 (1998).
- [65] Xu, J. and Pope, S., PDF Calculations of Turbulent Nonpremixed Flames with Local Extinction, *Combustion and Flame*, **123**:281–307 (2000).
- [66] Landefeld, T., Sadiki, A., and Janicka, J., A Turbulence-Chemistry Interaction Model Based on a Multivariate Presumed Beta-PDF method for Turbulent Flames, *Flow, Turbulence and Combustion*, **68**:111–135 (2002).
- [67] Pitsch, H. and Steiner, H., Large-eddy simulation of a turbulent piloted methane/air diffusion flame (Sandia Flame D), *Phys. Fluids*, **12**(10):2541–2554 (2000).
- [68] Roomina, M. and Bilger, R., Conditional moment closure (CMC) predictions of a turbulent methane-air jet flame, *Combustion and Flame*, **125**:1176–1195 (2001).

- [69] Jones, W. and Kakhi, M., PDF modeling of Finite-rate Chemistry Effects in Turbulent Nonpremixed Jet Flames, *Combustion and Flame*, **115**:210–229 (1998).
- [70] Muradoglu, M., Pope, S., and Caughey, D., The hybrid method for the PDF equations of Turbulent Reactive Flows: Consistency Conditions and Correction Algorithms, *Journal of Computational Physics*, **172**:841–878 (2001).
- [71] Maas, U. and Pope, S., Implementation of simplified chemical kinetics based on intrinsic low-dimensional manifolds, in *24th Symposium (Int.) on Combustion*, pp. 103–112, The Combustion Institute, Pittsburgh, PA, 1992.
- [72] Maas, U. and Pope, S., Simplifying chemical kinetics: Intrinsic low-dimensional manifolds in composition space, *Combustion and Flame*, **88**:239–264 (1992).
- [73] Sung, C., Law, C., and Chen, J., An Augmented Reduced Mechanism for Methane Oxidation with comprehensive Global Parametric Validation, *27th Symposium on Combustion/ The Combustion Institute*, pp. 295–304 (1998).
- [74] Sung, C., Law, C., and Chen, J., Further Validation of an Augmented Reduced Mechanism for Methane Oxidation : Comparison of Global Parameters and Detailed Structure, *Combust. Sci. and Tech.*, **156**:201–220 (2000).
- [75] Pope, S., Computationally efficient implementation of combustion chemistry using in situ adaptive tabulation, *Combustion theory and modeling*, **1**:41–63 (1997).
- [76] Subramaniam, S. and Pope, S., A mixing model for turbulent reactive flows based on Euclidean minimum spanning trees, *Combustion and Flame*, **115**:487–514 (1998).
- [77] Vervisch, L., Hauguel, R., Domingo, P., and Rullaud, M., Three facets of turbulent combustion modelling: DNS of premixed V-flame, LES of lifted non-premixed flame and RANS of jet-flame, *J. Turbulence*, **5**(4):2191–2198 (2004).
- [78] Pope, S. B., Computations of Turbulent Combustion: Progress and Challenges, in *Proceedings of 23rd Symp. (Int.) on Combustion*, pp. 591–612, The Combustion Institute, Pittsburgh, PA, 1990.
- [79] Pope, S. B., *Turbulent Flows*, Cambridge University Press, Cambridge, UK, 2000.
- [80] Peters, N., editor, *Turbulent Combustion*, Cambridge University Press, Cambridge, U.K., 2000.
- [81] Bilger, R. W., Future Progress in Turbulent Combustion Research, *Prog. Energy Combust. Sci.*, **26**:367–380 (2000).

- [82] Gao, F. and O'Brien, E. E., A Large Eddy Scheme for Turbulent Reacting Flows, *Phys. Fluids A*, **5**(6):1282–1284 (1993).
- [83] Réveillon, J. and Vervisch, L., Subgrid-Scale Turbulent Micromixing: Dynamic Approach, *AIAA J.*, **36**(3):336–341 (1998).
- [84] Colucci, P. J., Jaber, F. A., Givi, P., and Pope, S. B., Filtered Density Function For Large Eddy Simulation of Turbulent Reacting Flows, *Phys. Fluids*, **10**(2):499–515 (1998).
- [85] Garrick, S. C., Jaber, F. A., and Givi, P., Large Eddy Simulation of Scalar Transport in a Turbulent Jet Flow, in Knight, D. and Sakell, L., editors, *Recent Advances in DNS and LES, Fluid Mechanics and its Applications*, Vol. 54, pp. 155–166, Kluwer Academic Publishers, The Netherlands, 1999.
- [86] Jaber, F. A., Colucci, P. J., James, S., Givi, P., and Pope, S. B., Filtered Mass Density Function For Large Eddy Simulation of Turbulent Reacting Flows, *J. Fluid Mech.*, **401**:85–121 (1999).
- [87] Jaber, F. A., Large Eddy Simulation of Turbulent Premixed Flames via Filtered Mass Density Function, AIAA Paper 99-0199, AIAA, 1999.
- [88] James, S. and Jaber, F. A., Large Scale Simulations of Two-Dimensional Nonpremixed Methane Jet Flames, *Combust. Flame*, **123**:465–487 (2000).
- [89] Raman, V. and Pitsch, H., LES/Filtered-Density Function simulation of turbulent combustion with detailed chemistry, *CTR Annual Research Brief*, pp. 297–309 (2005).
- [90] Raman, V. and Pitsch, H., A consistent LES/filtered-density function formulation for the simulation of turbulent flames with detailed chemistry, *Proc. of the Comb. Inst.*, **31**:1711–1719 (2007).
- [91] Gicquel, L. Y. M., Givi, P., Jaber, F. A., and Pope, S. B., Velocity Filtered Density Function for Large Eddy Simulation of Turbulent Flows, *Phys. Fluids*, **14**:1196–1213 (2002).
- [92] Sheikhi, M. R. H., Drozda, T. G., Givi, P., and Pope, S. B., Velocity-scalar filtered density function for large eddy simulation of turbulent flows, *Phys. Fluids*, **15**(8):2321–2337 (2003).
- [93] Tong, C., Measurements of Conserved Scalar Filtered Density Function in a Turbulent Jet, *Phys. Fluids*, **13**(10):2923–2937 (2001).
- [94] Aldama, A. A., *Filtering Techniques for Turbulent Flow Simulations, Lecture Notes in Engineering*, Vol. 49, Springer-Verlag, New York, NY, 1990.
- [95] Williams, F. A., *Combustion Theory*, The Benjamin/Cummings Publishing Company, Menlo Park, CA, 2nd edition, 1985.

- [96] Rogallo, R. S. and Moin, P., Numerical Simulation of Turbulent Flow, *Ann. Rev. Fluid Mech.*, **16**:99–137 (1984).
- [97] Jaber, F., Colucci, P., James, S., Givi, P., and Pope, S., Filtered Mass density function for large-eddy simulation of turbulent reacting flows, *J. Fluid Mech.*, **401**:85–121 (1999).
- [98] Smagorinsky, J., General Circulation Experiments With the Primitive Equations. I. The Basic Experiment, *Monthly Weather Review*, **91**(3):99–164 (1963).
- [99] Lilly, D. K., On the Computational Stability of Numerical Solutions of Time-Dependent Non-Linear Geophysical Fluid Dynamics Problems, *Monthly Weather Review*, **93**(1):11–26 (1965).
- [100] Lilly, D. K., The Representation of Small-Scale Turbulence in Numerical Simulation Experiments, in *Proceedings of IBM Scientific Computing Symposium Environmental Sciences*, pp. 195–210, IBM Form No. 320-1951, 1967.
- [101] Germano, M., Piomelli, U., Moin, P., and Cabot, W. H., A Dynamic Subgrid-Scale Eddy Viscosity Model, *Phys. Fluids A*, **3**(7):1760–1765 (1991).
- [102] Germano, M., Turbulence: The Filtering Approach, *J. Fluid Mech.*, **238**:325–336 (1992).
- [103] Eidson, T. M., Numerical Simulation of the Turbulent Rayleigh-Benard Problem Using Subgrid Modelling, *J. Fluid Mech.*, **158**:245–268 (1985).
- [104] Moin, P., Squires, W., Cabot, W. H., and Lee, S., A Dynamic Subgrid-Scale Model for Compressible Turbulence and Scalar Transport, *Phys. Fluids A*, **3**(11):2746–2757 (1991).
- [105] Lesieur, M. and Metais, O., New Trends in Large Eddy Simulations of Turbulence, *Ann. Rev. Fluid Mech.*, **28**:45–82 (1996).
- [106] O’Brien, E. E., The Probability Density Function (PDF) Approach to Reacting Turbulent Flows, in Libby, P. A. and Williams, F. A., editors, *Turbulent Reacting Flows*, chapter 5, pp. 185–218, Springer-Verlag, Heidelberg, 1980.
- [107] Vreman, B., Geurts, B., and Kuerten, H., Realizability Conditions for the Turbulent Stress Tensor in Large-Eddy Simulation, *J. Fluid Mech.*, **278**:351–362 (1994).
- [108] Pope, S. B., An Improved Turbulent Mixing Model, *Combust. Sci. and Tech.*, **28**:131–145 (1982).
- [109] Miller, R. S., Frankel, S. H., Madnia, C. K., and Givi, P., Johnson-Edgeworth Translation for Probability Modeling of Binary Mixing in Turbulent Flows, *Combust. Sci. and Tech.*, **91**(1-3):21–52 (1993).

- [110] Jaberri, F. A. and Givi, P., Inter-Layer Diffusion Model of Scalar Mixing in Homogeneous Turbulence, *Combust. Sci. and Tech.*, **104**(4-6):249 (1995).
- [111] Borghi, R., Turbulent Combustion Modeling, *Prog. Energy Combust. Sci.*, **14**:245–292 (1988).
- [112] Sheikhi, M., Drozda, T., Givi, P., Jaberri, F., and Pope, S., Large eddy simulation of a turbulent nonpremixed piloted methane jet flame (Sandia Flame D, *Proc. of the Comb. Inst.*, **30**:549–556 (2005).
- [113] Cao, R. and Pope, S., The influence of chemical mechanisms on PDF Calculations of Nonpremixed Piloted Jet Flames, *Combustion and Flame*, **143**:450–470 (2005).
- [114] James, S., Zhu, J., and Anand, M., Large eddy simulations of turbulent flames using the filtered density function model, *Proc. of the Comb. Inst.*, **31**:1737–1745 (2007).
- [115] Lindstedt, R., Louloudi, S., and Váos, E., Joint scalar probability density function modeling of pollutant formation in piloted turbulent jet diffusion flames with comprehensive chemistry, *Proc. of the Comb. Inst.*, **28**:149–156 (2000).
- [116] Lindstedt, R. and Louloudi, S., Joint scalar transported probability density function modeling of turbulent methanol jet diffusion flames, *Proc. of the Comb. Inst.*, **29**:2147–2154 (2002).
- [117] Bisetti, F. and Chen, J. Y., LES of Sandia Flame D with Eulerian PDF and Finite-Rate Chemistry, Stanford, CA, 2005, Fall Meeting Western States Combustion Institute.
- [118] Raman, V., Fox, R., and Harvey, A., Hybrid finite-volume/transported PDF simulations of a partially premixed methane-air flame, *Combustion and Flame*, **136**:327–350 (2004).
- [119] Cha, C. M. and Trouillet, P., A subgrid-scale mixing model for large-eddy simulations of turbulent reacting flows using the filtered density function, *Phys. fluids*, **15**(6):1496–1504 (2003).
- [120] Pierce, C. and Moin, P., A dynamic model for subgrid-scale variance and dissipation rate of a conserved scalar, *Physics of Fluids*, **10**(12):3041–3044 (1998).
- [121] Fox, R. and Yeung, P., Improved lagrangian mixing models for passive scalars in isotropic turbulence, *Physics of Fluids*, **15**(4):961–985 (2003).
- [122] Madnia, C. K., Frankel, S. H., and Givi, P., Reactant Conversion in Homogeneous Turbulence: Mathematical Modeling, Computational Validations and Practical Applications, *Theoret. Comput. Fluid Dynamics*, **4**:79–93 (1992).

- [123] Kosály, G. and Givi, P., Modeling of Turbulent Molecular Mixing, *Combust. Flame*, **70**:101–118 (1987).
- [124] McMurtry, P. A. and Givi, P., Direct Numerical Simulations of Mixing and Reaction in a Nonpremixed Homogeneous Turbulent Flow, *Combust. Flame*, **77**:171–185 (1989).
- [125] Fox, R. O., Computational Methods For Turbulent Reacting Flows in Chemical Process Industry, *Revue De L'Institut Francais Du Petrole*, **51**(2):215–246 (1996).
- [126] Subramaniam, S. and Pope, S. B., A Mixing Model for Turbulent Reactive Flows Based on Euclidean Minimum Spanning Trees, *Combustion and Flame*, **115**:487–514 (1998).
- [127] Subramaniam, S. and Pope, S. B., Comparison of Mixing Model Performance for Nonpremixed Turbulent Reactive Flow, *Combust. Flame*, **117**:732–754 (1999).
- [128] Carpenter, M. H., A High-Order Compact Numerical Algorithm for Supersonic Flows, in Mortron, K. W., editor, *Proc. 12th International Conference on Numerical Methods in Fluid Dynamics, Lecture Notes in Physics*, Vol. 371, pp. 254–258, Springer-Verlag, 1990.
- [129] Solomon, T. H. and Gollub, J. P., Thermal Boundary Layers and Heat Flux in Turbulent Convection: The Role of Recirculating Flows, *Phys. Rev. A*, **43**(12):6683–6693 (1991).
- [130] Kee, R. J., Rupley, F. M., and Miller, J. A., The Chemkin Thermodynamic Database, Technical Report SAND87-8215B, Sandia National Laboratory, Livermore, CA, 1994.
- [131] Pope, S. B., Lagrangian PDF Methods for Turbulent Flows, *Ann. Rev. Fluid Mech.*, **26**:23–63 (1994).
- [132] Muradoglu, M., Jenny, P., Pope, S. B., , and Caughey, D. A., A Consistent Hybrid-Volume/Particle Method for the PDF Equations of Turbulent Reactive Flows, *J. Comp. Phys.*, **154**(2):342–371 (1999).
- [133] Xu, J. and Pope, S. B., Assessment of Numerical Accuracy of PDF/Monte Carlo Methods for Turbulent Reacting Flows, *J. Comp. Phys.*, **152**:192–230 (1999).
- [134] McDermott, R. and Pope, S., A particle formulation for treating differential diffusion in filtered density function methods, *Journal of Computational Physics*, **226**:947–993 (2007).
- [135] Risken, H., *The Fokker-Planck Equation, Methods of Solution and Applications*, Springer-Verlag, New York, NY, 1989.

- [136] Gardiner, C. W., *Handbook of Stochastic Methods*, Springer-Verlag, New York, NY, 1990.
- [137] Karlin, S. and Taylor, H. M., *A Second Course in Stochastic Processes*, Academic Press, New York, NY, 1981.
- [138] Gillespie, D. T., *Markov Processes, An Introduction for Physical Scientists*, Academic Press, New York, NY, 1992.
- [139] Kloeden, P. E. and Platen, E., *Numerical Solution of Stochastic Differential Equations, Applications of Mathematics, Stochastic Modelling and Applied Probability*, Vol. 23, Springer-Verlag, New York, NY, 1995.
- [140] Bui-Pham, M., Studies in Structures of Laminar Hydrocarbon Flames, *Ph.D Thesis, UCSD*, (1992).
- [141] Sung, C. J., Law, C. K., and Chen, J.-Y., An Augmented Reduced Mechanism For Methane Oxidation with Comprehensive Global Parametric Validation, in *Proceedings of 27th Symp. (Int.) on Combustion*, pp. 295–303, The Combustion Institute, Pittsburgh, PA, 1998.
- [142] Barlow, R., Sandia/TUD Piloted  $CH_4$ /Air Jet Flames, <http://www.ca.sandia.gov/TNF/DataArch/FlameD.html>, (2007).
- [143] Schneider, C., Dreizler, A., and Janicka, J., Flow field measurements of stable and locally extinguishing hydrocarbon-fuelled jet flames, *Combustion and Flame*, **135**:185–190 (2003).
- [144] Poinso, T. and Lele, S., Boundary Conditions for Direct Simulations of Compressible Viscous Flows, *J. Comp. Phys.*, **101**:104–129 (1992).
- [145] Tang, Q., Xu, J., and Pope, S., Probability density function calculations of local extinction and no production in piloted-jet turbulent methane/air flames, in *28th Symposium (Int.) on Combustion*, pp. 133–139, The Combustion Institute, Pittsburgh, PA, 2000.
- [146] Pitsch, H., Improved pollutant predictions in large-eddy simulations of turbulent non-premixed combustion by considering scalar dissipation rate fluctuations, *Proc. of the Comb. Inst.*, **29**:1971–1978 (2002).
- [147] Pitsch, H., Extended flamelet model for LES of non-premixed combustion, *CTR Annual Research Brief*, pp. 149–158 (2000).
- [148] Kim, S. and Huh, K., Second-order conditional moment closure modeling of turbulent piloted jet diffusion flames, *Combustion and Flame*, **138**:336–352 (2004).
- [149] Kronenburg, A. and Kostka, M., Modeling extinction and reignition in turbulent flames, *Combustion and Flame*, **143**:342–356 (2005).

- [150] Faeth, G. M., Current Status of Droplet and Liquid Combustion, *Prog. Energy Combust. Sci.*, **3**:191–224 (1977).
- [151] Faeth, G. M., Mixing, Transport and Combustion in Sprays, *Prog. Energy Combust. Sci.*, **13**:293–345 (1987).
- [152] Crowe, C. T., Troutt, T., and Chung, J. N., Numerical Models For Two-Phase Turbulent Flows, *Annu. Rev. Fluid Mech.*, **28**:11–43 (1996).
- [153] Crowe, C. T., Sommerfeld, M., and Tsuji, Y., *Multiphase Flows with Droplets and Particles*, CRC Press, Boca Raton, FL, 1998.
- [154] Gupta, A. K., Gas Turbine Combustion: Prospects and Challenges, *Energy Convers. Mgmt*, **38**(10–13):1311–1318 (1997).
- [155] Lakehal, D., On The Modeling of Multiphase Turbulent Flows for Environmental and Hydrodynamic Applications, *Int. J. of Multiphase Flow*, **28**:823–863 (2002).
- [156] Chigier, N. A., The Atomization and Burning of Liquid Fuel Sprays, *Prog. Energy Combust. Sci.*, **2**(2):97–114 (1976).
- [157] Borghi, R., The Links Between Turbulent Combustion and Spray Combustion and Their modelling, *In: The Proceedings of the 8th Symposium on Transport Phenomena in Combustion*, pp. 1–18 (1996).
- [158] Godsave, G. A. E., Studies of The Combustion of Drops in a Fuel Spray, *Proc. Combust. Inst.*, **4**:818–830 (1953).
- [159] Law, C. K., Recent Advances in Droplet Vaporization and Combustion, *Prog. Energy Combust. Sci.*, **8**:171–201 (1982).
- [160] Sirignano, W. A., Fuel Droplet Vaporization and Spray Combustion Theory, *Prog. Energy Combust. Sci.*, **9**:291–322 (1983).
- [161] Drew, D. A., Mathematical Modeling of Two-Phase Flow, *Annu. Rev. Fluid Mech.*, **15**:261–291 (1983).
- [162] Faeth, G. M., Evaporation and Combustion of Sprays, *Prog. Energy Combust. Sci.*, **9**:1–76 (1983).
- [163] Faeth, G. M., Spray Combustion Phenomena, *Proc. Combust. Inst.*, **26**:1593–1612 (1996).
- [164] Aggarwal, S. K., A Review of Spray Ignition Phenomena: Present Status And Future Research, *Prog. Energy Combust. Sci.*, **24**:565–600 (1998).
- [165] Birouk, M. and Gokalp, I., Current Status of Droplet Evaporation in Turbulent Flows, *Prog. Energy Combust. Sci.*, **32**:408–423 (2006).

- [166] Williams, F. A., Combustion of Droplets of Liquid fuels, *Combust. Flame*, **21**:1–31 (1973).
- [167] Sirignano, W. A., Fluid Dynamics of Sprays 1992 Freeman Scholar Lecture, *J. Fluids Eng.*, **115**:345–378 (1993).
- [168] Taylor, G. I., Diffusion by Continuous Movements, *Proc. Lond. Math. Soc.* (2), **20**:196–211 (1921).
- [169] Monin, A. S. and Yaglom, A. M., , Vol. 2, MIT Press, Cambridge, MA, 1975.
- [170] Kontomaris, K. and Hanratty, T. J., Effect of Molecular Diffusivity on Turbulent Diffusion in Isotropic Turbulence, *Int. J. Heat Mass Transfer*, **36**(5):1403–1412 (1993).
- [171] Borgas, M. S. and Sawford, B. L., A Family of Stochastic Models For Two-Particle Dispersion in Isotropic Homogeneous Stationary Turbulence, *J. Fluid Mech.*, **279**:69–99 (1994).
- [172] Annamalai, K. and Ryan, W., Interactive processes in gasification and combustion. Part I: Liquid drop arrays and clouds., *Prog. Energy Combust. Sci.*, **8**:221–295 (1992).
- [173] Bachalo, W. D., Injection, Dispersion, And Combustion of Liquid Fuels, *25th International Symposium on Combustion*, pp. 333–344 (1994).
- [174] Maly, R. R., State of The Art And Future Needs in S.I. Engine Combustion, *25th International Symposium on Combustion*, pp. 111–124 (1994).
- [175] Faeth, G. M., Structure and Atomization Properties of Dense Turbulent Sprays, *23rd International Symposium on Combustion*, pp. 1345–1352 (1990).
- [176] Faeth, G. M., Structure and Breakup Properties of Sprays, *Int. J. of Multiphase Flow*, **21**:99–127 (1995).
- [177] El-Banhawy, Y. and Whitelaw, J. H., Experimental Study of The Interaction Between a Fuel Spray and Surrounding Combustion Air, *Combust. Flame*, **42**:253–275 (1981).
- [178] Khalil, K. H., El-Mahallawy, F. M., and Moneib, H. A., Effects of Combustion Air Swirl on The Flow Pattern in a Cylindrical Oil Fired Furnace, *16th International Symposium on Combustion*, pp. 135–143 (1976).
- [179] Edwards, C. and Rudoff, R., Structure of S Swirl-Stabilized Spray Flame by Imaging, Laser Doppler Velocimetry, and Phase Doppler Anemometry, *23rd International Symposium on Combustion*, pp. 1353–1359 (1990).
- [180] Widmann, J. F. and Presser, C., A Benchmark Experimental Database for Multiphase Combustion Model Input and Validation, *Combust. Flame*, **129**:47–86 (2002).

- [181] Sommerfeld, M. and Qiu, H. H., Detailed Measurements in a Swirling Particulate Two-Phase Flow by a Phase-Doppler Anemometer, *Int. J. Heat and Fluid Flow*, **12**(1):20–28 (1991).
- [182] Sommerfeld, M. and Qiu, H. H., Experimental Studies of Spray Evaporation in Turbulent Flow, *Int. J. Heat and Fluid Flow*, **19**(1):10–22 (1998).
- [183] Karpetis, A. N. and Gomez, A., An Experimental Study of Well-Defined Turbulent Nonpremixed Spray Flames, *Combust. Flame*, **121**:1–23 (2000).
- [184] Khalil, K. H. and Whitelaw, J. H., Aerodynamic and Thermodynamic Characteristics of Kerosene Spray Flames, *16th International Symposium on Combustion*, pp. 569–576 (1976).
- [185] Sangiovanni, J. J. and Kesten, A. S., Effect of Droplet Interaction on Ignition in Monodispersed Droplet Streams, *16th International Symposium on Combustion*, pp. 577–592 (1976).
- [186] Tsushima, S. S., Saitoh, H., Akamatsu, F., and Katsuki, M., Observation of Combustion Characteristics of Droplet Clusters in A Premixed-Spray Flamee By Simultaneous Monitoring of Planar Spray Images and Local Chemiluminescence, *27th International Symposium on Combustion*, pp. 196–1974 (1998).
- [187] Presser, C., Gupta, A. K., Avedisian, C. T., and Semerjian, H. G., Fuel Property Effects on The Structure of Spray Flames, *23rd International Symposium on Combustion*, pp. 1361–1367 (1990).
- [188] Gupta, A. K., Linck, M., and Yu, K. H., Investigation of Two-Phase Reacting Flow Control for Advanced Navy Propulsion: Part 2 Combustion Control of Flame Signatures for Underwater Propulsion, *Proceedings of the Seventeenth ONR Propulsion Meeting*, pp. 19–26 (2004).
- [189] Yu, K. H., Parr, T. P., Wilson, K. J., Schadow, K. C., and Gutmark, E. J., Active Control of Liquid-Fueled Combustion Using Periodic Vortex-Droplet Interaction, *26th International Symposium on Combustion*, pp. 2843–2850 (1996).
- [190] Yu, K. H., Wilson, K. J., and Schadow, K. C., Liquid-Fueled Active Instability Suppression, *27th International Symposium on Combustion*, pp. 2039–2046 (1998).
- [191] Hsu, O., Pang, B., and Yu, K. H., Active Control Studies for Advanced Propulsion: Temperature Dependence of Critical Fuel Flux, *Proceedings of the 14th ONR Propulsion Meeting*, pp. 19–24 (2001).
- [192] Pang, B., Stamp, G., Marshall, A. W., and Yu, K. H., Investigation of Two-phase Flowfield in Actively Controlled Dump Combustor, *39th AIAA/ASME/SAE/ASEE Joint Propulsion Conference*, (2003).

- [193] Pang, B., Ahn, K., Stamp, G., Gupta, A. K., and Yu, K. H., Investigation on Two-Phase Reacting Flow Control for Advanced Navy Propulsion: Part 1. Enabling Technology Demonstration, *Proceedings of the 17th ONR Propulsion Meeting*, pp. 13–18 (2004).
- [194] Chung, T. J., *Computational Fluid Dynamics*, Cambridge University Press, 2002.
- [195] Salman, H. and Soteriou, M., Lagrangian Simulation of Evaporating Droplet Sprays, *Physics of Fluids*, **16**(12):4601–4622 (2004).
- [196] Mashayek, F. and Pandya, R., Analytical Description Particle/Droplet-Laden Turbulent Flows, *Prog. Energy Combust. Sci.*, **29**:329–378 (2003).
- [197] Pandya, R. and Mashayek, F., Two-Fluid Large-Eddy Simulation Approach For Particle-Laden Turbulent Flows, *Int. J. Heat Mass Trans.*, **45**(24):4753–4759 (2002).
- [198] Cuenot, B., Boileau, M., Pascaud, S., Mossa, J. B., Riber, E., Poinso, T., and Bérat, C., Large Eddy Simulation of Two-phase Reacting Flows, *ECCOMAS CFD 2006*, ():(2006).
- [199] Navaz, H. K. and Berg, R. M., Numerical Treatment of Multi-Phase Flow Equations with Chemistry and Stiff Source Terms, *Aerospace Science and Technology*, **2**(3):219–229 (1998).
- [200] Navaz, H., Dang, A., and Gross, K., Eulerian-Eulerian Treatment of Turbulent Dense Spray Combustion in a Bipropellant Liquid Rocket Engine, *In: JANNAF Combustion Meeting*, (1992).
- [201] Wan, Y. P. and Peters, N., Application of the Cross-Sectional Average Method to Calculations of the Dense Spray Region in a Diesel Engine, *SAE Paper 972866*, (1997).
- [202] Baumgarten, C., *Mixture Formation in Internal Combustion Engines*, Springer, 2006.
- [203] Peters, N., Reducing Mechanisms, in Smooke, M. D., editor, *Reduced Kinetic Mechanisms and Asymptotic Approximations for Methane-Air Flames, Lecture Notes in Physics*, Vol. 384, chapter 3, pp. 48–67, Springer-Verlag, Berlin, 1991.
- [204] von Berg, E., Edelbauer, W., Alajbegovic, A., and Tatschl, R., Coupled Calculation of Cavitating Nozzle Flow, Primary Diesel Fuel Break-up and Spray Formation with an Eulerian Multi-Fluid Model, *ICLASS*, (2003).
- [205] Beck, J. C. and Watkins, A. P., The Simulation of Fuel Sprays Using the Moments of the Drop Number Size Distribution, *Int. J. Engine Res.*, **5**(1):1–21 (2004).

- [206] Aggarwal, S. K. and Sirignano, A. W., Ignition of Fuel Sprays: Deterministic Calculations for Idealized Droplet Arrays, *20th International Symposium on Combustion*, **20**:1773–1780 (1984).
- [207] Sirignano, W. A., *Fluid Dynamics and Transport of droplets and Sprays*, Cambridge University Press, 1999.
- [208] Loth, E., Approaches for Motion of Dispersed Particles, Droplets and Bubbles, *Prog. Energy Combust. Sci.*, **26**:161–223 (2000).
- [209] Menon, S. and Patel, N., Subgrid Modeling for Simulation of Spray Combustion in Large-Scale Combustors, *AIAA Journal*, **44**(4):709–723 (2006).
- [210] Zhu, M., Bray, K. N. C., and Rogg, B., PDF Modelling of Spray Autoignition in High Pressure Turbulent Flow, *Combust. Sci. Tech.*, **120**:357–379 (1996).
- [211] Liu, Z., Zheng, C., and Zhou, L., A Joint PDF Model for Turbulent Spray Evaporation/Combustion, *Proc. Combust. Inst.*, **29**:561–568 (2002).
- [212] Sankaran, V. and Menon, S., , Vol. 3, 2002.
- [213] Salewski, M. and Fuchs, L., Consistency Issues of Lagrangian Particle Tracking Applied to A Spray Jet in Crossflow, *Int. J. of Multiphase Flow*, **33**:394–410 (2007).
- [214] Ying-wen, Y., Jian-xing, Z., Jing-zhou, Z., and Yong, L., Large-Eddy Simulation of Two-Phase Spray Combustion For Gas Turbine Combustors, *Int. J. of Multiphase Flow*, **28**(11).
- [215] Naud, B., PDF Modeling of Turbulent Sprays and Flames Using a Particle Stochastic Approach, Phd thesis, Technische Universiteit Delft, Delft, NL, 2003, See also URL [www.ws.tn.tudelft.nl/downloads/Thesis\\_Naud.pdf](http://www.ws.tn.tudelft.nl/downloads/Thesis_Naud.pdf).
- [216] Rangel, R. H., Heat Transfer in Vortically Enhanced Mixing of Vaporizing Droplet Sprays, *Annu. Rev. Heat Transfer*, **4**:331–362 (1992).
- [217] Sirignano, W. A., Theoretical Foundations for the Analysis of Laminar and Turbulent Spray Flows, *Proceedings of the Western States Section/Combustion Institute Fall Meeting*, (2003).
- [218] Vervisch, L., Hauguel, R., Domingo, P., and Rullaud, M., Three Facets of Turbulent Combustion Modelling: DNS of Premixed V-flame, LES of Lifted Nonpremixed Flame and RANS of Jet Flame, *J. of Turb.*, **5**(4) (2004).
- [219] Rèveillon, J. and Vervisch, L., Analysis of Weakly Turbulent Diluted-Spray Flames and Spray Combustion Diagram, *J. Fluid Mech.*, **537**:317–347 (2005).
- [220] Schroll, P., Wandel, A., Cant, R., and Mastorakos, E., Direct Numerical Simulations of Autoignition in Turbulent Two-Phase Flows, *Proc. Combust. Inst.*, (2008).

- [221] Y. Wang, C. R., Effects of Temperature and Equivalence Ratio on The Ignition of n-Heptane Fuel Spray in Turbulent Flow, *Proc. Combust. Inst.*, **30**:893–900 (2005).
- [222] Sreedhara, S. and Huh, K. Y., Conditional Statistics of Nonreacting and Reacting Sprays in Turbulent Flows by Direct Numerical Simulation, *Proc. Combust. Inst.*, **31**:2335–2342 (2007).
- [223] Y. Wang, C. R., Direct Numerical Simulations of Ignition in Turbulent n-Heptane Liquid-Fuel Spray Jets, *Combustion and Flame*, **149**(4):353–365 (2007).
- [224] J. Rèveillon, F. D., Evaporating Droplets in Turbulent Reacting Flows, *Proc. Combust. Inst.*, **31**(2):2319–2326 (2007).
- [225] Klose, G., Schmehl, R., Meier, R., Meier, G., Koch, R., Wittig, S., Hettel, M., Leuckel, W., and Zarzalis, N., Evaluation of Advanced Two-Phase Flow and Combustion Models for Predicting Low Emission Combustors, *ASME Turbo Expo 2000. 45th ASME GasTurbine and Aeroengine Congress*, (2000).
- [226] Datta, A., Influence of Inlet Flow Conditions on the Performance of a Swirl-Stabilized Combustor Burning Liquid Fuel Spray, *Int. J. Energy Res.*, **24**:373–390 (2000).
- [227] Guo, Y., Chan, C. K., and Lau, K. S., A Pure Eulerian Model for Simulating Dilute Spray Combustion, *Fuel*, **81**(16):2131–2144 (2002).
- [228] Ham, F., Apte, S., Iaccarino, G., Wu, X., Hermann, M., Constantinescu, G., Mahesh, K., and Moin, P., Unstructured LES of Reacting Multiphase Flows in Realistic Gas Turbine Combustors, *Annual Research Briefs-Center for Turbulence Research*, (2003).
- [229] Sankaran, V. and Menon, S., LES of Spray Combustion in High Reynolds Number Swirling Flows, *Presented in 2nd International Symposium on Turbulence and Shear Flow Phenomena*, (2001).
- [230] Bellan, J., Perspective on Large Eddy Simulations for Sprays: Issues And Solutions, *Atom. Sprays*, **10**:409–425 (2000).
- [231] Almeida, T. G. and Jaber, F. A., Large-Eddy Simulation of a Dispersed Particle-Laden Turbulent Round Jet, *Int. J. Heat Mass Transfer*, **51**:683–695 (2008).
- [232] Mahesh, K., Constantinescu, G., Apte, S., Iaccarino, G., Ham, F., and Moin, P., Progress Towards Large-Eddy Simulation of Turbulent Reacting and Non-reacting Flows in Complex Geometries, *Ann. Research Briefs*, pp. 115–142 (2002).

- [233] Mahesh, K., Constantinescu, G., and Moin, P., A Numerical Method for Large-Eddy Simulation in Complex Geometries, *J. Comput. Phys.*, **197**:215–240 (2004).
- [234] Apte, S. V., Gorokhovski, M., and Moin, P., Large-Eddy Simulation of Atomizing Spray With Stochastic Modeling of Secondary Breakup, *ASME Turbo Expo 2003- Power for Land, Sea and Air*, p. (2003).
- [235] Pascaud, S., Boileau, M., Cuenot, B., and Poinso, T., Large Eddy Simulation of Turbulent Spray Combustion in Aeronautical Gas Turbines, *ECCOMAS Thematic Conference on Computational Combustion*, p. (2005).
- [236] Okong'o, N. and Bellan, J., Consistent Large-Eddy Simulation of a Temporal Mixing Layer Laden With Evaporating Drops. Part 1: Direct Numerical Simulation, Formulation, and A priori Analysis, *J. Fluid Mech.*, **499**:1–47 (2004).
- [237] Leboissetier, A., Okong'o, N., and Bellan, J., Consistent Large-Eddy Simulation of a Temporal Mixing Layer Laden With Evaporating Drops. Part 2: A Posteriori Modeling, *J. Fluid Mech.*, **523**:37–78 (2005).
- [238] Patel, N., Kirtas, M., Sankaran, V., and Menon, S., Simulation of Spray Combustion in a Lean Direct Injection Combustor, *Proc. Combust. Inst.*, **31**(2):2327–2334 (2007).
- [239] Mahesh, K., Constantinescu, G., Apte, S., Iaccarino, G., Ham, F., and Moin, P., Large-Eddy Simulation of Reacting Turbulent Flows in Complex Geometries, *J. Applied Mech.*, **73**:374–381 (2006).
- [240] Afshari, A., Almeida, T., Mehravan, K., and Jaber, F. A., Large Scale Simulations of Turbulent Combustion and Propulsion Systems, *Proceedings of the Seventeenth ONR Propulsion Meeting*, pp. 41–51 (2004).
- [241] Afshari, A. and Jaber, F. A., Large Eddy Simulation of Turbulent Flows in an Axisymmetric Dump Combustor, *AIAA Journal*, **46**(7):1576.
- [242] Jaber, F. A. and Colucci, P. J., Large Eddy Simulation of Heat And Mass Transport in Turbulent Flows. Part 1: Velocity Field, *Int. J. Heat and Mass Trans.*, **46**(10):1811.
- [243] Jaber, F. A. and Colucci, P. J., Large Eddy Simulation of Heat And Mass Transport in Turbulent Flows. Part 2: Scalar field, *Int. J. Heat and Mass Trans.*, **46**(10):1827.
- [244] Yaldizli, M., Mehravan, K., and Jaber, F. A., Large-Eddy Simulations of Turbulent Methane Jet Flames with Filtered Mass Density Function, *Combustion and Flame*, (2008), in review.

- [245] Mashayek, F. and Jaber, F. A., Dispersion And Polydispersity of Droplets in Stationary Isotropic Turbulence, *Int. J. Multiphase Flow*, **23**(2):337–355 (1997).
- [246] Jaber, F. A., Temperature Fluctuations in Particle-Laden Homogeneous Turbulent Flows, *Int. J. Heat Mass Transfer*, **41**:4081–4093 (1998).
- [247] Mashayek, F. and Jaber, F. A., Particle Dispersion in Forced Isotropic Low-Mach-Number Turbulence, *Int. J. Heat Mass Trans.*, **42**:2823–2836 (1999).
- [248] Jaber, F. A. and Mashayek, F., Temperature Decay in Two-Phase Turbulent Flows, *Int. J. Heat Mass Trans.*, **43**:993–1005 (2000).
- [249] Almeida, T. G. and Jaber, F. A., Direct Numerical Simulations of A Planar Jet Laden With Evaporating Droplets, *Int. J. Heat Mass Transfer*, **49**:2113–2123 (2006).
- [250] Miller, R. S., Effects of Nonreacting Solid Particle and Liquid Droplet Loading on An Exothermic Reacting Mixing Layer, *Physics of Fluids*, **13**(11):3303–3320 (2001).
- [251] Miller, R. S. and Bellan, J., Direct Numerical Simulations of a Confined Three-Dimensional Gas Mixing Layer With One Evaporating Hydrocarbon-Droplet-Laden Stream, *J. Fluid Mech.*, **384**:293–338 (1999).
- [252] Jaber, F. A., Colucci, P. J., James, S., Givi, P., and Pope, S. B., Filtered Mass Density Function for Large Eddy Simulation of Turbulent Reacting Flows, *J. Fluid Mech.*, **401**:85–121 (1999).
- [253] Jaber, F. A., Large Eddy Simulation of Turbulent Premixed Flames via Filtered Mass Density Function, *37th AIAA Aerospace Sciences Meeting and Exhibit, Reno, NV*, (1999).
- [254] Garrick, S. C., Jaber, F. A., and Givi, P., Large eddy Simulation of Scalar Transport in a Turbulent Jet Flow, *Recent Advances in DNS and LES, Fluid Mechanics and its Applications*, **54**:155–166 (1999).
- [255] Kennedy, C., Low storage, explicit Runge-Kutta schemes for the compressible Navier-Stokes Equations, *NASA Technical paper*, (1997).
- [256] Crowe, C. T., Sharma, M. P., and Stock, D. E., The Particle-Source in Cell (Psi-Cell) Model for Gas-Droplet Flows, *J. Fluids Eng.*, **6**:325–332 (1977).
- [257] Pope, D. N. and Gogos, G., Numerical Simulation of Fuel Droplet Extinction due to Forced Convection, *Combust. Flame*, **142**:89–106 (2005).
- [258] Rudy, D. and Strikwerda, J., Boundary Conditions for Subsonic Compressible Navier-Stokes Calculations, *J. Comp. Phys.*, **36**:327–338 (1980).

- [259] Bossard, J. A. and Peck, R. E., Droplet Size Distribution Effectst in Spray Combustion, *26th International Symposium on Combustion*, pp. 1671–1677 (1996).
- [260] Mashayek, F., Direct Numerical Simulations of Evaporating Droplet Dispersion in Forced Low Mach Number Turbulence, *Int. J. Heat Mass Transfer*, **41**(17):2601–2617 (1998).
- [261] Jaber, F. A. and James, S., Effects of Chemical Reaction on Two-Dimensional Turbulence, *J. Sci. Comp.*, (1999), in press.
- [262] Park, T. W. and Aggarwal, S. K., A Numerical Study of Droplet-Vortex Interactions in An Evaporating Spray, *Int. J. Heat Mass Transfer*, **39**(11):2205–2219 (1996).
- [263] Khatumria, V. C. and Miller, R. S., Numerical Simulation of A Fuel Droplet Laden Exothermic Reacting Mixing Layer, *Int. J. Multiphase Flow*, **29**:771–794 (2003).

MICHIGAN STATE UNIVERSITY LIBRARIES



3 1293 03062 6257